The petrography and mineral chemistry of melt-intruded mantle xenoliths from the Chidliak kimberlite field, Baffin Island, Canada

By

Brody Cameron Myers

A thesis submitted in partial fulfillment of the requirements for the degree of

Master of Science

Department of Earth and Atmospheric Sciences
University of Alberta

Abstract:

The nature of kimberlitic melts at mantle depths and their interaction with mantle wall-rocks is poorly constrained. This is due to the scarcity of mantle xenoliths and xenocrysts that have preserved this interaction without disaggregating during their transport to Earth's surface. This thesis presents the petrography and geochemistry of a set of unaltered mantle xenoliths containing unique, crystallized melt pockets and veins that represent the interaction of mantle melts with wall-rocks.

The xenoliths in this study were collected from diamond drill core from the Upper Jurassic CH-6 and Lower Cretaceous CH-7 kimberlite pipes in the Chidliak kimberlite field, Baffin Island, Canada. The sample suite consists of peridotites, a pyroxenite, and an eclogite. Major-, minor-, and trace-element compositions of xenolith minerals and kimberlite whole-rocks from CH-6 and -7 were determined. In addition, the isotopic composition of the CH-6 and -7 kimberlite whole-rocks were determined.

Using conventional element exchange geothermobarometry, the xenoliths were found to have been entrained from a range of depths and temperatures in the mantle including both the spinel and garnet stability fields, which is consistent with their mineralogy. The eclogite equilibration pressure was determined by calculating the temperature it last equilibrated at in the mantle, then projecting it onto the Chidliak mantle geotherm of Pell et al. (2013). Thermobarometric calculations indicate the xenoliths last equilibrated in the mantle at temperatures between 646 and 1238 °C at depths from ~ 63 to 213 km.

Melt in garnet-bearing peridotites form both pocket and vein textures. In contrast, the eclogite only contains melt veins that follow grain boundaries and occasionally transect garnet grains. Spinel peridotites contain melt veins with textures indicating brittle fracture associated with injection of fluid/melt. The melts crystallised as complex intergrown assemblages of spinel group minerals, apatite, perovskite, ilmenite, and Ni-sulphides with secondary serpentine, brucite, carbonates, and mica. Melt-pockets contain both Cr-rich and Cr-poor spinels with a range of magnesian ülvospinel-magnetite compositions that extend to more oxidized compositions than found in kimberlite groundmass spinels from CH-6 and CH-7. The mineral assemblage and mineral compositions in the melt intrusions are compatible with kimberlite melt infiltrating these xenoliths. Petrographic evidence of the host kimberlite infiltrating the edges of xenoliths, combined with compositional overlap of spinel group minerals, ilmenite, and perovskite in the melt intrusions with the kimberlite groundmass, suggests that the infiltrating melt was the host kimberlite. Cr-rich spinels in some of the melt intrusions indicate the intrusions crystallized from a relatively un-evolved phase of kimberlite, but the relative scarcity of fine-grained ilmenite in the melt intrusions indicates that the intrusion event did not occur until almost all ilmenite had crystallized as megacrysts and/or in the fine-grained kimberlite groundmass. The evidence suggests that the xenoliths were intruded by kimberlitic melt shortly prior to, or during mantle transit of CH-6 and CH-7 kimberlite magmas from 68 to 20 kbar.

The highly depleted character of most of the peridotites in the xenolith suite (> 40% melt extraction) indicated by the lack of orthopyroxene and high olivine content (> 90%), suggests that clinopyroxene was re-introduced into the xenoliths after initial exhaustion during partial melting in the spinel stability field. Garnets in the peridotite xenoliths typically have $Cr_2O_3 >$ 3 wt% and are interpreted to have formed via metamorphism during subduction and lithospheric thickening, based on the model of Brey and Shu (2018) to produce high-Cr_2O_3 garnets. The high CaO content of the garnets relative to typical garnets from highly depleted peridotites, suggests they have been metasomatically-enriched in CaO. This metasomatic agent could have been the same agent that re-introduced clinopyroxene into the xenoliths. The trace element compositions of the garnets in CH-7 xenoliths reveal they were dominantly metasomatized by an Fe-Ti-rich melt. In contrast, two xenoliths with CaO-rich garnets have trace element compositions consistent with carbonatitic metasomatism.

Preface:

This thesis is an original work by Brody Myers. No part of this thesis has been previously published.

Acknowledgments:

I would first like to thank my supervisors Bob Luth and Graham Pearson for their exceptional mentorship throughout my graduate studies. As my main supervisor, Bob met with me weekly to answer my questions, offer valuable insights, and simply chat. Both supported my career endeavours every summer and I'm tremendously grateful for the opportunities they allowed me to take part in, as well as imparting a wealth of knowledge about mantle petrology to me. Bob also taught me the difference between "which" and "that", which greatly improved my writing.

Thank you to my committee members Bob Luth, Graham Pearson, Bruce Kjarsgaard, and chair Thomas Stachel for your insightful comments that improved the final product and will aid any future publications from this research.

This research benefitted tremendously from many people I met throughout my graduate studies. Matt Hardman went above and beyond to answer my questions, edit my work, and teach me many things about mantle petrology any time I asked. Connor Elzinga, Mark Labbe, Walt Harley, Andrew Locock, Yan Luo, Chiranjeeb Sarkar, Sarah Woodland, Alex Sheen, and Ian Beitz all contributed significantly to the sample preparation and excellent data that was collected for this thesis. Andrew and Chiranjeeb also provided excellent mentorship on topics of mineralogy and geochemistry.

Jennifer Pell (formerly with Peregrine Diamonds Ltd.) is gratefully acknowledged for discovering and collecting the samples that became the focus of this study, as well as Herman Grütter who recognized the significance of the melt pockets and facilitated this research project. Thanks to Mike Seller and De Beers Canada for their continued support and interest in this research after they purchased the Chidliak project. This project was funded through the DERTS program at the U of A and NSERC Discovery grants from Bob Luth and Graham Pearson.

I would like to thank Anetta Banas for her excellent job running the Diamond Exploration and Research Training School. Graduate school was greatly enhanced by the friendships and experiences I enjoyed with my colleagues. Finally, thank you to my wonderful family for supporting me from start to finish.

Table of Contents

List of tables

List of figures

Chapter 1 : Introduction

1.1 Introduction and Background

1.1.1 Thesis goals and objectives

The main goal of this thesis is to characterize the nature of ancient metasomatism and a more recent melt infiltration event that acted in the lithospheric mantle beneath Baffin Island, Nunavut, Canada. This is accomplished by studying the petrography and elemental compositions of minerals from a set of metasomatized mantle xenoliths containing fully crystallized former melt veins and pockets. The xenoliths in this study were hosted by the CH-6 and CH-7 kimberlites from the Chidliak kimberlite field in Baffin Island. Using the elemental compositions of minerals in their host xenoliths, I constrain the pressure-temperature conditions at which the xenoliths last equilibrated in the lithospheric mantle. Using major- and trace-element compositions of host xenolith minerals and the polymineralic melt intrusions, I examine the compositional characteristics of the metasomatic agents that acted upon the xenoliths. The major- and trace-element compositions of the polymineralic intrusions are compared with CH-6 and CH-7 kimberlite whole-rocks to determine if the intrusions are related to the kimberlite magmas that entrained the xenoliths.

1.1.2 Background and previous work

The rigid subcontinental lithospheric mantle (SCLM) beneath cratons forms a deep root extending to as deep as 250 km (e.g., Heaman and Pearson, 2010). The SCLM is chemically, thermally, and physically distinct from the underlying asthenosphere. Heat transfer in the SCLM is by conduction, rather than convection, and the SCLM is depleted in radioactive heat producing elements (eg., K, U, Th) (e.g., Pollack and Chapman, 1977; Stachel and Harris, 2008); characteristics that translate to colder temperatures than the convecting mantle at similar depths. Statistical studies of mantle concentrate minerals transported to the surface by kimberlites, demonstrate that globally the upper mantle sampled by kimberlite is dominated by peridotite (> 95%) with minor eclogite varying from 1 to 5% (Dawson and Stephens, 1975; Schulze, 1989) depending on locality. The process of partial melt extraction that produces the peridotite in the SCLM results in geochemical depletion relative to primitive upper mantle in elements such as Ca, Al, and Fe (Jordan, 1978). The removal of these elements causes the SCLM to become rheologically stronger and more buoyant than the underlying convecting asthenosphere. Small volume fluids/melts rich in incompatible major, minor, and trace elements from the underlying asthenosphere, may percolate through the

SCLM and refertilize the originally depleted SCLM (e.g., McKenzie, 1989). This metasomatic process has been extensively studied (e.g., Dawson, 1984; Erlank, 1987; Harte et al., 1975; Menzies, 1983). The effects of metasomatism can sometimes be deduced petrographically when minerals additional to the original residual peridotite assemblage have crystallized ("modal" metasomatism) (Harte, 1983). Conversely, the effects of metasomatism may be invisible petrographically, as metasomatism may just make subtle changes to the compositions of existing phases ("cryptic" metasomatism) (Dawson, 1984). Collectively, modal and cryptic metasomatism are classified as "primary metasomatic" features (Harte, 1983). Initially, researchers focused on modal metasomatism that resulted in the addition of hydrous and other exotic phases such as phlogopite, amphibole, and ilmenite (e.g., Dawson and Smith, 1982; Erlank and Rickard, 1977; Jones et al., 1982). More recently, researchers have studied elemental compositions of anhydrous minerals (clinopyroxene, orthopyroxene, garnet, olivine) for evidence of modal and cryptic metasomatism (Pearson and Wittig, 2014 and references therein).

Melt veins in xenoliths have been termed "late secondary" features (Harte, 1983) and are typically interpreted to represent melt infiltration shortly prior to, or during, entrainment by the host kimberlite. Melt infiltrated xenoliths and megacrysts have been the focus of a number of studies (e.g., Bussweiler et al., 2016; Dawson et al., 2001; Haggerty and Boyd, 1975; Howarth and Büttner, 2019; Kinny and Dawson, 1992; Schulze, 1985; van Achterbergh et al., 2002). These studies have suggested that melt infiltration of wall rocks in magma chambers and in megacrysts likely occurs in the short timescales leading up to the kimberlite eruption and transport to surface. This timing was confirmed by U-Pb geochronology of zircons within melt intruded veins in a harzburgite xenolith from the Bultfontein kimberlite, which had an age indistinguishable from the eruption age (Kinny and Dawson, 1992). Bussweiler et al. (2016) describes finding compositional zoning in megacryst hosts in the areas surrounding the melt inclusions. They suggest that because equilibrium is quickly achieved under lithospheric mantle P-T conditions, the compositional zoning requires that melt intruded before kimberlite eruption or during their rapid ascent to surface. Additionally, van Achterbergh et al. (2002) found isotopic disequilibrium between melt intrusions and their megacryst hosts, indicating a close temporal link to the kimberlite eruption.

Researchers have interpreted the compositions of melt intrusions in a variety of ways, such as: early unevolved kimberlite (e.g., Bussweiler et al., 2016; Haggerty and Boyd, 1975), trapped kimberlite melt from the same magma that crystallized the host megacryst (e.g., Schulze, 1985), several pulses of kimberlite-related liquids (e.g., Jones et al., 1982), carbonated/carbonatitic kimberlite melt (e.g., Dawson et al., 2001; Howarth and Büttner, 2019), and kimberlite fractionation resulting in both carbonatitic and ultramafic endmember melt inclusions (Araújo et al., 2009).

Primary kimberlite compositions are poorly constrained because of contamination by crustal and mantle material, late-stage deuteric alteration, and post-emplacement fluid migration caused by exsolution of volatiles (e.g., Le Roex, 2003). Therefore, kimberlite-whole rock samples are inaccurate representatives of the initial primary magma composition (e.g., Mitchell, 2008). Therefore, melts trapped within xenoliths and xenocrysts offer the potential to give us a glimpse of kimberlite melts at mantle conditions.

1.1.3 Geological setting

The Chidliak kimberlite field ("Chidliak") occurs on the Hall Peninsula in Baffin Island, Nunavut, Canada. The kimberlites are dominantly emplaced into 2.92-2.80 Ga gneisses of the Hall Peninsula Block (Scott, 1999; Whalen et al., 2010). The location and crustal geology of Chidliak is outlined in Figure 1.1.1.

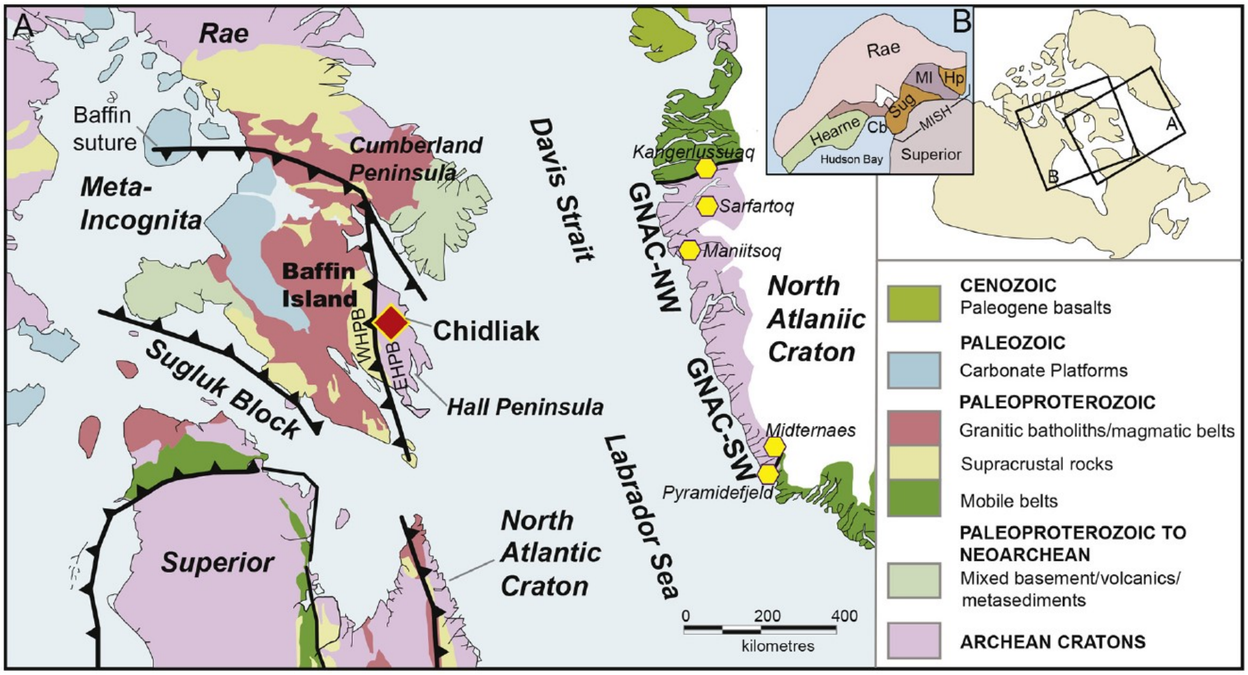

Figure 1.1.1 - Location map of the Chidliak kimberlite field showing the regional geology of Baffin Island and the Hall Peninsula (Xu et al., 2021).

1.1.4 Chidliak kimberlites

To date, 74 kimberlites have been located at Chidliak (Heaman et al., 2015), 42 of which have been proven to be diamondiferous (Pell et al., 2013). The kimberlites occur as steeply dipping dyke and pipe-like bodies, with surface areas ranging from < 1 to 5 hectares

(Pell et al., 2013). Kimberlites CH-7 and CH-6, relevant to this study, have surface areas of ~1 hectare each. CH-7 contains at least two distinct lobes that are elliptical in shape, and CH-6 is a single body with a kidney to elliptical shape (Pell et al., 2013). The groundmass mineralogy of Chidliak kimberlites includes spinel, perovskite, monticellite, phlogopite, apatite, carbonate and serpentine (Pell et al., 2013), indicating they are Group I (Skinner, 1986; Smith, 1983) or archetypal (Mitchell, 1995) kimberlites.

Heaman et al. (2015) used U-Pb perovskite geochronology to determine the emplacement ages of 44 of the kimberlites, which range from 157.0 to 139.1 Ma (Upper Jurassic to Lower Cretaceous). CH-7 was emplaced at 143.0 ± 1.6 Ma and CH-6 at 149.9 ± 1.0 Ma. The emplacement age and Sr/Nd isotopic composition of the groundmass perovskites from Chidliak are similar to some Jurassic kimberlites from the North Atlantic Craton in SW Greenland, which have emplacement ages between 149.7 and 152.0 Ma (Heaman et al., 2015, and references therein). This led Heaman et al. (2015) to suggest the kimberlites have a common origin from a similar mantle source region. They suggest that the origin of the kimberlites could be from low-degree partial melting of metasomatized peridotite in the deep lithosphere, triggered by heating from adiabatic upwelling of the asthenosphere.

1.1.5 Previous studies on Chidliak mantle xenoliths and diamonds

Previous researchers have studied the mineralogy and mineral chemistry of mantle-derived fragments that are hosted in Chidliak kimberlites. The kimberlites contain olivine macrocrysts and mantle xenocrysts of Cr-pyrope garnet, eclogitic/websteritic garnets, clinopyroxene, spinel, and picroilmenite (Pell et al., 2013). Some bodies contain fresh spinel- and garnet lherzolite, garnet harzburgite, garnet wehrlite, garnet websterite and eclogite xenoliths (Kopylova et al., 2019; Pell et al., 2013; Pobric et al., 2020). The calculated pressure-temperature of last equilibration in the mantle of peridotite xenoliths and clinopyroxene xenocrysts dominantly lie on model conductive geotherms with between 35 and 39 mW/m^2 surface heat flow (Kopylova et al., 2019; Pell et al., 2013). However, at pressures between 62 – 68 kbar, near the base of the lithosphere, the mantle shows signs of thermal disturbance by having large temperature differences (up to 200 °C) at similar pressures (Kopylova et al., 2019; Pell et al., 2013).

CH-6 peridotite xenoliths studied by Kopylova et al. (2019) last equilibrated in the mantle between 600 and 1300 °C and pressures of 28-75 kbar, and CH-7 peridotite xenoliths were dominantly entrained at calculated temperatures between 1000 and 1300 °C, and pressures between 50 and 75 kbar. Eclogite xenoliths studied by Pobric et al. (2020) had calculated P-T values clustering in two groups, low-temperature: 840 to 990 °C at 41 to 50 kbar, and high-temperature, super-adiabatic: > 1320 °C at P > 70 kbar. Most studied xenoliths from Chidliak last equilibrated within the diamond stability field. Nitrogen-based mantle residence temperatures of Chidliak diamonds studied by Nichols (2014) range from ~ 980 to 1350 °C, and mineral inclusions in Chidliak diamonds equilibrated between ~ 1050 and 1150 °C (Xia, 2018).

In a study of 120 peridotite and pyroxenite xenoliths from Chidliak, Kopylova et al. (2019) found the mineral assemblages, textures, and major element geochemistry indicate a complex and protracted metasomatic history. Widespread wehrlitization, with the occasional development of ilmenite, was suggested to be a result of Proterozoic silicate-carbonate metasomatism by Kopylova et al. (2019). Clinopyroxene mantles on garnet (indicating re-introduction of clinopyroxene), bulk rock compositions of the peridotites indicating high levels of melt depletion followed by enrichment in Ca and Al, occasional development of ilmenite in wehrlites, higher fayalite content in wehrlitic olivines, and higher modal abundance of olivine compared to typical cratonic xenoliths were used as evidence to support this. These authors suggest that subsequent metasomatism led to enriched Ti and Na in garnet, clinopyroxene, and orthopyroxene in xenoliths from CH-1, -7, and -44 kimberlites, but not in CH-6 xenoliths. The emplacement age of CH-6 is within error of the age of CH-1 (Heaman et al., 2015), which suggests this metasomatic event was spatially restricted rather than temporally. Along with Ti and Na, orthopyroxene shows enrichment of Al, Ca, and Cr. The metasomatic event was interpreted to be concurrent with high temperature deformation, which sheared the lithospheric mantle between pressures of 55 and 65 kbar. More recent textures that may have formed during ascent in the kimberlite are observed in some xenoliths such as spongy textures in clinopyroxene and garnet, indicative of partial melting, as well as rims of monticellite on clinopyroxene, and clinopyroxene overgrowths on orthopyroxene.

Pobric et al. (2020) interpreted the high MgO and low FeO contents of Chidliak eclogites to have resulted from carbonated ultramafic melt metasomatism. Additional evidence of carbonate metasomatism was identified by these authors in four eclogite xenoliths with enriched whole-rock LREE and Sr. The authors suggest that possible effects of the Ti-metasomatism identified by Kopylova et al. (2019) between 55 and 65 kbar, could be reflected in some of the eclogites that exceed 1.5 wt% TiO_2 in their re-constructed whole rock compositions, as well as the elevated calculated temperatures of three eclogites that have super-adiabatic temperatures (Pobric et al., 2020).

Kopylova et al. (2019) used evidence from similar silicate-carbonate metasomatism, bulk-rock geochemistry, mineral chemistry, as well as the olivine-rich, orthopyroxene-poor nature of the Chidliak peridotites to propose that the Hall Peninsula Block, in which Chidliak outcrops, is a rifted fragment of the North Atlantic Craton (NAC) that also outcrops in West Greenland. Additional support of this is the broadly consistent Re-depletion age of samples from both cratonic mantles (Liu et al., 2017; Xu et al., 2021).

1.1.6 Chidliak diamonds

As of 2013, caustic fusion analyses had been performed on 46 of the kimberlites, revealing that 42 were diamondiferous, including CH-6 and CH-7 (Pell et al., 2013). The diamonds are dominantly sourced from an eclogitic paragenesis, with nitrogen-based mantle residence temperatures between ~ 980 to 1350 °C (80% fall between 1050-1150 °C) (Hogberg et al., 2016). This agrees with the findings of Xia (2018), who used diamond inclusions to calculate equilibration temperatures of ~ 1050 to 1150 °C. The temperature range of diamond residence corresponds to depths between ~ 150 and 200 km in the SCLM. Yellow diamonds from CH-7 were documented as having two temporally distinct growth events involving different diamond forming fluids (Lai et al., 2020). The authors propose an initial stage that crystallized colourless cores, and a second that formed yellow rims that crystallized very close to the timing of kimberlite emplacement.

1.1.7 Chidliak melt-bearing mantle xenoliths

A suite of melt-bearing mantle xenoliths from diamond drill core from CH-6 and CH-7 kimberlites were discovered by Herman Grütter (formerly of Peregrine Diamonds Ltd.) and are the focus of this study. These melt intrusions are important because they represent an intrusion event that occurred with a close temporal link to the CH-6 and CH-7 kimberlites. Also, they may trap kimberlitic melt at basal lithospheric P/T conditions, prior to extensive evolution during lithosphere transit and possible assimilation. Therefore, these former melts can help to understand the possible early stages of kimberlite melt evolution, and the nature and origin of melts that occurred in the subcontinental lithospheric mantle beneath Chidliak. Additionally, they may provide more context to the metasomatic history of Chidliak, particularly for recent metasomatic events such as the one that crystallized yellow rims on diamonds.

Chapter 2 : Methods

2.1 Sample description

2.1.1 Introduction

The mantle xenoliths in this study were collected from diamond drill core by Herman Grütter (formerly of Peregrine Diamonds Ltd.) in 2016, who primarily selected them for study of their melt inclusions. The suite consists of three xenoliths that were hosted by the CH-6 kimberlite (two are melt-bearing) and 22 that were hosted by CH-7 kimberlite (19 are melt-bearing). Kimberlite whole-rock samples were sampled as well, from pieces of drill core adjacent to the xenoliths.

2.1.2 Sample preparation

All xenoliths were photographed before small blocks (~ 1 x 4 x 3 cm) were cut from them for preparation of 30 μm thick polished thin sections. An Isomet slow-speed saw and a high speed-wafering saw that were lubricated with isopropyl alcohol and ethylene glycol were used to cut the xenolith blocks from the drill core. The thin sections were polished using silicon carbide lubricated with ethylene glycol and isopropyl alcohol. This was done to preserve any water-soluble minerals in the xenoliths and/or melt-intrusions, which were not identified in any subsequent analyses. Multiple thin sections were created from some of the xenoliths, these are identified by adding the arbitrary letter "M" or "V" to the end of the original xenolith I.D.

Kimberlite whole-rock samples were cut with a high-speed wafering saw using water lubrication. All surfaces were then abraded with silicon carbide paper to remove potential surface contamination, before being washed in an ultrasonic bath. The samples were then crushed using a rock hammer. Obvious crustal xenoliths – such as carbonate sedimentary clasts - were removed from the samples using a binocular microscope before being powdered in an agate ball mill. Pure quartz was used to clean the apparatus in-between each sample. The resulting powders were placed in separate plastic containers to be used for X-ray fluorescence, high resolution inductively-coupled plasma mass spectrometry, and thermal ionization mass spectrometry.

Sampling of melt pockets in xenoliths was conducting using a New Wave Research/Merchantek MicroMill closely following procedures outlined in Charlier et al. (2006). This study used conical-tipped tungsten carbide drill bits supplied by New Wave Research (part number: 2500-0033), with a tip angle of ~ 23.5°. Before each micromilling session, the sample and drill bit were cleaned in an ultrasonic bath immersed in milliQ water and ethanol, respectively. Samples were excavated by drilling holes arranged in rectangular grids on cut blocks of four different xenoliths. Each drill hole was set to a drill depth of 300 µm, divided into ten passes at 30 µm increments. Depending on the size of the pocket, between 33 and 105 holes were excavated per sample, with a spacing of 150 µm between the centre of each hole in both X and Y directions. Before drilling, a ~ 1 × 1 cm piece of parafilm was applied on the sample surface, with a ~ 3 × 3 mm hole cut out in the centre directly overlaying the drill area. A droplet of milliQ water was then placed over the cut-out hole, which secured the droplet in place. Drilling took place at the base of the water droplet, which served to collect the excavated sample powder and prevent the drill bit from overheating. The excavated sample powder, suspended in the water droplet, was drawn up with a pipette. It was observed that some sample fragments remained on the sample surface, either due to being larger in size or being trapped in drilled holes. The sample slurry was pipetted into custom-made PTFE weighing boats and were dried down overnight at 70°C before weighing.

2.1.3 Sample petrography

Sample mineralogy and textures were documented from each xenolith by examination of the thin sections using a petrographic microscope. Mineral modal abundances were mostly estimated visually in thin sections using a petrographic microscope. However, more precise modal abundances of orthopyroxene and clinopyroxene in peridotite samples (except the harzburgite) were determined by tracing the outlines of the grains in scanned thin sections on Adobe Illustrator and calculating the area they occupied.

2.2 Elemental compositions

2.2.1 Major- and minor-elements

Quantitative major- and minor-element analyses of minerals were determined by electron probe microanalysis (EPMA) on polished thin sections using a CAMECA SX100 and a JEOL8900R at the Electron Microprobe Lab in the Department of Earth and Atmospheric Sciences, University of Alberta. The EPMA instruments are equipped with five wavelength dispersive spectrometers (WDS) for quantitative element analysis and one energy dispersive spectrometer (EDS) for qualitative element analysis. Backscattered-electron (BSE) images of minerals in thin sections were collected with the EPMA instruments to be used in this study. Multiple analytical points were taken on larger grains to assess compositional heterogeneity within single grains. The spectrometer settings, standards, lower limit of detection (LLD), and peak count times of each mineral group are described below and tabulated in Appendix A, Table A.1. The LLD for oxides vary by mineral type and analytical condition; they are generally between 0.01 and 0.04 wt%.

Silicate and oxide minerals were usually analyzed with 20 kV accelerating voltage, 20-30 nA beam current, < 1-2 μm beam diameter, and peak count times ranging from 20-50 s. Combined off-peak count times are equal to on-peak for all elements. A 15 kV accelerating voltage and 15 nA beam current was used for a small number of pyroxene and monticellite analyses because they were analysed during sessions that the electron probe was set up to analyze volatile-bearing phases.

Volatile-bearing phases (serpentine, mica, amphibole, carbonates) were dominantly analyzed with either 15 or 20 kV accelerating voltage, 15 nA beam current, 2-10 μm beam diameter and 20-30 s on-peak count times. Some mica and amphibole analyses utilized a 20-30 nA beam current and < 1-10 μm beam diameter when the electron microprobe was setup to analyze volatile-free silicates. The combined off-peak count times are equal to on-peak for all elements.

Perovskite was analyzed with a 20 kV accelerating voltage, 20 nA beam current, < 1 μm beam diameter and 30 s on-peak count times.

Apatite was analyzed with a 15 kV accelerating voltage, 20 nA beam current, 5 μm beam diameter and 30 s on-peak count times for all elements except fluorine, which was 120 s. Combined off-peak count times are equal to on-peak for all elements.

A 200 x 200 μm grid of points was analyzed in four melt pockets from two different thin sections to quantify their bulk major and minor element chemistry. The analyses utilized a 40 kV accelerating voltage, 40 nA beam current, 20 μm beam diameter and 10 s on-peak count times. Combined off-peak count times are equal to on-peak for all elements. The spot analyses were not separated by any gaps and each grid consisted of 400 analyses (398 in 0413D grid due to an error setting points).

Kimberlite whole-rock major- and trace-element geochemistry of three samples from CH-7 and one from CH-6 were determined by XRF using a PANalytical 2404 X-ray fluorescence vacuum spectrometer equipped with a PW2540 X-Y sample handler and a 4 kW Rh super sharp X-ray tube. Analyses were completed by Stan Mertzman at Franklin and Marshall College, Lancaster, Pennsylvania. The samples were analyzed as fused glass discs made from the whole-rock powders (detailed procedures and long-term repeatability given in Waterton et al. (2020)).

2.2.2 Trace elements

Trace element compositions of garnet, clinopyroxene, orthopyroxene, olivine, melt pockets, and kimberlite groundmass in thin sections were determined by sector-field laser ablation inductively-coupled plasma mass spectrometry (LA-ICP-MS) at the Arctic Resources Laboratory in the Department of Earth and Atmospheric Sciences, University of Alberta. Silicate minerals with major- and minor-element concentrations determined by EPMA were targeted for analysis. Multiple analytical points were taken on larger grains to assess trace-element homogeneity within single grains. The analyses were performed on an Element IIXR coupled with a Resonetics RESOlution M-50 LR 193 nm excimer laser system. NIST612 glass was used as a primary calibration standard with ^{29}Si as the internal standard. Data were processed offline using Iolite version 3.32. Garnet PHN3511, BIR-1G USGS basaltic glass, and SC-GB olivine from San Carlos, Arizona were used as secondary standards to assess the accuracy of the results. The operating conditions and secondary standards used for the analysis are provided in Appendix A, Table A.2 . The average, 2σ uncertainty, and accuracy of the secondary standards are listed in Table A.3 and Table A.4.

Trace element compositions of four kimberlite whole-rock samples, and eight micromilled melt pockets from four xenoliths, were determined by high-resolution magnetic sector inductively-coupled plasma mass spectrometry (HR-ICP-MS) at the Arctic Resources Laboratory in the Department of Earth and Atmospheric Sciences, University of Alberta, using a method modified from Ottley et al. (2003). The analyses were completed on a Thermo Scientific Element XR coupled with an ESI PC3 (a Peltier cooled spray chamber), using an ESI Teflon nebulizer with an uptake rate of approx. 50 µL/min.

Small amounts of the powder from each whole rock sample and standards (~100 mg) were weighed into 15 mL Savillex Teflon beakers, pre-cleaned using HF/HNO_3. Samples were dissolved in 2.5 mL concentrated HNO_3 and 4 mL of concencrated HF at 150 °C for 48 hours. All acids used are Teflon distilled in-house. Insoluble fluorides were removed by addition of 1 mL concentrated HNO_3 and evaporated to near dryness twice. The dried samples were diluted to 10 mL by addition of a stock solution of 3% HNO_3, with trace HF, doped with 1 ppb In as an internal standard.

The samples were then placed on a hotplate at 80 °C overnight to ensure dissolution. At this stage no undigested grains were visible. After cooling, each sample solution was diluted further to give a final dissolution factor of x5000. At each step of dilution, the same stock diluent with In internal standard was used in order to ensure consistency of the internal standard, later used to correct samples for fluctuations in instrumental conditions through the sample run.

A calibration line was set up daily on the Element XR using a standard solution with concentrations that mimic element dissolution in a Basic silicate rock. The standard was made up to five different dilutions, for a five-point calibration line, using the same stock as the samples. This stock solution was used as the calibration blank and from there the rock standard forms a line of increasing concentrations up to at least x5000 dilution so that it brackets the expected element concentrations in the samples.

The Element XR was tuned to give a signal sensitivity equivalent to 1.2 MCPS on 115 In (1 ppb) and oxide formation rate of around 3% (UO/U). The auxiliary gas was 0.78 ml/min and the sample gas 1.012 l/min. Each measurement cycle lasted ~ 3 minutes and involved 6 runs and 4 passes, 50 samples per peak with 0.01 sec sampling times.

Ontario Geological Survey Geoscience Laboratories komatiite powder (OKUM) and IAG ultramafic rock powder MUH-1 were analyzed as secondary standards for the melt pocket samples. The accuracy of both standard materials relative to their accepted values is generally within 10% for elements measured in low resolution mode, and generally within 20% for elements analyzed in medium resolution mode (Mg, Ca, Sc, Ti, V, Cr, Mn, Co, Cu, Ga, and Zr) (Appendix A, Table A.5). International USGS rock standards: BCR2-2, BHVO-2, and AGV-2 were analyzed as secondary standards for the kimberlite whole rock samples. The accuracy of the three standard materials relative to their accepted values is generally within 10% (Appendix A, Table A.6). The data were processed using an in-house spreadsheet produced by P. Waterton at the University of Alberta.

2.2.3 Isotopes

A relatively small amount (mg) of powders from each of the four kimberlite whole rock samples were dissolved in a mixture of concentrated HF (48%) and HNO_3 (16N) in a 2:1 ratio on a hotplate at 120 °C for 48-72 hrs. Two aliquots of USGS Hawaiian basalt standard BHVO-2 were dissolved simultaneously as secondary standards. The solutions were evaporated to dryness before converting into chloride form to pass through the column chemistry. Neodymium and Sm were separated from other REE and major elements using a cation column (AG 50W X8 200-400 mesh) followed by a Ln spec column chemistry following a similar procedure described by Scrivner et al. (2004). The Rb–Sr-Ba fraction was collected in

2.5M HCl from the cation column. Strontium was further purified from this fraction by elution with 0.05M HNO_3 through Sr spec resin (Eichrom 50–100 µm) columns following the procedure described by Pin et al. (1994).

Following the column chromatography, chemically purified Sm and Nd fractions were dried and re-dissolved into 1 ml of a 2% nitric acid solution. Neodymium and Sm isotopic compositions were measured from these solutions using a Neptune Plus Inductively Coupled Plasma Mass Spectrometer (ICP-MS) at the Arctic Resources Laboratory, University of Alberta. Neodymium isotopes were measured in static mode with a ratio of 60 and integration of 8 s while 30 Sm ratios were measured with 4 s integrations. Mass fractionation of Nd isotopes was exponentially corrected by applying a $^{146}Nd/^{144}Nd$ ratio of 0.7219 outlined by Vance and Thirlwall (2002). The ^{149}Sm signal was monitored and the invariant ratio of $^{149}Sm/^{144}Sm$ was used to correct for any isobaric interference of Sm on ^{144}Nd. A 100 ppb solution of JNdi-1 was used as a primary standard and it was measured repeatedly throughout the session. An average of 10 measurements of the JNdi-1 yielded a value of 0.512043 ± 0.000024 (2σ) which is slightly lower (~ 100 ppm) than the accepted value (Jochum et al., 2005) (Table A.7). Thus, all the secondary standards and the samples were standard-corrected using a simple factor. Both measurements of the BHVO-2 secondary standards were within analytical uncertainty (Table A.8). Initial $^{143}Nd/^{144}Nd$ isotope ratios were calculated using a ^{147}Sm decay constant of $6.539 \times 10^{-12} \pm 9.9 \times 10^{-14}$ (Lugmair and Marti, 1978) and the U-Pb perovskite age of the CH-7 and CH-6 kimberlites reported in Heaman et al. (2015).

Strontium isotope ratios were also measured in the Triton plus Thermal Ionisation Mass Spectrometer (TIMS) instrument at the same lab in a static mode using multiple faraday cups connected to a mixture of 10^{11} Ω and 10^{12} Ω amplifiers. Purified Sr fractions from the chromatographic columns were dried down with 1 µL of 0.1M H_3PO_4 and loaded with 1 µL $TaCl_5$ activator on a previously outgassed, zone refined Re single filament. NBS987 solution containing 50–100 ng Sr was used as primary standard. Accuracy and instrument stability for Sr isotope analyses were monitored by repeat measurement of the NBS987 standard, which gave a weighted average value of $^{87}Sr/^{86}Sr = 0.710254 \pm 0.000010$ (MSWD=1.1, $n = 9$) during the study period (Table A.9). No systematic correction was made to any of the reported sample data on the basis of the NBS987 measurements. An excess scattering uncertainty of 0.0018% has been propagated to all samples that reflects the repeatability of the reference material measurements. Each sample and BHVO-2 filaments were replicated, and the values were always within analytical uncertainty (Table A.10).

Chapter 3 : Results

3.1 Petrography

3.1.1 Xenolith overview

The peridotite xenoliths in this study are named according to the IUGS convention (Le Maitre et al., 2002), with mineralogical modifiers used to note the presence of minerals such as: spinel, garnet, clinopyroxene, orthopyroxene, and ilmenite that are not implicit in the name. For conciseness, dunites with both clinopyroxene and orthopyroxene are henceforth referred to as pyroxene dunites, or px dunites.

The sample suite consists of 23 peridotites (1 lherzolite, 1 harzburgite, 21 dunites) and one olivine websterite. The remaining olivine-free, garnet-clinopyroxene bearing rock is classified as eclogite on the basis that it is a garnet-clinopyroxene rock without olivine and orthopyroxene (hence in the clinopyroxenite field of the IUGS classification), with omphacitic clinopyroxene (jadeite component > 20 %) (Desmons and Smulikowski, 2007).

The xenoliths range in size from ~ 1.5 x 1.5 cm to ~ 5 x 10 cm and are generally very fresh. The normalized modes of olivine, clinopyroxene, and orthopyroxene from each xenolith are plotted on the IUGS ternary of ultramafic rocks after Le Maitre et al. (2002) (Figure 3.1.1). The peridotites in this study contain olivine modes between 55 to 96 % (mean 87 %). The lithology, texture, mineralogy, and modal abundances of each xenolith are tabulated in Table 3.1.1.

3.1.2 Xenolith petrography

The textural nomenclature of Harte (1977) is used to classify the olivine-bearing xenoliths in this study. Consequently, 11 xenoliths classify as coarse and can further be refined for the three spinel peridotites that have coarse-equant texture, and the garnet harzburgite has coarse-tabular texture. The remaining peridotites classify as porphyroclastic (*n* = 10), in which four have fluidal clinopyroxene; mosaic porphyroclastic (*n* = 3); and equant-granuloblastic (*n* = 1). The eclogite has a coarse-grained granoblastic texture. Olivine grains in the xenoliths range from 2 to 14 mm, but in sheared xenoliths the porphyroclasts are restricted to ~ 2 to 8 mm and are surrounded by smaller olivine neoblasts, commonly < 0.5 mm; no other minerals are observed as neoblasts. Clinopyroxene and orthopyroxene typically range in size from ~ 0.5 to 6 mm, and garnets range from ~ 0.5 to 8 mm. Coarse xenolith 0411I is the only xenolith with garnets that appear to have completely recrystallized into smaller grains. The smaller grains are not separated by other minerals and are enclosed by a coherent, irregular-shaped boundary; therefore, this is not considered a disrupted texture. Spinel peridotites have spinel grains that range in size from 0.1 to 1 mm. The eclogite has garnets ranging in size from 3 to 15.3 mm, and clinopyroxene from 2.5 to 7.2 mm.

Garnets with kelyphite rims comprised of euhedral phlogopite laths and chrome-rich spinel (and pargasite in the olivine websterite) are commonly found in the xenoliths. Mineral inclusions in garnet are common, ranging from ilmenite, spinel group minerals, pargasite, rutile, and olivine. Fe-rich exsolution lamellae in ilmenite inclusions was identified by EDS in four of the five xenoliths with ilmenite inclusions in garnet.

Clinopyroxene is observed as rims on garnets in six of the fifteen garnet-bearing peridotites, and orthopyroxene as rims on garnets in two of the pyroxene dunites. In two xenoliths, clinopyroxene sometimes mantles the edge of olivine porphyroclasts, and occasionally completely envelopes smaller olivine grains. Many of the clinopyroxene grains in this study have spongy margins that Kopylova et al. (2019) attributed to partial melting. Thin rims of monticellite around clinopyroxene are common and appear as dark rims in plane polarized light in thin sections. Clinopyroxene overgrowths on orthopyroxene are frequently observed, and less commonly, secondary clinopyroxene rims on clinopyroxene grains. Potassic richterite is sometimes found as overgrowths on orthopyroxene in pyroxene dunites. Phlogopite is commonly found along both clinopyroxene and orthopyroxene rims. In xenoliths with < 1 % modal orthopyroxene, the orthopyroxene grain(s) are partially pseudomorphed by a combination of clinopyroxene + phlogopite + serpentine ± tetraferriphlogopite and are almost always in contact with a melt vein or melt pocket in the plane of the thin section. Less commonly, clinopyroxene displays exsolution lamellae that were identified with EDS as being more orthopyroxene rich. Annotated images of representative hand samples and scanned thin sections are shown in Figure 3.1.2 and Figure 3.1.3. Scanned images of thin sections from each xenolith in the sample set, as well as photomicrographs of some xenoliths are in Appendix B, Figure B.1 and Figure B.2, respectively.

Rutile (< 1 modal %) occurs as ~ 250 – 500 µm grains in garnet olivine websterite 0405D1, and as larger grains up to 1.7 mm in eclogite 0405H. The grains in both xenoliths are often rimmed by ilmenite, less frequently jeppeite, and in one case, freudenbergite in 0405H. Rutile in 0405D1 commonly has thin (< 5 µm), whispy lamellae that were not analyzed but appear the same brightness as jeppeite and ilmenite on a BSE image (e.g. Appendix B, Figure B.3, image O). In some grains, ilmenite and rutile have complex zoning, which obscures the core-rim relationship.

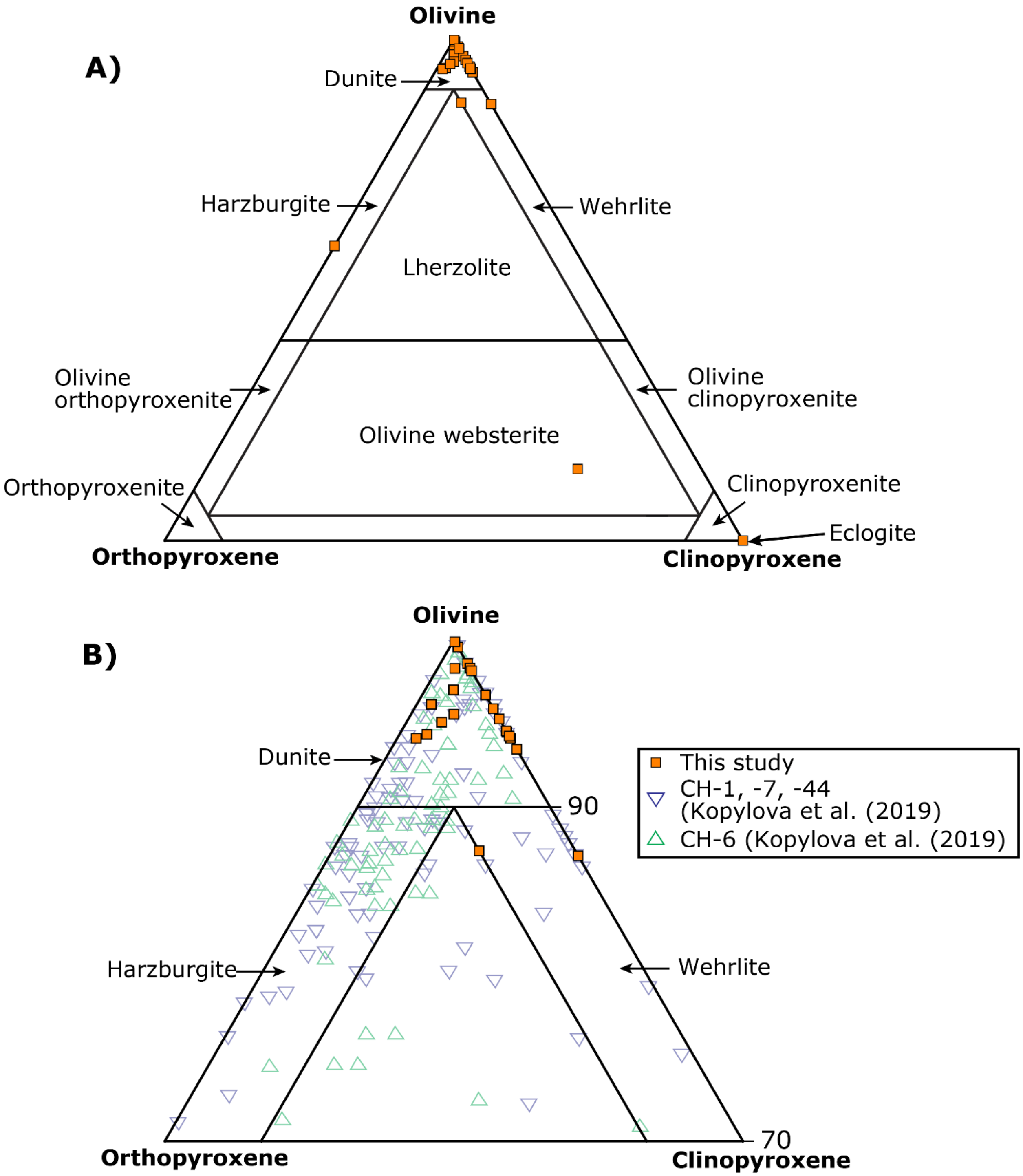

Figure 3.1.1 – A) IUGS ternary plot after Le Maitre et al. (2002) of xenoliths from this study normalized to 100. Eclogite xenolith 0405H is shown in the clinopyroxenite quadrant. B) Focused IUGS ternary of xenoliths with olivine modes ≥ 70%, with background data from Kopylova et al. (2019).

3.1.3 Petrography of the melt intrusions

Melt intrusions are present in 21 of the xenoliths, in the form of pockets (*n* = 15), veins (*n* = 4), and a combination of pockets and veins (*n* = 2). Melt pockets typically have irregular shapes with smoothly curving edges, which often conform to the grain boundary of adjacent olivine grains, but also occur as round pockets in olivine grains. They range in size from ~ < 200 x 200 μm, to larger pockets ~ 1 x 1 cm, with average size ~ 1.5 x 1.5 mm. The abundance of melt pockets in the xenoliths mostly varies from < 1 to ~ 5 % but reaches ~ 15 % in ilmenite wehrlite 0404C. Melt veins typically follow along grain boundaries in xenoliths, but may also transect olivine, clinopyroxene, or spinel. The abundance of melt veins in xenoliths is ~ 1%.

In plane polarized light, the melt pockets often appear "spotted" white and black, or brown and black. In many cases, large areas in the melt pockets appear texturally featureless, and are light green or white. The mineral assemblage associated with the melt intrusions is predominantly serpentine, carbonates, brucite, spinel group minerals, and apatite; with lower modal abundance of perovskite, mica, monticellite, ilmenite, and Ni-Fe-Cu-bearing sulphides.

Large ilmenite and clinopyroxene grains are often found along the margins of melt pockets, and may be completely enveloped by melt, as seen in xenoliths 0411J and 0413B. The prevalence of clinopyroxene and ilmenite in contact with melt pockets gives the appearance of them having crystallized from the melt in these cases. The grain size of ilmenite and clinopyroxene are noticeably larger than the other melt pocket phases, with ilmenite ranging from ~ 0.25 mm to 1 cm, and clinopyroxene ~ 1.5 – 3.5 mm. In contrast, the spinels, apatite, perovskite, and sulphides in the melt intrusions are almost always < 150 μm. Ilmenite grains on the edge of melt pockets have spinel rims that form almost exclusively at the interface of the ilmenite grain edge and melt, and in one case the ilmenite grain acts as a nucleation site for spinel with atoll texture. Granoblastic polygonal textures with triple-point grain boundaries occur in ilmenites in xenoliths 0404B1, 0404C, and 0411E. The other four ilmenite-bearing xenoliths have ilmenite grains with smoothly curving grain boundaries but lack granoblastic polygonal texture with triple-point boundaries. In some cases, the ilmenites contain Fe-rich exsolution lamellae, identified by EDS. Xenoliths with large ilmenite grains along the edge of melt pockets exclusively occur in xenoliths that have garnet with inclusions of ilmenite, except for both garnet-free ilmenite clinopyroxene dunites, and garnet clinopyroxene 0411K - where ilmenite occurs as inclusions in garnet but was not documented in melt pockets (though they appear to be present in the visible light scanned image of the thin section).

In six xenoliths, discrete ~ 40-50 μm ilmenite grains occur in very low abundance in melt veins and pockets. It also occurs as a rim on a spinel grain in xenolith 0411F3. Rutile is very rare in melt intrusions but is present in wehrlite 0411J. The observed rutile is part of the same grain as an ilmenite; however, the core/rim relationship is unclear.

Besides ilmenite and clinopyroxene, the coarsest crystalline phases are typically located along the margins of the melt intrusions. These phases can be spinel, apatite, perovskite, and monticellite. Apatite is commonly observed as skeletal oikocrysts < 50 μm in size (maximum observed size = 325 μm), with euhedral or anhedral boundaries, and may contain inclusions of serpentine. Perovskite occurs as discrete crystals with anhedral to euhedral boundaries, mantles on spinel grains, or cores of spinel grains. The grain size is typically ~ 10 - 30 μm but can be up to 90 μm. Spinel grains occur as discrete crystals, rims and cores of perovskite grains, and rims on ilmenite. Their grain size is typically 5 to 50 μm but can be as large as ~ 100 μm. Their shape varies from euhedral to anhedral and sometimes displays atoll texture. Compositional zoning is common, but it is rarely unambiguous which part of the grain is the core and rim.

Monticellite sometimes occurs along the margins of melt pockets in five xenoliths that also have monticellite distributed throughout the xenolith on olivine and/or clinopyroxene rims. It also occurs in the central and rim part of melt veins in seven xenoliths. It occurs as discrete anhedral grains that range in size from ~ 10 - 130 μm. The monticellite grains in melt veins appear to have crystallized directly from the intrusion because their high abundance and often central location within the veins. In contrast, the occurrence of monticellite along the edges of melt pockets is rare, and monticellite is confirmed elsewhere in the xenolith away from the melt pockets. Therefore, its association with melt pockets is more ambiguous.

The central regions of the melt pockets are dominated by serpentine, carbonate, and brucite. Serpentine sometimes forms globular clusters ranging in diameter from ~ 10 - 90 μm, as well as spherulitic textures (Figure 4.1.7), with fine grained magnetite (≤ 1 μm) and sulphides disseminated throughout. Brucite is commonly found in anhedral patches set in a serpentine matrix. Acicular clusters of tetraferriphlogopite, typically comprised of individual grains ≤ 1 μm wide and ~ 10-30 μm in length, are common along the edges of melt pockets.

Carbonates may form colloform textures that grade from calcite to dolomite to magnesite (or vice-versa), as well as anhedral grains set in a serpentine matrix. The most abundant carbonate phase is calcite, with dolomite, magnesite, and strontianite occurring less frequently. Strontianite was found in only one sample, located in the melt veins of spinel peridotite 0405B1. The strontianite occurs as thin veins, ~20 μm wide, with a halo of Sr-rich calcite surrounding it.

Fine-grained (typically < 10 μm) Fe-Ni-Cu bearing sulphides are a common, but volumetrically insignificant phase within the melt pockets. Additionally, djerfisherite occurs as ~20 μm thick rims along parts of some ilmenite grains in xenolith 0404C, and in the kimberlitic melt veins of 0405H. It was not identified elsewhere.

Annotated photomicrographs of melt pockets in two xenoliths, along with a corresponding BSE image of each melt pocket is shown in Figure 3.1.4. Annotated BSE images of representative melt pockets from the sample set are in Figure B.3.

Table 3.1.1 – Summary table of xenolith petrography.

Sample	Pipe	Lith	Ol	Grt	Cpx	Opx	Sp	Ilm	Rt	Phl	Melt	Texture[1]	Textural mod.[1]
			Modal abundance (%)										
0404B1	CH-6	Cpx il dun	79.6	-	0.4	-	-	15.0	-	-	5.0	Mosaic-porphy	-
0404B2	CH-6	Cpx gt dun	95.7	2.0	1.9	-	-	-	-	0.5	0.0	Porphyroclastic	-
0404C	CH-6	Cpx il dun	64.2	-	5.8	-	-	15.0	-	-	15.0	Porphyroclastic	-
0405A	CH-7	Sp lherz	83.8	-	7.6	5.1	3.0	0.0	-	0.5	0.0	Coarse	Equant
0405B1	CH-7	Opx cpx sp dun	92.0	-	1.5	1.5	3.0	0.0	-	-	2.0	Coarse	Equant
0405C	CH-7	Gt cpx dun	89.9	3.0	4.1	-	-	0.0	-	-	3.0	Coarse	-
0405D1	CH-7	Gt ol web	9.5	30.0	45.0	15.0	-	-	0.5	-	0.0	Coarse	-
0405E	CH-7	Gt cpx dun	86.1	3.0	5.9	-	-	0.0	-	-	5.0	Porphyroclastic	Fluidal cpx
0405H	CH-7	Eclogite	-	49.0	49.0	-	-	-	-	-	2.0	Coarse	-
0411C	CH-7	Opx cpx sp dun	92.1	-	2.2	2.2	3.0	0.0	-	-	0.5	Coarse	Equant
0411D	CH-7	Cpx dun	93.6	-	1.4	-	-	0.0	-	-	5.0	Porphyroclastic	-
0411E	CH-7	Cpx gt dun	87.7	1.0	3.3	-	-	3.0	-	-	5.0	Porphyroclastic	Fluidal cpx
0411F1	CH-7	Cpx gt opx dun	91.6	2.0	1.0	4.9	-	-	-	-	0.5	Coarse	-
0411F2	CH-7	Cpx opx dun	94.2	-	0.7	3.1	-	0.0	-	-	2.0	Mosaic-porphy	-
0411F3	CH-7	Gt cpx dun	90.5	1.0	6.5	-	-	0.0	-	-	2.0	Porphyroclastic	-
0411G	CH-7	Cpx dun	91.3	-	4.7	-	-	-	-	-	4.0	Porphyroclastic	-
0411H	CH-7	Gt wehr	81.6	0.5	12.9	-	-	-	-	-	5.0	Coarse	-
0411I	CH-7	Cpx gt dun	91.8	3.0	1.7	-	-	0.5	-	-	3.0	Coarse	-
0411J	CH-7	Cpx gt dun	86.1	5.0	5.4	-	-	0.5	-	-	3.0	Porphyroclastic	Fluidal cpx
0411K	CH-7	Gt cpx dun	88.5	3.0	5.5	-	-	0.0	-	-	3.0	Porphyroclastic	Fluidal cpx
0413A	CH-7	Cpx opx gt dun	86.1	8.0	1.8	3.1	-	-	-	-	1.0	Coarse	-
0413B	CH-7	Cpx gt dun	96.2	1.0	0.9	0.8	-	0.1	-	-	1.0	Porphyroclastic	-
0413C	CH-7	Gt harz	55.0	10.0	-	35.0	-	-	-	-	0.0	Coarse tabular	-
0413D	CH-7	Cpx opx gt dun	88.9	5.0	1.4	4.2	-	0.0	-	-	0.5	Mosaic-porphy	-
0413E	CH-7	Gt dun	94.9	3.5	0.5	-	-	0.1	-	-	1.0	Granuloblastic	Equant

Cpx = clinopyroxene, dun = dunite, grt = garnet, harz = harzburgite, ilm = ilmenite, lherz = lherzolite, lith = lithology, mosaic-porphy = mosaic-porphyroclastic, ol = olivine, opx = orthopyroxene, phl = phlogopite, rt = rutile, sp = spinel, web = websterite, wehr = wehrlite.

[1] Textural classification of (Harte, 1977).

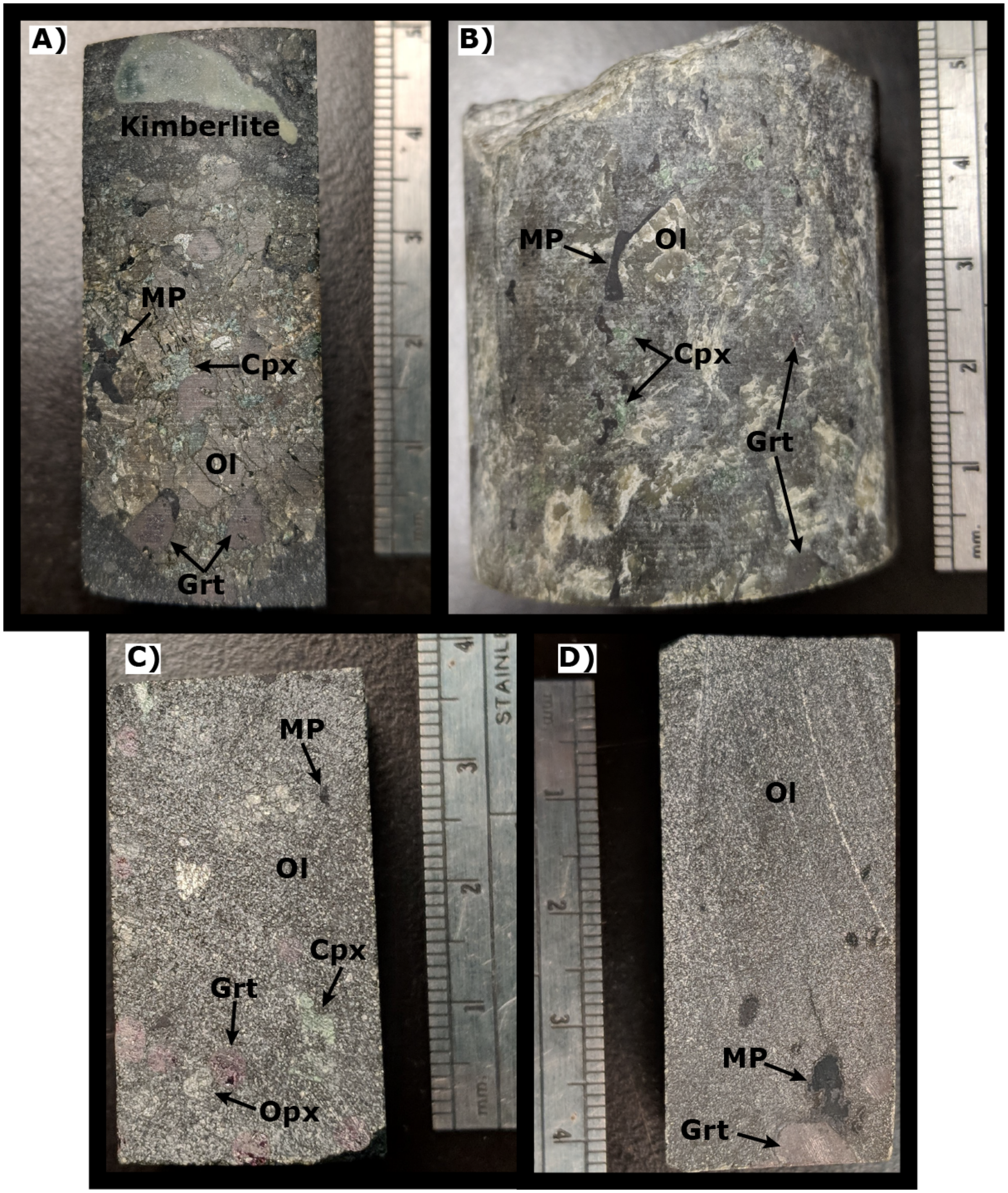

Figure 3.1.2 – MP = melt pocket. Representative hand samples of melt-bearing xenoliths A) coarse garnet cpx dunite 0405C, B) porphyroclastic garnet cpx dunite 0405E, C) mosaic-porphyroclastic garnet px dunite 0413D, and E) granuloblastic garnet dunite 0413E.

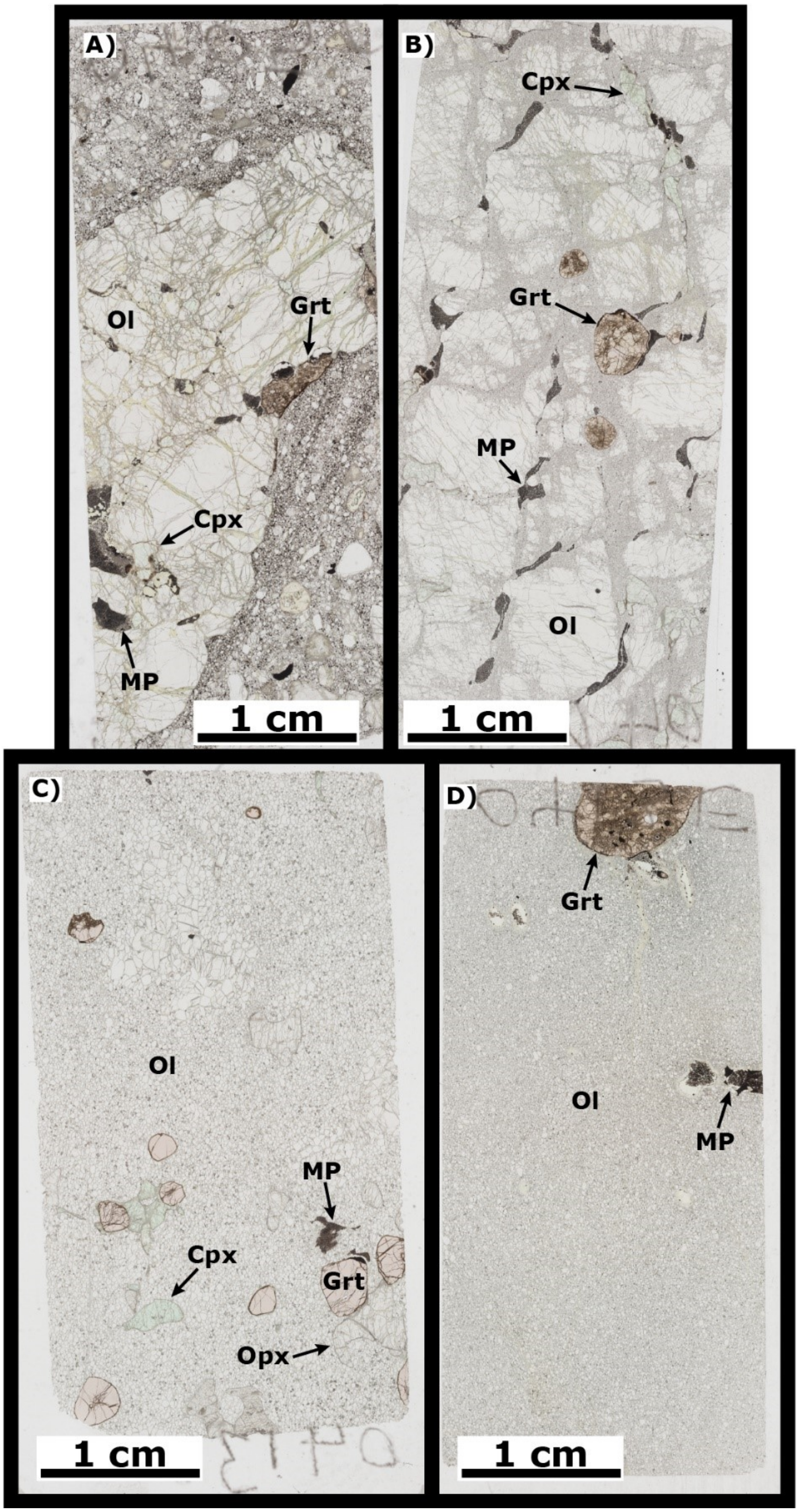

Figure 3.1.3 – Visible light thin section scans of A) coarse garnet cpx dunite 0405C, B) porphyroclastic garnet cpx dunite 0405E, C) mosaic-porphyroclastic garnet px 0413D, and E) granuloblastic garnet dunite 0413E.

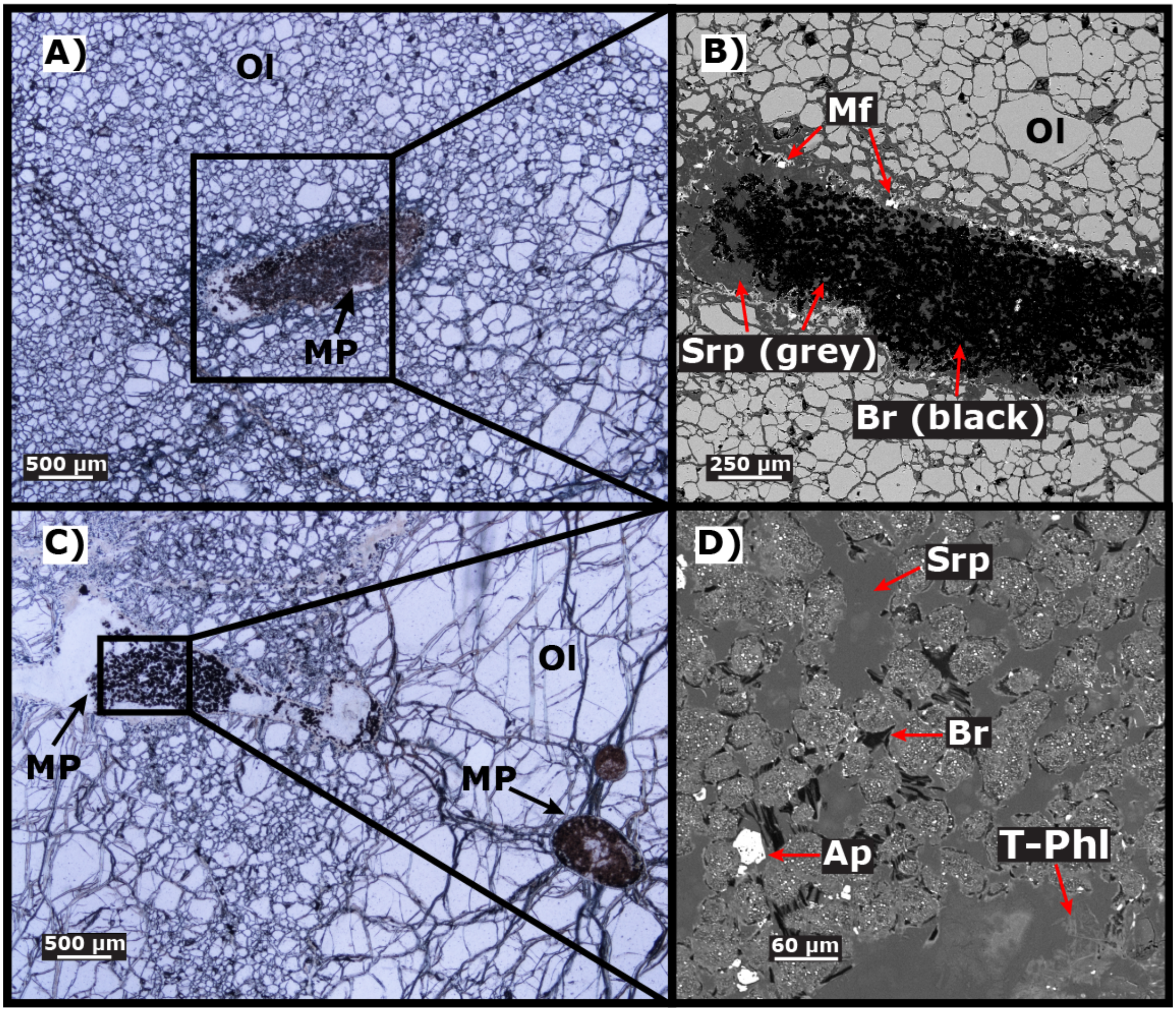

Figure 3.1.4 – Photomicrographs in plane polarized light of a thin section from xenolith A) px dunite 0411F2V with B) corresponding BSE image of the featured melt pocket; and C) garnet cpx dunite 0413BV with D) corresponding BSE image of the featured melt pocket.

3.1.4 Kimberlite whole-rock sample petrography

The CH-6 and CH-7 kimberlite samples are characterized by a groundmass consisting of apatite, perovskite, spinel-group minerals, monticellite, phlogopite, carbonate and serpentine. Crustal xenoliths composed of carbonate sedimentary rocks are rarely observed in the samples and make up approximately ≤ 1% by volume. Thin section scans in visible light showing a representative part of the kimberlite are displayed in Figure 3.1.5, with some of the kimberlite components labelled using the terminology of Scott Smith et al. (2013). The CH-6 kimberlite sample contains olivine macrocrysts but lacks other distinct kimberlite components such as magmaclasts and accretionary clasts. In contrast, both 0405C and 0411I xenoliths appear to be armoured clasts within the kimberlite, and all three CH-7 samples contain kimberlite components such as olivine macrocrysts, accretionary clasts, and/or magmaclasts.

Table 3.1.2 – Source of each kimberlite whole-rock sample.

Sample ID	**Kimberlite Pipe**	**Drillhole ID**	**Sample depth interval (m)**
0404B	CH-6	CHI-050-15-DD31	146.07 – 146.33
0405C	CH-7	CHI-251-15-DD26	143.35 – 143.50
0411I	CH-7	CHI-251-15-DD28	162.38 – 162.50
0413D	CH-7	CHI-251-15-DD29	194.44 – 194.54

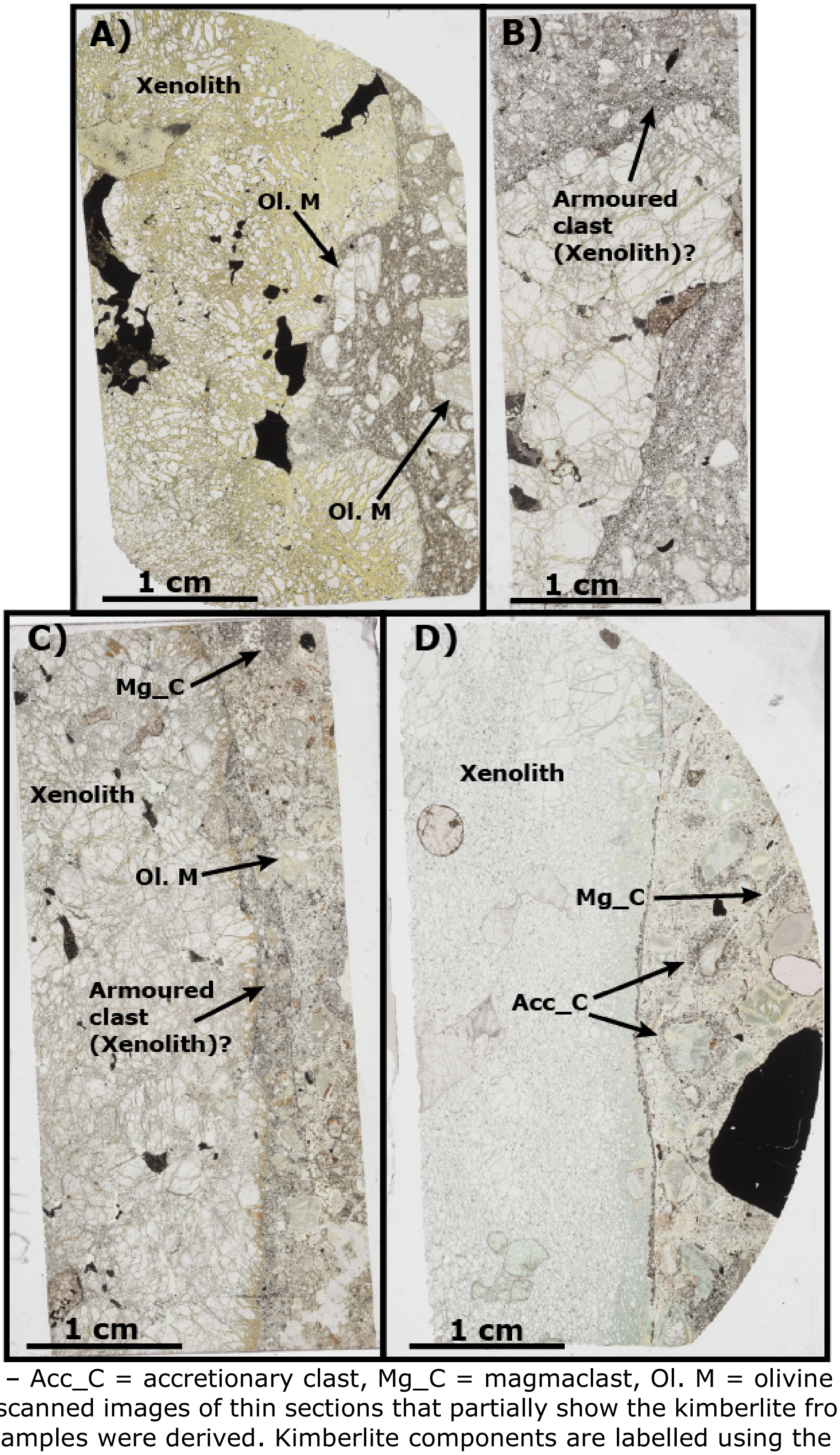

Figure 3.1.5 – Acc_C = accretionary clast, Mg_C = magmaclast, Ol. M = olivine macrocryst. Visible light scanned images of thin sections that partially show the kimberlite from which the whole rock samples were derived. Kimberlite components are labelled using the terminology of Scott Smith et al. (2013). Thin sections correspond to kimberlite whole rocks A) 0404B1 (CH-6), B) 0405C (CH-7), C) 0411I (CH-7), and D) 0413D (CH-7).

3.2 Geothermobarometry

This study applies conventional geothermobarometry to calculate the P-T conditions at which the xenoliths last equilibrated in the mantle. Thermobarometric calculations were performed using major-element compositions determined by EPMA, as well as trace-element compositions of olivine determined by LA-ICP-MS. All data were screened for quality using the following criteria, similar to Nimis and Grütter (2010): oxide totals between 98.5 and 101.5 wt %; cation sums for pyroxene ≥ 3.990 apfu (6-oxygen basis), olivine ≥ 2.990 apfu (4-oxygen basis), garnet ≥ 7.990 apfu (12-oxygen basis), and spinel ≥ 2.990 apfu (4-oxygen basis). One exception was made for the P-T calculation of eclogite 0405H, which had a lower clinopyroxene cation total of 3.981 apfu because all replicate core analyses totaled < 3.990 apfu. This sample may have a Ca-Eskola component on the basis that the cations total < 3.990 apfu and there is an "excess" of Si compared to the other cations (Schroeder-Frerkes et al., 2016). Equilibrium between clinopyroxene and orthopyroxene in peridotite xenoliths was verified using the recommendations of Nimis and Grütter (2010); where disequilibrium between both pyroxenes is defined as the difference in calculated temperature between the Taylor (1998) two-pyroxene thermometer (TA98) and corrected Ca-in-opx thermometer of Brey and Köhler (1990) larger than 90°C (at $\mathrm{T}_{\mathrm{TA98}}^{\mathrm{Cpx-Opx}}$ < 900°C), 70°C (at $\mathrm{T}_{\mathrm{TA98}}^{\mathrm{Cpx-Opx}}$ = 900-1200°C), or 50°C (at $\mathrm{T}_{\mathrm{TA98}}^{\mathrm{Cpx-Opx}}$ > 1200°C). Garnet-pyroxene equilibrium was assessed using the difference between the calculated temperature of the Fe-Mg clinopyroxene-garnet thermometer of Krogh (1988) ($\mathrm{T}_{\mathrm{Krogh88}}$) and two-pyroxene thermometer of Taylor (1998). Clinopyroxene in clinopyroxene dunites were verified for having equilibrated with orthopyroxene using the criteria suggested by Ziberna et al. (2016), where clinopyroxene with Ca/(Ca+Mg) > 0.5 and/or calculated temperatures < 700°C should be considered as possibly not having equilibrated with orthopyroxene. Additional composition checks were established for application of the Nimis and Taylor (2000) single clinopyroxene thermobarometer (NT00), using composition filters of Grütter (2009) and Ziberna et al. (2016). The filters verified that the clinopyroxenes equilibrated in the garnet stability field and had compositional overlap with those used in the original calibration. One exception was made for spinel- and garnet-free lherzolite 0411F2 that had Cr# = 0.51, slightly outside the range criteria of Grütter (2009) of 0.06 to 0.50, but within the expanded 0.10 – 0.65 range of Ziberna et al. (2016). Additionally, Figure 3.2.1 and Figure 3.2.2 suggest that 0411F2 equilibrated with garnet because it plots in the garnet peridotite fields. Olivines were screened using the compositional criteria of Bussweiler et al. (2017) ($\mathrm{T}_{\mathrm{B17}}$).

Equilibrium and compositional filters resulted in rejection of five spinel- and garnet-free peridotites that did not meet the requirements of any of the available thermobarometers. In plots of Cr_2O_3 vs Al_2O_3 and Al_2O_3 vs MgO (wt%) of averaged clinopyroxene core analyses from each xenolith (Figure 3.1.2 and Figure 3.1.3, respectively), three out of the five clinopyroxene dunites that P-T could not be calculated from, plot within the "eclogite, megacryst or cognate" (Figure 3.2.1) and five out of five plot in the "garnet-free and/or metasomatized peridotites" (Figure 3.2.2) fields of Ramsay (1995).

For xenoliths that passed equilibrium and compositional tests, a variety of geothermobarometers were used to calculate their equilibrium P-T conditions. Table 3.2.1 shows several thermobarometer outputs for samples that were solved iteratively, with asterisks indicating formulations that did not pass the compositional requirements for a particular thermometer or barometer. Figure 3.2.3 shows the preferred thermometer-barometer combination for each xenolith in this study. For xenoliths with an available thermometer but no barometer (e.g. garnet dunite, eclogite), pre-set pressures were used that gave a temperature output that fell on the geotherm of Pell et al. (2013). Spinel peridotites used pre-set pressures of 20 and 30 kbar to model the different calculated temperatures of TA98 at those pressures. The pressures were chosen because Kopylova et al. (2019) constrained the spinel-garnet transition between 26 and 30 kbar at Chidliak.

The thermobarometer combinations depict the xenoliths as having equilibrated along conductive geotherms with surface heat flow between 35 and 38 mW/m^2 (Hasterok and Chapman, 2011) before their entrainment in the kimberlite. This is within the 35-39 mW/m^2 range found by Kopylova et al. (2019). Thermobarometric calculations show that the xenoliths were sampled from pressures ranging from 20 – 68 kbar, corresponding to depths ~ 63 – 214 km, and temperatures 646 - 1238 °C. Spinel peridotites at pre-set pressures of 20 kbar plot higher than the 40 mW/m^2 geotherm. At pre-set pressures of 30 kbar, the samples plot on conductive geotherms with surface heat flow between 35 and 40 mW/m^2 and have a calculated temperature range of 133 °C. This suggests the spinel lherzolites experienced a transient heating event shortly before or during their entrainment or were sampled over a range of depths in the mantle.

Equilibration temperatures were calculated using the cpx-garnet Fe-Mg thermometer of Krogh (1988) for seven garnet clinopyroxene dunites with compositionally zoned garnets. The calculations used both core and rim compositions to see if the zonation records a transient heating event experienced by the xenoliths. Calculated temperature differences between garnet cores and rims using this method show they are within ± 30°C of each other, with no consistent higher or lower temperature between cores and rims in six of the xenoliths. The seventh xenolith has contradictory relations between two different garnet cores and their rims. The first calculation showed the rims equilibrated 65 °C higher than its core, and the other had rims giving a 51 °C cooler temperature than its core.

Table 3.2.1 - Comparison of different temperatures (°C) and pressures (kbar) determined using different thermometer and barometer pairs solved iteratively for xenoliths with mineral compositions that passed the compositional and equilibrium criteria for some or all geothermobarometers listed.

Sample	Lith	T_{BKN}	P_{BKN}	T_{NT}	P_{NT}	T_{TA98}	P_{NG85*}	T_{B17}	P_{NT}	T_{B17}	P_{NG85*}	T_{Harley}	P_{NG85*}	T_{NG10}	P_{NG85*}
0413C	Gt harz	-	-	-	-	-	-	-	-	-	-	1022	49	1110	54
0411F1	Gt px dun	1124	59	1022	50	1060	57	-	-	-	-	1006	54	1131	60
0411F2	Px dun	-	-	1199	63	-	-	-	-	-	-	-	-	-	-
0413A	Gt px dun	1065	52*	949*	55*	960	49	-	-	-	-	895	45	903	45
0413D	Gt px dun	1263	69	1189	59	1231	68	1167	58	1211	67	1030	57	1190	65
0405E	Gt cpx dun	-	-	1009	54	-	-	1184	62	-	-	-	-	-	-
0411F3	Gt cpx dun	1155*	48*	1092	52	1096*	46	1117	53	1073	45	1002	41	1013	41
0411G	Cpx dun	-	-	1111	58	-	-	-	-	-	-	-	-	-	-
0411K	Gt cpx dun	-	-	957	52	-	-	1183	62	-	-	-	-	-	-
0413B	Gt cpx dun	-	-	1182	61	1400*	116	1189*	61	1501*	123	1577	129	3503	269
0405D1	Gt ol web	704*	31	618*	17*	644*	26	-	-	-	-	757	33	637	25

*Did not pass compositional or equilibrium requirements of the thermometer or barometer.

"-" = not applicable

TA98 = Taylor (1998), NG85* = Nickel and Green (1985) with Al in M1 calculated after Carswell and Gibb (1987), BKN = two-pyroxene thermobarometer of Brey and Köhler (1990), NT = Nimis and Taylor (2000), B17 = Bussweiler et al. (2017).

Gt = garnet, harz = harzburgite, lherz = lherzolite, ol = olivine, web = websterite.

Table 3.2.2 - Comparison of different temperatures (°C) determined by inputting a pressure for each of the xenoliths that passed the composition and equilibrium criteria for some, or all thermometers listed. Pressures were determined by manual input when the output temperature of a preferred thermometer matched with the Chidliak geotherm of Pell et al. (2013). None of the xenoliths passed the requirements for use of P_{NT}, but it is displayed along with the preset temperature to be used as a reference for comparison with the preset pressure.

Sample	Lith	Pre-set P (kbar)	Pre-set T (°C)	T_{TA98}	$T_{Krogh88}$	T_{EG}	$T_{Ca\text{-}in\text{-}opxNG10}$	$T_{Na\text{-}in\text{-}opx}$	T_{B17}	T_{Zn}	P_{NT}
0413E	Gt dun	63	-	-	-	-	-	-	1193	-	-
0405A	Sp lherz	20	853	776	-	-	771	847	-	672	13*
0405B1	Sp px dun	20	786	711	-	-	832	722	-	625	13*
0411C	Sp px dun	20	708	646	-	-	729	598	-	642	15*
0405D1	Gt ol web	26	697	644	681	784	774	-	-	-	19*
0405C	Gt cpx dun	61	-	-	1134	1125	-	-	1091	-	52*
0411E	Gt cpx dun	63	-	-	1214	1235	-	-	1192	-	68*
0411I	Gt cpx dun	58	-	-	1076	1079	-	-	1065	-	55*
0411J	Gt cpx dun	63	1193	-	1239	1216	-	-	1193		67*
0404B2	Gt cpx dun	62	988	962	1165	1198	901	1019	-	-	-
0405H	Ecl	64	-	-	1238	1209	-	-	-	-	-

*Did not pass all composition filters of Grütter (2009) and/or Ziberna et al. (2016).

"-" = not applicable.

BKN = two-pyroxene thermobarometer of Brey and Köhler (1990), Krogh88 = Krogh (1988), TA98 = Taylor (1998), Ca-in-opxNG10 = Brey and Köhler (1990) with correction of Nimis and Grütter (2010) for T<900°C, Na-in-opx = Brey and Köhler (1990), NT = Nimis and Taylor (2000), B17 = Bussweiler et al. (2017), Zn = Zinc-in-spinel thermometer of Ryan et al. (1996).

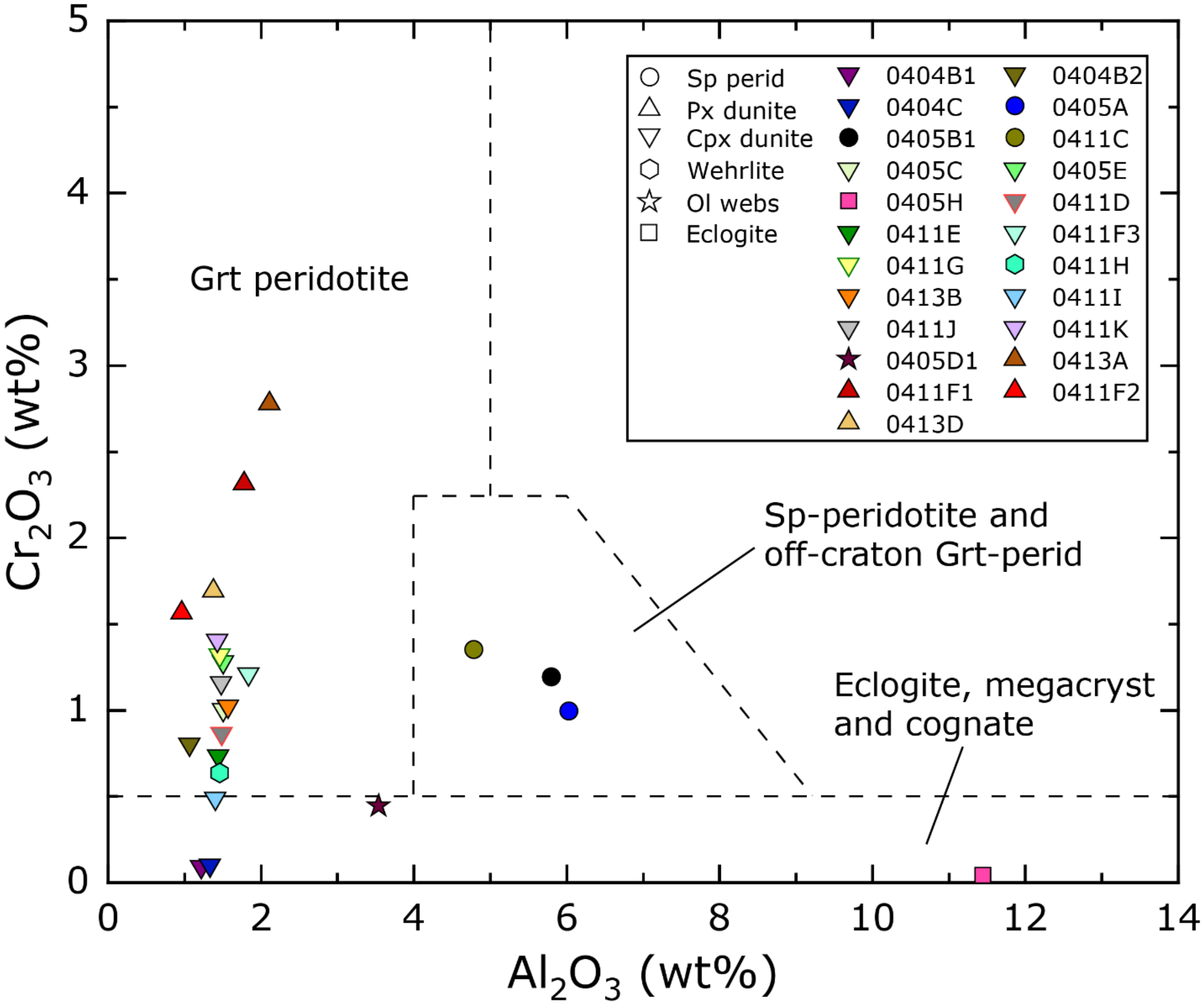

Figure 3.2.1 – Cr_2O_3 (wt%) vs Al_2O_3 (wt%) plot of clinopyroxene cores in xenoliths from this study with source-rock fields after Ramsay (1995).

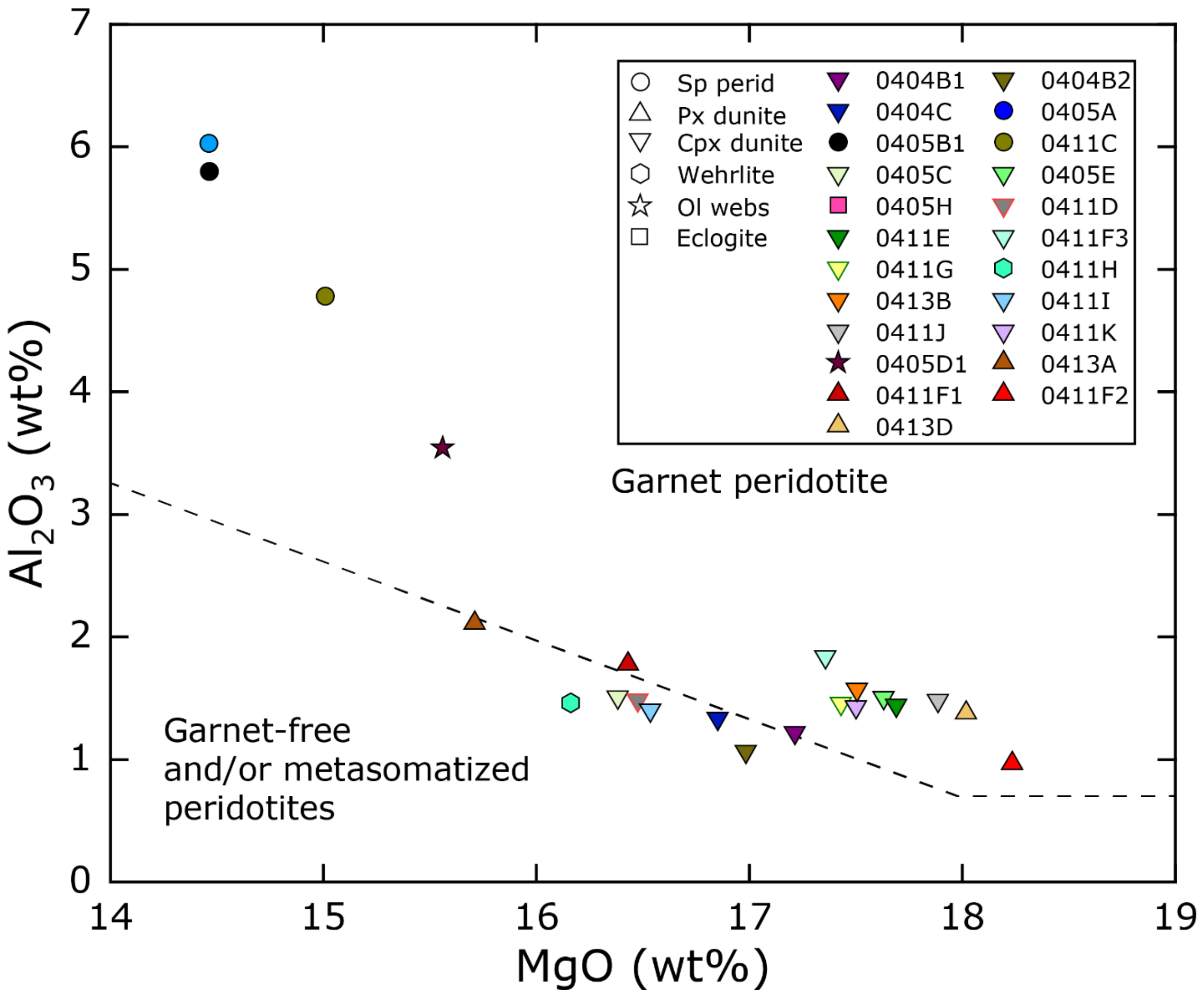

Figure 3.2.2 – Al_2O_3 (wt%) vs MgO (wt%) plot of clinopyroxene cores in xenoliths from this study. Fields of garnet peridotites, and garnet-free (mostly spinel-bearing) and/or metasomatized peridotites are after Ramsay (1995). Not plotted is eclogite 0405H, which has mean Al_2O_3 = 11.44 wt% and mean MgO = 8.93 wt%.

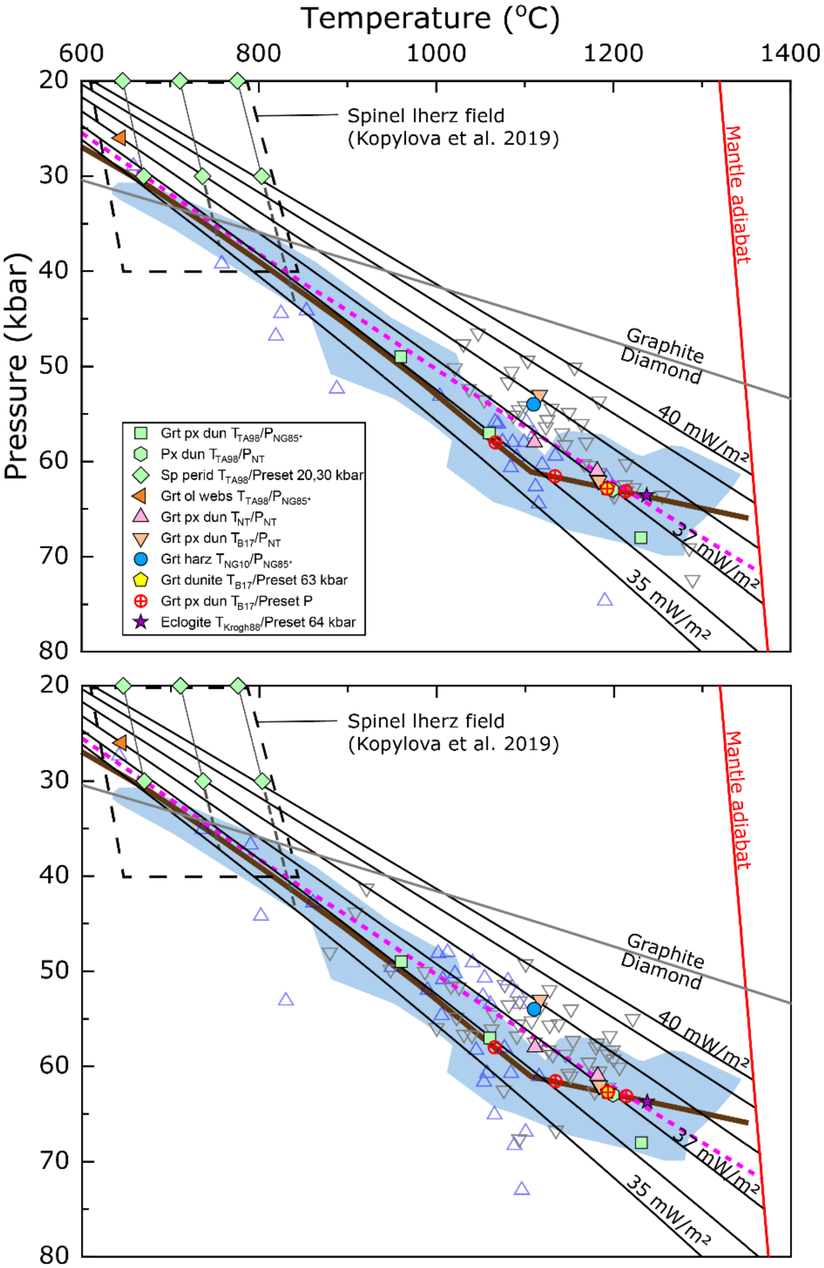

Figure 3.2.3 – Pressure-temperature plot of six different thermobarometer combinations solved iteratively, and three thermobarometer combinations solved with pre-set pressures from xenoliths in this study. Calculated temperatures for spinel lherzolites are shown at both 20 and 30 kbar, and projected through the geotherms to illustrate the range of temperature space they occupy at those pressures. The data is compared with A) P_{NG85} vs T_{Ta98} peridotite xenolith calculations for CH-6 (blue triangles) and CH-1, -7, -44 (grey triangles) from Kopylova et al. (2019), and single grain Chidliak clinopyroxene P_{NT} vs T_{NT} data from Pell et al. (2013) (blue shaded field); and B) P_{NT} vs T_{NT} peridotite xenolith calculations for CH-6 (blue triangles) and CH-1, -7, -44 (grey triangles) from Kopylova et al. (2019), and single grain Chidliak clinopyroxene P_{NT} vs T_{NT} data from Pell et al. (2013) (blue shaded field). The brown and pink lines are the Chidliak geotherms from Pell et al. (2013) and Kopylova et al. (2019). Reference geotherms are from Hasterok and Chapman (2011) (solid black lines) and the graphite-diamond transition (grey line) is from Day (2012).

3.3 Major element geochemistry of xenolith minerals

Major-element compositions reported in this section are available in the University of Alberta UAL Dataverse under "Brody Myers MSc thesis Supplementary Online Dataset" (https://doi.org/10.7939/DVN/VWFTSN). Ferric iron in oxide minerals is calculated assuming ideal stoichiometry using the method of Droop (1987), and spinel group minerals are classified using the nomenclature of Bosi et al. (2019). Reported olivine, clinopyroxene, orthopyroxene, and garnet analyses have oxide totals between 98.50 and 101.50 wt%. Filters of oxide totals between 95.00 and 101.50 wt% are used for oxide and hydrous minerals after ferric iron and/or OH^- calculation. All non-silicate phases are screened for $SiO_2 < 1.00$ wt%, except apatite, which was filtered based on $SiO_2 < 2.50$ and $MgO < 2.00$ wt% to exclude analyses with secondary fluorescence from serpentine. Reported carbonates (calcite, dolomite, magnesite) have oxide totals between 98.50 and 101.50 wt% after CO_2 calculation from stoichiometry, except for strontianite and Sr-rich calcite analyses, which are between 101.00 and 104.00 wt%. The expanded range was considered acceptable due to the uncertainties associated with calculating CO_2 from stoichiometry, and all analyses have SiO_2 below the analytical limit of detection.

3.3.1 Olivine

Olivine in the 23 peridotites and one pyroxenite have a wide range in Mg# (Mg/[Mg+Fe]), from 84.9 to 92.5 (mean 90.1 ± 4.6 [2σ]). Within individual xenoliths, olivine porphyroclasts and neoblasts have the same Mg#. Both clinopyroxene ilmenite dunites have the lowest Mg# (Mg# = 84.9 and 85.2). The average, minimum, and maximum Mg# from olivine cores from each lithology are given in Table 3.3.1. MgO and NiO are usually lower in cpx dunites, the dunite, and the wehrlite, and higher in FeO relative to the other peridotite lithologies.

Olivines in contact with melt pockets and/or serpentine-filled fractures, occasionally have altered patches along their edges that have lower FeO and NiO, and higher MgO than their respective cores. The Mg# for the altered olivine patches analyzed in three melt-bearing xenoliths and one melt-free xenolith, ranges from 92.8 to 95.2.

Table 3.3.1 – Average and ranges of olivine Mg# from each lithology.

Lithology	*n*	Mg# (avg)	Mg# (min)	Mg# (max)
Dunite	1	89.8	89.8	89.8
Harzburgite	1	91.6	91.6	91.6
Px dunite	4	91.9	91.6	92.2
Cpx dunite	13	89.2	84.9	92.5
Wehrlite	1	86.6	86.6	86.6
Spinel peridotite	3	91.9	91.6	92.1
Olivine websterite	1	92.5	92.5	92.5

n = number of xenoliths of each lithology in the suite.

3.3.2 Clinopyroxene

Clinopyroxenes from the peridotite and pyroxenite xenoliths are chrome-bearing diopsides (*n* = 9) and Cr-bearing augites (*n* = 13) in the nomenclature of Morimoto (1988) (Figure 3.3.1). The average core compositions range from 0.09 to 2.78 Cr_2O_3 wt% (*n* = 22) with a mean of 1.11 ± 1.27 wt% [2σ]. The Mg# ranges from 87.1 to 94.4 with a mean of 91.6 ± 3.7 [2σ]. Both clinopyroxene ilmenite dunites contain Cr-poor augites with average Cr_2O_3 ranging from 0.09 to 0.10 wt%. The Mg# of their clinopyroxenes (87.1 and 87.6) is the lowest of all the peridotites and pyroxenite. Peridotites and the pyroxenite have average TiO_2 = 0.19 ± 0.12 [2σ] wt% (*n* = 19), and spinel peridotites have TiO_2 = 0.56 ± 0.24 [2σ] wt% (*n* = 3). Clinopyroxene in the eclogite is omphacite with average Na# (Na# = Na/[Na+Ca]) 0.44, Mg# = 0.81, and Cr_2O_3 = 0.04 wt%. The Al_2O_3 and Cr_2O_3 composition, Mg#, Na#, and clinopyroxene-type in each xenolith is given in Table 3.3.2.

Clinopyroxene margins with a "spongy" texture were analyzed in two xenoliths and have higher CaO and lower Na_2O and Al_2O_3 relative to their cores. Thin overgrowths of clinopyroxene on orthopyroxene grains typically have lower Na_2O, Cr_2O_3, and Al_2O_3, and higher CaO, TiO_2, and MgO than the cores of primary clinopyroxene grains in the same xenolith. The TiO_2 content ranges from 0.1 – 0.7 wt% in the coronas.

Thin overgrowths of clinopyroxene on primary clinopyroxene grains usually yielded analyses with oxide totals < 98.5 wt% or with elevated K_2O (0.64 wt% in one case). These analyses may be a mixture of clinopyroxene and a hydrous K-bearing phase such as phlogopite or potassic richterite. Consequently, the analyses did not pass quality filters except for one in spinel pyroxene dunite 0411C, which had an oxide total 100.48 wt% and slightly elevated K_2O of 0.08 wt% (compared to K_2O below LOD in core analyses). Despite most not passing quality control filters, all the analyses of clinopyroxene rims on clinopyroxene grains have higher CaO, lower Na_2O, and usually lower Al_2O_3 compositions than primary clinopyroxene core analyses from their respective xenolith. Their Mg# relative to their respective core varies from higher to lower in the four xenoliths analyzed.

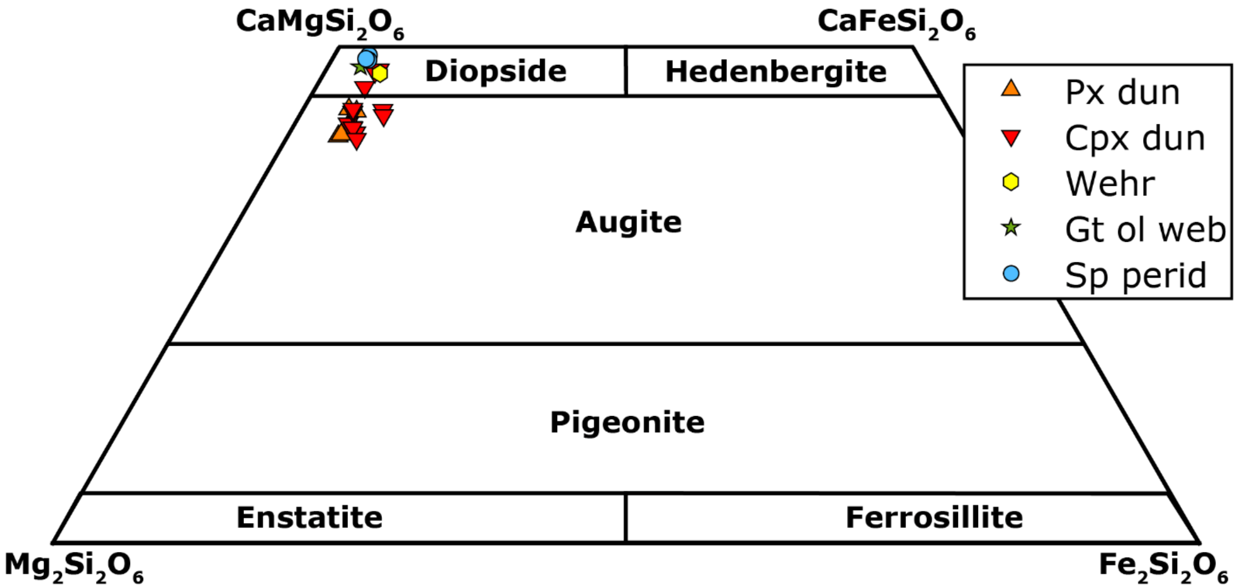

Figure 3.3.1 – Pyroxene quadrilateral with fields after Morimoto (1988) showing the clinopyroxene compositions from the peridotite and pyroxenite xenoliths in this study.

Table 3.3.2 – Averaged clinopyroxene statistics and mineral classification from each xenolith.

Sample	Al_2O_3 (wt%)	Cr_2O_3 (wt%)	Mg#	Na#	Mineral	Lithology
0404B1	1.22	0.09	87.6	8.6	AUGITE	Cpx dun
0404C	1.33	0.10	87.1	9.5	AUGITE	Cpx dun
0405E	1.50	1.28	92.1	11.9	AUGITE	Cpx dun
0411E	1.44	0.74	90.1	11.5	AUGITE	Cpx dun
0411F3	1.84	1.21	91.9	14.1	AUGITE	Cpx dun
0411G	1.46	1.32	91.1	12.9	AUGITE	Cpx dun
0411J	1.48	1.16	90.9	12.1	AUGITE	Cpx dun
0411K	1.43	1.41	92.3	11.8	AUGITE	Cpx dun
0413B	1.57	1.02	89.7	13.5	AUGITE	Cpx dun
0411F1	1.78	2.32	92.9	16.4	AUGITE	Px dun
0411F2	0.97	1.57	92.2	10.5	AUGITE	Px dun
0413A	2.11	2.78	91.6	21.3	AUGITE	Px dun
0413D	1.38	1.69	92.5	13.0	AUGITE	Px dun
0404B2	1.08	0.84	92.1	9.7	DIOPSIDE	Cpx dun
0405C	1.51	1.01	91.8	9.5	DIOPSIDE	Cpx dun
0411D	1.49	0.87	91.3	9.4	DIOPSIDE	Cpx dun
0411I	1.40	0.49	91.1	8.1	DIOPSIDE	Cpx dun
0405D1	3.54	0.45	94.4	15.7	DIOPSIDE	Ol webs
0405A	6.03	1.00	94.1	15.2	DIOPSIDE	Sp lherz
0405B1	5.80	1.19	93.8	16.5	DIOPSIDE	Sp px dun
0411C	4.78	1.35	94.3	13.8	DIOPSIDE	Sp px dun
0411H	1.46	0.64	90.7	9.2	DIOPSIDE	Wehr
0405H	11.44	0.04	81.4	43.5	OMPHACITE	Eclogite

Mg# = Mg/[Mg+Fe]*100, Na# = Na/[Na+Ca]*100.

3.3.3 Orthopyroxene

Orthopyroxene grains with minimal alteration that were analyzed in nine peridotites and one pyroxenite xenolith are enstatite, with Mg# ranging from 91.8 to 93.7, with mean 92.8 ± 1.28 [2σ]. Garnet-facies orthopyroxenes have lower Al_2O_3 and FeO, and higher MgO, Na_2O, and SiO_2 than spinel-facies. Of the 13 orthopyroxene-bearing samples, three exclusively contain orthopyroxene partially pseudomorphed by clinopyroxene + serpentine ± phlogopite ± tetraferriphlogopite, another only contains small patches of orthopyroxene along the edge of some clinopyroxene grains. These grains have higher CaO and Cr_2O_3, and lower MgO than orthopyroxenes with minimal alteration. Additionally, the orthopyroxenes in three out of four of these xenoliths have the highest TiO_2 and FeO.

3.3.4 Garnet

Garnets in the peridotites and olivine websterite have 47.8 – 73.1 mol% pyrope component, whereas the eclogitic garnets in xenolith 0405H have 36.5 mol% pyrope, 27.9 mol% grossular, and 31.3 mol% almandine component, as calculated with the procedure of Locock (2008). Figure 3.3.2 shows the normalized Fe-Mg-Ca concentrations of garnets in each xenolith in the suite. The classification scheme of Grütter et al. (2004) was utilized to differentiate the samples further. Multiple analyses per grain were taken where possible, to evaluate compositional homogeneity between the core (grain centre), mantle (between the centre and edge) and rim (grain edge). The CaO – Cr_2O_3 systematics of the cores, mantles, and rims are shown in Figure 3.3.4, and the variation of garnet-classes between cores, mantles and rims is shown in Figure 3.3.5. The garnets in this study classify as G12, G9, G10, G5, G4, G3, G11 and G1. Several of the xenoliths have garnet analyses that classify in two (n = 8) to three (n = 1) of the classification fields of Grütter et al. (2004), testifying to their geochemical heterogeneity. Additionally, the averaged composition of garnets in 11 xenoliths, plot in the high-TiO_2 megacryst field after Schulze (1997) (Figure 3.3.3). The average Mg# of garnets in peridotites and olivine websterite ranges from 67.9 to 83.2 (n = 16) with a mean of 78.6 ± 9.5 [2σ]. Garnet Cr# (Cr/[Cr + Al]*100) of the peridotites and olivine websterite ranges from 1.7 to 35.6, with mean 17.9 ± 18.5 [2σ]. The eclogite has garnets with average Mg# = 54.6 and Cr# = 0.15.

Compositional variation of individual garnets in xenoliths is most significant in seven clinopyroxene dunites and the pyroxene-free dunite, which have standard deviation ≥ 0.75 wt% in at least one of: Al_2O_3, Cr_2O_3, MgO, or CaO. Garnets with high variance have rims with lower Cr_2O_3 and usually have higher Al_2O_3 than their cores. The TiO_2, MgO, and CaO contents in the rims may differ from their cores, but systematic deviations of higher or lower concentrations in the rims relative to their cores is not observed. Often different garnets within the same xenolith have contrasting trends of higher or lower concentrations of these oxides in their rims relative to cores. In the other nine garnet-bearing xenoliths (olivine websterite, harzburgite, eclogite, pyroxene dunites, and two clinopyroxene dunites - that allowed fewer analyses due to rare and small garnets in the thin sections), there is comparatively lower variation in Al_2O_3, Cr_2O_3, MgO, and CaO, based on the standard deviation ≤ 0.65 wt% for each oxide. FeO and Na_2O in rims are almost always the same as their core compositions across all xenoliths.

Inclusions of ilmenite, magnesiochromite, spinel, olivine, rutile, and pargasite (in one case) were found in several garnets. Alteration halos up to ~ 250 μm around inclusion-rich zones in garnet sometimes occur. An analysis of one of these halos had higher TiO_2, Al_2O_3, FeO, and MgO, and lower Cr_2O_3 and Na_2O than its core composition.

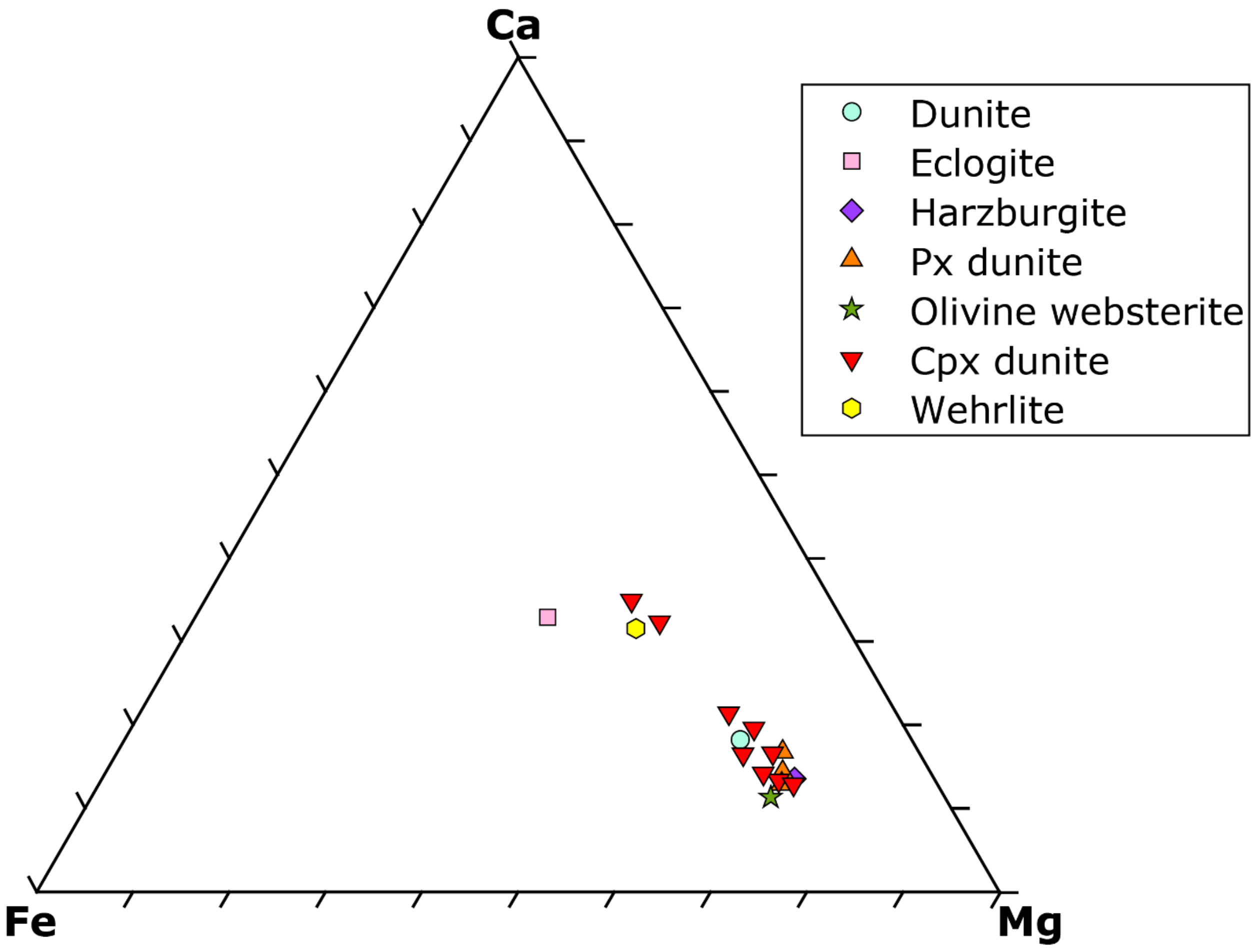

Figure 3.3.2 – Ternary plot of averaged core and rim compositions of garnets from each garnet-bearing xenolith in this study.

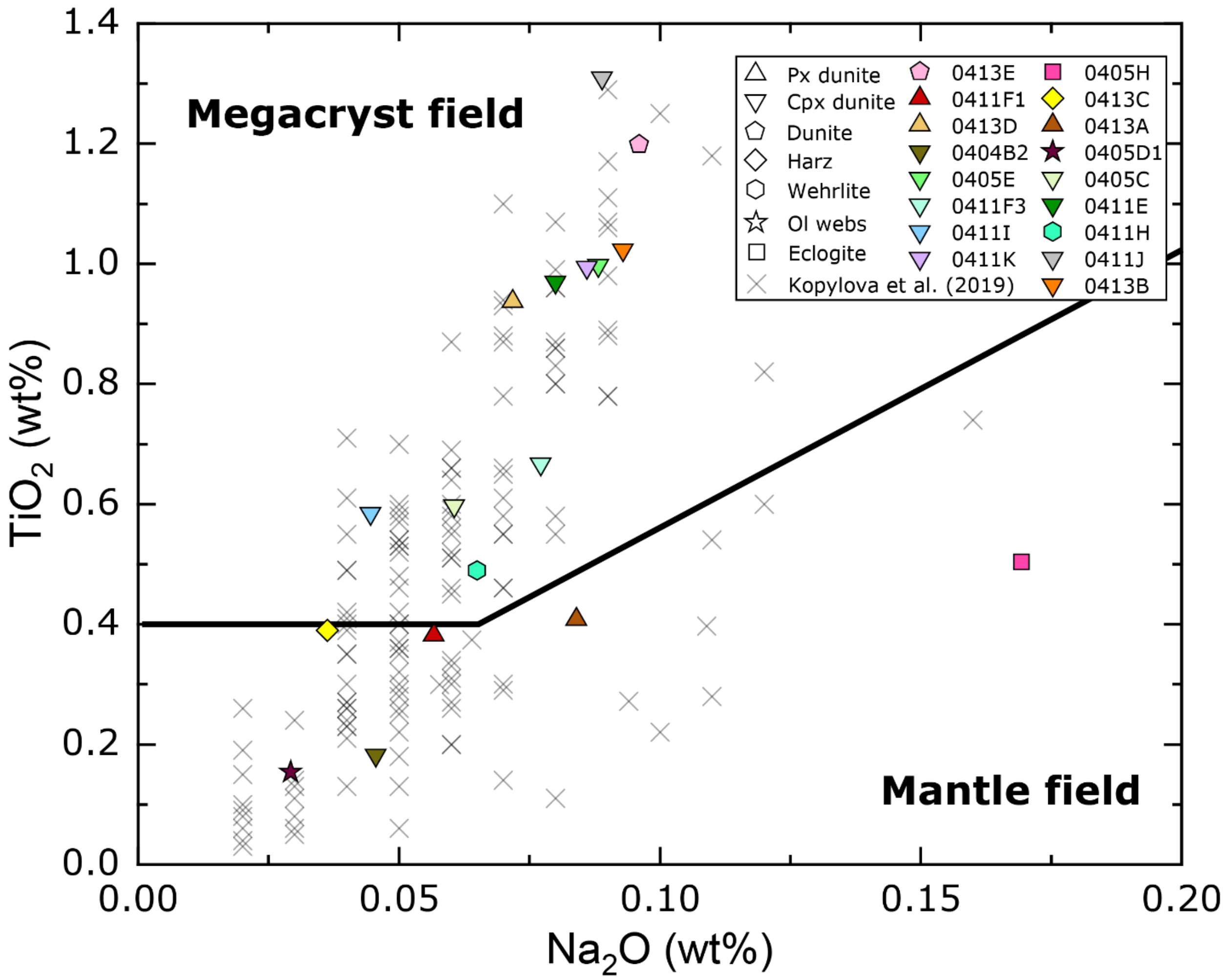

Figure 3.3.3 – Na_2O vs TiO_2 plot of averaged garnet analyses from this study compared with garnet analyses from Chidliak peridotites reported by Kopylova et al. (2019). Megacryst and mantle fields are from Schulze (1997).

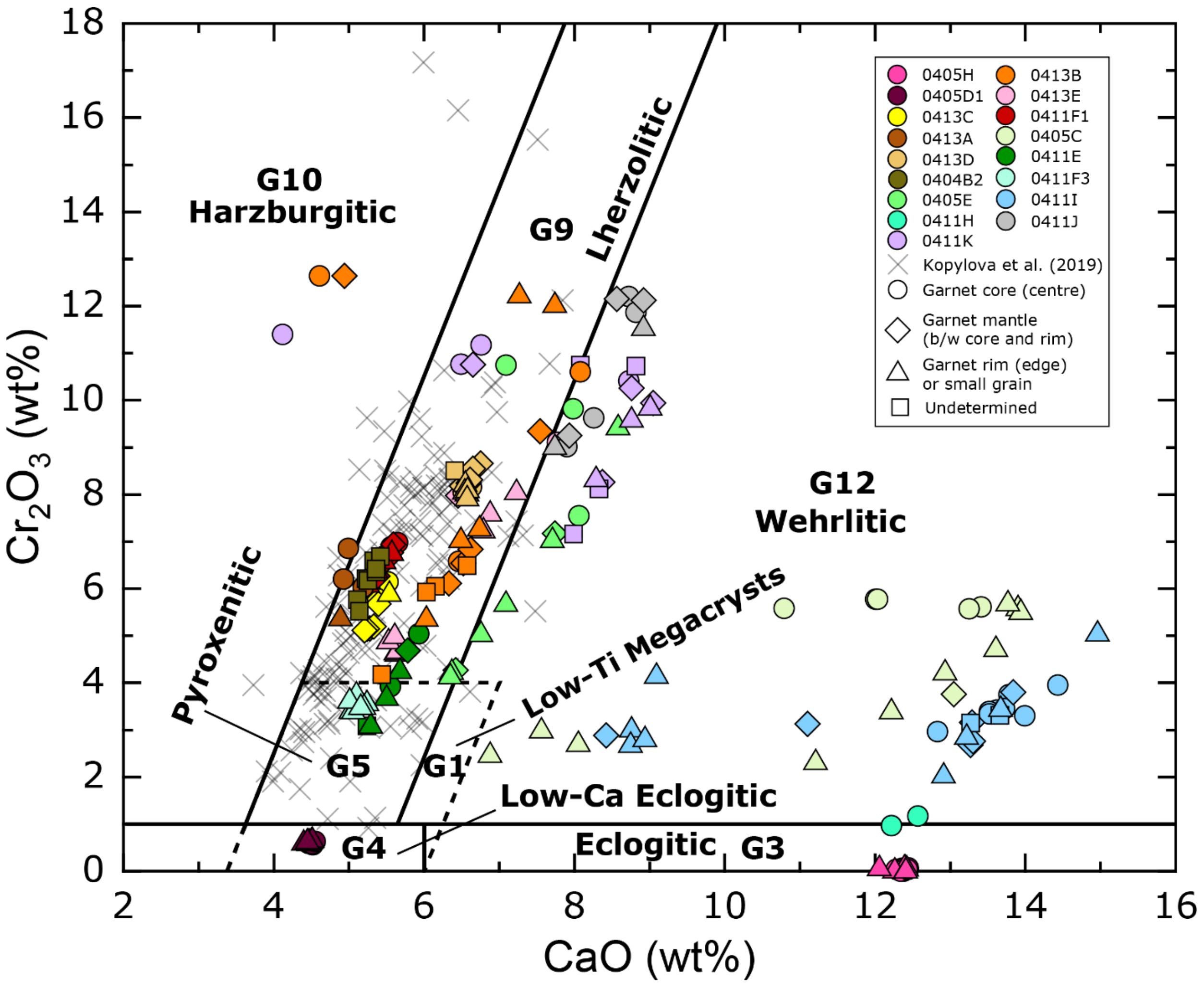

Figure 3.3.4 – CaO versus Cr_2O_3 (wt%) plot of garnet analyses from grain cores (centres), mantles (midway between core and edge), rims (edges), small (same symbol as rims), and not determined (ND), with classification fields after Grütter et al. (2004). Background data are garnet compositions from Chidliak peridotites reported by Kopylova et al. (2019).

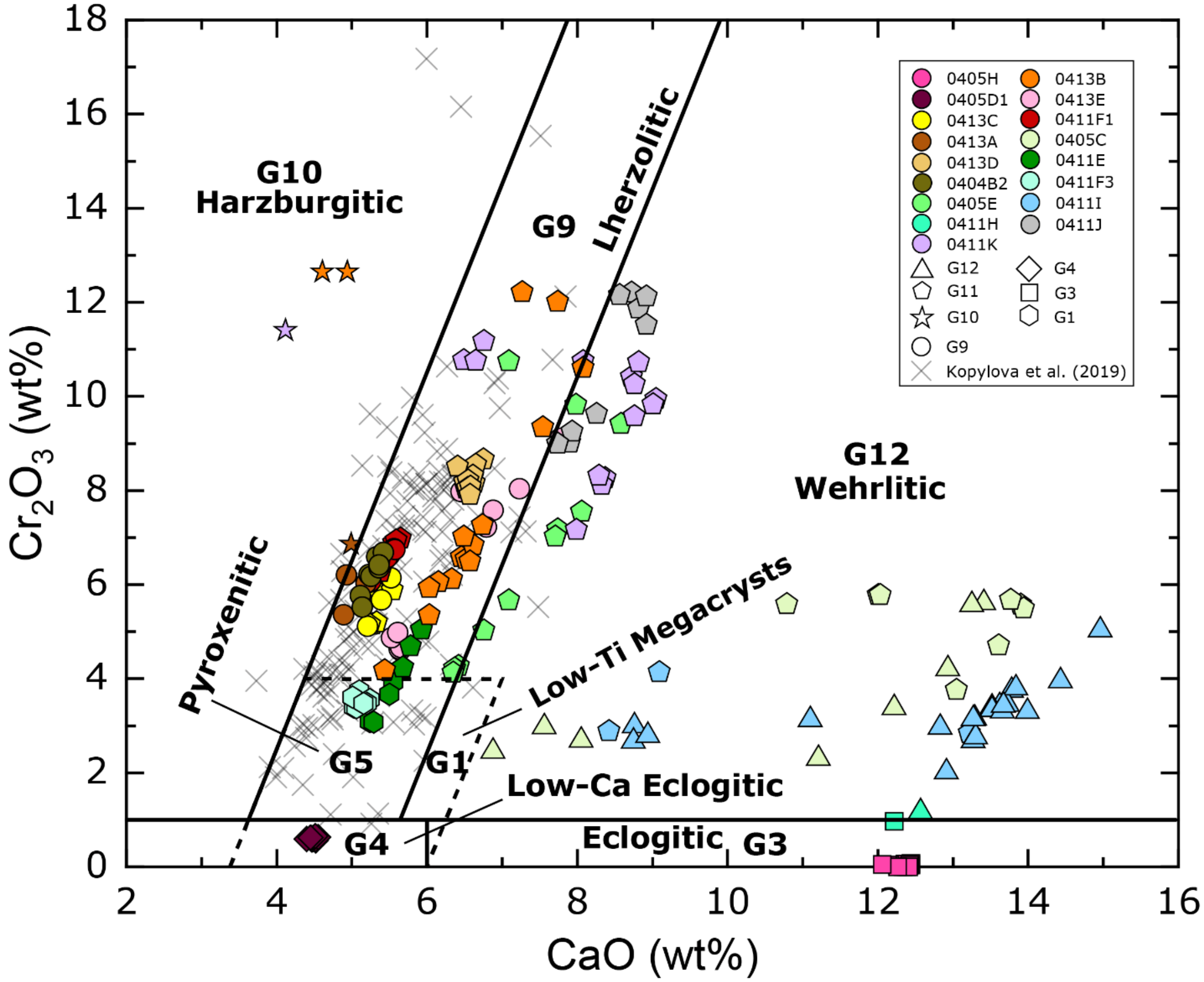

Figure 3.3.5 - CaO versus Cr_2O_3 (wt%) plot of garnet analyses from this study showing the variation in garnet classification between core, mantle, and rim analyses, after Grütter et al. (2004). Garnet classification may not correspond to the field it plots in due to the higher order of preference for which G11 and G1 garnets are classified. Background data are averaged garnet analyses from Chidliak peridotites reported by Kopylova et al. (2019).

3.3.5 Spinel

Spinel from spinel-bearing peridotites are Al_2O_3-rich and are classified as spinel from the nomenclature of Bosi et al. (2019). Al_2O_3 and Cr_2O_3 wt% ranges from 42.8 – 54.5 and 14.3 – 25.1 wt%, respectively. Secondary spinel rims with different composition than the grain core were analyzed in 0405A. The rims have lower Al_2O_3 and FeO, and higher TiO_2, Fe_3O_2, MgO, MnO and NiO than the grain core composition.

3.4 Major element geochemistry of “exotic” phases

3.4.1 Ilmenite

Compositions of the cores and rims of ilmenites in garnet inclusions and coarse ilmenites along melt pockets often have minimal compositional variance within individual grains. However, a few rims on grains along the edge of melt pockets have higher MgO and lower FeO relative to their cores. The MgO range of core analyses from large ilmenite grains in contact with melt pockets is from 5.9 to 15.1 wt%, and rims 7.2 to 18.6 wt%. The compositions of coarse ilmenites in contact with melt pockets have different compositions than kimberlite groundmass ilmenite, as well as the rare, small ilmenite grains in melt veins/pockets. The most pronounced compositional differences are in TiO_2, MgO, V_2O_3, and MnO, which are plotted in Figure 4.1.2 and Figure 4.1.3. The compositions of coarse ilmenites in contact with melt pockets typically have lower TiO_2, MgO, and MnO, and higher V_2O_3 than kimberlite groundmass and melt intrusion ilmenites.

3.4.2 Rutile, jeppeite and freudenbergite

Rutile in the pyroxenite, eclogite, an inclusion in garnet in a peridotite, and a grain in a melt pocket, have TiO_2 ranging from 94.7 to 99.1 wt%. Jeppeite $[(K,Ba)_2(Ti,Fe^{3+})_6O_{13}]$ rims on rutile in the eclogite and pyroxenite have TiO_2 ranging from 75.1 to 82.9 wt%, with K_2O and BaO ranging from 8.4 to 12.4 wt%, and 0.5 to 2.3 wt%, respectively. The single freudenbergite $[Na_2(Ti,Fe^{3+})_8O_{16}]$ analysis on a rutile rim in the eclogite has TiO_2 = 79.4 wt% and Na_2O = 8.3 wt%.

3.4.3 Melt pocket, metasomatic, and kimberlite groundmass spinels

Melt pockets and veins in xenoliths from CH-7 contain spinel group minerals that include magnetite, magnesioferrite, magnesiochromite, spinel, qandilite, ülvospinel and chromite. Some of the compositions of spinels from CH-7 melt pockets overlap with CH-7 kimberlite groundmass spinel (Figure 3.4.1 and Figure 3.4.2). However, most CH-7 kimberlite groundmass spinels consist of chromite, magnesiochromite, magnesioferrite, and lesser spinel and qandilite. These compositions have distinctly lower Fe_2O_3 concentrations than most of the spinels in the melt intrusions.

Melt-bearing xenoliths from CH-6 contain spinels ranging from magnetite, magnesioferrite and qandilite. The more restricted range of spinel group minerals may reflect the lower numbers of melt-bearing CH-6 xenoliths in the suite (n = 2). The compositions of spinel in melt-bearing xenoliths from CH-6 are lower in Al_2O_3 and Cr_2O_3 than CH-6 kimberlite groundmass spinels, which consist mainly of chromite, magnesiochromite and lesser magnetite.

The calculated Fe_2O_3 wt% of melt pocket spinels in CH-6 and CH-7 xenoliths are generally much higher than the kimberlite groundmass spinels from both kimberlites (Figure 3.4.1). The spinels with high Fe_2O_3 belong to magnetite and magnesioferrite grains in the melt pockets. Magnetite and magnesioferrite are scarce in the kimberlite groundmass and have lower Fe_2O_3 content than ones in melt pockets.

Compositionally zoned melt-pocket spinels with an identifiable core and rim were analyzed in six different grains. Compared to their cores, the rims typically have higher Fe_2O_3 (n = 5), lower Cr_2O_3 (n = 4) and V_2O_3 (n = 5), and inconsistently higher-and-lower FeO, MgO, Al_2O_3, TiO_2 and MnO. Compositional zoning is frequent in kimberlite groundmass spinels. The composition difference between core and rim is not always consistent, however. In six zoned kimberlite groundmass spinels (five from CH-6, one from CH-7), the rims have higher MgO (n = 5), TiO_2 (n = 6), Fe_2O_3 (n = 4) and MnO (n = 5); lower Al (n = 4) and V_2O_3 (n = 5); and mixed higher and lower FeO and Cr_2O_3, compared to their cores. The zoning of both melt pocket and kimberlite groundmass spinels is broadly similar to that of Trend 1 (Mitchell, 1986) (Figure 3.4.1).

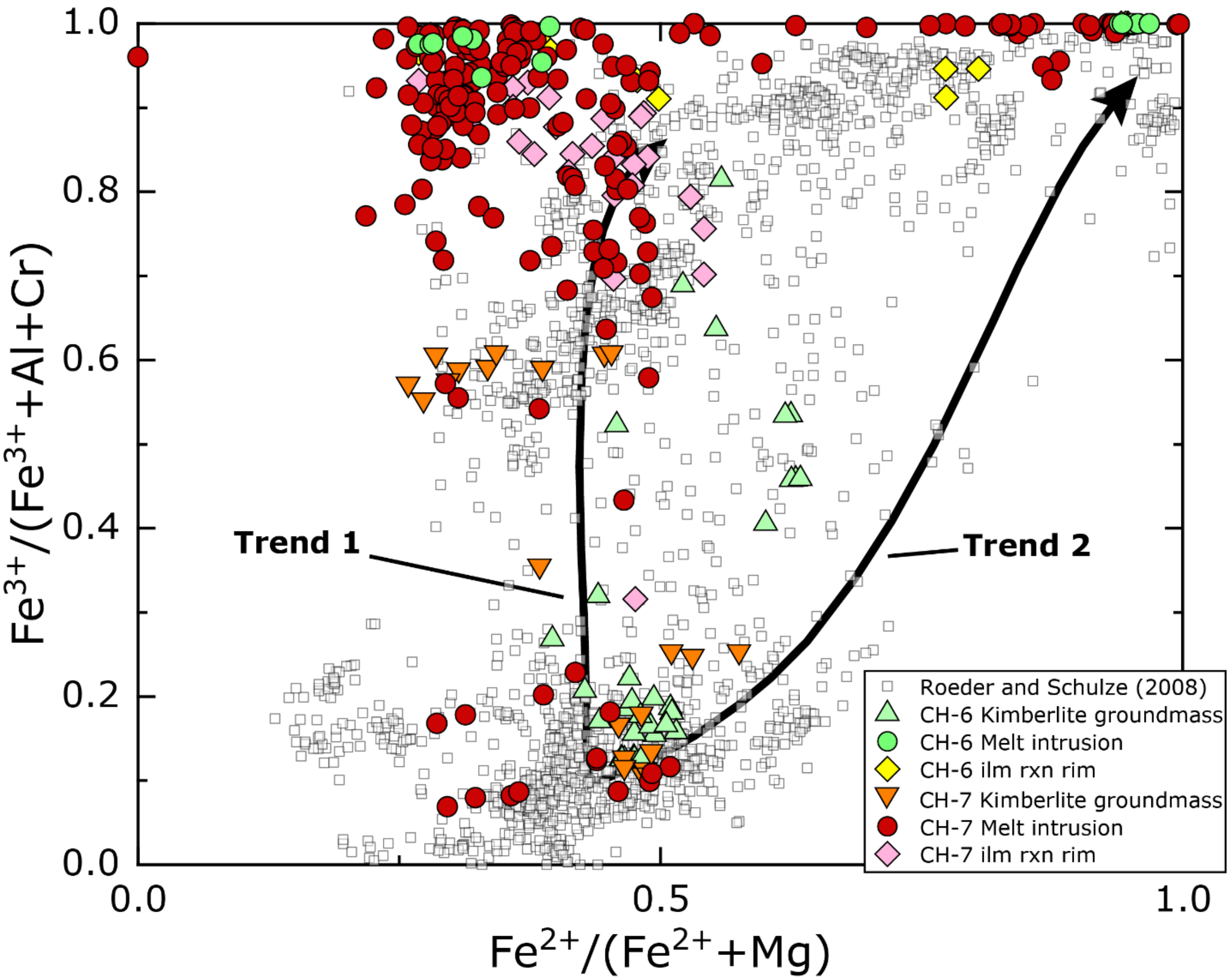

Figure 3.4.1 – $Fe^{3+}/(Fe^{3+}+Al+Cr)$ versus $Fe^{2+}/(Fe^{2+}+Mg)$ plot of CH-7 and CH-6 kimberlite groundmass spinels compared with spinels analyzed in xenolith melt intrusions as well as spinel reaction rims on coarse ilmenites in contact with melt intrusions (ilm rxn rim). Small squares are kimberlite groundmass spinels from Roeder and Schulze (2008). Trend 1 and Trend 2 lines are after Mitchell (1986).

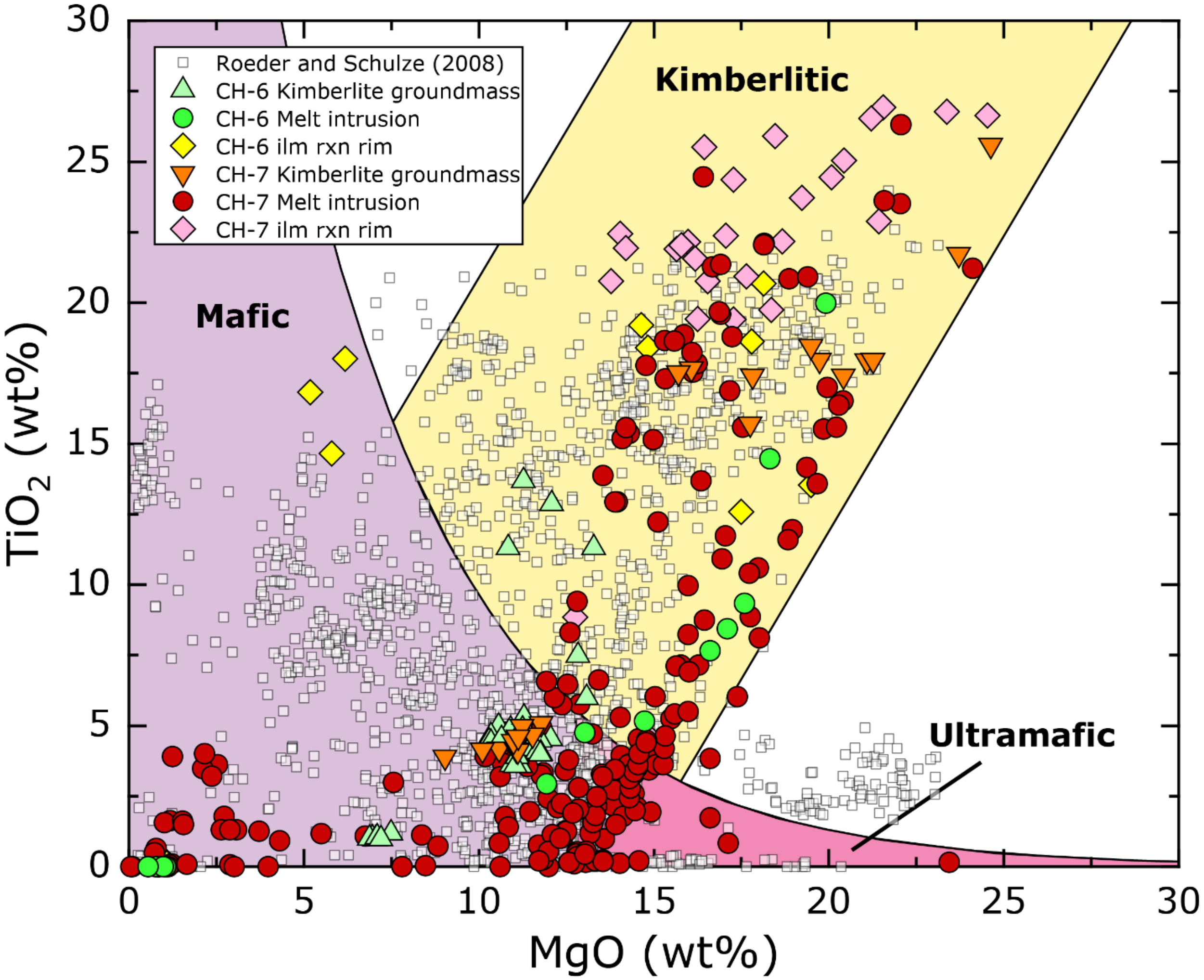

Figure 3.4.2 – TiO_2 versus MgO (wt%) plot of spinels from CH-7 and CH-6 kimberlite groundmass, compared with those analyzed in xenolith melt intrusions as well as spinel reaction rims on coarse ilmenites in contact with melt intrusions (ilm rxn rim). Composition fields for mafic, kimberlitic, and ultramafic spinels are from Creighton and Stachel (2008).

3.4.4 Hydrous phases

The compositions of the serpentine in the melt pockets and veins are consistent with that of antigorite; with MgO ranging from 34.7 – 40.5 wt% (*n* = 12), with mean 39.1 ± 4.3 [2σ] wt%. FeO ranges from 2.78 – 10.3 wt% with mean and standard deviation 6.66 ± 4.71 [2σ] wt%, and Al_2O_3 ranges from BDL to 3.04 wt%, with mean 0.61 ± 1.74 [2σ] wt%.

Averaged brucite analyses from five melt pockets in different xenoliths range in MgO from 62.3 – 66.9 wt% (*n* = 5), with mean 65.2 ± 2.0 [2σ] wt%. Al_2O_3 ranges from 0.04 to 0.12 wt% with mean 0.06 ± 0.03 [2σ] wt%.

Potassic-richterite on orthopyroxene rims in spinel lherzolite 0405A and garnet pyroxene dunite 0411F1, as well as in an un-documented part of clinopyroxene garnet dunite 0404B2, have K_2O and TiO_2 ranging from 4.46 to 5.82 and 0.07 to 0.18 wt%, respectively. FeO and MgO range from 2.96 to 4.59 and 22.0 to 24.0 wt%, respectively. Al_2O_3 ranges from 0.14 to 0.32 wt%.

Pargasite in spinel lherzolite 0405A, garnet olivine websterite 0405D1, and garnet clinopyroxene dunite 0405C, has K_2O and TiO_2 ranging from 0.36 to 1.20 and 0.91 to 2.03, respectively. FeO and MgO range from 2.22 to 6.85 and 15.8 to 17.7 wt%, respectively. Al_2O_3 ranges from 13.4 to 14.9 wt%.

The Mg# of metasomatic phlogopite (i.e. not spatially associated with garnet or pyroxene rims) grains from two xenoliths is 94.0 and 95.1. This is higher than the Mg# 89.0 to 93.0 range of phlogopites on garnet and pyroxene rims, with a mean of 91.2 ± 2.9 [2σ] (*n* = 8). Metasomatic phlogopites have lower FeO and Cr_2O_3 than those on garnet and pyroxene rims. The Al_2O_3 content of the two grains is 13.3 and 15.9 wt%.

Tetraferriphlogopite has Mg# equal to 84.0 and 84.9 where it was analyzed on an orthopyroxene rim partially pseudomorphed by clinopyroxene + serpentine + phlogopite, and on a clinopyroxene rim located in a melt vein in spinel pyroxene dunite 0411C, respectively. The Al_2O_3 concentration in those grains is 0.27 and 5.02 wt%, respectively.

3.4.5 Carbonates

The CaO in calcite varies from 52.6 – 55.9 wt% with mean 54.7 ± 2.4 [2σ] wt% (*n* = 10), respectively. Dolomite has MgO ranging from 16.3 – 21.9 with mean 18.3 ± 4.7 [2σ] wt%, and CaO ranging from 30.4 – 35.6 with mean 33.1 ± 4.6 [2σ] wt% (*n* = 5), respectively. The MgO in magnesite is 45.5 and 46.5 wt% (*n* = 2). Strontianite has SrO = 60.39 wt% (*n* = 1), with CaO = 9.47 wt%. A rim surrounding the strontianite consists of calcite-strontianite solid solution with SrO = 10.55 wt% and CaO = 48.16 wt%.

3.4.6 Perovskite

Perovskite from melt pockets, melt veins, and CH-7 kimberlite groundmass are dominantly perovskite-endmember ($CaTiO_3$) composition (> 75%), with REE varying from major to minor abundances (> 1.0 to 0.01 wt%). The oxide totals of perovskites analyzed in melt veins in xenolith 0405H (95.2 to 97.4 wt%, mean 96.6 wt% (*n* = 6)) are higher than those analyzed in melt pockets in xenolith 0411H (95.2 to 95.7 wt%, mean 95.5 wt% (*n* = 3). Consequently, the perovskites from veins and pockets are discussed separately, as the lower totals may have been affected by secondary fluorescence of serpentine. This could also be partially due to melt pocket perovskites often having skeletal, "spongy" textures with finely disseminated holes that complicate analysis by EPMA. In contrast, the grains in melt veins had less holes, and kimberlite groundmass had none. CH-7 kimberlite groundmass perovskites oxide totals range from 97.8 to 99.7 wt%, with mean 98.7 wt% (n = 11).

The melt pocket, kimberlite groundmass, and most melt vein perovskites plot near the perovskite apex in a Perovskite – Loparite – Lueshite ternary plot (Figure 3.4.4) (Locock and Mitchell, 2018). However, there is slight deviation in the sub-groups of melt vein perovskites in eclogite 0405H in a Perovskite – Loparite – Tausonite ternary plot (Figure 3.4.3) (Locock and Mitchell, 2018). They classify as niobian perovskite, niobian ceroan perovskite, ceroan perovskite, and perovskite. The REE concentrations of melt vein perovskites are similar to CH-7 groundmass perovskite, but have lower TiO_2, and higher Fe_2O_3 and Na_2O. Melt pocket/vein perovskites overlap with compositions of CH-7 kimberlite groundmass perovskites (Figure 3.4.3 and Figure 3.4.4). However, the melt pocket perovskites have much lower La_2O_3, Ce_2O_3, Pr_2O_3, and Nd_2O_3 than both CH-7 kimberlite groundmass and melt vein perovskites in xenolith 0405H.

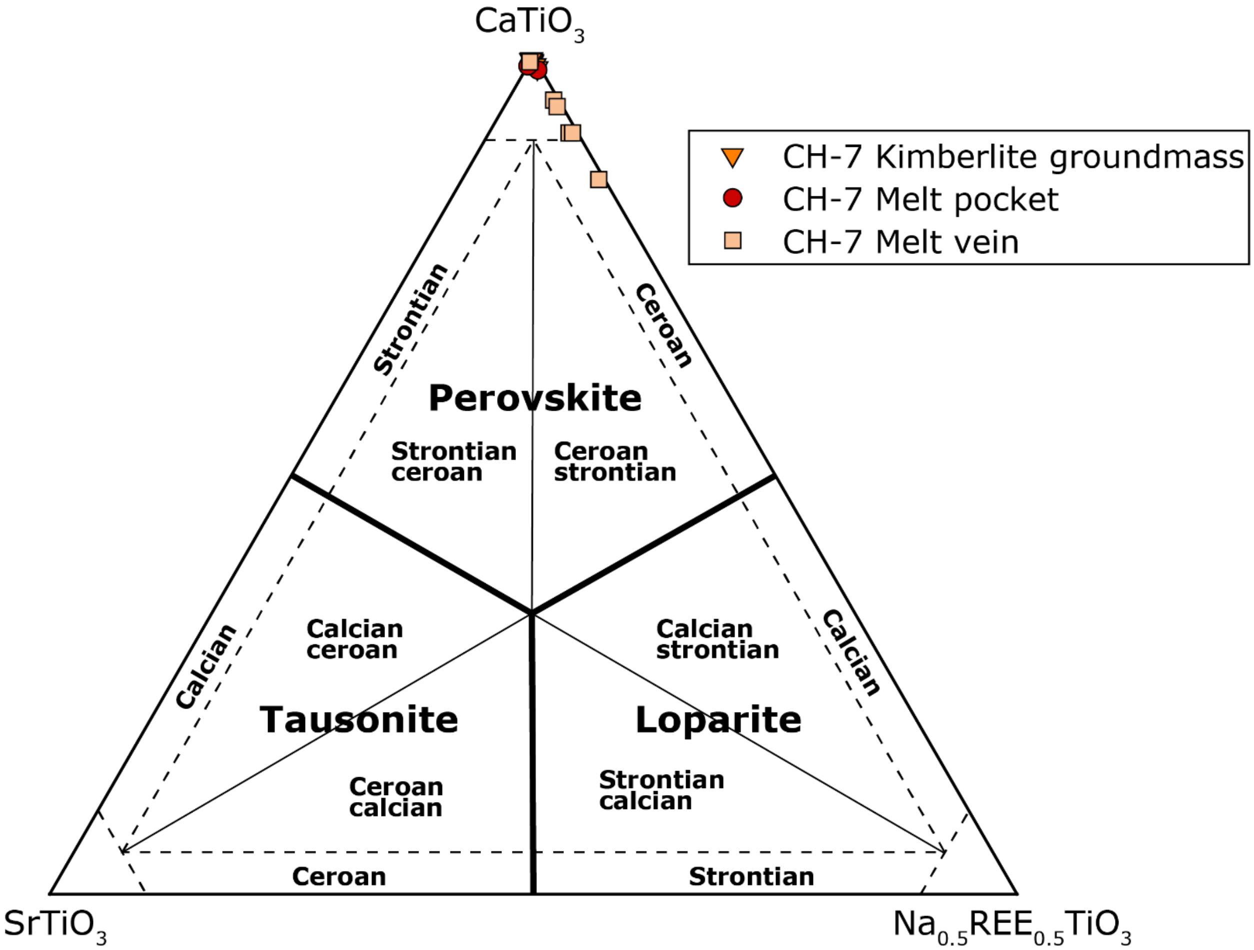

Figure 3.4.3 – Perovskite – Loparite – Tausonite ternary plot (Locock and Mitchell, 2018) of perovskites in CH-7 kimberlite groundmass (oxide totals 97.8 - 99.7 wt%), melt veins intruded in eclogite 0405H (oxide totals 95.18 - 97.42 wt%) and melt pockets in xenolith 0411H (oxide totals 95.2 - 95.7 wt%). CH-7 kimberlite groundmass perovskites plot at the perovskite apex of the ternary and are obstructed from view by other data points.

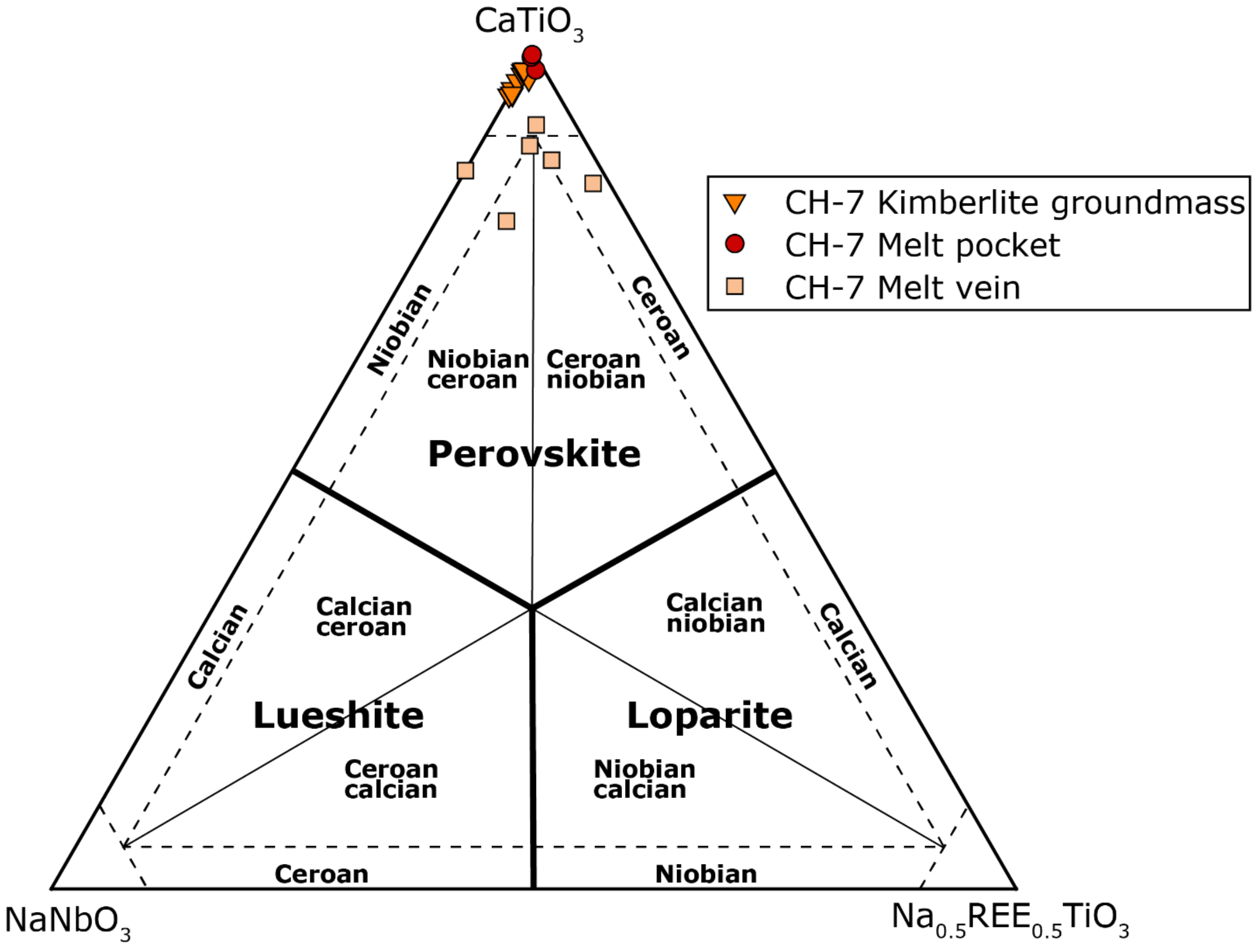

Figure 3.4.4 - Perovskite – Loparite – Lueshite ternary plot (Locock and Mitchell, 2018) of perovskites in CH-7 kimberlite (oxide totals 97.8 - 99.7 wt%), kimberlitic melt veins intruded in eclogite 0405H (oxide totals 95.2 – 97.4 wt%) and melt pockets in xenolith 0411H (oxide totals 95.2 - 95.7 wt%).

3.4.7 Apatite

Apatites present in the melt pockets and veins are a solid solution between fluorapatite and hydroxylapatite. In 52 analyses, fluorine ranges from 1.1 to 2.8 wt%, with mean 1.8 ± 0.6 [2σ] wt%, and Cl ranges from BDL to 0.43 wt%, with mean 0.06 ± 0.14 [2σ] wt%. Hydroxyl concentration calculated from stoichiometry ranges from 1.7 to 1.8 wt%, with mean 1.8 ± 0.04 [2σ] wt%.

3.4.8 Monticellite

The compositions of melt pocket/vein monticellites overlap with the compositions of those occurring along grain edges of clinopyroxene, orthopyroxene, and olivine in the xenoliths. In 51 analyses, FeO ranges from 0.8 to 5.7 wt%, with mean 2.3 ± 3.2 [2σ] wt%. MgO ranges from 21.6 to 28.1 wt%, with mean 24.4 ± 2.7 [2σ].

3.5 Major-element geochemistry of melt pockets and kimberlites

3.5.1 Melt pocket grids

Melt pockets were analyzed by EPMA in a grid fashion as described in Section 2.2.1. Annotated images of each melt pocket grid are shown in Figure 3.5.1. The averaged oxide compositions (wt%) from each grid are tabulated in Table 3.5.1. Average oxide totals for each melt pocket are low, ranging from 65.0 to 72.6 wt% for three grids completed in the carbonate-rich melt pockets of garnet clinopyroxene dunite 0405C; and 82.9 wt% for the more serpentine-rich melt pocket in clinopyroxene orthopyroxene garnet dunite 0413D. Low totals are partially because of unanalyzed volatiles (CO_2 and OH^-), mixtures of phases in individual analyses, unmeasured oxides, and a variably defocussed beam because of relief created between minerals of different hardness during polishing. Minor elements from 0405C and 0413D melt pockets have similar compositions, but deviate significantly in SiO_2, MgO, and CaO composition mainly due to different groundmass compositions (carbonate-dominated versus serpentine-dominated).

Table 3.5.1 Averaged major element geochemistry in oxide wt% of three carbonate-dominated melt pockets in xenolith 0405C and a serpentine-dominated melt pocket from 0413D, determined from EPMA grids.

Sample	**Statistic**	**n**	**SiO_2**	**TiO_2**	**Al_2O_3**	**Cr_2O_3**	**FeO**	**MgO**	**CaO**	**Na_2O**	**K_2O**	**P_2O_5**	**Total**
0405C	mean	3	14.94	0.29	0.42	0.04	10.23	22.55	18.88	0.04	0.02	0.51	67.91
0405C	2σ	3	2.31	0.72	0.75	0.11	10.69	0.98	5.05	0.02	0.03	0.80	8.19
0413D	mean	1	36.06	0.04	0.22	0.01	9.78	35.19	0.88	0.07	0.17	0.46	82.87

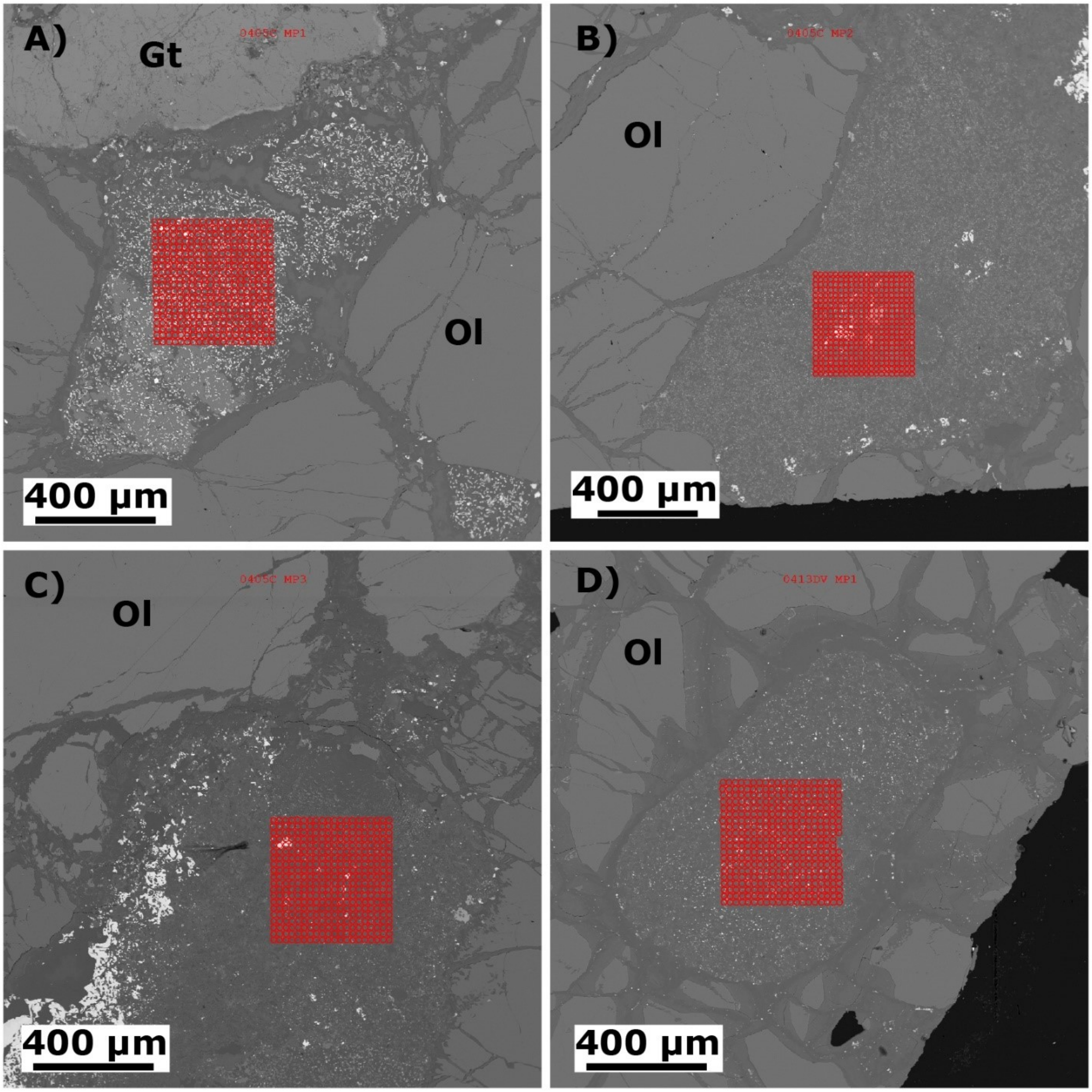

Figure 3.5.1 – Annotated BSE images of EPMA grids from: A) 0405C melt pocket 1; B) 0405C melt pocket 2; C) 0405C melt pocket 3; and D) 0413D melt pocket 1.

3.5.2 Kimberlite whole-rocks

The major- and trace-element geochemistry (determined by XRF) of the Chidliak kimberlite whole-rocks are available in the University of Alberta UAL Dataverse under "Brody Myers MSc thesis Supplementary Online Dataset" (https://doi.org/10.7939/DVN/VWFTSN). Crustal contamination of the kimberlite whole-rock samples were also evaluated using the Clement Contamination Index (C.I.) (C.I. = $[SiO_2 + Al_2O_3 + Na_2O]/[MgO + 2K_2O]$) (Clement, 1982). Contamination Index values range from 0.94 – 1.07 for all four samples, suggesting they have minimal to no crustal contamination, because values near unity are considered uncontaminated (Clement, 1982; Mitchell, 1986).

3.6 Trace element geochemistry of xenolith phases

Trace-element compositions reported in this section are available in the University of Alberta UAL Dataverse under "Brody Myers MSc thesis Supplementary Online Dataset" (https://doi.org/10.7939/DVN/VWFTSN). The trace-element normalized plots in this section use the C1 chondrite ($_N$) values of McDonough and Sun (1995). Only trace elements that are above the limit of quantitation (3 x LOD) are discussed and plotted.

3.6.1 Garnet

Trace elements in garnets from ten peridotite xenoliths were analyzed. Considerable variation is observed in the chondrite-normalized trace element patterns of garnets across the different xenoliths, as well as in cores and rims of some individual garnets. The patterns were grouped into five types (Figure 3.6.1). Type Ia "Enriched LREE Normal" and Type Ib "Enriched LREE Humped", have La_N between 1 and 10 times chondritic, with a negative slope to Ce_N, and a steep positive slope to Sm_N. From Sm_N to Lu_N, Type Ia is near flat to slightly positive, and Type Ib differs by having a negative slope from Tb_N to Lu_N. Type II "Normal" patterns have steep positive slopes from La_N to Sm_N, with shallow positive slopes to maxima at Gd_N - Dy_N, where they become near flat to Lu_N. Type III "Humped" patterns have steep positive slopes from La_N to maxima at Sm_N - Gd_N, followed by negative slopes to Lu_N. Type IV "Sinusoidal" patterns have steep positive slopes from La_N to maxima at Sm_N - Gd_N, negative slopes to minima at Er_N or Tm_N, and positive slopes to Lu_N.

Core-rim composition differences occur in garnets from several of the xenoliths (Figure 3.6.2). Garnets from clinopyroxene dunite xenoliths 0411K, 0411J, 0405E, 0413B, and pyroxene dunite 0413D, have cores/mantles/rims with Type IV REE patterns. In addition, they have at least one rim analysis with either Type II or Type III REE patterns that have higher MREE and HREE. Type III patterns in core/mantle analyses of pyroxene-free dunite 0413E have Type II patterns in rims. Type Ia patterns are found exclusively in rims and mantles (and one core analysis) of clinopyroxene dunite 0405E, the other cores and mantles plots as Type III and Type IV. Clinopyroxene dunite 0411I has mantles and rims with Type Ia patterns, and cores, mantles, and rims with Type II patterns. Type Ib patterns are found in two core analyses of clinopyroxene dunite 0405C, the remaining core, mantle, and rim analyses of garnets from 0405C plot as Type III.

Chondrite-normalized multi-element plots of the garnets in this study (Figure 3.6.3) show that the high field strength elements (HFSE) (Ti-Hf-Zr-Nb) are enriched relative to chondrite, with Ti, Hf, and Zr between 5 to 45x chondrite, and Nb ranges between 1 and 8x chondrite (except for one pyroxene dunite ~ 0.6x chondrite). Large-ion lithophile elements (LILE) (Rb-Sr-Ba-Eu) are typically subchondritic (< 1x chondrite), except for Eu, which ranges from 5 to 33x chondrite. Thorium and U are near chondritic, and Pb is subchondritic with values < 0.3x chondrite.

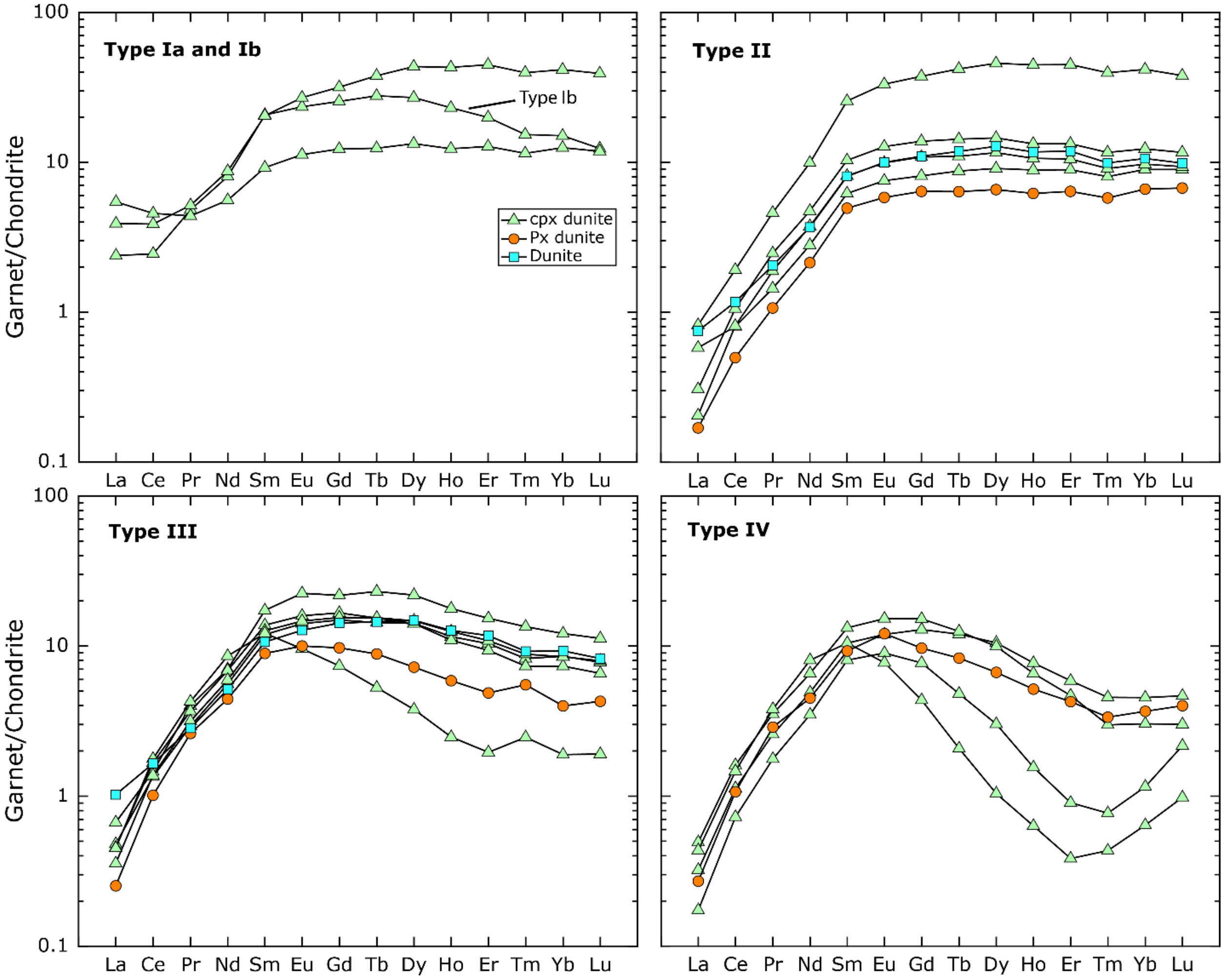

Figure 3.6.1 – Chondrite-normalized REE patterns of garnets in this study.

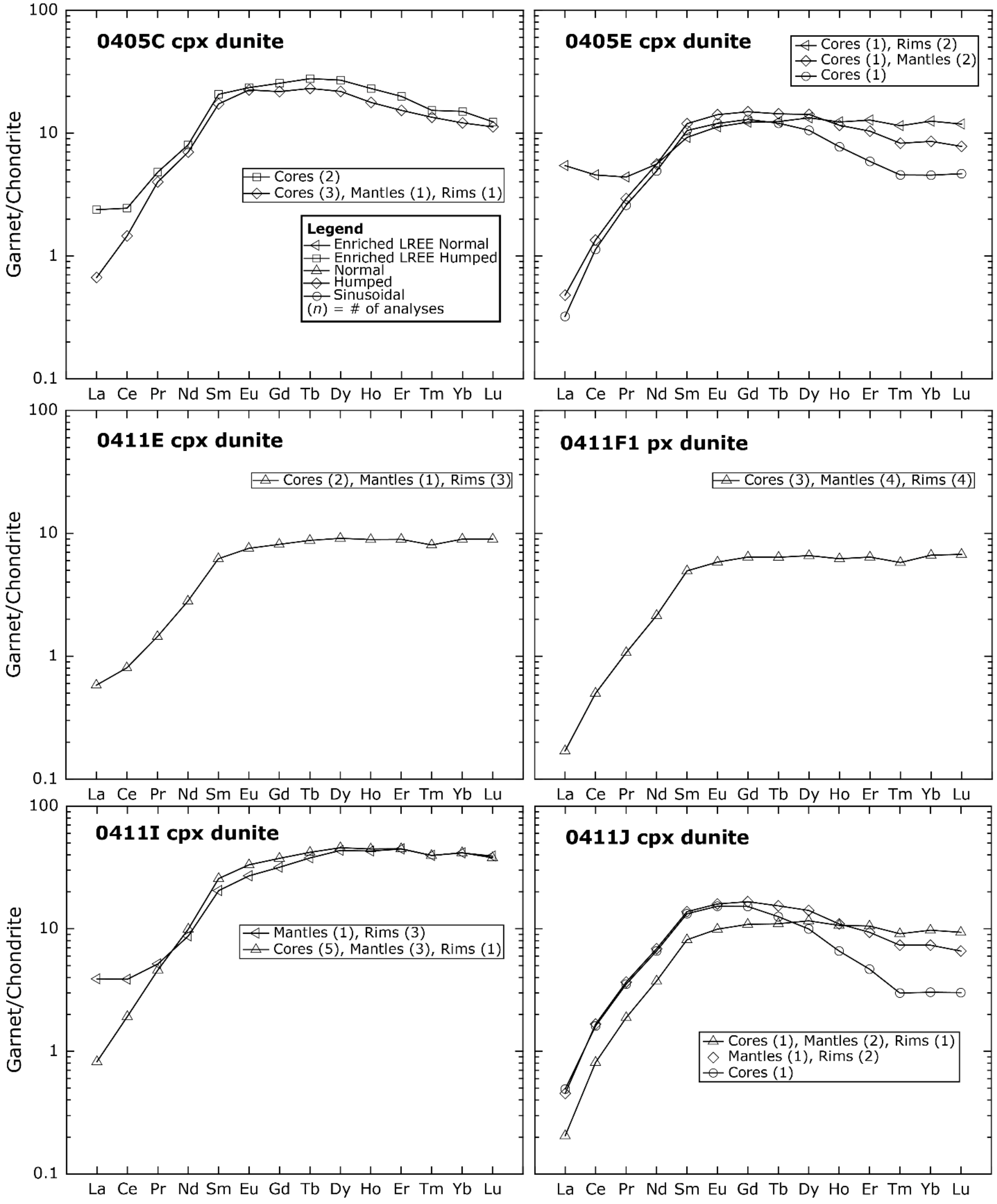
0405C cpx dunite
Cores (2)
Cores (3), Mantles (1), Rims (1)
Legend
Enriched LREE Normal
Enriched LREE Humped
Normal
Humped
Sinusoidal
(*n*) = # of analyses
0405E cpx dunite
Cores (1), Rims (2)
Cores (1), Mantles (2)
Cores (1)
0411E cpx dunite
Cores (2), Mantles (1), Rims (3)
0411F1 px dunite
Cores (3), Mantles (4), Rims (4)
0411I cpx dunite
Mantles (1), Rims (3)
Cores (5), Mantles (3), Rims (1)
0411J cpx dunite
Cores (1), Mantles (2), Rims (1)
Mantles (1), Rims (2)
Cores (1)
Garnet/Chondrite
100
10
1
0.1
La Ce Pr Nd Sm Eu Gd Tb Dy Ho Er Tm Yb Lu

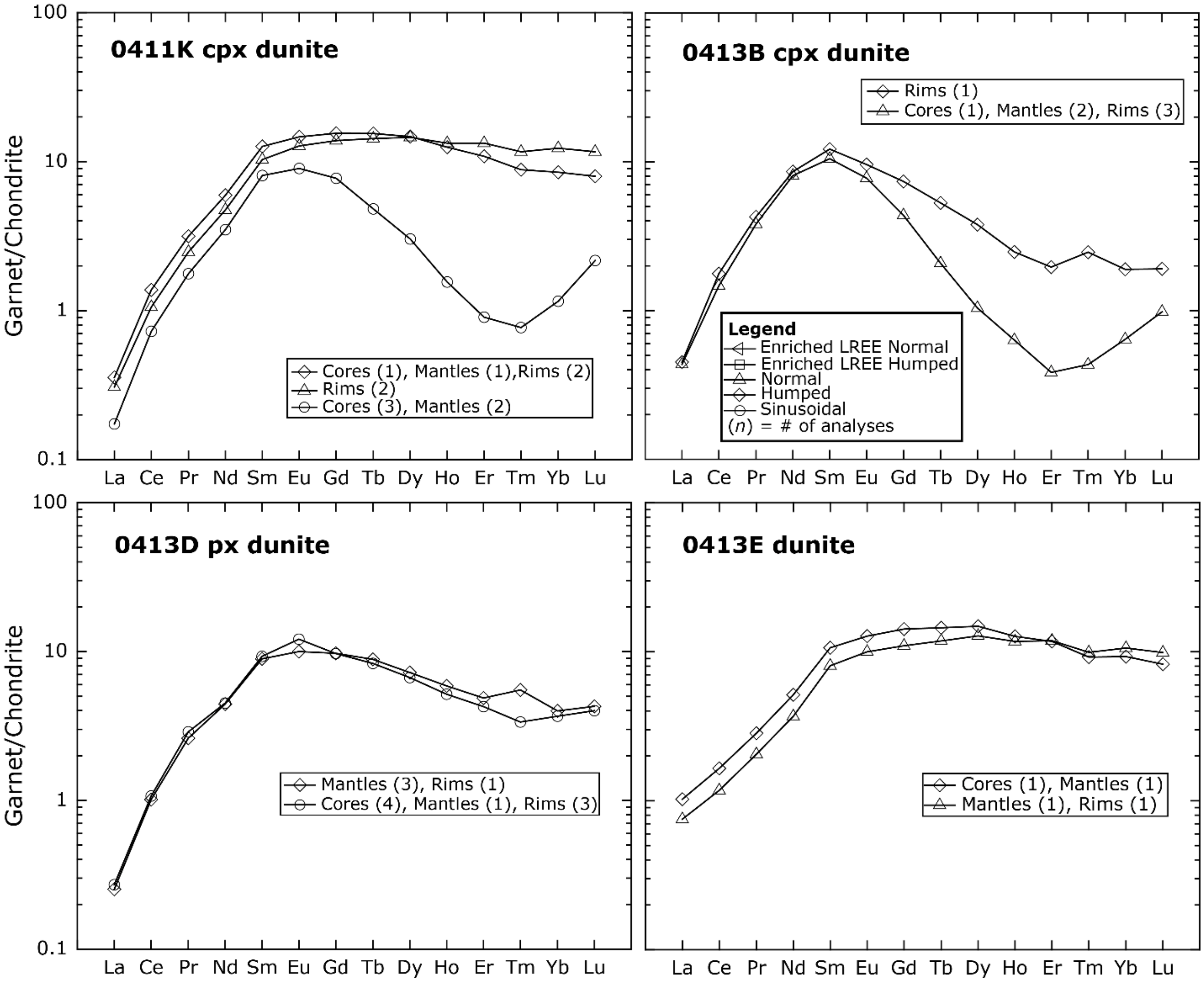

Figure 3.6.2 – Chondrite-normalized REE plot of garnets from each xenolith analyzed in this study. Symbols correspond to pattern type, and parentheses indicate the number of core, mantle, and rim analyses that were used in the averaged pattern.

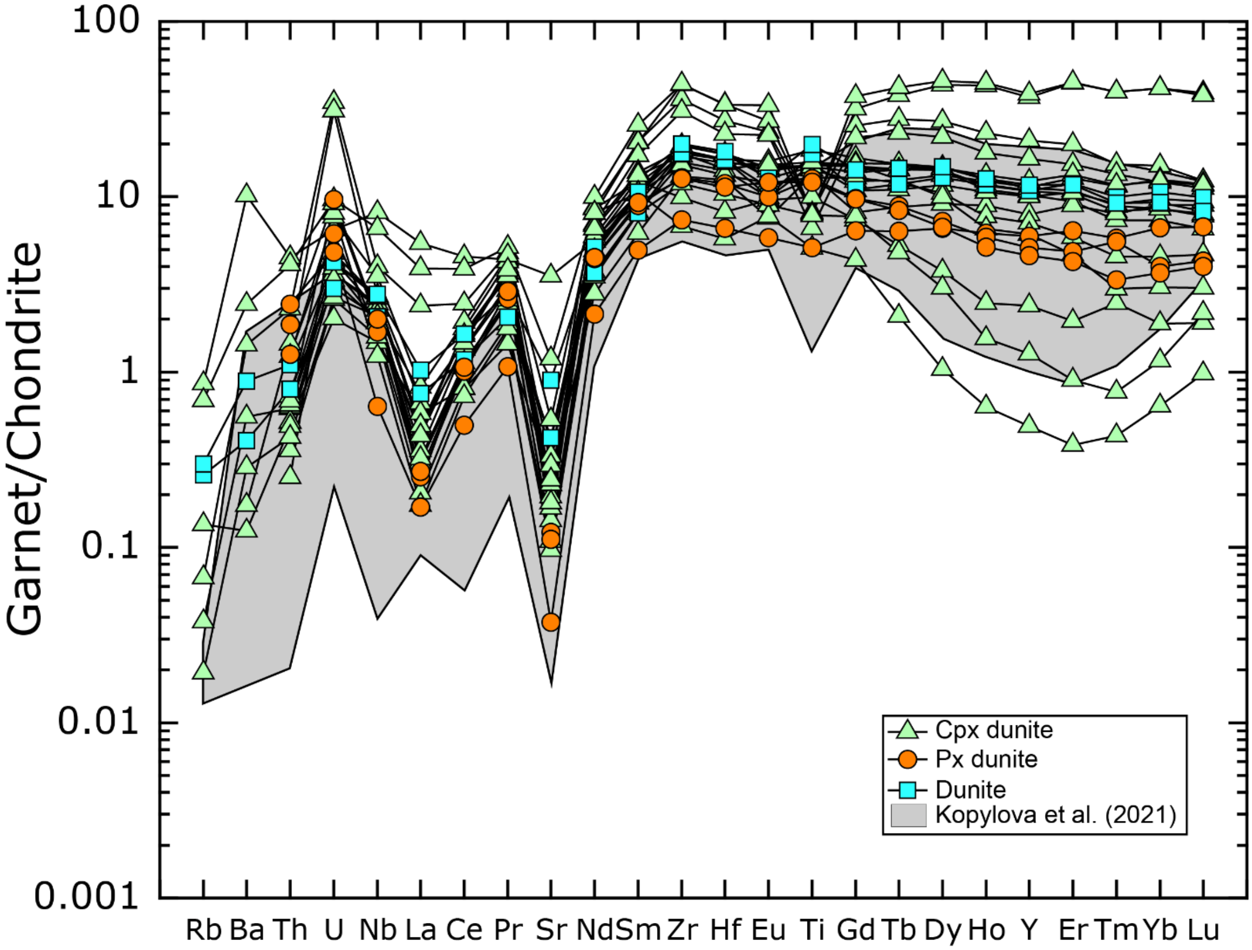

Figure 3.6.3 – Chondrite normalized multi-element plot of garnet compositions from this study compared with CH-7 garnets in melt-free lherzolites and harzburgites studied by Kopylova et al. (2021).

3.6.2 Clinopyroxene

Trace elements in clinopyroxenes were analyzed in eleven different peridotite xenoliths. In 58 analyses, Rb, Lu and U were the only elements below the limit of quantitation (LOQ) (3 x LOD) in 19% (*n* = 11), 10% (*n* = 6) and 2% (*n* = 1) measurements. Uranium was the only element below the LOD in a single analysis. The trace element patterns from this study are all LREE_N-enriched and HREE_N-depleted relative to C1 chondrite (Figure 3.6.4). The patterns have LREE_N enrichment up to ~ 10x chondrite, with a positive slope from La_N to maxima at Nd_N, followed by a negative slope to Lu_N in 10 of the xenoliths. One different pattern exists in a pyroxene dunite that has maxima at La_N (~ 26x chondrite), with a shallow negative slope to Nd_N (~ 16x chondrite), then a similar, steep negative slope as the other patterns from Nd_N to Lu_N. The clinopyroxene REE-compositions in pyroxene dunites differ from those in clinopyroxene dunites, by being slightly more depleted from Dy to Lu.

Chondrite-normalized multi-element plots (Figure 3.6.5) of the clinopyroxenes show that all the xenoliths have similar patterns from Rb to Hf, but have a wider spread in Nb, Th, and U composition. The HFSE are almost all superchondritic, with values between 1 and 10x chondrite. Rubidium is always subchondritic (0.01 to 0.2x chondrite), and Ba, Th, and U have wide ranging compositions, from subchondritic to superchondritic.

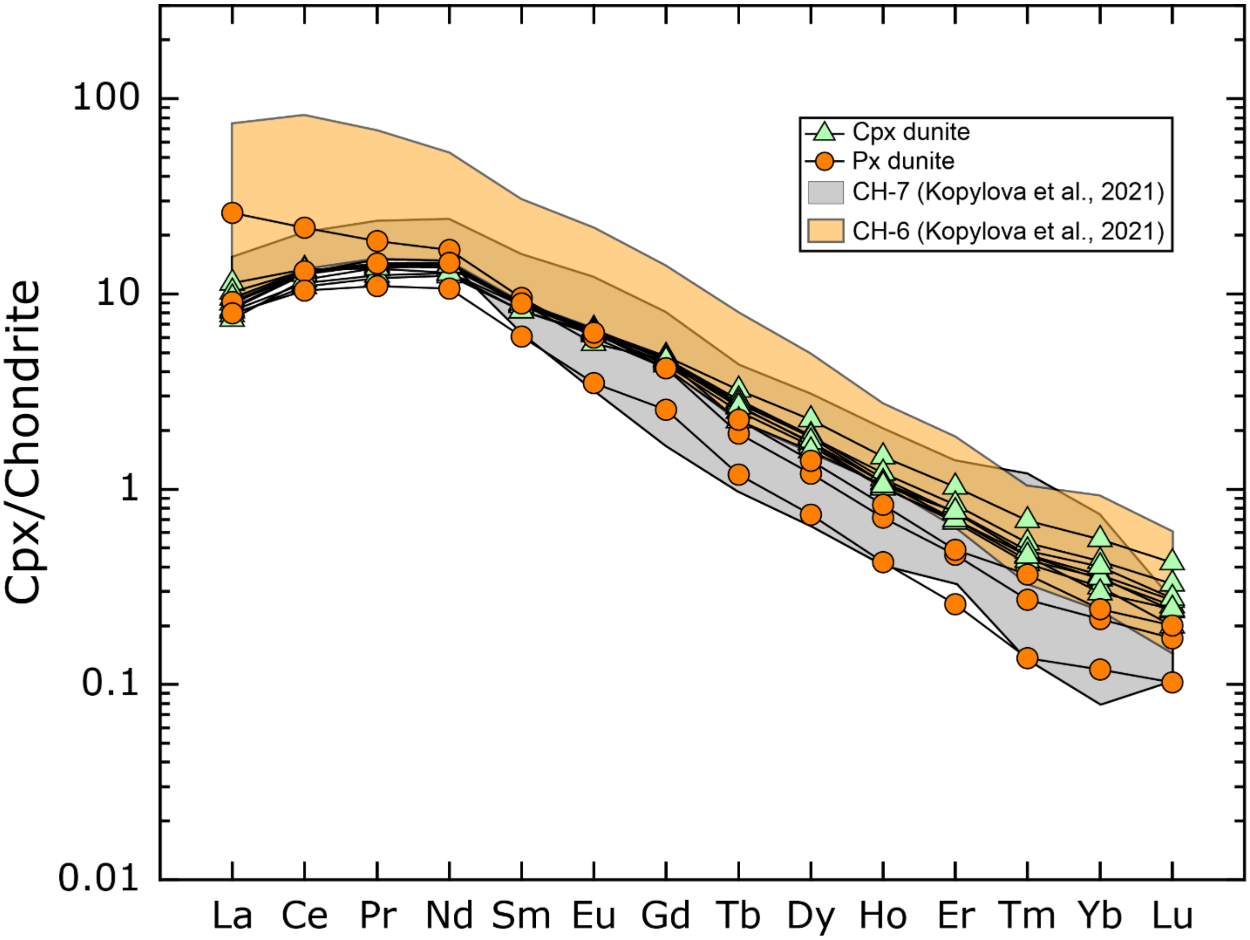

Figure 3.6.4 – Chondrite-normalized REE of clinopyroxenes from clinopyroxene dunites and pyroxene dunites in this study compared with clinopyroxene from melt-free Chidliak peridotites from CH-6 and -7 (Kopylova et al., 2021).

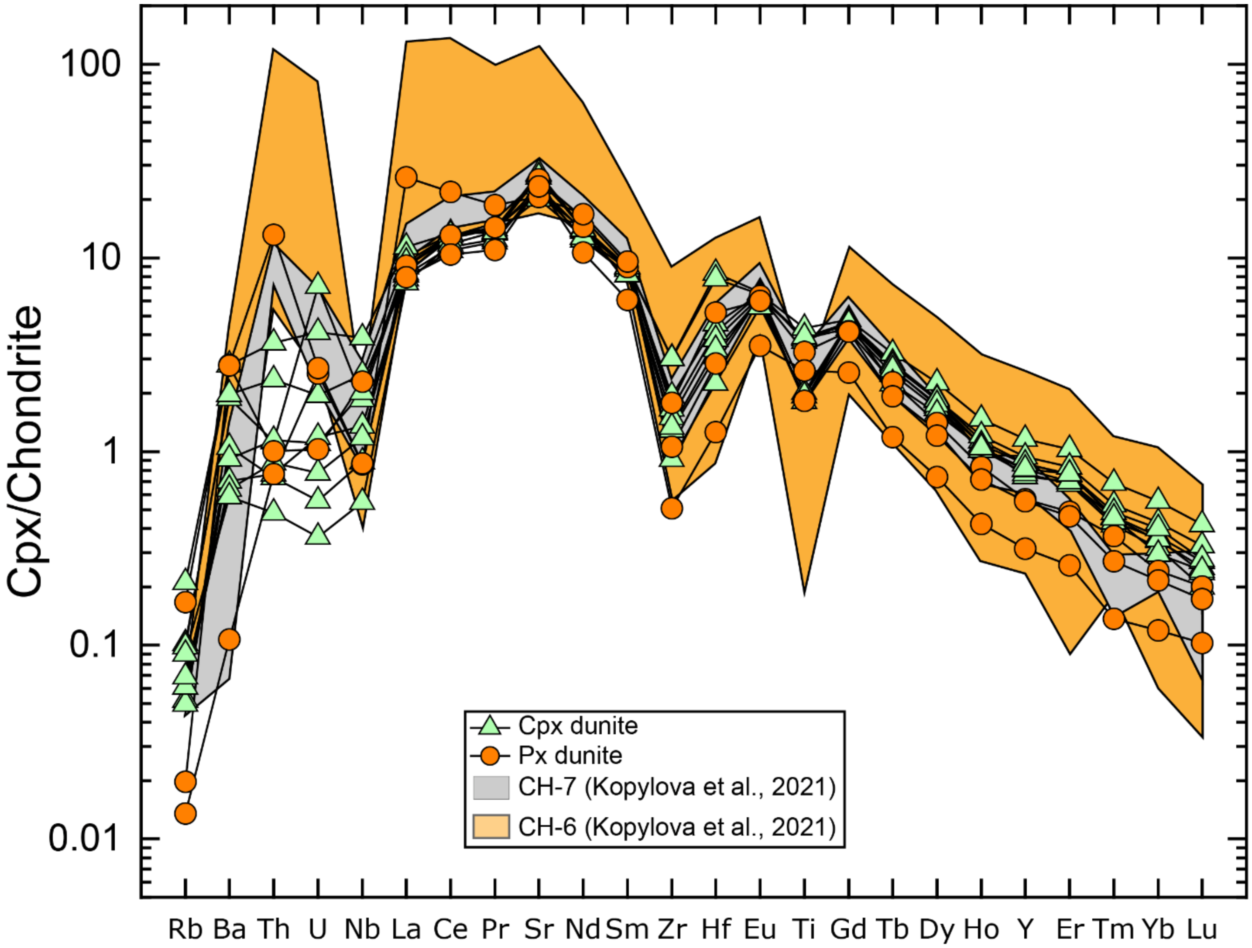

Figure 3.6.5 – Chondrite-normalized multi-element plot of clinopyroxenes from clinopyroxene dunites and pyroxene dunites in this study compared with clinopyroxene from melt-free Chidliak peridotites from (Kopylova et al., 2021).

3.6.3 Olivine

Trace-elements in olivine were analyzed in 11 different xenoliths primarily to obtain their Al concentration to allow use of the aluminum-in-olivine thermometer of Bussweiler et al. (2017). Many of the trace elements analyzed are below the analytical detection limit of the instrument, particularly incompatible trace elements. Out of 68 measurements, 67.2% (*n* = 1142) of incompatible trace elements are above the LOD, and 48.9% (*n* = 831) are above the LOQ. Figure 3.6.6 shows the Al versus V (ppm) relationship of olivine in the 11 peridotites.

The 11 xenoliths in which olivine trace elements were analyzed, equilibrated over a limited pressure and temperature range between 53.3 and 68.5 kbar and 1076 and 1231 °C, respectively. Bearing in mind the small sample set and range in calculated P-T conditions, Al, Ca, Ti, V, Cr, and Cu are often higher with increasing P-T, and Zr is lower. Additionally, Zn and Mn are usually lower with decreasing temperature.

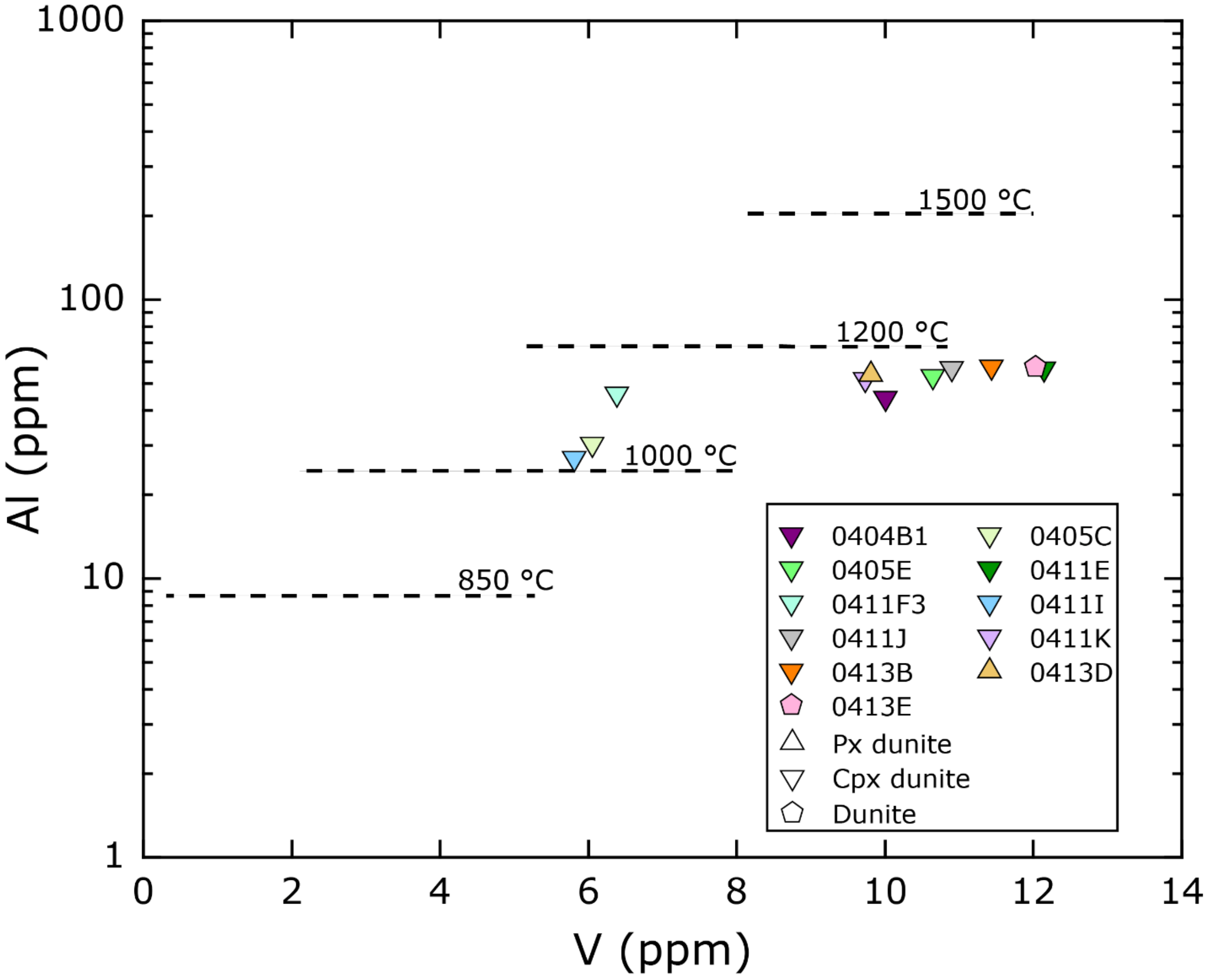

Figure 3.6.6 – Al versus V concentration of olivines from 11 clinopyroxene dunites and pyroxene dunites in this study. Temperature contours are from Bussweiler et al. (2017), which were calculated by projecting Al-in-olivine temperatures onto a cratonic geotherm of 38 mW/m^2.

3.7 Trace element geochemistry of melt pockets and kimberlites

3.7.1 Melt pockets and kimberlite whole rock

Trace elements in melt pockets from 12 xenoliths and CH-7 kimberlite groundmass in one thin section were analyzed by in-situ LA-ICP-MS. All melt intrusion LA-ICP-MS analyses were normalized using the same ^{29}Si internal standard determined from the EPMA grid in xenolith 0413D. This may result in quantitative errors in the trace element concentrations from this method. Out of ninety-three analyses, Th, Yb, Lu and Hf are the only elements with measurements below the LOQ, in *n* = 3, *n* = 15, *n* = 22, and *n* = 4 measurements, respectively. Chondrite-normalized REE have $LREE_N$ enriched patterns with La_N between ~ 20 and 1000x chondrite, with negative slopes to the HREE with Lu_N between 0.2 and 4x chondrite (Figure 3.7.1). CH-7 kimberlite groundmass plots within the concentrations of the melt pockets and has a similar REE_N pattern.

Chondrite-normalized multi-element diagrams of the melt pockets typically have positive Sr anomalies (*n* = 9), and positive Zr, Nb, and U anomalies relative to adjacent elements on the plot (Figure 3.7.2). In contrast, Hf, Th and Tb have negative anomalies relative to their adjacent elements. Kimberlite groundmass has a plateau from Ti-Zr-Hf that is not observed in melt pockets, and a humped pattern from Nb-Th-U that was only observed in melt pockets from xenolith 0411J. Titanium, Hf, and Th in CH-7 kimberlite groundmass is higher than the melt pockets in all 12 xenoliths.

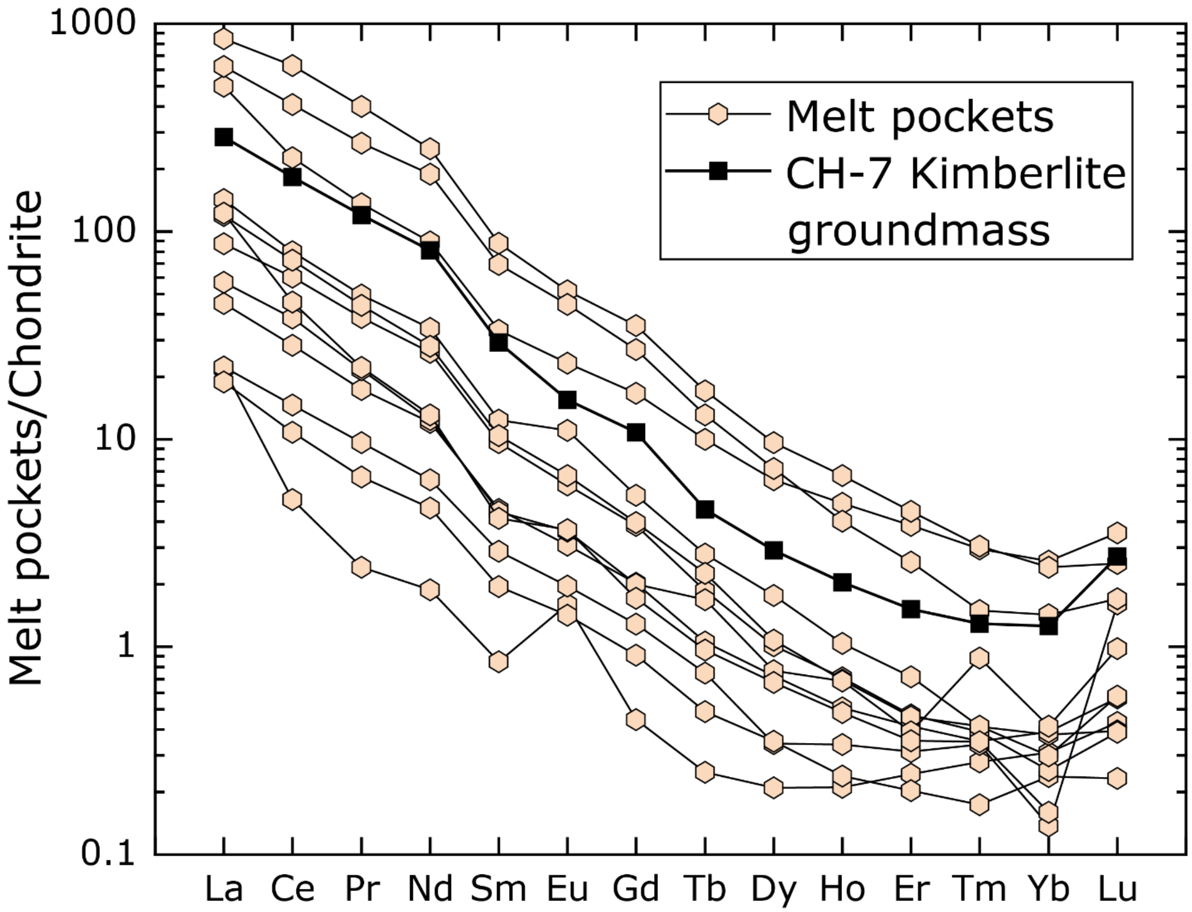

Figure 3.7.1 – Chondrite-normalized REE of melt pockets from twelve xenoliths and CH-7 kimberlite groundmass analyzed in one thin section by in-situ LA-ICP-MS.

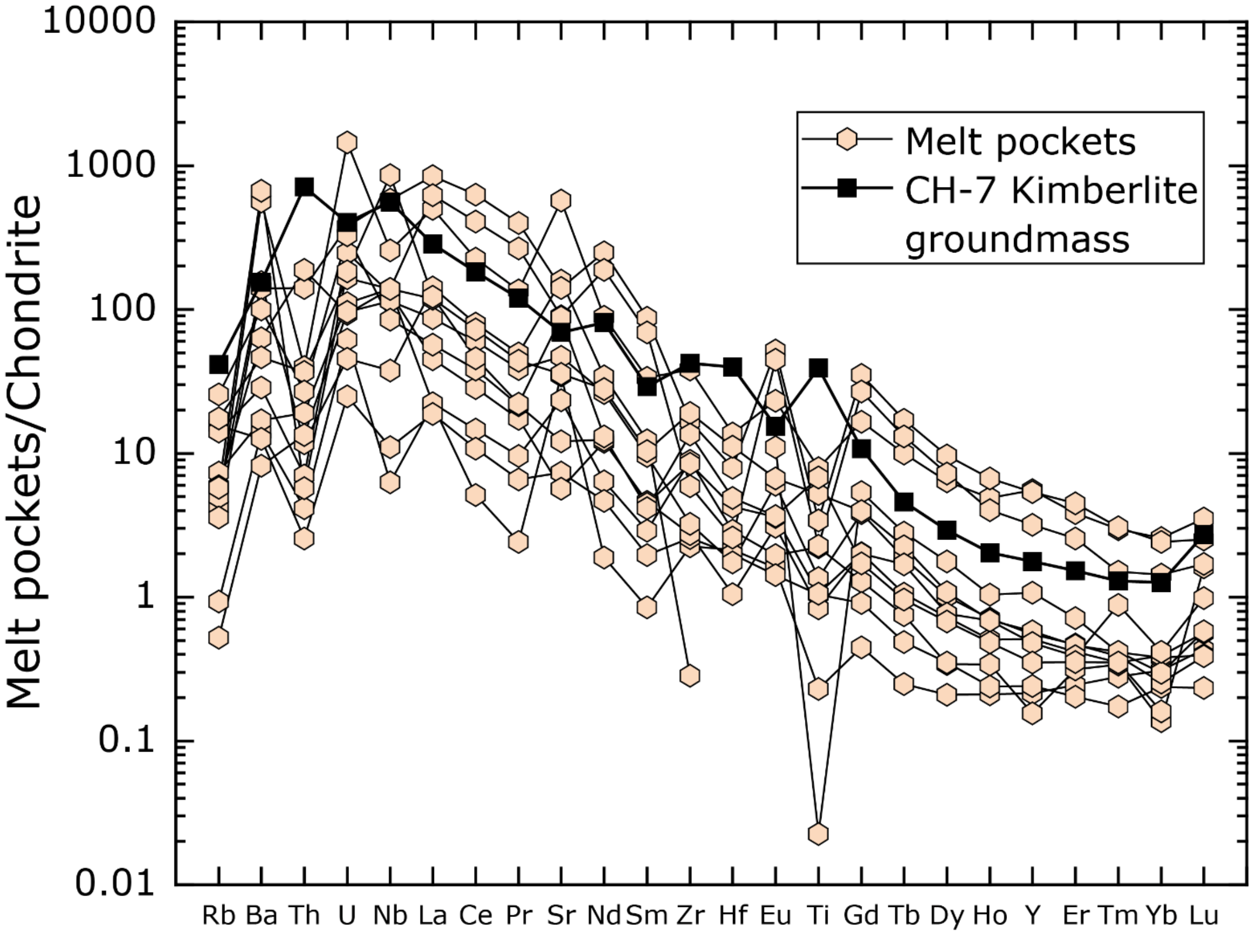

Figure 3.7.2 – Chondrite-normalized multi-element diagram of melt pockets from twelve xenoliths and CH-7 kimberlite groundmass from one thin section determined by in-situ LA-ICP-MS.

The trace elements in melt pockets from four xenoliths were also analyzed by bulk dissolution HR-ICP-MS, using the powders extracted from micromilling. The slopes of REE_N patterns from CH-7 melt pockets determined by bulk dissolution HR-ICP-MS are similar to those determined from in-situ LA-ICP-MS (Figure 3.7.3). The main difference is a flat slope from Eu to Gd in bulk dissolution samples, which is negative in LA-ICP-MS samples. The single CH-6 melt pocket determined by bulk dissolution has significantly lower HREE and a negative slope from Dy to Lu, unlike its respective LA-ICP-MS analysis.

Chondrite-normalized multi-element plots (Figure 3.7.4) show that the melt intrusions determined by in-situ LA-ICP-MS and bulk dissolution HR-ICP-MS generally have similar slopes but differ in concentration. This could be due to an incorrect internal standard (^{29}Si) used for LA-ICP-MS analyses, which was determined from the average Si of the EPMA melt pocket grids. For this reason, the trace elements determined by bulk dissolution HR-ICP-MS are used henceforth when discussing quantitative results for trace elements in melt pockets.

The LA-ICP-MS compositions from melt pockets are used as background data for qualitative comparison only.

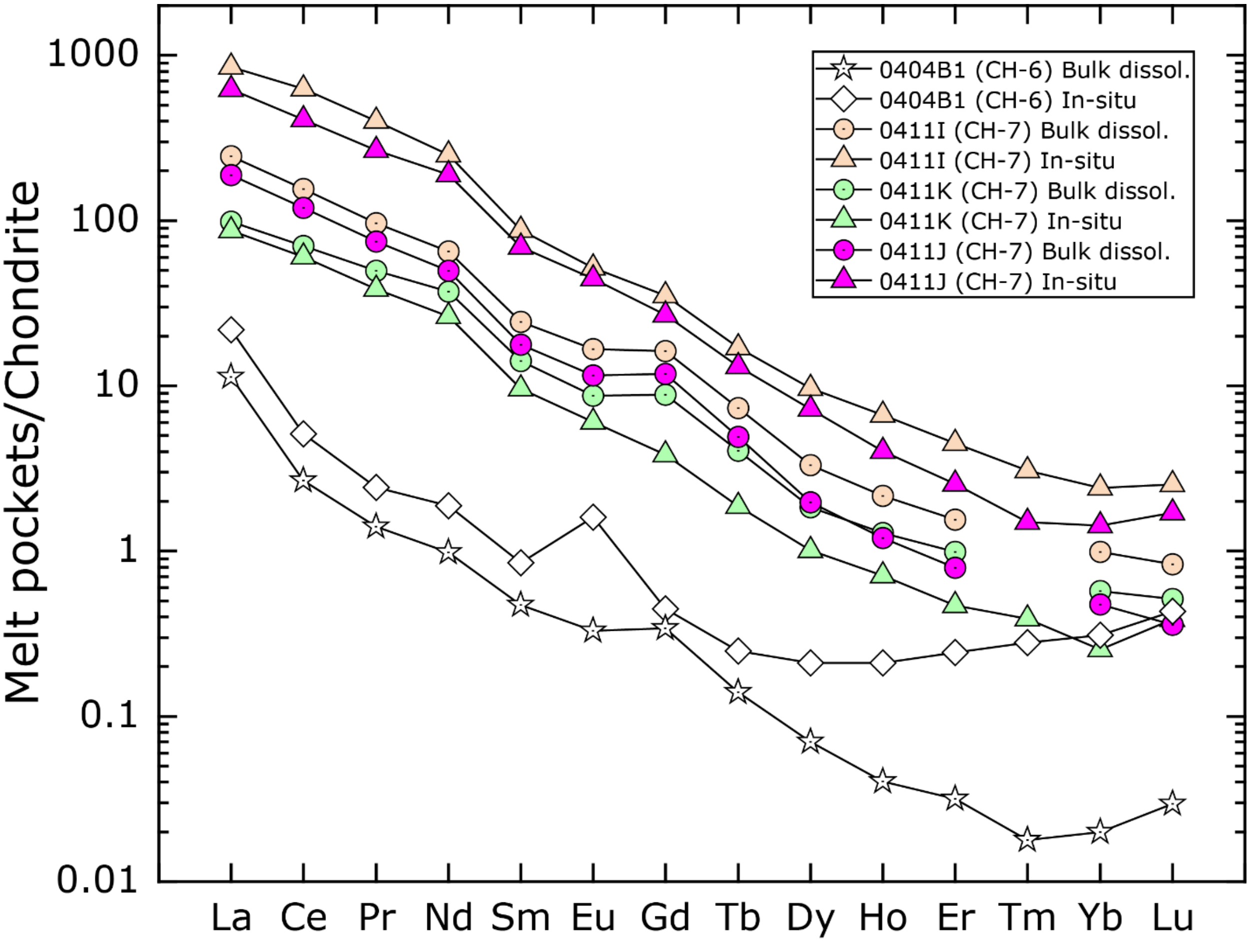

Figure 3.7.3 – Chondrite-normalized REE diagram showing the differences between melt intrusion compositions determined by in-situ LA-ICP-MS (In-situ) and bulk dissolution HR-ICP-MS (Bulk dissol.) of micromilled powders.

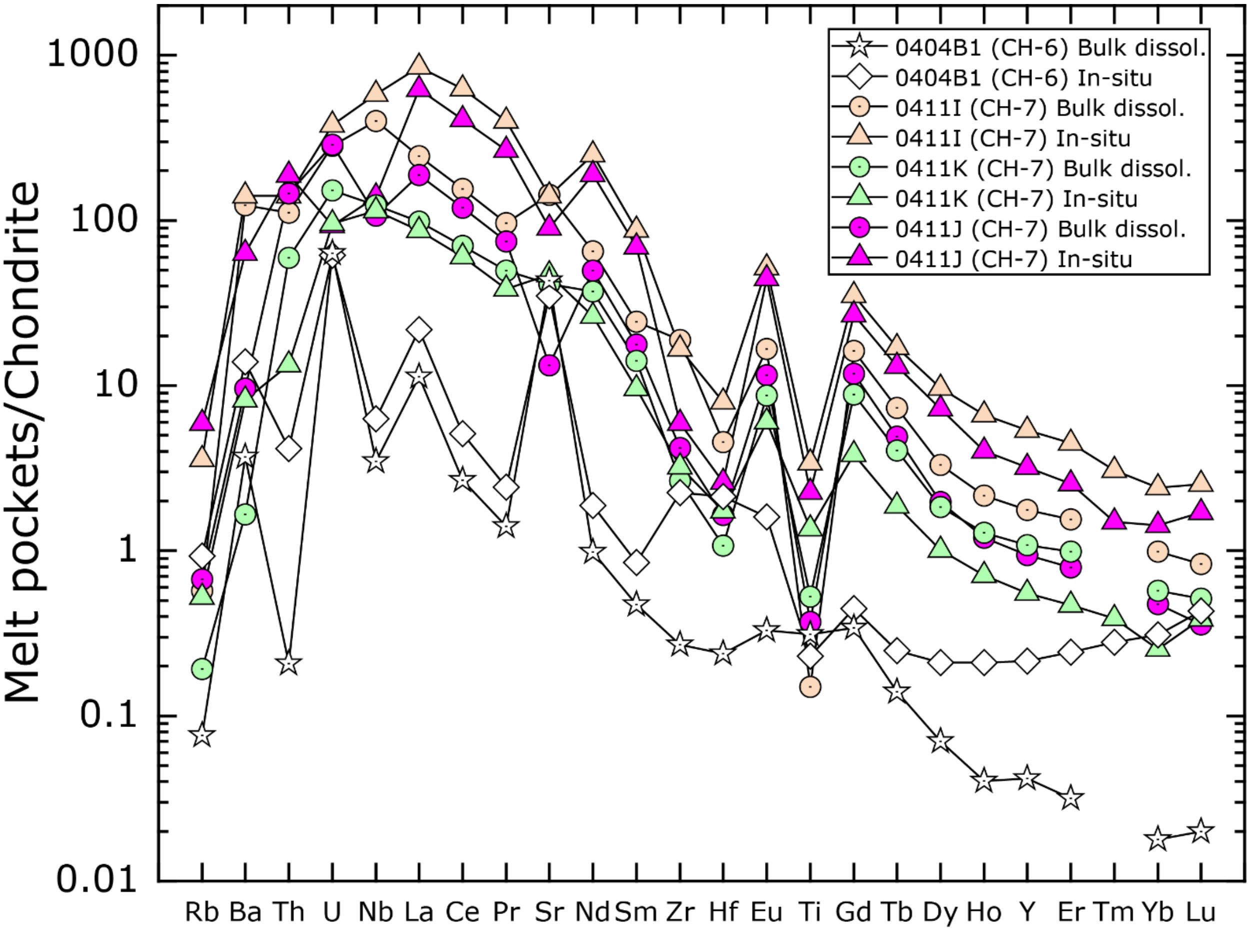

Figure 3.7.4 – Chondrite-normalized multi-element plot of melt intrusions analyzed by in-situ LA-ICP-MS (In-situ) compared with the results from bulk dissolution HR-ICP-MS (Bulk dissol.) of micro-milled powders.

3.7.2 – Kimberlite whole rock trace elements

Some of the same elements were measured by both bulk dissolution HR-ICP-MS and XRF in the kimberlite whole-rock powders, namely Rb, Sr, Y, Nb, Ba, La, Ce, Pb, Th, U, Sc, V, Cr, Ti, Mg, Ca, Mn, Co, Ni, Cu, Zn, Ga, and Zr. The average absolute percent difference between elements for the different analytical methods is < 20%, except for Y, Ce, U, and Zr, which are between 20 and 40%; and Zn and Ga are 87% and 52%, respectively. The trace-element compositions obtained by bulk dissolution HR-ICP-MS are used for plotting and quantitative discussion in this study instead of XRF, because they cover a larger range of trace elements, have lower detection limits, and for consistency with the analysis method used to obtain trace elements in melt pockets.

The kimberlite whole-rock samples have enriched LREE between ~ 300 to 700x chondrite, with negative slopes to the HREE that are ~ 2x chondrite (Figure 3.7.5). Both CH-6 and CH-

7 kimberlite whole-rock samples have similar REE$_N$ slopes, but CH-6 has slightly higher LREE$_N$ and MREE$_N$ than CH-7.

Chondrite-normalized multi-element patterns (Figure 3.7.6) of the three CH-7 kimberlite whole-rocks are very similar in concentration and slope. The CH-6 kimberlite whole-rock sample generally has a higher concentration of chondrite-normalized trace elements than CH-7 whole-rocks and has a distinct positive Sr/Nd slope that is not present in CH-7 samples.

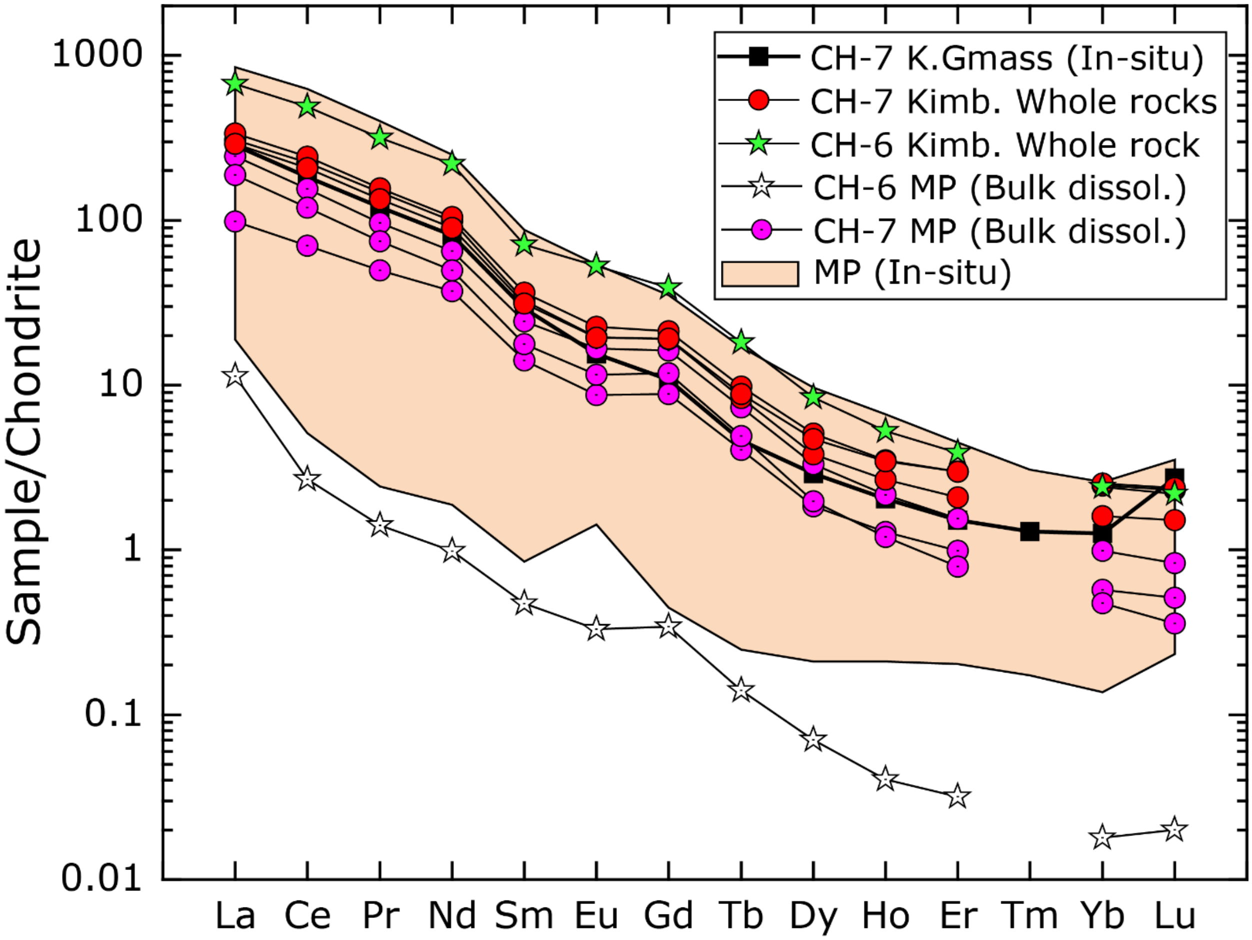

Figure 3.7.5 – Chondrite normalized REE of CH-7 and CH-6 kimberlite whole-rocks determined by bulk dissolution HR-ICP-MS, compared to bulk dissolution HR-ICP-MS analysis of melt pockets, in-situ LA-ICP-MS analysis of CH-7 kimberlite groundmass, and the range of compositions of averaged melt pocket (MP) in-situ LA-ICP-MS analyses from 12 xenoliths.

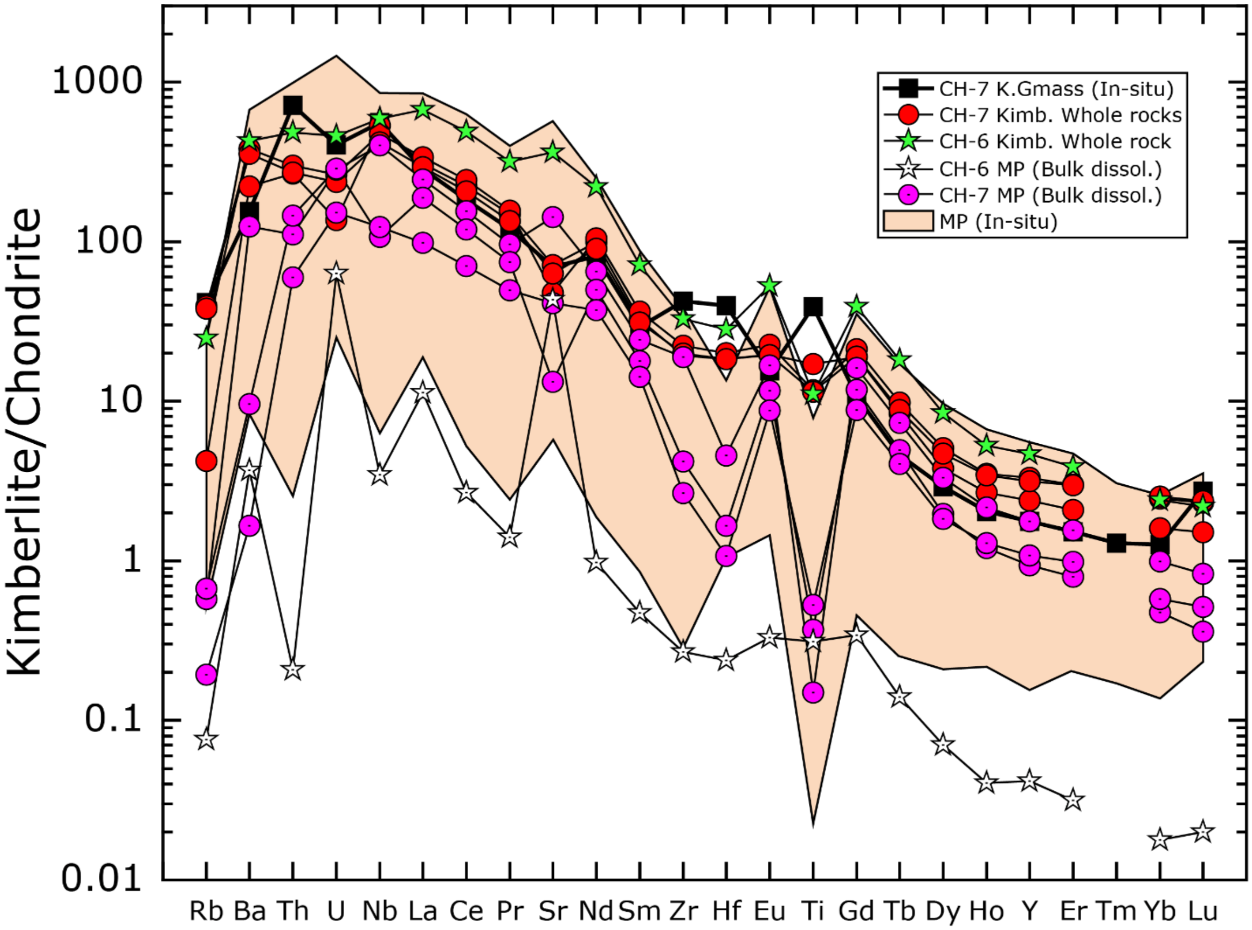

Figure 3.7.6 – K.Gmass = kimberlite groundmass. Chondrite normalized multi-element plot of kimberlite whole rocks determined from bulk dissolution HR-ICP-MS (Bulk dissol.), compared to bulk dissolution HR-ICP-MS analysis of melt pockets, in-situ LA-ICP-MS (In-situ) analysis of CH-7 kimberlite groundmass, and the range of compositions of averaged melt pocket (MP) in-situ LA-ICP-MS analyses from 12 xenoliths.

3.8 Isotope geochemistry of kimberlites

Isotopic compositions of the kimberlite whole-rocks reported in this section are available in the University of Alberta UAL Dataverse under "Brody Myers MSc thesis Supplementary Online Dataset" (https://doi.org/10.7939/DVN/VWFTSN).

3.8.1 Kimberlite whole rock Sm-Nd

Neodymium isotopes measured on the four kimberlite whole-rocks were corrected for radiogenic ingrowth of ^{143}Nd using the perovskite U-Pb recommended emplacement ages of CH-6 (149.9 ± 1.0 Ma) and CH-7 (143.0 ± 0.9 Ma) from Heaman et al. (2015). The ^{143}Nd/^{144}Nd$_i$ for the single CH-6 whole-rock is 0.512661 ± 0.000006 (2SE) with εNd 4.21 ± 0.11 (2SE). Initial ^{143}Nd/^{144}Nd ratios for the three CH-7 whole rocks range from 0.512504 ±

0.000010 (2SE) to 0.512578 ± 0.000009 (2SE) with εNd values ranging from 0.97 ± 0.20 (2SE) to 2.43 ± 0.17 (2SE) (average εNd = 1.63). A plot of εNd_T versus $(^{87}Sr/^{86}Sr)_i$ of the kimberlite whole-rocks compared with perovskite data from 35 Chidliak kimberlites from Heaman et al. (2015) is shown in Figure 3.8.1.

3.8.2 Kimberlite whole rock Rb-Sr

Strontium isotopes measured on the four kimberlite whole rocks were corrected for radiogenic ingrowth of ^{87}Sr using the perovskite U-Pb recommended emplacement ages of CH-6 (149.9 Ma) and CH-7 (143.0 Ma) from Heaman et al. (2015). Initial $^{87}Sr/^{86}Sr$ of the CH-6 whole-rock is 0.703603 ± 0.000016 (2SE). The initial $^{87}Sr/^{86}Sr$ ratios from CH-7 whole-rocks range from 0.705792 ± 0.000017 (2SE) to 0.706384 ± 0.000022 (2SE). A plot of εNd_T versus $(^{87}Sr/^{86}Sr)_I$ of whole rocks from this study compared with perovskite data from 35 Chidliak kimberlites from Heaman et al. (2015) is shown in Figure 3.8.1.

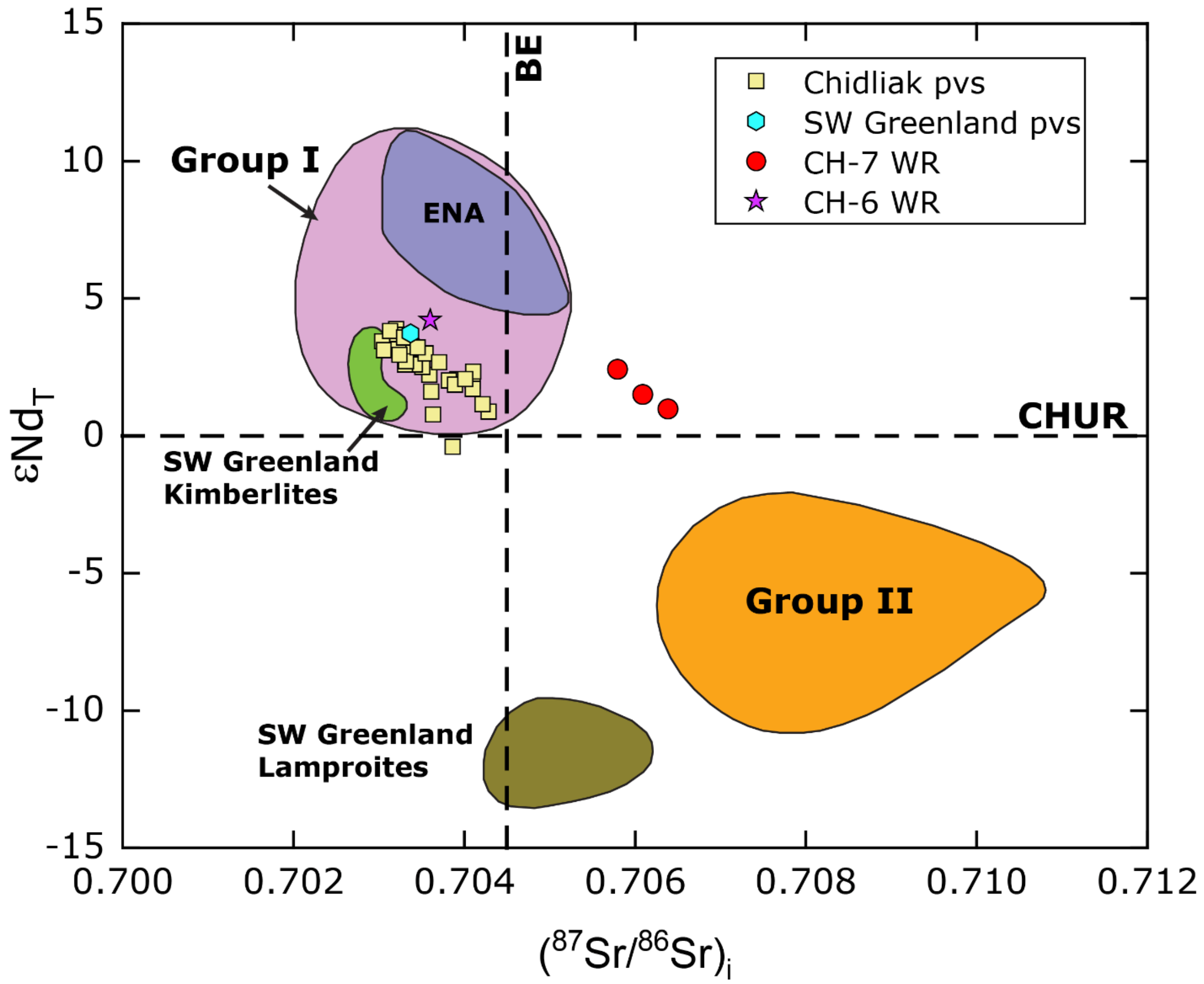

Figure 3.8.1 – εNd$_T$ versus (^{87}Sr/^{86}Sr)$_i$ plot of CH-6 and CH-7 whole rocks from this study compared with Chidliak and SW Greenland Midternaes perovskite data from Heaman et al. (2015). The fields of Mesozoic southern Africa Group I and II kimberlitic perovskite, Jurassic eastern North American kimberlites (ENA), and SW Greenland Jurassic/Neoproterozoic kimberlites and Mesoproterozoic lamproites are from Heaman et al. (2015) and references therein. CHUR = Chondritic uniform reservoir, BE = Bulk Earth reservoir.

Chapter 4 : Discussion

4.1 Melt intrusion petrology

The discussion in this section focuses on the petrology of the melt intrusions in the xenoliths. First, the mineral compositions of the melt intrusion phases, as well as the bulk major-, minor-, and trace-element compositions of the melt pockets are compared to other mantle-derived melts to examine the possible origin of the melts. Later, the possible process of melt entrapment and the timing of the intrusions are discussed.

The mineralogy of the melt intrusions in Chidliak xenoliths are characterised by the presence of spinel group minerals, apatite, perovskite, serpentine, brucite, mica, carbonates, monticellite, and ilmenite. This mineral assemblage is consistent with the groundmass assemblage of Group I (Skinner, 1986) or archetypal (Mitchell, 1986) kimberlites, and hence Chidliak kimberlites.

4.1.1 Spinel

In kimberlites, lamprophyres, and carbonatites, spinel compositions generally evolve from early crystallizing Cr-rich spinel to Cr-poor magnesio-ulvöspinel-magnetite (MUM) compositions (Mitchell, 1986; Roeder and Schulze, 2008). Compositional zoning trends in CH-6 and CH-7 kimberlite groundmass and melt intrusion spinels broadly fit this trend (Figure 3.4.1). However, there is a relatively low abundance of Cr-rich spinels that have compositions that overlap the origin of the Trend 1 and 2 lines, and many more with much more evolved, Fe^{3+}-rich compositions. Some of these very oxidized spinels (magnesioferrite and magnetite) are likely a product of serpentinization (e.g., Afanasyev et al., 2014) and are not primary. Zoned spinel grains in melt pockets and Chidliak kimberlite groundmass generally document a core to rim trend of decreasing Cr# (Cr/[Cr+Al]) and increasing Fe(III)# ($Fe^{3+}/[Fe^{3+}+Al+Cr]$) and Ti# (Ti/[Ti+Al+Cr]), at relatively constant Fe# ($Fe^{2+}/[Fe^{2+}+Mg]$) (Figure 4.1.1). Therefore the rim compositions, as well as later forming discrete spinel phases, evolve upwards along the spinel compositional "Trend 1" after Mitchell (1986), which is the dominant trend of kimberlitic spinel compositions (Mitchell, 1986; Roeder and Schulze, 2008).

The spinels in melt intrusions can further be identified as having crystallized from kimberlite by their TiO_2 and MgO compositions. The spinel compositional evolution in kimberlites is from early crystallizing Cr-rich phases towards magnesian-ulvöspinel, which results in both Ti and Mg-enrichment that is unique among all other magmatic source rocks (Creighton and Stachel, 2008). Other magmatic spinel sources such as carbonatites, lamprophyres, lamproites, minettes, etc. lack concurrent Ti and Mg-enrichment in spinel crystallization trends, thus plotting in the mafic and ultramafic fields defined by Creighton and Stachel (2008). In contrast, some of the evolved spinels from the xenolith melt intrusions, as well as CH-6 and CH-7 kimberlite groundmass, plot in the kimberlite field after Creighton and Stachel (2008) (Figure 3.4.2). This suggests that the melt intrusions could be sourced from kimberlite.

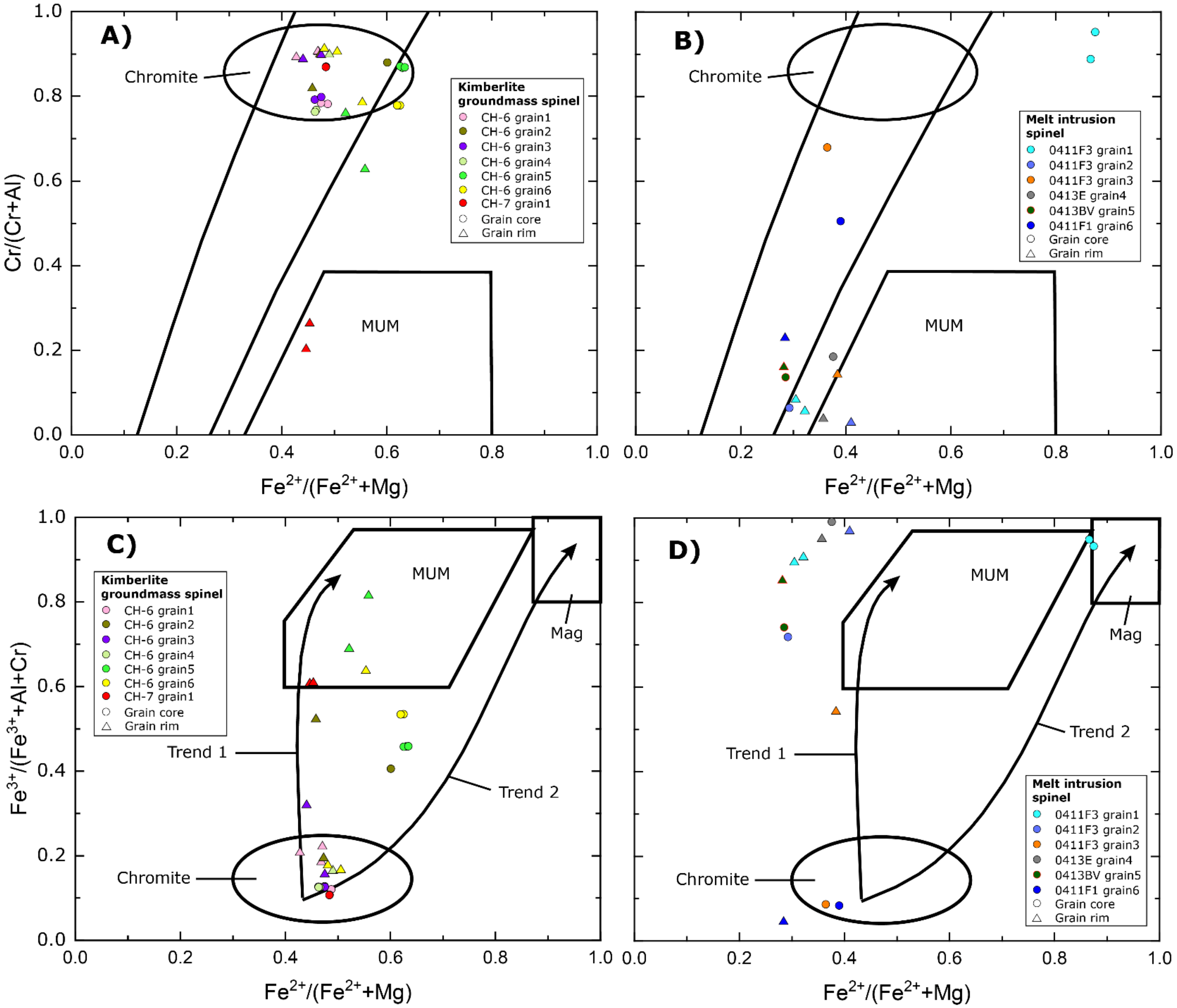
A)
B)
C)
D)
Chromite
MUM
Mag
Trend 1
Trend 2
Cr/(Cr+Al)
Fe^{3+}/(Fe^{3+}+Al+Cr)
Fe^{2+}/(Fe^{2+}+Mg)
0.0
0.2
0.4
0.6
0.8
1.0
Kimberlite groundmass spinel
CH-6 grain1
CH-6 grain2
CH-6 grain3
CH-6 grain4
CH-6 grain5
CH-6 grain6
CH-7 grain1
Grain core
Grain rim
Melt intrusion spinel
0411F3 grain1
0411F3 grain2
0411F3 grain3
0413E grain4
0413BV grain5
0411F1 grain6
Grain core
Grain rim

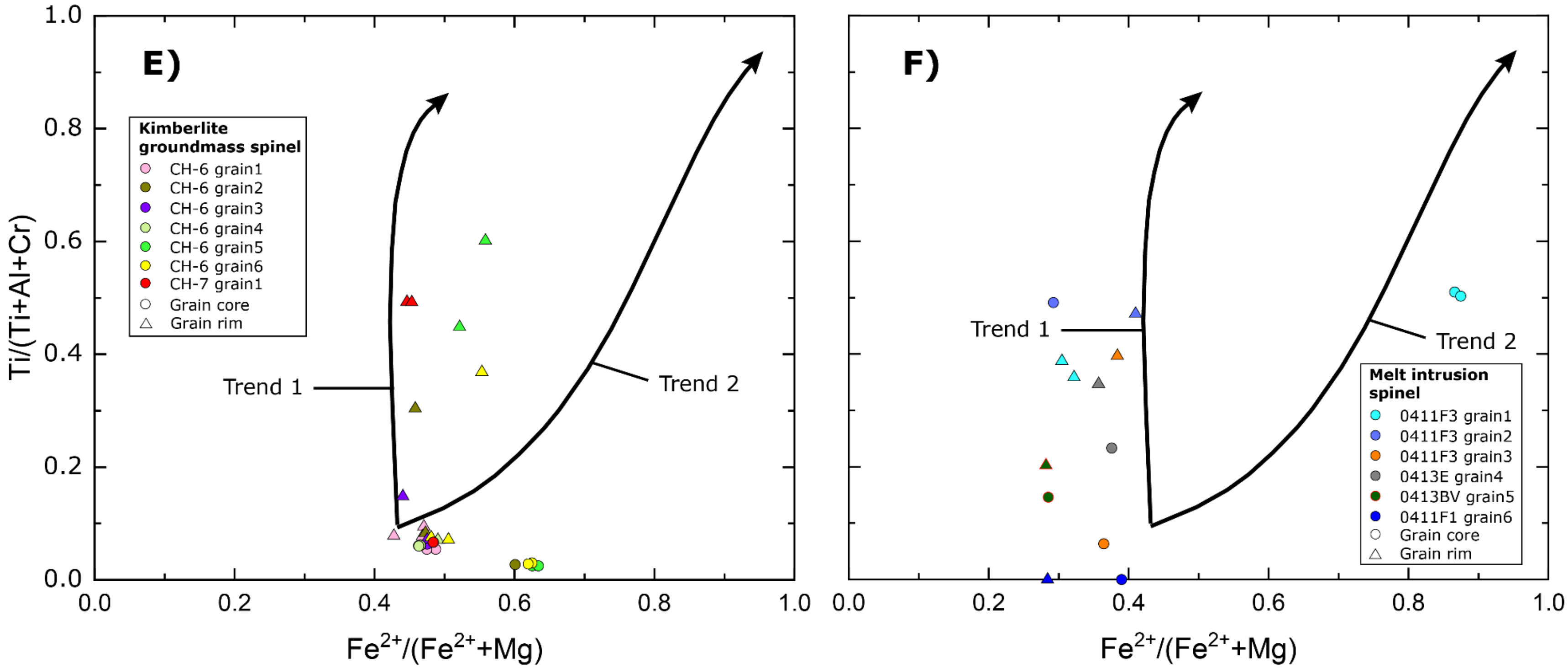

Figure 4.1.1 – (A, B) Plots of Cr/(Cr+Al) vs. $Fe^{2+}/(Fe^{2+}+Mg)$; (C, D) $Fe^{3+}/(Fe^{3+}+Al+Cr)$ vs. $Fe^{2+}/(Fe^{2+}+Mg)$; and (E, F) Ti/(Ti+Al+Cr) vs. $Fe^{2+}/(Fe^{2+}+Mg)$ for compositionally zoned spinels. Plots on the left are spinels in CH-6 and CH-7 groundmass, and plots on the right are spinels in melt intrusions in xenoliths 0411F3, 0413E, 0413BV, and 0411F1. Fields labelled Chromite, MUM (magnesio-ulvöspinel-magnetite), and Mag (magnetite) are after Roeder and Schulze (2008). Spinel evolution Trend 1 and 2 lines are after Mitchell (1986).

4.1.2 Ilmenite

Ilmenite grains in CH-6 and -7 melt intrusions and CH-7 kimberlite groundmass, CH-6 and -7 coarse ilmenites in xenoliths, garnet inclusions in CH-7 xenoliths, rims on phlogopite, and rims on rutile in melt-free garnet olivine websterite 0405D1, have MgO and TiO_2 compositions that plot in the kimberlitic field of Wyatt et al. (2004) (Figure 4.1.2). This suggests they were derived from kimberlite magma- or ilmenite associated with kimberlite (e.g. megacrysts, disaggregated metasomatized peridotites, etc.). This contrasts with the fine-grained ilmenites in the CH-6 kimberlite groundmass, which plot well into the "non-kimberlitic" field, suggesting they are xenocrysts from a source rock unrelated to kimberlite (possibly crustal-derived). The ilmenite rims on rutile in eclogite 0405H, and one in olivine websterite 0405D1, plot within the non-kimberlitic field. This could possibly be due to equilibration with rutile, resulting in elevated TiO_2.

The compositions of ilmenite on phlogopite rims, and the rare, fine-grained ilmenites in CH-7 melt intrusions, overlap with the compositions of CH-7 kimberlite groundmass ilmenite (Figure 4.1.2, Figure 4.1.3, and Figure 4.1.4). This implies the fine-grained melt intrusion ilmenites crystallized from a melt with similar composition to the CH-7 kimberlite, or the same one. In contrast, the coarse ilmenites in xenoliths in contact with CH-6 and -7 melt intrusions, CH-7 ilmenite inclusions in garnet, CH-7 rims on rutile, and the single fine-grained ilmenite found in a CH-6 melt intrusion, have compositions that are different from the compositions of ilmenites on phlogopite rims, fine-grained ilmenites in CH-7 melt intrusions, and CH-7 kimberlite groundmass (Figure 4.1.2, Figure 4.1.3, and Figure 4.1.4). This suggests they crystallized from a melt with a different composition than the melt that crystallized as the melt intrusions or the CH-7 kimberlite groundmass. The compositions of coarse ilmenites in contact with the melt intrusions are more similar to Monastery megacrysts (Moore et al., 1992), and proto-kimberlite ilmenite veins in peridotite xenoliths from the Bultfontein and De Beers mines (South Africa) (Wyatt and Lawless, 1984) (Figure 4.1.2, Figure 4.1.3, and Figure 4.1.4). The single CH-6 "melt intrusion" ilmenite analysis is very similar in composition to the coarse CH-6 ilmenites, and therefore could be a small fragment from a coarse ilmenite, given its proximity.

The overall high Cr_2O_3 (between ~ 0.5 and 6 wt%) and MgO (between ~ 8 and 20 wt%), and low MnO (typically < 0.50 wt%) composition of most of the different ilmenite associations in this study are different than ilmenite in typical carbonatites, which have low MgO (< 5 wt%) and Cr_2O_3 (< 0.1 wt%), and high MnO (0.5 – 20.0 wt%) (Mitchell, 1986). The ilmenite on phlogopite rims and in melt veins in the eclogite, are compositionally distinct from the other ilmenites in this study because they have low Cr_2O_3, equal to 0.17 and 0.14 wt%, respectively. Their high MgO contents (20.04 and 9.71 wt%, respectively), suggests they did not crystallize from a carbonatitic melt. Instead, perhaps intruding kimberlite melt reacted with the low-Cr phlogopite and rutile to produce the low-Cr ilmenite.

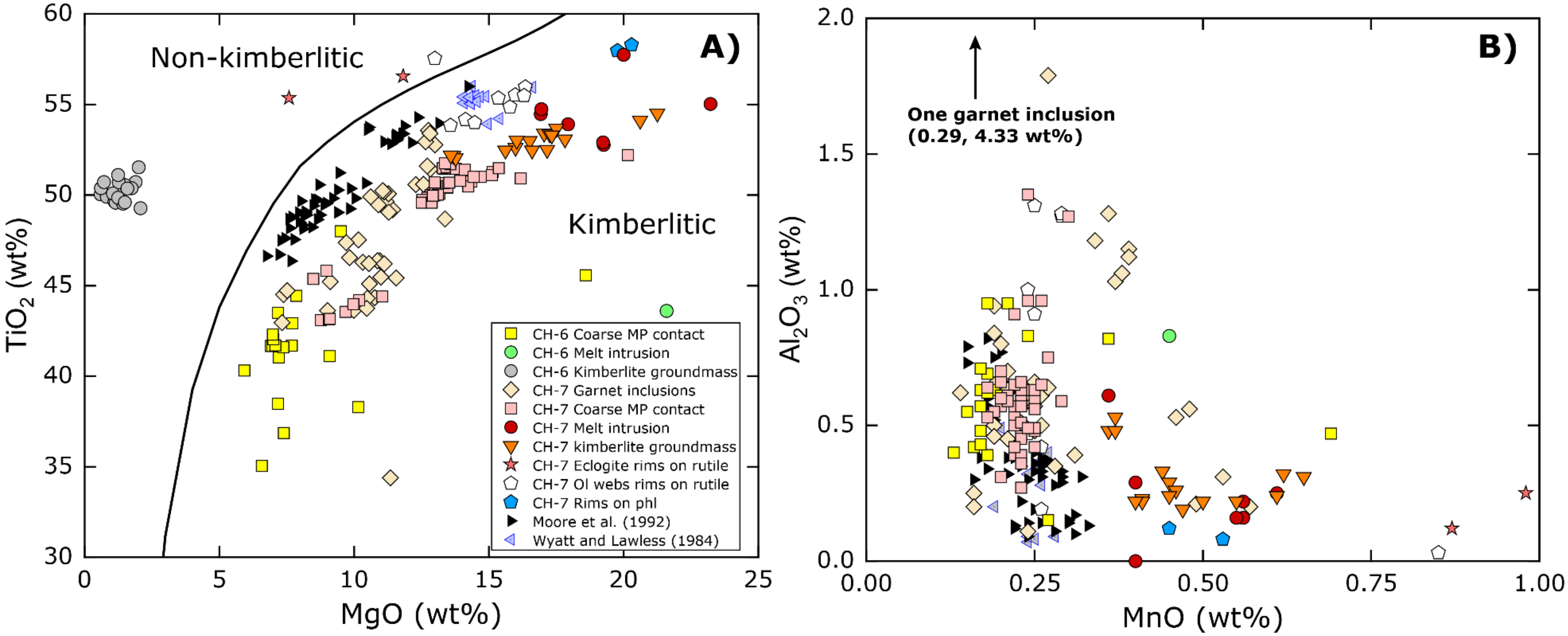

Figure 4.1.2 – Bivariate plots of A) MgO vs. TiO_2 (wt%) and B) MnO vs. Al_2O_3 (wt%) for ilmenites from this study with supplementary ilmenite megacryst data from the Monastery Mine, South Africa (Moore et al., 1992), and compositions of ilmenite veins in peridotite xenoliths from the Bultfontein and De Beers mine, South Africa (Wyatt and Lawless, 1984). The black line in A) separates non-kimberlitic from kimberlitic-derived ilmenites (Wyatt et al., 2004).

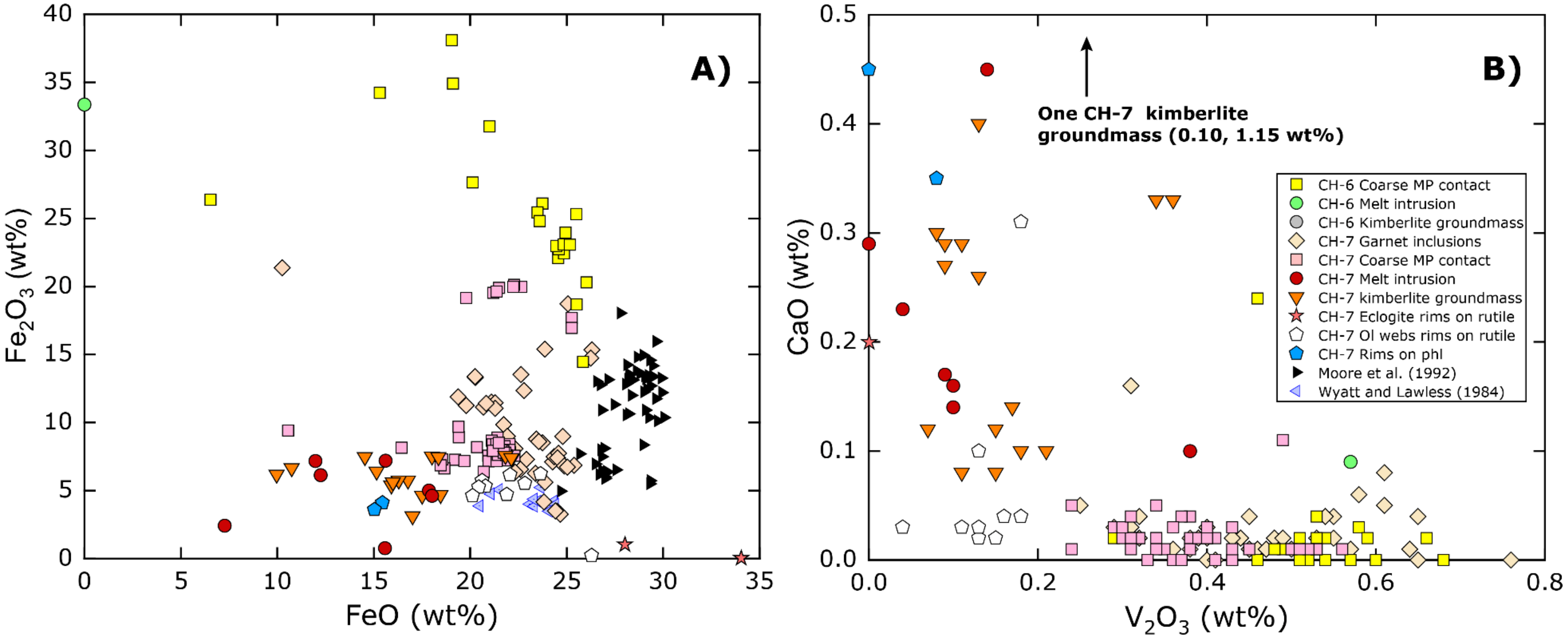

Figure 4.1.3 – Bivariate plots of A) FeO vs. Fe_2O_3 (calculated) (wt%) and B) V_2O_3 vs. CaO (wt%) of ilmenites from this study with supplementary ilmenite megacryst data from the Monastery Mine, South Africa (Moore et al., 1992), and compositions of ilmenite veins in peridotite xenoliths from the Bultfontein and De Beers mine, South Africa (Wyatt and Lawless, 1984) (CaO and/or V_2O_3 compositions not published).

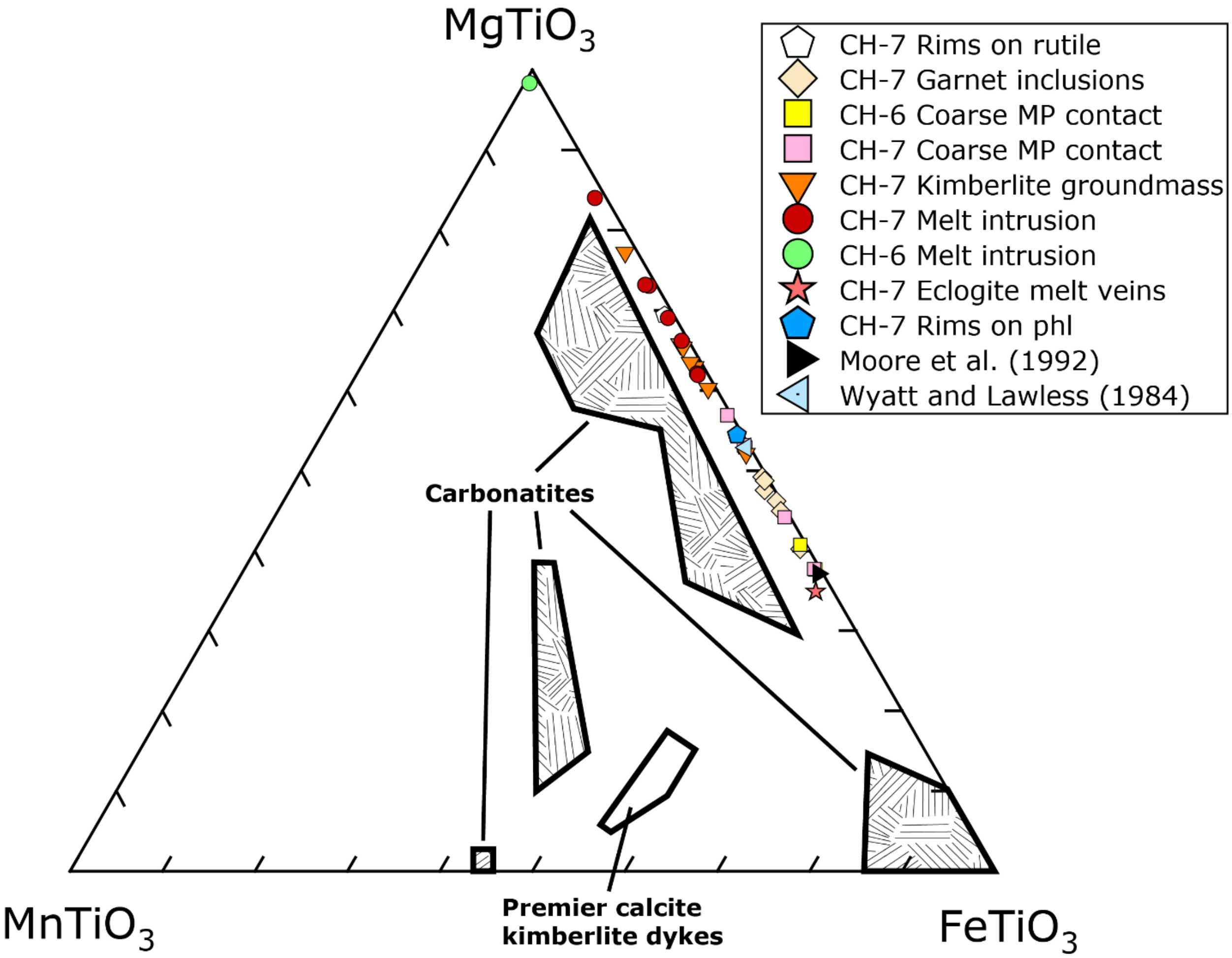

Figure 4.1.4 – Averaged ilmenite compositions from this study compared with averaged ilmenite megacryst data from the Monastery Mine, South Africa (Moore et al., 1992), and ilmenite veins in peridotite xenoliths from the Bultfontein and De Beers mine, South Africa (Wyatt and Lawless, 1984) in the system $MgTiO_3$ – $FeTiO_3$ – $MnTiO_3$. Fields of ilmenite from carbonatites and Premier calcite kimberlite dykes are from Mitchell (1986) and references therein.

4.1.3 Perovskite

Both melt intrusion and Chidliak kimberlite perovskites have relatively pure perovskite compositions ($CaTiO_3$), with minor substitutions of REE for Ca and Ti in the crystal structure. This is consistent with compositions of kimberlitic perovskite from other localities (Chakhmouradian and Mitchell, 2000; Mitchell, 1986), in contrast to carbonatitic perovskite that has extensive solid solution towards leushite and loparite endmembers (Mitchell, 1986). Additionally, resorption textures are common in kimberlitic perovskite (e.g., Chakhmouradian and Mitchell, 2000; Mitchell and Chakhmouradian, 1998), such as the skeletal and spongy textures observed in most melt pocket perovskites in this study. These resorption textures form during the final stages of kimberlite evolution due to perovskite's instability with a CO_2-bearing, weakly acidic fluid with high SiO_2 activity (Chakhmouradian and Mitchell, 2000; Mitchell and Chakhmouradian, 1998).

4.1.4 Apatite

Apatite in kimberlites are relatively pure solid-solutions between fluoroapatite and hydroxlyapatite (Mitchell, 1986). The compositions of apatites in kimberlites worldwide match well with the compositions of apatites in the melt intrusions, however, there is also compositional overlap with apatites from carbonatites, orangeites/lamproites, and aillikites (Figure 4.1.5).

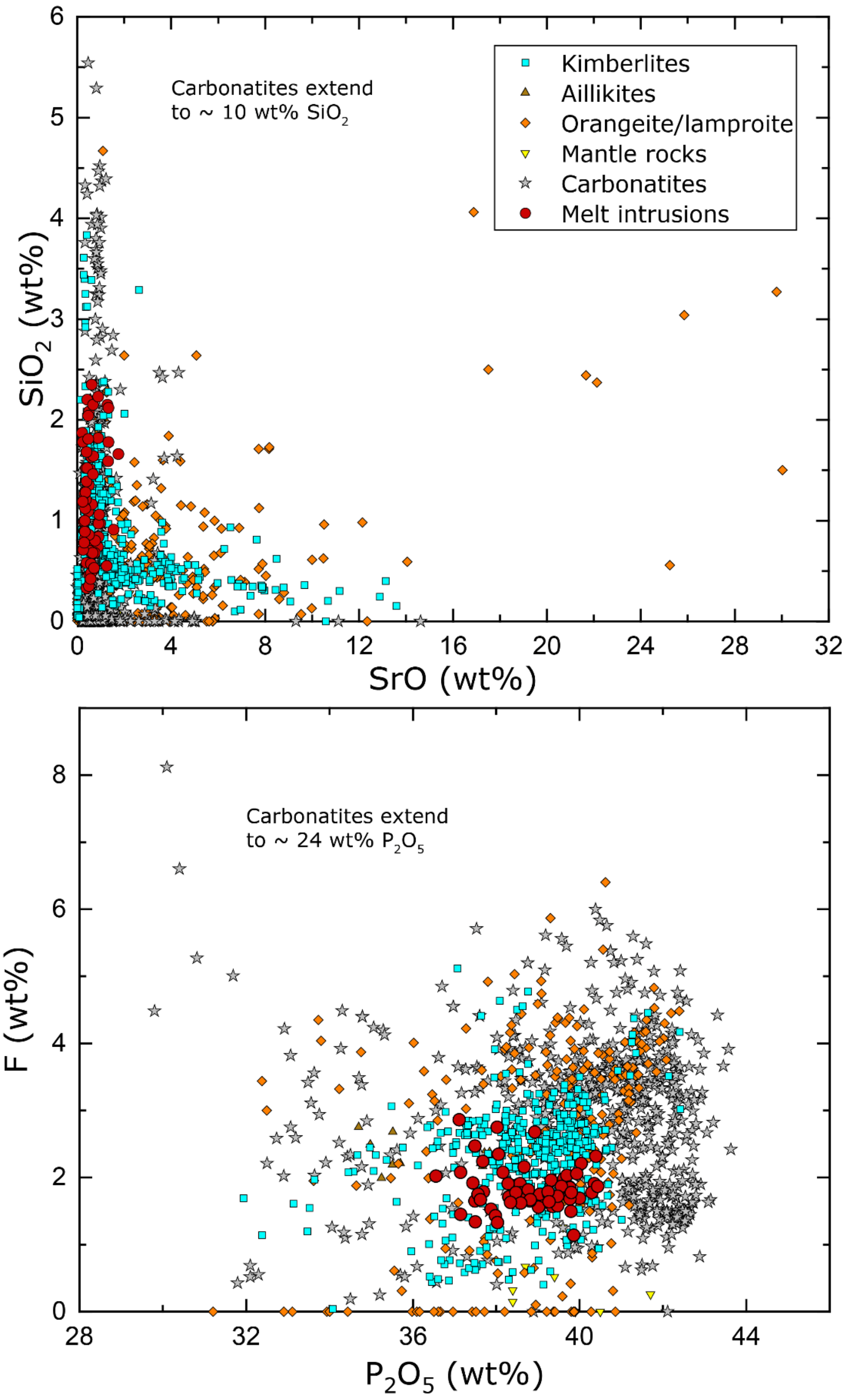

Figure 4.1.5 – SiO_2 vs. SrO and F vs. P_2O_5 (wt%) plots of apatite from xenolith melt intrusions (this study) compared with compiled apatite data from worldwide kimberlites, apatite in aillikites, carbonatites, orangeites/lamproites, and mantle rocks (Soltys et al., 2020 and references therein).

4.1.5 Monticellite

Monticellite compositions from melt veins and melt pocket margins are compositionally indistinguishable from those on clinopyroxene and olivine rims in the xenoliths (Figure 4.1.6). The FeO and MgO compositions are similar to those reported by Kopylova et al. (2019), although the range in FeO from monticellite in this study extends lower (0.8 to 5.7 wt%, compared to 3.7 to 5.5 wt%), and the MgO range extends higher (22 to 28 wt%, compared to 22 to 24 wt%). The compositions of monticellites from this study have some overlap with kimberlite groundmass monticellite from various localities compiled by Mitchell (1986) (Figure 4.1.6).

Kopylova et al. (2021) suggests that the preferential crystallization of monticellite around clinopyroxene rims in Chidliak peridotites is a result of the reaction: clinopyroxene + $CaCO_3$ (liquid) → monticellite + CO_2. They suggest the reaction occurred at < 40 km depth and the source of the carbonate is from carbonate-bearing fluids in the ascending kimberlite. The fact that monticellite exclusively occurs along the margins of only a few melt pockets, and never in the centre, implies that it may not be part of the melt intrusion paragenesis, or that the melt pockets and veins had completely crystallized in most of the xenoliths at depths > 40 km. The only exceptions to this may be in xenolith 0411F1, which has monticellite in the central parts of its melt veins, and xenolith 0411F2V, which has monticellite grains in a zone where the host kimberlite is observed intruding the xenolith in the plane of the thin section.

Monticellite rims on olivine in kimberlite groundmass were observed by Abersteiner et al. (2018). They suggest that it formed from the decarbonation reaction: olivine + carbonate (melt) → monticellite + periclase + CO_2, where periclase in the groundmass subsequently altered to brucite. These reaction products are similar to the mineral assemblages observed in close contact with some of the olivine and melt pockets in xenoliths in this study. Similarly with brucite in the melt pockets, which could have been former periclase.

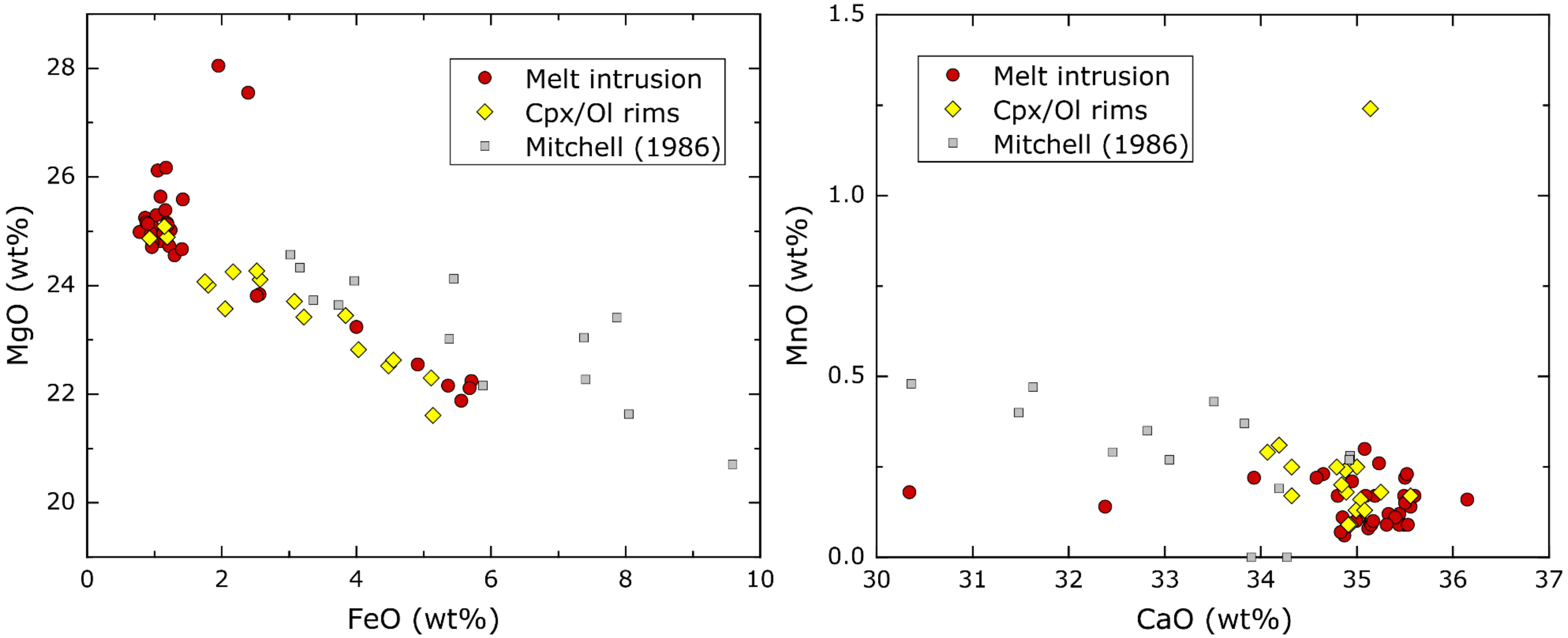

Figure 4.1.6 – Bivariate plots of monticellite compositions from rims of melt pockets, melt veins, and monticellite rims on pyroxenes and olivine. Grey squares are kimberlite groundmass monticellites from various localities (Mitchell, 1986, and references therein).

4.1.6 Volatile-bearing phases

Serpentine in the CH-6 and -7 melt intrusions has compositions within the range of kimberlitic serpentine reported by Mitchell (1986). The principal composition variation of serpentine is in FeO and Al_2O_3, which range from 2.78 to 10.26 wt% and 0.00 to 3.04 wt%, respectively, in the melt pockets. Mitchell (1986) reports wide ranges in FeO, from 2 to 14 wt%, and Al_2O_3 up to 7.5 wt% from various kimberlites. Serpentine in kimberlites can occur as pseudomorphic replacements of earlier minerals, as primary groundmass, or non-pseudomorphic prograde replacements (Mitchell, 1986). The lack of pseudomorphic textures of former minerals, and the presence of spherulite-texture serpentine observed in some melt pockets (Figure 4.1.7), suggests it is a product of devitrification of former quenched glass. Similar spherulites were observed in melt pockets in olivine megacrysts studied by Howarth and Büttner (2019), who interpreted the serpentine to be a secondary-replacement of quenched glass. This supports the findings of previous researchers such as Skinner and Marsh (2004) and Willcox et al. (2015) that have suggested that some serpentine in kimberlites is former glass.

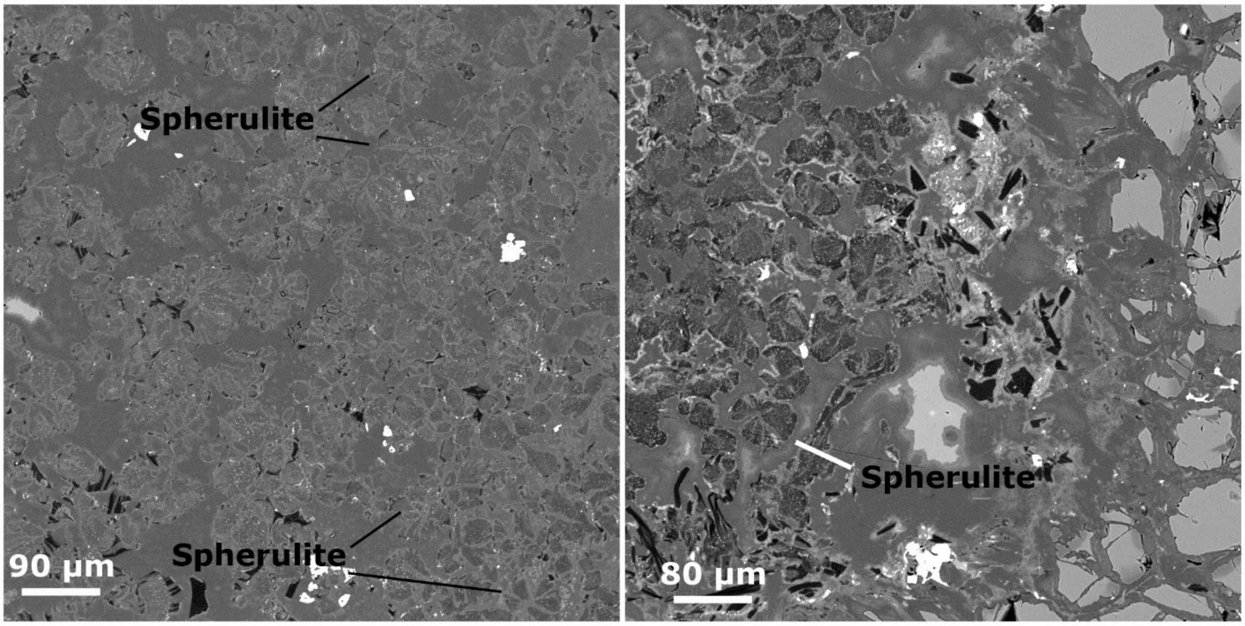

Figure 4.1.7 – Annotated BSE images of spherulite texture in melt pockets from two different xenoliths. The spherulites are radial aggregates of serpentine with very fine grained (≤ 1 µm), disseminated magnetite crystals.

Brucite in the melt pockets have similar compositions to kimberlitic brucite described by Mitchell (1986). Mitchell (1986) suggests that brucite in kimberlites is a product of deuteric alteration in the shallow subsurface, when olivine is replaced by serpentine and brucite. Monticellite along the margins of the melt pockets is rare-to-absent, thus it is unlikely that most of the brucite present in the melt pockets is the result of secondary alteration of periclase formed by the reaction: olivine + carbonate (melt) → monticellite + periclase + CO_2 suggested by Abersteiner et al. (2018).

The carbonates in the melt intrusions are mostly within the range of reported Ca# (Ca/[Ca+Mg+Fe]) and MnO contents of hypabyssal Lac de Gras kimberlites (Armstrong et al., 2004), but extend to lower Ca# due to two magnesite analyses, which was not a phase reported in Lac de Gras kimberlites (Figure 4.1.8). Most SrO compositions are within the range of Lac de Gras kimberlites, except for the much higher SrO in a single strontianite vein from a melt intrusion and its Sr-rich calcite overgrowth.

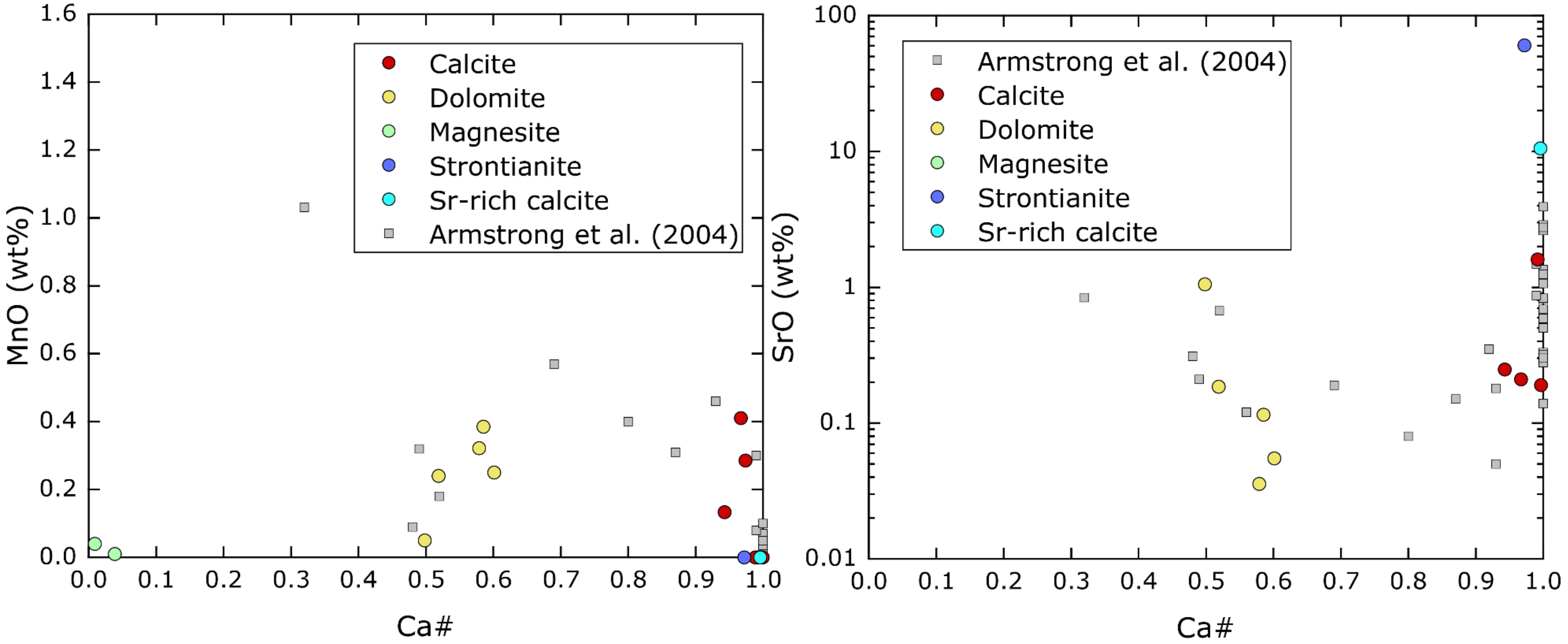

Figure 4.1.8 – Bivariate plots of carbonates from melt intrusions compared to carbonate compositions in Lac de Gras hypabyssal kimberlites (Armstrong et al., 2004).

4.1.7 Sulphides

The common, but volumetrically low sulphide content in the xenolith melt intrusions is also a common feature in most kimberlite groundmass (Mitchell, 1986). The occurrence of irregular-shaped, single crystal sulphides, and distinct globules in some of the melt pockets, are textural features that are consistent with crystallization from primary immiscible sulphides (Mitchell, 1986). Fine grained Ni-sulphides in serpentine veins and fractures of olivine grains are consistent with derivation from the sulphurization of olivine that accompanies serpentinization (Mitchell, 1986).

Djerfisherite is a common phase in many kimberlites (e.g., Abersteiner et al., 2019) and was recognized in the melt veins of the eclogite. Abersteiner et al. (2019) proposes two crystallization methods for djerfisherite in kimberlite: 1) existing Fe-Ni-Cu sulphides reacting with K-Cl rich melts/fluids in the mantle or transporting kimberlite; and 2) crystallization directly from the kimberlite. Either one of these methods are reasonable possibilities of its occurrence in the eclogite veins.

4.1.8 Melt intrusion major element composition

Except for Na_2O and P_2O_5, the major-element compositions of melt pockets determined by EPMA grids have little-to-no overlap with estimates of primary kimberlite melts (Kjarsgaard et al., 2009, and references therein), nor kimberlite whole-rock samples from other localities including Chidliak (this study) (Figure 4.1.9). This could be a result of the heterogenous phase distribution in melt pockets, where most acicular mica grains and larger crystals of spinels, perovskite, and apatite are usually more concentrated along the intrusion margins, in contrast to the central areas that are typically dominated by serpentine and/or carbonates. Since the EPMA grids were in the central regions of the melt pockets, their major-element chemistry may not be an accurate reflection of the melt pocket bulk composition. Furthermore, post-emplacement deuteric alteration by volatile-rich fluids, resulting in serpentinzation and crystallization of carbonate phases in the melt pockets, could have modified the major-element chemistry of the primary melt. Supporting this idea is that the EPMA grid in xenolith 0413D has an average composition similar to serpentine, and the three grids in xenolith 0405C are similar to mixed calcite + dolomite + serpentine compositions.

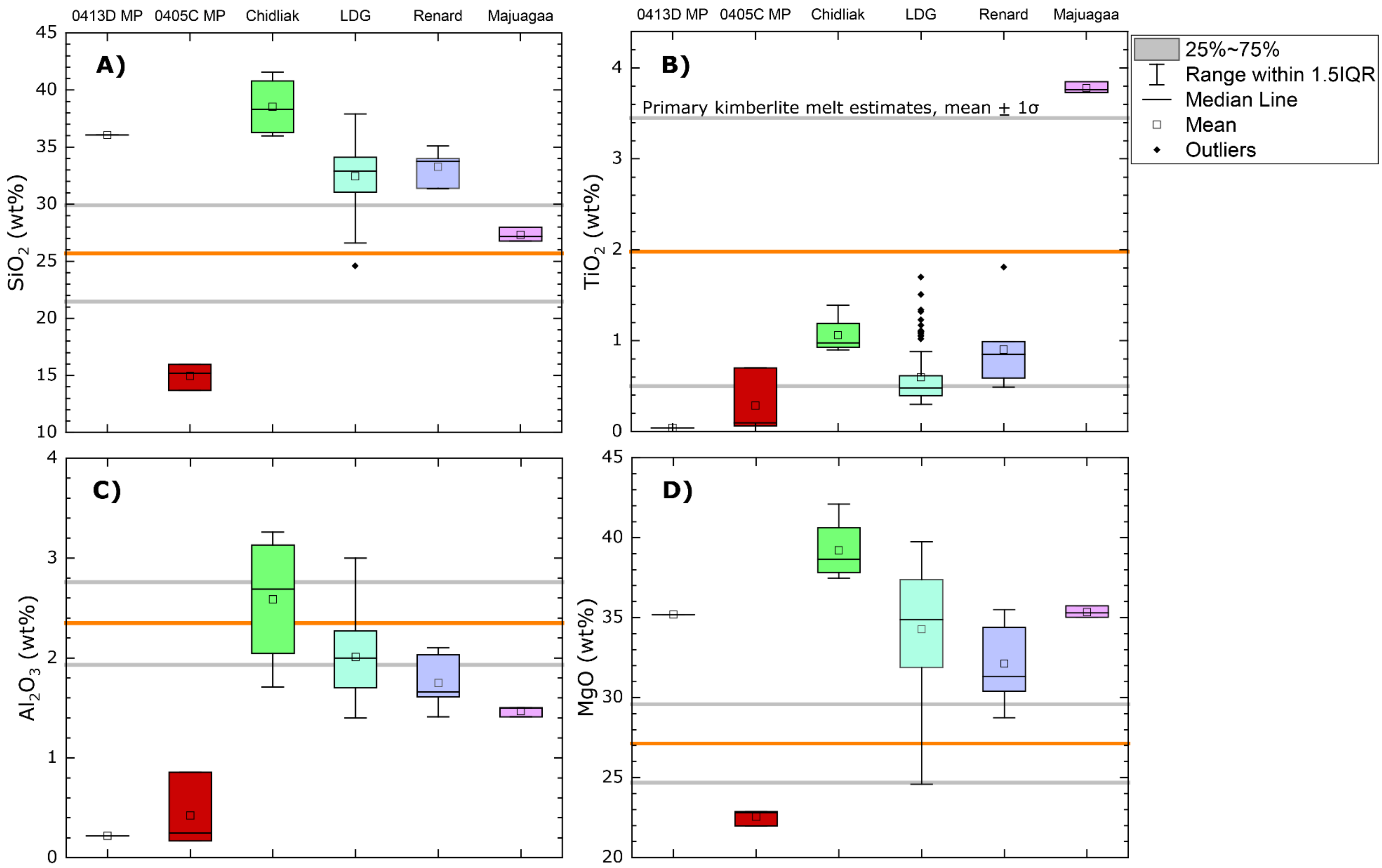
0413D MP
0405C MP
Chidliak
LDG
Renard
Majuagaa
A)
SiO_2 (wt%)
45
40
35
30
25
20
15
10
B)
TiO_2 (wt%)
Primary kimberlite melt estimates, mean ± 1σ
4
3
2
1
0
C)
Al_2O_3 (wt%)
D)
MgO (wt%)
25%~75%
Range within 1.5IQR
Median Line
Mean
Outliers

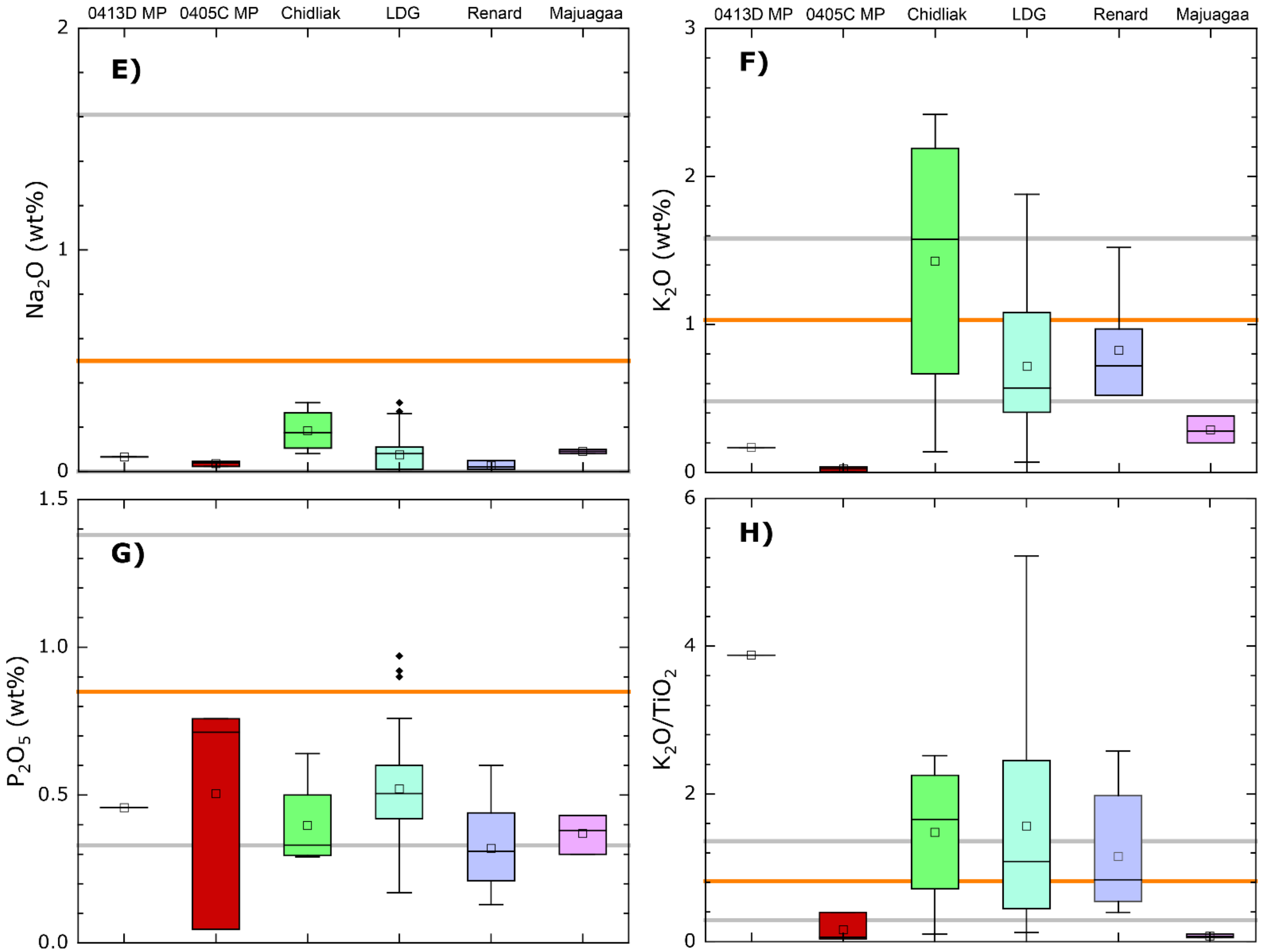

Figure 4.1.9 – Box and whisker plot of oxide compositions from EPMA melt pocket grids in xenoliths 0413D and 0405C, as well as Group I kimberlite whole-rock samples from Chidliak (this study), "uncontaminated" Lac de Gras kimberlites (Canada) (Kjarsgaard et al., 2009), Renard kimberlite (Canada) (Birkett et al., 2004), and Majuagaa kimberlite (Maniitsoq, Greenland) (Nielsen and Sand, 2008). Grey lines represent the range in composition of various estimates of parental kimberlite (Kjarsgaard et al., 2009), with the orange line being the average.

4.1.9 Melt intrusion trace-element composition

The REE_N pattern of CH-7 kimberlite whole-rocks compared to the bulk dissolution HR-ICP-MS results from micromilled CH-7 melt pockets in xenoliths are very similar (Figure 3.7.5). In a chondrite-normalized multi-element plot (Figure 3.7.6), the CH-7 whole rock samples have similar patterns to the micromilled melt pockets, but the CH-7 whole-rocks are generally more enriched in all elements. This is especially notable in Rb, Ba, Ti, and Hf, which are usually more than 10x greater in the CH-7 whole-rocks.

The REE_N composition of the CH-6 kimberlite whole-rock is significantly more enriched than the micromilled CH-6 melt pockets (Figure 3.7.5), and the CH-6 whole-rock lacks the positive Eu/Sm slope that is present in the melt pocket. The single CH-6 whole-rock is much more enriched in chondrite-normalized trace elements than the CH-6 melt pocket, having on average ~ 135x higher concentration (Figure 3.7.6).

Primitive mantle (PM)-normalized trace element patterns from melt pockets (determined by bulk dissolution HR-ICP-MS), are broadly similar to averaged CH-6 and -7 patterns of Chidliak kimberlite whole-rock samples (this study), as well as other kimberlites (Figure 4.1.10). The LREE enrichment relative to HREE of melt intrusions, is a typical feature of kimberlites (Pearson et al., 2019). More distinctive features in PM-normalized trace elements of melt intrusions, such as the Zr-Hf trough, and steep positive Eu/Hf slope, distinguish the melt intrusions from orangeites, ultramafic lamprophyres, and lamproites (Pearson et al., 2019). These melt intrusion features are similar to the other kimberlites plotted in Figure 4.1.10 (A). In contrast, the Ce/Pb and Ba/Nb systematics of the melt intrusions are highly variable relative to other kimberlites (Figure 4.1.11 (A)). The melt intrusions also differ by having highly variable Th/Nb and U/Pb (Figure 4.1.11 (B)).

Both CH-6 and -7 melt pockets have much lower PM-normalized concentrations of Rb, Ba, Th, Hf, and Ti than other mantle derived melts (Figure 4.1.10), and CH-6 has much lower abundances of all trace-elements except for Pb. These discrepancies could be an effect of late stage deuteric alteration and fluid migration through the melt pockets, which was likely responsible for serpentinization. In a study of kimberlite compositions from Kimberley, South Africa, Le Roex (2003) found that late-stage, high-temperature fluids from the kimberlite perturbed the initial concentrations of immobile incompatible elements such as Zr, Nb, La, and Hf, and alkaline and alkaline earth elements such as Rb, K, Ba, Sr, and Pb. Additionally, the lower Th, U, Zr, Hf, and Ti in the melt pockets could be due to the lower abundance of perovskite in them relative to the kimberlite groundmass.

The strong negative Ti anomaly (relative to PM) in both CH-6 and -7 melt pockets may be due to the low abundance of Ti-rich phases (such as perovskite and especially ilmenite) in the melt pockets (notably in the central areas where the micromill sampled). The scarcity of these phases could be due to crystallization of ilmenite megacrysts in the kimberlite magma prior to its intrusion in the xenoliths. Alternatively, negative Ti anomalies could be produced by a slab-derived melt with residual rutile. This type of melt would have fractionated HFSE such as Nb, Ta, Zr, Hf, and Ti, which are compatible in rutile (e.g., Foley et al., 2000). However, this type of melt would likely produce tonalite-trondhjemite-granodiorite (TTG) type magmas (e.g., Aulbach, 2020), which is not consistent with the mineralogy and mineral chemistry of the melt pockets. Therefore, perhaps the simplest explanation for the negative Ti anomalies in CH-6 and -7 melt pockets, is early crystallization of ilmenite megacrysts and/or groundmass in the kimberlite.

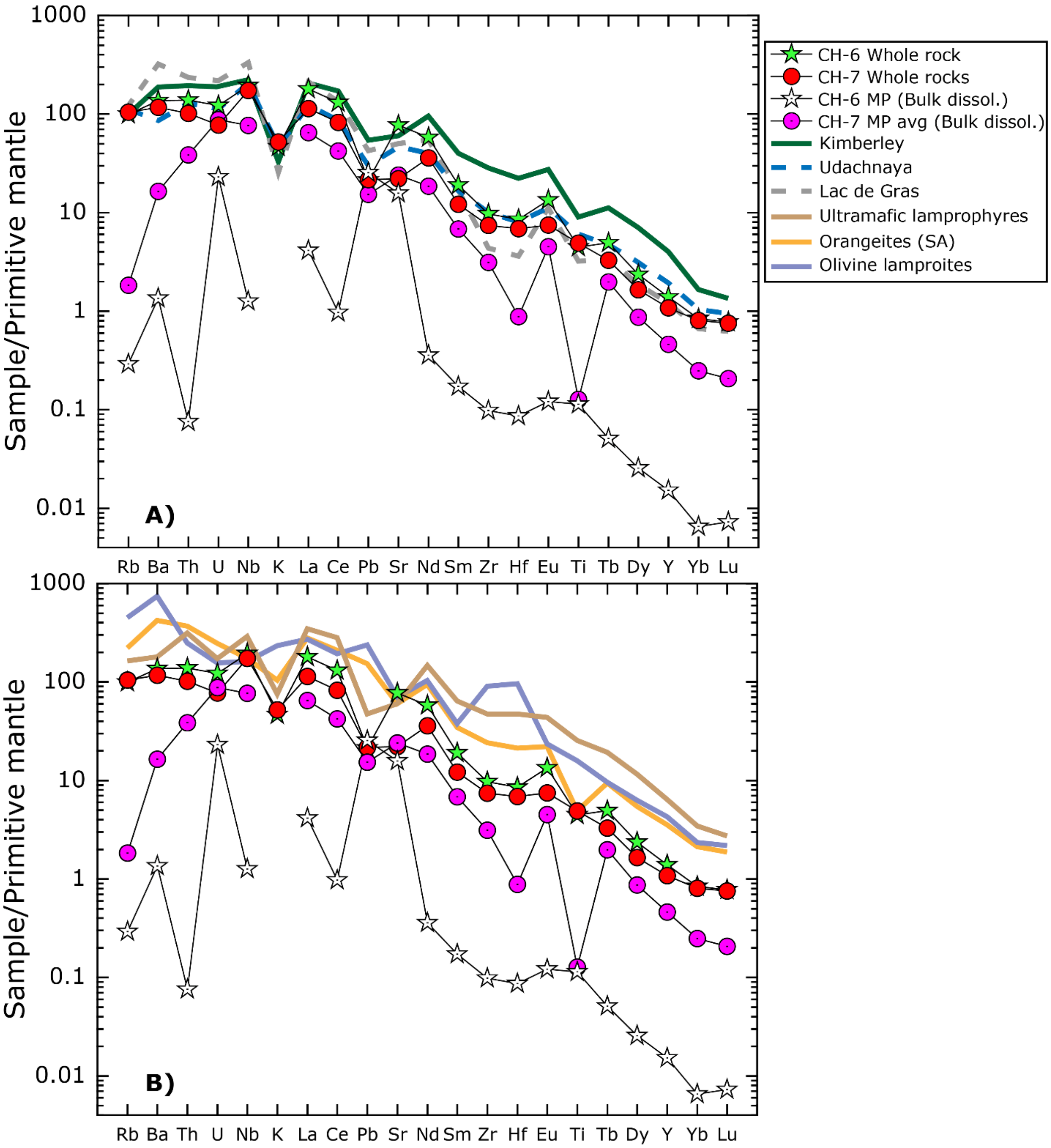

Figure 4.1.10 – Plots of primitive mantle-normalized incompatible trace elements of average melt pockets and Chidliak kimberlite whole-rocks determined by bulk dissolution HR-ICP-MS (Bulk dissol.). The data are compared with A) Archetypal Group I kimberlites from Lac de gras (Canada), Udachnaya (Russia), and Kimberley (South Africa); and B) orangeites from South Africa (SA), olivine lamproites from Western Australia, and ultramafic lamprophyres. Data are from Pearson et al. (2019, and references therein).

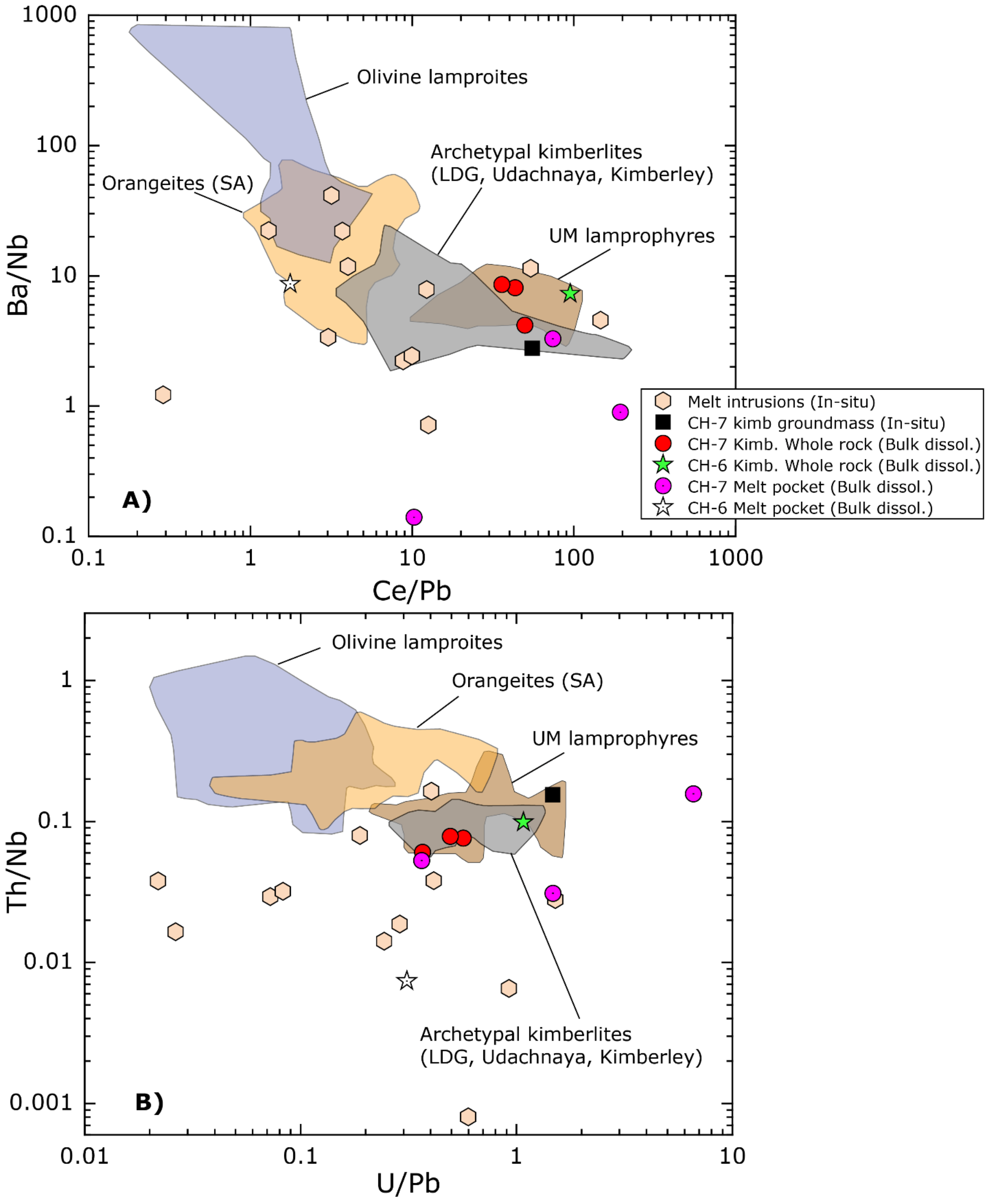

Figure 4.1.11 – Plots of A) Ce/Pb versus Ba/Nb and B) U/Pb versus Th/Nb for the same rocks in Figure 4.1.10, and melt intrusions measured by in-situ LA-ICP-MS (In-situ). Supplementary data are from Pearson et al. (2019), and references therein. LDG = Lac de Gras, UM lamprophyres = ultramafic lamprophyres.

4.1.10 Melt mineralogy differences between spinel- and garnet-stable xenoliths

The melt veins in peridotites from the spinel stability field are mineralogically different than those in xenoliths from the garnet stability field. The veins in spinel peridotites consist of rare perovskite + sulphides ± monticellite ± clinopyroxene, and are dominated by secondary serpentine and rare carbonates. The veins lack spinel and apatite, which are abundant in the melt pockets and veins in xenoliths from the garnet stability field. This difference could be due to a more evolved melt intruding the spinel peridotites, as the observed mineral assemblage is similar to kimberlite, although it lacks the complete groundmass assemblage.

4.1.11 Silicate versus carbonate dominated melt pockets

Melt intrusions dominated by serpentine are likely a product of secondary replacement of kimberlitic glass. The replacement process would likely have occurred post-emplacement in the crust, likely resulting from deuteric alteration by water-rich fluids (Le Roex, 2003). Similarly, carbonate-rich melt intrusions may simply be the result of concentrated carbonates in residual fluids in the kimberlite, which altered the melt intrusions in a smaller number of the xenoliths (Le Roex, 2003). The colloform texture commonly observed in carbonate-dominated melt intrusions (Figure B.3, image H.2) supports a model in which the carbonates precipitated out of a fluid at relatively low P-T conditions, rather than crystallizing directly from the melt intrusions at mantle conditions.

4.1.12 Kimberlite whole rocks

Contamination Index values range from 0.94 – 1.07 for all four kimberlite whole rock samples in this study, suggesting they have minimal crustal contamination, since values near one are considered uncontaminated (Clement, 1982; Mitchell, 1986). However, the incorporation of peridotitic material in the whole-rock samples may be masking crustal contamination, because the two have mutually opposing effects on the contamination index (Kjarsgaard et al., 2009). The major-element compositions of the Chidliak kimberlite whole-rocks are generally similar to other kimberlites plotted in Figure 4.1.9, as well as estimates of primary kimberlite melts (Kjarsgaard et al., 2009, and references therein), but extend to higher SiO_2, MgO, Al_2O_3, and K_2O. Primitive mantle normalized trace element compositions of the kimberlite whole rocks are very similar to the others plotted in Figure 4.1.10.

The single CH-6 whole-rock analyzed has εNd = 4.2 ± 0.1 (2SE), higher than the εNd from CH-6 perovskite (εNd = 3.7) (Heaman et al., 2015). The average εNd from the CH-7 whole-rocks (εNd = 1.6) is lower than the εNd from CH-7 perovskite (εNd = 2.1) (Heaman et al., 2015). Both CH-6 and CH-7 kimberlite whole rocks have εNd values within the range of Mesozoic southern Africa Group I kimberlite perovskites (Figure 3.8.1). However, CH-6 is slightly higher than the εNd range of Chidliak perovskites reported by Heaman et al. (2015), and CH-7 is within the range. This suggests the kimberlite whole rocks have experienced little alteration of their $^{143}Nd/^{144}Nd$ ratios.

The initial $^{87}Sr/^{86}Sr$ of the CH-6 whole-rock is 0.703603 ± 0.000016 (2SE), which is more radiogenic than the CH-6 perovskites (0.703216 ± 0.000024 (2SE)) (Heaman et al., 2015). The initial $^{87}Sr/^{86}Sr$ ratios from CH-7 whole rocks range from 0.705792 ± 0.000017 (2SE) to 0.706384 ± 0.000022 (2SE), considerably more radiogenic than the value from CH-7 perovskite of 0.7039190 ± 0.000016 (2SE) (Heaman et al., 2015). Highly radiogenic initial $^{87}Sr/^{86}Sr$ ratios of kimberlite whole rocks compared to individual phases such as perovskite, is a well-documented phenomenon (e.g., Berg and Allsopp, 1972; Heaman, 1989; Malarkey et al., 2010; Paton et al., 2007). The studies suggest that incorporation of potentially isotopically enriched radiogenic cratonic crust into the kimberlite, coupled with hydrothermal alteration syn- and post-emplacement, increases the $^{87}Sr/^{86}Sr$ ratio of kimberlites. Thus, primary kimberlite groundmass phases such as perovskite are a more faithful record of the initial $^{87}Sr/^{86}Sr$ ratio (e.g., Heaman, 1989). The higher $^{87}Sr/^{86}Sr$ initial ratios of the kimberlite whole-rocks in this study compared to their respective ratios from perovskite (Heaman et al., 2015) suggests that the kimberlite whole-rock samples have had their initial $^{87}Sr/^{86}Sr$ ratios altered to more radiogenic values. This could be due to a combination of incorporation of cratonic crust and hydrothermal alteration of the CH-6 and CH-7 kimberlites.

4.1.13 Melt intrusion metasomatism of wall-rock phases

The metasomatic effects of the melt-intrusions in contact with xenolith minerals is petrographically and geochemically apparent in olivine, coarse ilmenites, and orthopyroxene. In the simplest geochemical case, olivine rims in contact with melt intrusions occasionally exhibit zoning to higher MgO and NiO, which suggests the melt was enriched in both Mg and Ni.

Spinel reaction rims on coarse ilmenites in contact with melt intrusions record a decrease of Ti, Cr, and V, and an increase in Mg, Fe^{2+}, Fe^{3+}, Al, Mn, Ni, and Zn. The fact that spinel reaction rims are preferentially formed at the interface of the ilmenite grains and the melt intrusions, suggests that the primary ilmenite was not in chemical equilibrium with the melt. Similar rims on ilmenite megacrysts from the Monastery mine (South Africa) were documented by Kamenetsky et al. (2014). In their study, the ilmenite megacrysts contained melt inclusions from what they interpreted to be a crystallized kimberlite melt. The reaction rims were dominated by Fe-Mg-Ti oxides, but differed from this study as they also contained titanite [$CaTiSiO_5$], perovskite, kassite [$CaTi_2O_4(OH)_2$], freudenbergite [$Na_2Fe^{3+}{}_2Ti_6O_{16}$], and priderite [$K_2(Ti,Fe^{3+})_8O_{16}$].

Orthopyroxene grains in contact with melt are commonly pseudomorphed by a mixture of clinopyroxene ± phlogopite ± tetraferriphlogopite + serpentine (Figure B.3, image A.1). This combination of phases signals melt addition of Ca, Cr, Ti, K, OH^-, Fe^{2+}, and Fe^{3+} (when tetraferriphlogopite is present). The observed mineralogical replacement is consistent with a geochemical reaction occurring between orthopyroxene and kimberlitic melt. Orthopyroxene dissolution in kimberlitic melt during its ascent from high pressure mantle conditions to surface has been predicted in modelling by Luth (2009). This is supported by observations of similar alteration of orthopyroxene in contact with melt veins in mantle xenoliths (e.g., Dawson et al., 2001), and the lack of orthopyroxene macrocrysts in kimberlites (e.g., Kopylova et al., 2007; Le Roex, 2003; Mitchell, 2008).

4.1.14 Process of melt entrapment

One process by which melt may have entered and crystallized in the xenoliths is by infiltration along grain boundaries. Several thin section scans that show this process caught in the act are shown in Figure B.1, images: M.2) 0411IV, U) 0411F2V, Q.2) 0413BV, and Y) 0405H. This process, termed "necking down" by Roedder (1984), has been suggested as the process that caused entrapment of melt in megacrysts in several studies (e.g., Araújo et al., 2009; Bussweiler et al., 2016; Schulze, 1985; van Achterbergh et al., 2002; van Achterbergh et al., 2004). The process occurs by melt infiltrating the host crystal along fractures and cleavage planes by dissolution and recrystallization (Bussweiler et al., 2016). Larger melt pools are formed by surface area reduction and the coalescence of discrete inclusions. In the case of the Chidliak melt intrusions, the only two obvious exceptions to this are observed in spinel lherzolites 0405B and 0411C, where melt veins cross-cut olivine grains and do not appear to follow any pre-existing fractures. This cross-cutting feature suggests that the melt veins formed from a high-pressure injection event, perhaps facilitated by higher degrees of CO_2 exsolution from the kimberlite melt at these lower pressures.

4.1.15 Depth and timing of melt entrapment

The rarity of mantle xenoliths entrained by kimberlites worldwide that contain crystallized melt pockets, suggests that the melt intrusion event(s) in the Chidliak xenoliths did not occur during their entrainment and ascent in the kimberlite. If this event had occurred during their ascent with the melt intrusions in liquid form, it seems likely the xenoliths would have disaggregated. Instead, the melt pockets could be proto-kimberlite melts that were trapped and completely crystallized at mantle depths, prior to the xenolith's entrainment and ascent in the kimberlite. The proto-kimberlite melt that intruded the xenoliths would have crystallized at the solidus, and due to their loss of primary volatiles, the solidus temperature would have increased. Thus, when the final kimberlite pulse that entrained the xenoliths occurred, it was not sufficiently hot to re-melt the crystallized intrusions. The presence of two different "styles" of melt pockets in some of the xenoliths supports a model where they crystallized prior to their entrainment in the kimberlite, as these may represent multiple intrusion events. One of the styles has rounded edges in olivine porphyroclasts, suggesting they reacted with the grain, and they appear brown to black in PPL. The other has non-rounded, irregular shaped edges that occur in-between grain boundaries in the xenoliths, which suggests they did not have enough time to react with the host xenolith grains and become rounded. In PPL they appear as fine grained "spotted" mixtures of white and black grains, or with relatively large sections completely white or light green, or black to brown. This style of melt pocket often contrasts the colour in PPL of the ones with rounded edges in olivine porphyroclasts, when they occur together in xenoliths.

Another possibility is that the host kimberlite intruded the xenoliths during their entrainment, and the melt pockets and veins crystallized relatively quickly during their ascent to surface. Several thin sections were cut on a plane that shows the kimberlite groundmass intruding the xenoliths, causing one to partially disaggregate (Figure 4.1.12).

The presence of Cr-rich spinels in some of the melt intrusions, which are the earliest crystallizing spinel in kimberlite (Mitchell, 1986; Roeder and Schulze, 2008) is a potential clue that would suggest that the melt intrusions are an early phase of kimberlite. The timing of the melt intrusions can be constrained by the similar spinel reaction rims at the interface between "primary" coarse ilmenite grains in xenoliths and melt intrusions, and those coarse ilmenites and kimberlite groundmass (Figure 4.1.13). The similar thickness of the rims suggests that they formed over a similar time frame. The rims in contact with the kimberlite groundmass constrain this time to their entrainment and ascent in the kimberlite. Additionally, the presence of orthopyroxene grains only partially replaced to clinopyroxene ± phlogopite ± tetraferriphlogopite + serpentine suggests that the melt intrusions crystallized relatively quickly before the dissolution reaction could reach completion. The complete lack of monticellite in the central areas of the melt pockets suggests that the melt pockets had completely crystallized by ~ 1 GPa - a minimum constraint on when the melt pockets crystallized. In this scenario, the rare monticellite grains along the margins of some melt pockets are not part of the melt pocket mineral assemblage, and instead crystallized from late-stage host kimberlite related fluids intruding the xenolith. The only exception to this may be in xenolith 0411F1, which has monticellite in the central parts of its melt veins.

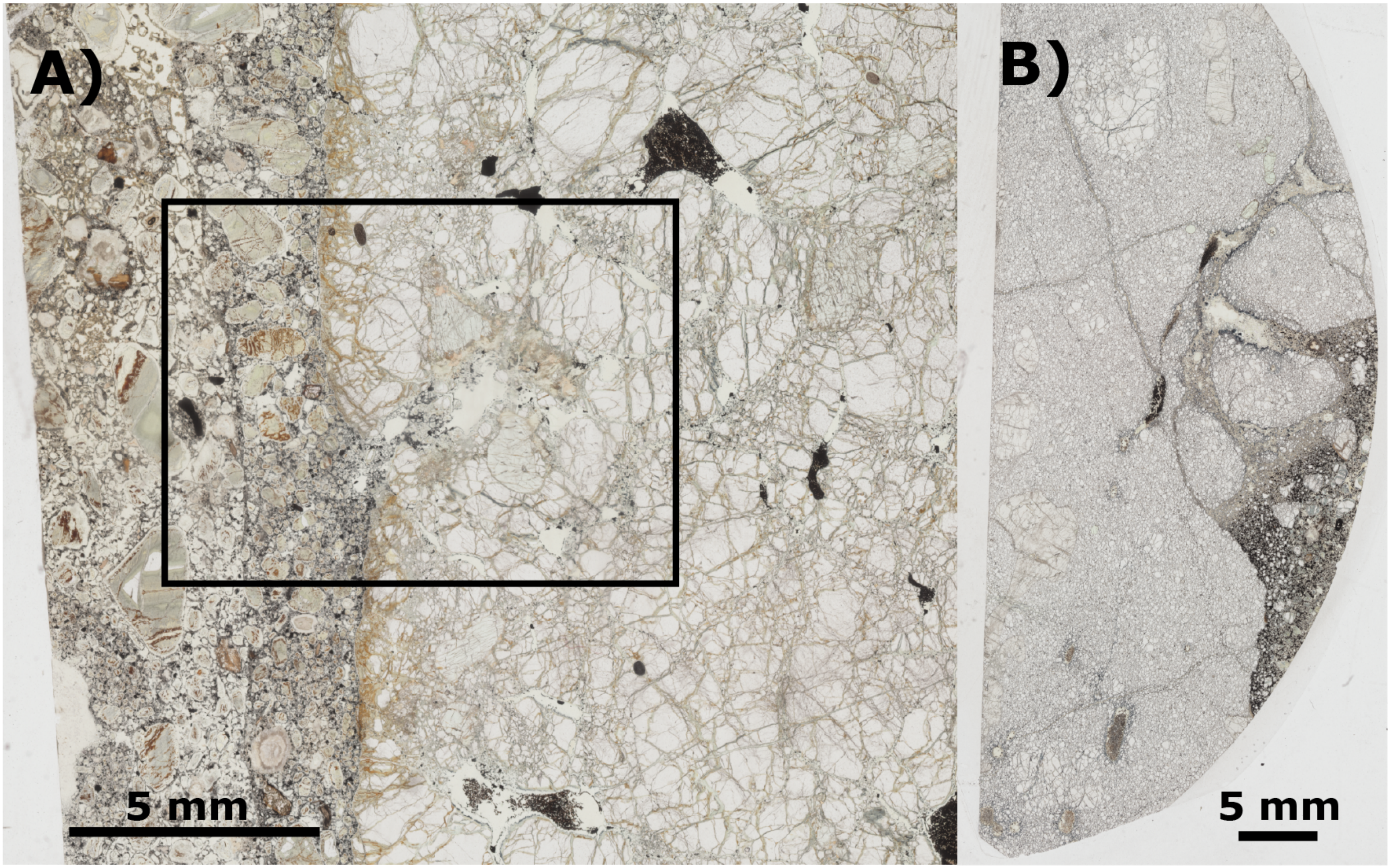

Figure 4.1.12 – Thin section images in visible light showing A) kimberlite infiltration into xenolith 0411IV, which forms a melt pocket; and B) kimberlite infiltrating xenolith 0411F2V, which appears to be forming pockets and causing the xenolith to disaggregate.

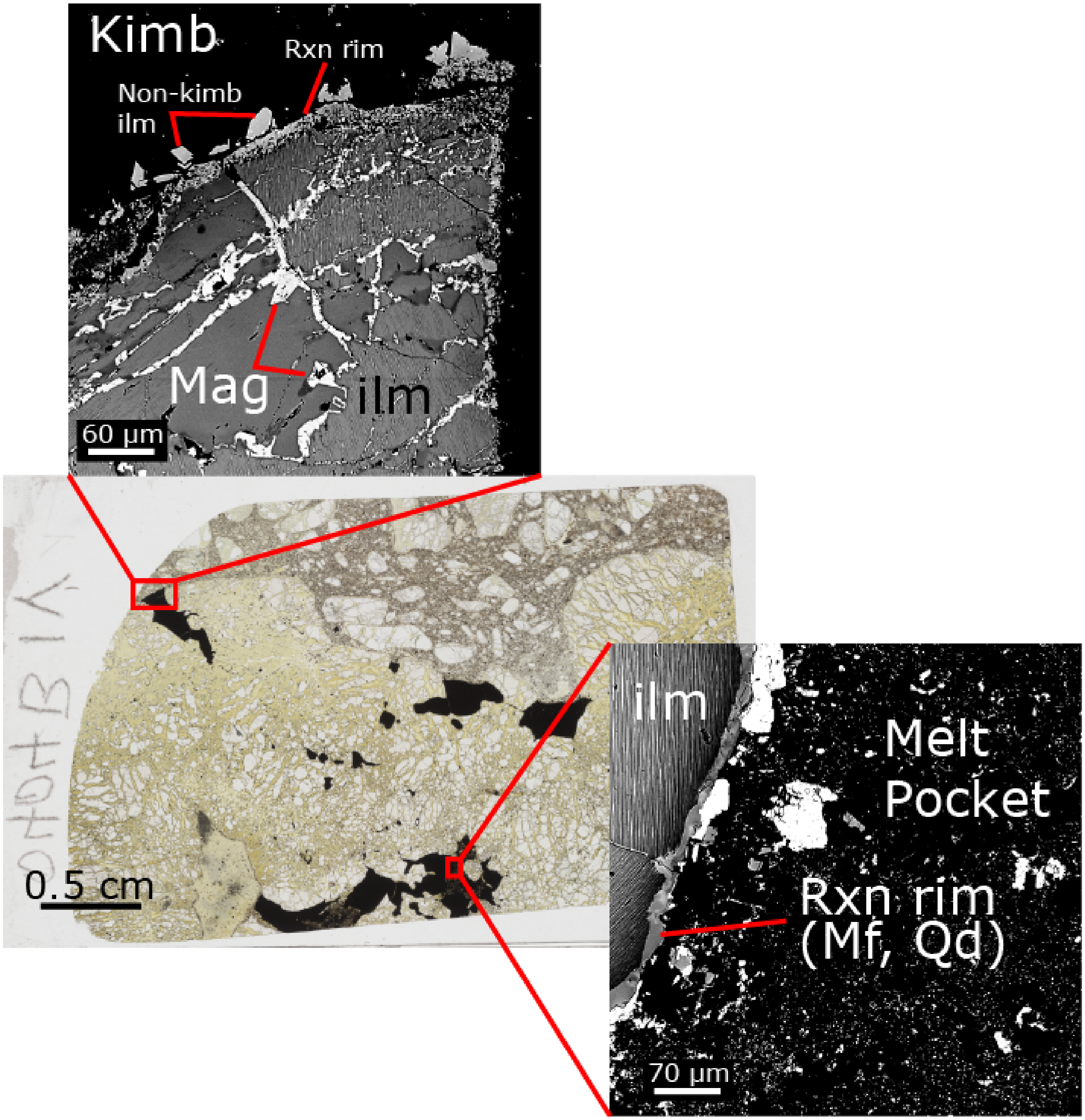

Figure 4.1.13 – Thin section scan in visible light of xenolith 0404B1V with BSE images showing the reaction rims that formed on the coarse ilmenite grains due to reaction with the kimberlite (top image), and reaction with a melt pocket (lower right). ilm = ilmenite, Kimb = CH-6 kimberlite groundmass, Mag = magnetite Mf = magnesioferrite, Qd = qandilite, Rxn = reaction.

4.2 Melt depletion and modal metasomatism of the Chidliak mantle

4.2.1 Melt depletion trend

Modal mineralogy estimates of xenoliths in this study suggests they are dominantly dunites in the IUGS classification scheme. This agrees well with the large proportion of olivine-rich peridotites studied by Kopylova et al. (2019) (Figure 3.1.1). To produce dunites from an initial fertile peridotite, melt extraction in excess of 40% is required (Takahashi et al., 1993). Clinopyroxene is removed from the rock at ~ 20% melt extraction (Kushiro, 1996), followed by orthopyroxene at ~ 40% melt extraction (Bernstein et al., 2006). This melt depletion results in an increase in bulk rock Mg#, which is reflected in the residual mineral phases.

4.2.2 Olivine

Olivine in residual peridotites is considered to be a good bulk rock Mg# tracer, with Mg# increasing with higher degrees of melt depletion (Pearson et al., 2014). Cratonic peridotites have residual olivine Mg# ranging from 91 to 94, but silicate melt metasomatism generally enriches olivine in iron and hence lowers their Mg# (Pearson et al., 2014). In contrast, carbonatitic metasomatism may introduce Mg, which increases their Mg# (Pearson et al., 2014). The olivine Mg# is < 91 in eleven of the peridotites in this study (Figure 4.2.1), which suggests they have experienced silicate melt metasomatism and/or the olivine crystallized from a silicate melt. Metasomatic crystallization of olivine is consistent with the findings of Kopylova et al. (2019), who suggests that olivine addition may also be reflected texturally in Chidliak xenoliths by the presence of coarse olivine grains (up to 2 cm). These authors invoke a silicate-carbonate melt as being responsible for this.

The Mg# of olivines in xenoliths in this study are within the 85.1 to 93.1 Mg# range of the Chidliak xenoliths studied by Kopylova et al. (2019) (Figure 4.2.1 and Figure 4.2.2), except for ilmenite clinopyroxene dunite 0404C with Mg# 84.9. Additionally, 13 of the 24 olivine-bearing xenoliths have olivine Mg# within the Chidliak diamond inclusion range of 91.0 to 93.2 (Xia, 2018). The oxide compositions of olivines in this study mostly overlap with the compositions reported by Kopylova et al. (2019), except for SiO_2, which is on average 1.2 wt% lower in this study.

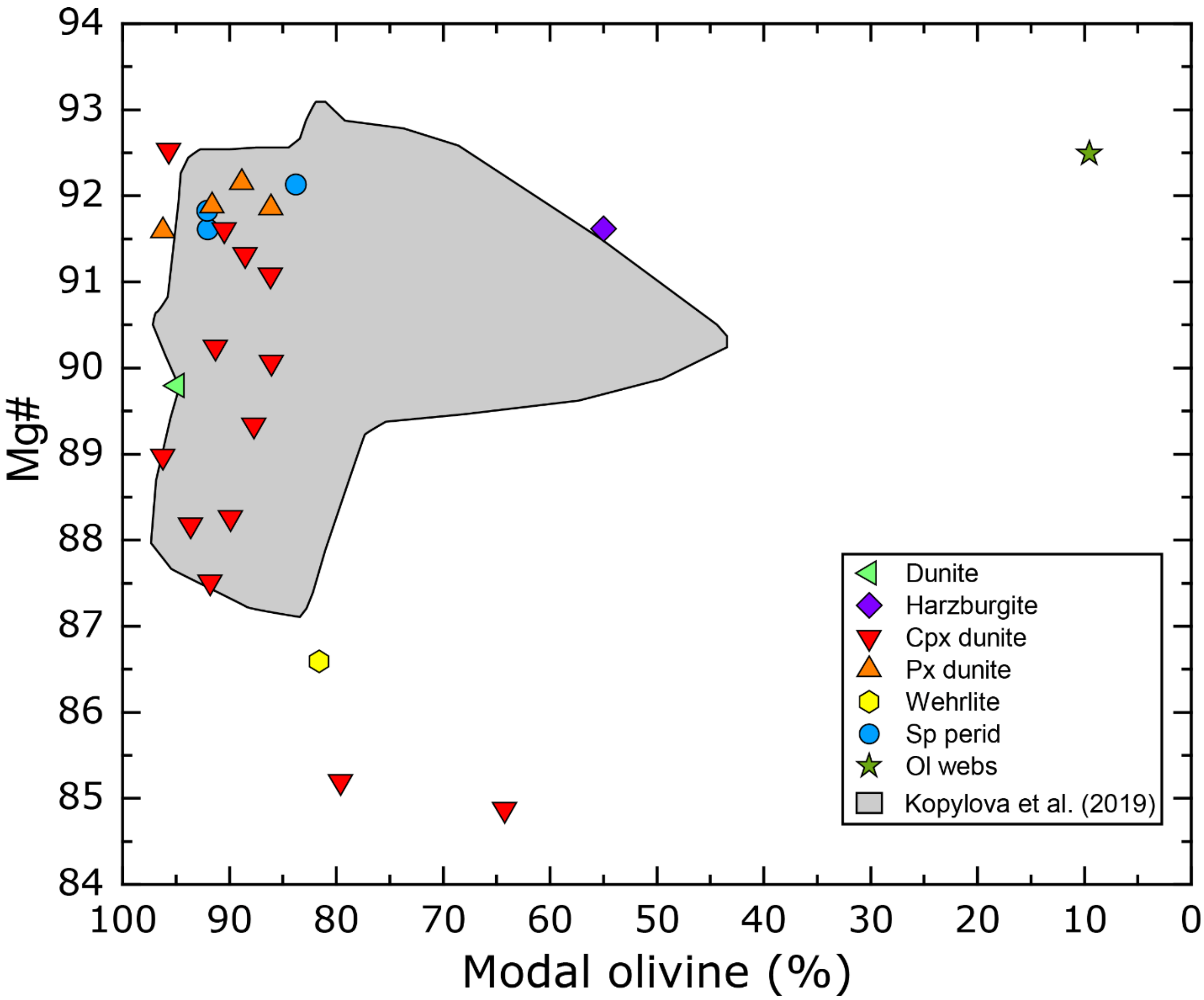

Figure 4.2.1 – Olivine mode versus Mg# for xenoliths from this study compared to CH-1, -6, -7, and -44 xenoliths from Kopylova et al. (2019) (grey field).

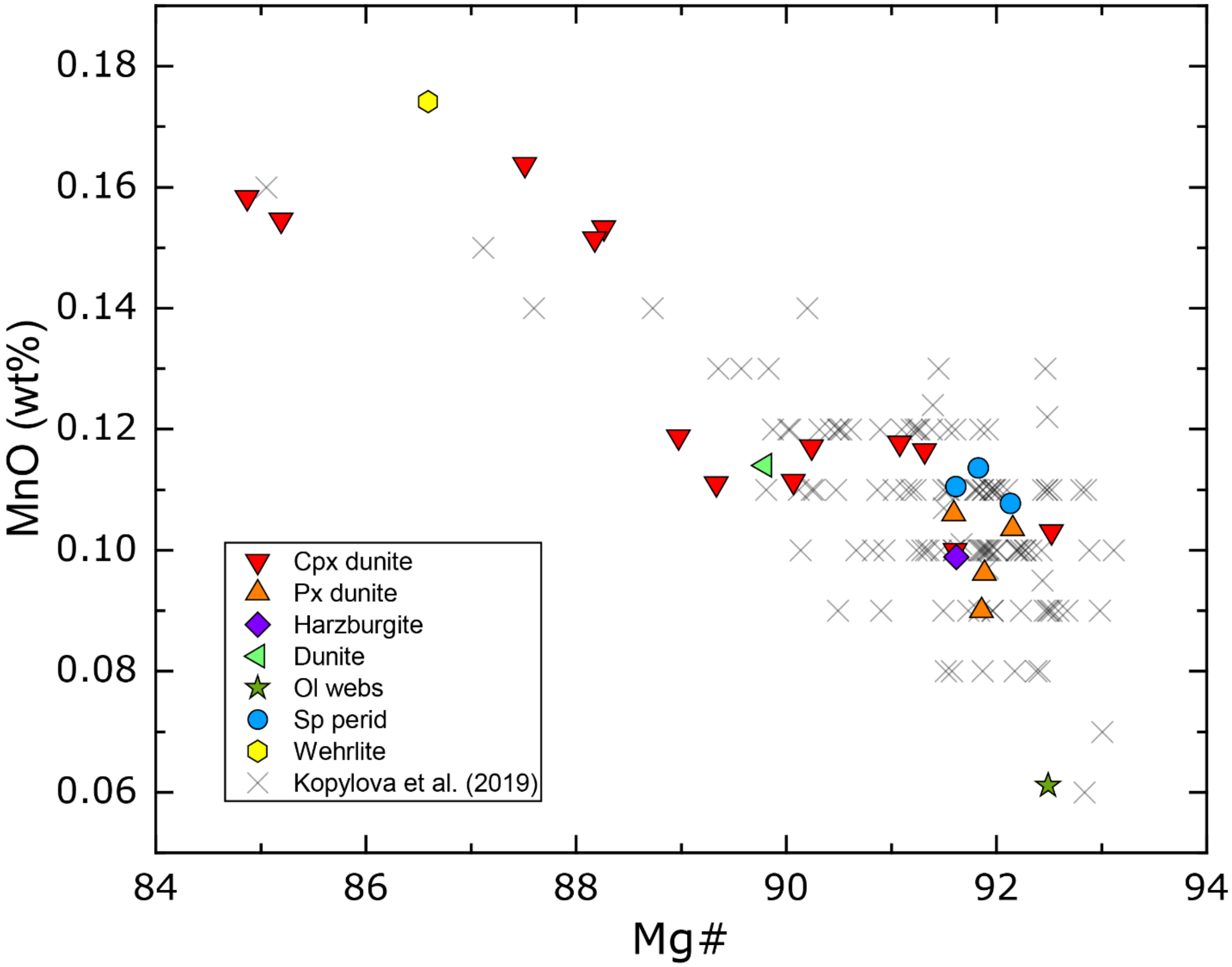

Figure 4.2.2 – Mg# versus MnO plot of olivine grains from xenoliths in this study compared to other Chidliak xenoliths studied by Kopylova et al. (2019).

4.2.3 Orthopyroxene

The Mg# range of primary orthopyroxenes in xenoliths in this study are within the range reported by Kopylova et al. (2019) of 91.0 – 93.8. Additionally, all oxides overlap in composition, except for two xenoliths in this study which have slightly higher MgO. The compositions of the orthopyroxenes are consistent with them being primary residual phases in the xenoliths.

4.2.4 Peridotitic Cr-pyrope garnets

Peridotitic garnets in this study have major-element compositions that mostly overlap with the compositions of Chidliak peridotites and pyroxenites reported by Kopylova et al. (2019). However, cpx dunites 0405C, 0411I, and wehrlite 0411H, have significantly higher CaO (> 5 wt%), and slightly higher MnO (0.01 to 0.08 wt%) than the highest values reported by Kopylova et al. (2019). The garnet composition from wehrlite 0411H also has the lowest Cr_2O_3 (0.60 wt%), compared to the minima of 0.92 wt% reported by Kopylova et al. (2019). All remaining oxides are within or are very close to the range of Chidliak peridotitic and pyroxenitic garnets from published literature. The eclogite garnets in xenolith 0405H in this study have an overlapping major-element composition with the eclogitic garnets studied by Pobric et al. (2020).

The CaO – Cr_2O_3 systematics of garnet compositions in peridotites are considered to reflect the relative amount of melt extraction that a rock has experienced, and hence can be used to predict the lithology they equilibrated with (e.g., Grütter et al., 1999; Sobolev et al., 1973). Garnets from lherzolitic assemblages are expected to classify as G9, and garnets in clinopyroxene-free harzburgites have lower CaO (and possibly higher Cr_2O_3) and classify as G10 (harzburgitic) (Grütter et al., 2004). Garnets with CaO < 1.8 wt% classify as ultra-depleted G10, indicating their host rock experienced higher degrees of melt-extraction to the point of orthopyroxene exhaustion; hence these garnets are generally from ultra melt-depleted dunites (Grütter et al., 1999). In contrast, most of the garnet compositions in harzburgitic and dunitic xenoliths from this study do not reflect their lithology. For example, the composition of all eight EPMA analyses in garnet harzburgite 0413C classify as G9 and G11 (high-TiO_2 peridotitic), which contrasts with typical harzburgitic garnets that classify as G10. In the three-garnet orthopyroxene clinopyroxene-bearing dunites, the analyses almost exclusively classify as G9 and G11 (except one G10 analysis in 0413A). Typical garnets in dunite xenoliths at other localities classify as G10. In the garnet clinopyroxene dunites, there is often considerable variation in garnet composition within individual xenoliths, and hence, garnet classification. In these nine xenoliths, the garnets range in classification from G10, G9, G12, G11, and G1 (low-Cr megacrysts). Similarly, garnet compositions in analyses from the pyroxene-free dunite (0413E) all classify as G11. The wehrlite, olivine websterite, and eclogite have garnet compositions consistent with their mineral assemblages.

The discrepancy between lithologies predicted by garnet composition alone (Grütter et al., 2004) and the IUGS classification scheme based on sample mineralogy, could be due to the modal mineralogy from the thin sections being unrepresentative of the xenoliths. Hence, in some or all of the thin sections, the proportions of olivine, clinopyroxene, and orthopyroxene, may not be a true representation of the xenolith. However, Kopylova et al. (2019) studied 120 peridotite and pyroxenite xenoliths from Chidliak and showed that a large portion had modal mineralogy, calculated from mass balance, that classifies as harzburgite and dunite based on the IUGS classification scheme. In their study, only ten of the garnets classify as G10 (Figure 3.3.4). Therefore, it is unlikely that unrepresentative thin sections are the dominant reason for the discrepancy between the two classification methods.

The geochemistry of garnets in highly depleted peridotites (harzburgite and dunite) that classify as G9 instead of G10, or have rims with higher CaO than their cores, has been documented at other localities (Griffin et al., 1999; Kopylova et al., 1999; Schulze, 1995). One reason for this could be due to metasomatic processes that increase CaO and decrease Cr_2O_3 in the garnets, which shifts their compositions closer to garnets derived from lherzolites (e.g., Griffin et al., 1999; Schulze, 1995). Other studies have documented evidence for metasomatic garnet re-introduction into xenoliths (e.g., Shimizu, 1999; Simon, 2003). At Chidliak, Kopylova et al. (2019) suggested that the high melt depletion of the mantle (> 35%) would have exhausted garnet in addition to clinopyroxene. Therefore, the authors suggest that the close spatial association of garnet and clinopyroxene in the xenoliths – including some with touching boundaries -, and the unusually high whole-rock Al_2O_3:Mg/Si ratios, which are inconsistent with the trend of global mantle peridotites, are evidence for the simultaneous re-introduction of garnet and clinopyroxene into previously melt-depleted peridotitic mantle at Chidliak.

An alternate view of the origin of the peridotitic garnets in Chidliak xenoliths, is that they were produced via metamorphism of depleted spinel peridotite from the reaction: orthopyroxene + spinel → garnet + olivine (Brey and Shu, 2018). This reaction is triggered by subduction and lithospheric thickening and was shown by Brey and Shu (2018) to be the sole method that can produce peridotitic garnets with > ~3 wt% Cr_2O_3. The Chidliak garnets may have then been subjected to metasomatism by a Ca-rich agent, which is why most of the garnets are not subcalcic G10s that are typical of dunites. This metasomatic agent may have been the one responsible for the crystallization of clinopyroxene in the xenoliths, as it would have been enriched in Ca.

4.2.5 Clinopyroxene re-introduction

The Mg# of peridotitic clinopyroxenes in this study are within the range reported by Kopylova et al. (2019) of 87.6 to 96.3, except for the clinopyroxene composition from ilmenite-bearing clinopyroxene dunite 0404C (Mg# = 87.1). However, both ilmenite-bearing clinopyroxene dunites have lower Cr_2O_3, and slightly higher FeO than the range of clinopyroxene compositions from Chidliak peridotites reported by Kopylova et al. (2019). All other oxides from the peridotites in this suite have overlapping compositions, except for the clinopyroxenes from the spinel peridotites, which have lower SiO_2 and higher Al_2O_3. The CH-7 clinopyroxenes in this study have a large range in TiO_2 composition, similar to the findings of Kopylova et al. (2019) for CH-1, -7, and -44 (Figure 4.2.4 Figure 4.2.3).

Clinopyroxene in the eclogite in this study is omphacitic and overlaps with the compositions of primary clinopyroxenes in Chidliak eclogites reported by Pobric et al. (2020), except Al_2O_3 is 0.17 wt% higher. The 41% jadeite component (calculated after Soto and Soto (1995) using WinPyrox software (Yavuz, 2013)) is on the upper end of the 13 to 45% jadeite component range of the primary clinopyroxenes reported by Pobric et al. (2020).

The dunitic lithology of most of the peridotite xenoliths containing melt intrusions indicate they have undergone high melt-depletion, well beyond the ~ 20% required to completely exhaust clinopyroxene from the rock (e.g., Takahashi et al., 1993). The fact that most of the xenoliths are orthopyroxene-free, clinopyroxene-bearing dunites, contradicts the melt depletion trend of fertile lherzolites, which should exhaust clinopyroxene before orthopyroxene. This suggests that clinopyroxene, and potentially some olivine, has been re-introduced into the xenoliths, and is not a primary residual phase. Kopylova et al. (2019) made this observation in Chidliak peridotites and used the textural features of clinopyroxene mantles on garnet and olivine, as well as its occurrence as parallel grains in linear zones in the xenoliths, as evidence. They also found that bulk rock peridotite compositions from Chidliak reflect re-introduction of clinopyroxene and garnet, which is evidenced by their high CaO content and high ratio of Al_2O_3 to Mg/Si compared to other cratonic peridotites. The origin of secondary clinopyroxene in xenoliths is often from infiltration of the host magma (Pearson et al., 2014), or from modal metasomatism in the mantle (e.g., Simon, 2003), but it can also be produced along with garnet from the exsolution of orthopyroxene in high-T harzburgites during cooling (e.g., Canil, 1991; Cox et al., 1987). The clinopyroxene textures and bulk-rock composition of Chidliak peridotites suggests that clinopyroxene was introduced during modal metasomatism, possibly by silicate-carbonate melts/fluids (Kopylova et al., 2019). The similar major- and trace-element compositions (Figure 3.6.4 and Figure 3.6.5) of clinopyroxene in melt-free Chidliak xenoliths to those in melt-bearing xenoliths, suggests that clinopyroxene was not introduced by the magma that crystallized in the melt intrusions. However, the preferential crystallization of melt intrusions adjacent to clinopyroxene grains could be due to the melt exploiting pre-existing structural weaknesses that were present when the clinopyroxene crystallized.

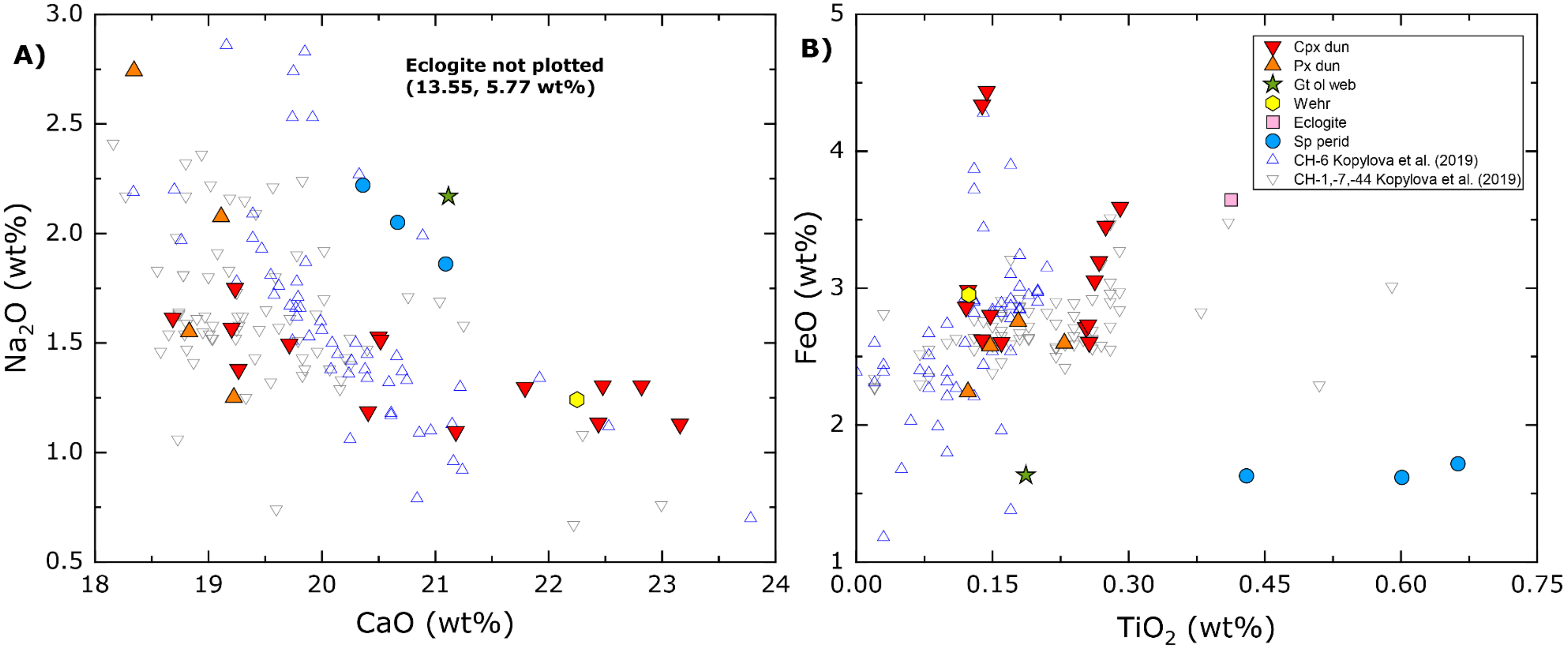

Figure 4.2.3 – A) CaO versus TiO_2 and B) TiO_2 versus FeO plots of clinopyroxene cores in this study compared to clinopyroxene cores from CH-1, -7, -44 (grey triangles) and CH-6 (Kopylova et al., 2019)

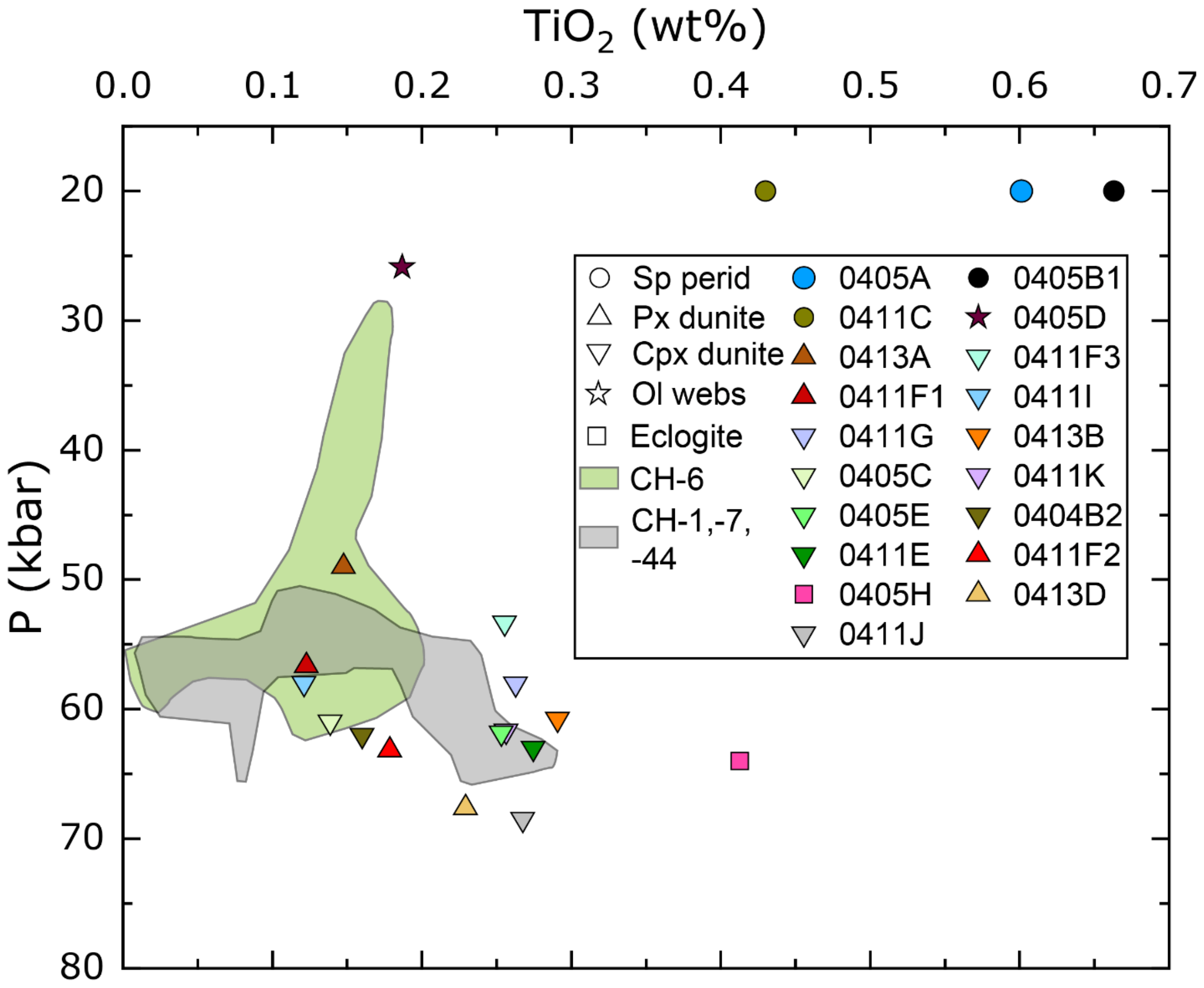

Figure 4.2.4 – TiO_2 (wt%) versus Pressure (kbar) of clinopyroxene grains in this study compared to Chidliak peridotitic clinopyroxene data from Kopylova et al. (2019).

4.2.6 Hydrous phases

Hydrous minerals such as phlogopite and amphibole are commonly found in mantle xenoliths that have experienced modal metasomatism (e.g., Dawson and Smith, 1982; Frey and Green, 1974; Wilshire and Trask, 1971). The occurrence of hydrous phases as disseminated/discrete grains in xenoliths, or replacing garnet and/or pyroxenes, are believed to be the product of fluid percolation and metasomatic reactions (Ionov et al., 1997). The occurrence of discrete, equilibrated hydrous-phases in the xenoliths in this suite, as well as those studied by Kopylova et al. (2019), are very rare. This suggests that most of the older modal metasomatism of the Chidliak mantle was by anhydrous agents, except for possibly in the spinel-facies. Evidence of modal metasomatism by a hydrous-bearing agent is present in spinel pyroxene dunite xenolith 0405A, which has phlogopite and pargasite occurring in contact with each other. This suggests they were introduced during the same metasomatic event. Furthermore, the grains have equilibrated with the xenolith with respect to size and texture, suggesting the modal metasomatic event occurred prior to their entrainment in the kimberlite. The mineral compositions of both phases suggests they crystallized from a fluid or melt containing appreciable Si, Ti, Al, Mg, Ca, Na, K, and OH^-. The phlogopite that crystallized from this has a composition similar to kimberlite groundmass phlogopites, which suggests the agent had kimberlitic affinity (Figure 4.2.5).

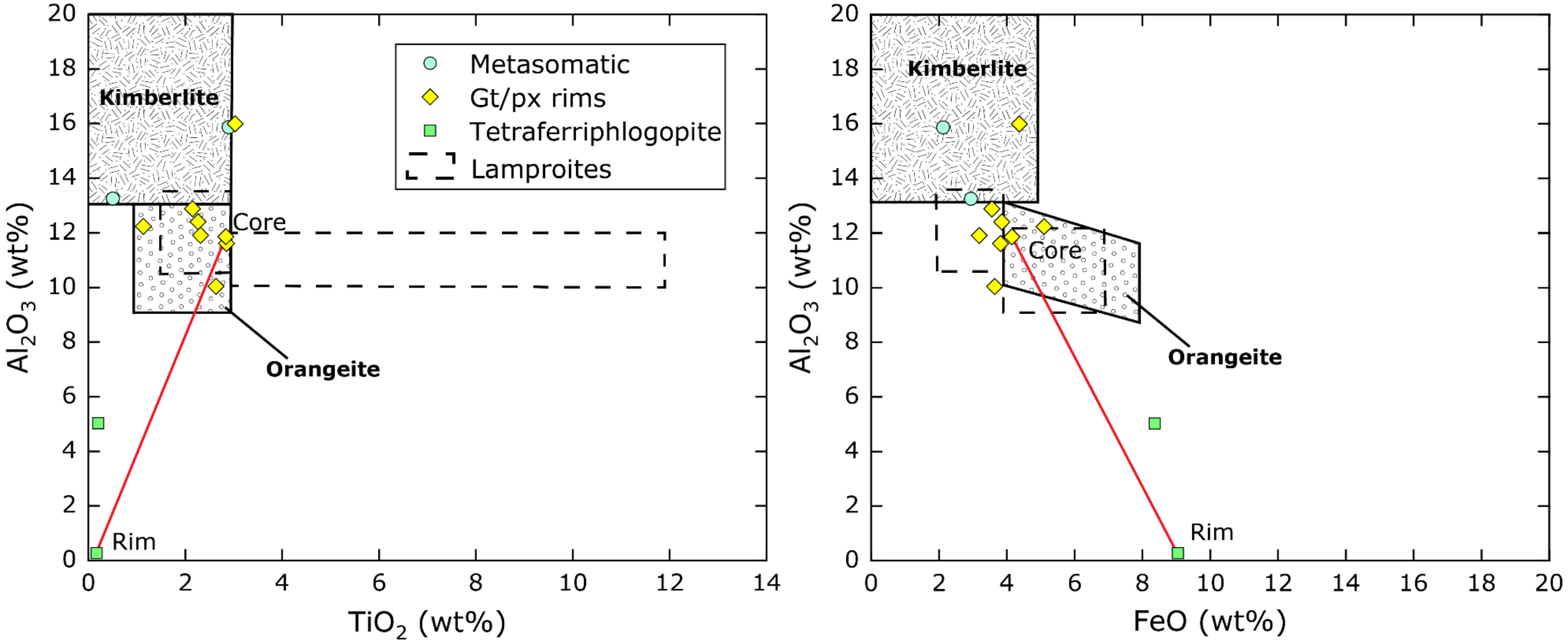

Figure 4.2.5 – Bivariate plots of phlogopite compositions from discrete grains in two xenoliths ("metasomatic"), phlogopites on garnet and pyroxene rims, and tetraferriphlogopite rims on phlogopite (red tie line of core phlogopite to tetraferriphlogopite rim) and a rim on a clinopyroxene in a melt vein. Compositional fields of micas in kimberlite groundmass, orangeites, and lamproites are from Mitchell (1995).

4.2.7 Evidence for lamproitic or fractionated kimberlite metasomatism

Potassian barian titanites (jeppeite and freudenbergite) that form complex rims on rutile in the olivine websterite and eclogite, are minerals that are characteristic of lamproites (Mitchell et al., 1991). Harris et al. (2018) found similar rims on rutile in a metasomatized pyroxenite xenolith from the Darby kimberlite (Rae craton) and suggested they may have formed due to lamproitic metasomatism. Alternatively, Anzolini et al. (2019) suggested that the complex Na-K-Ti-rich rims on rutile in that same sample may have crystallized from infiltration and reaction with a fractionated Na-rich kimberlite melt. The latter seems more likely for the rocks in this study, given the widespread indications of kimberlite melt intrusion in the other xenoliths. Additionally, Kamenetsky et al. (2012) found Na-K-Ti-rich mineral phases formed at the interface of ilmenite megacrysts and trapped kimberlite melt intrusions from the Monastery kimberlite (South Africa). Thus, the authors showed that kimberlite melt reacting with Ti-rich phases can form such phases and that locally, at basal lithospheric depths, kimberlitic melts can evolve to form such minerals via reaction with suitable hosts.

4.3 Cryptic metasomatism of garnet and clinopyroxene

4.3.1 Garnet metasomatic agent(s)

Peridotitic garnets in this study have a range of chondrite-normalized REE patterns (Figure 3.6.2). The three basic REE_N pattern types found in cratonic peridotites worldwide are: highly sinusoidal (Type IV in this study), moderately sinusoidal (Type Ib and III in this study), and normal (Type Ia and II in this study) (Stachel and Harris, 2008). Garnets in cratonic peridotites with “normal” patterns (Type Ia and II) are typically found in sheared lherzolitic xenoliths that have equilibrated at high-T, and are less commonly observed in harzburgitic parageneses (Stachel et al., 2004). These patterns are consistent with those expected from garnet-facies melt residues, or produced by equilibration with a silicate melt (Pearson et al., 2003). Type Ia and II patterns occur in the pyroxene-free dunite, clinopyroxene dunites, and a pyroxene dunite, and typically correspond to areas in the garnets with G11 classification, but also include G9, G12, and G1 (Grütter et al., 2004). These garnets do not have a residual G10 signature that would be typical of dunites, therefore their REE_N patterns may indicate equilibration with a silicate melt.

Sinuous patterns are classified by Pearson et al. (2003) as having maxima in the MREE, $Sm_N > Dy_N$, and can have fairly flat HREE or $Yb_N > Er_N$. By this classification, Type Ib, III, and IV patterns in garnets in this study are considered sinuous. This pattern type is common in low-

T cratonic xenoliths (harzburgites), and diamond inclusion garnets with low Ca and high Cr, that have not equilibrated with clinopyroxene (Pearson et al., 2003, and references therein). The origin of these complex REE patterns is more contentious than garnets with normal REE_N patterns. One possibility is that sinuous patterns are a disequilibrium feature created by metasomatism of originally refractory garnets, which results in sinuous patterns from the different diffusion coefficients of REE in garnet (Hoal et al., 1994). Another hypothesis is that sinuous patterns could be produced by multi-stage melt depletion followed by metasomatism by a highly-fractionated metasomatic fluid with high LREE/HREE, such as CHO fluids (Stachel and Harris, 2008; Stachel et al., 1998). Stachel and Harris (2008) suggest that the transition from garnets with highly sinuous, to normal REE_N patterns correspond to a change from fluid to melt dominated metasomatism. Considering individual garnets with numerous pattern types in this study, the patterns with the highest degree of sinuosity are generally found in cores, patterns with lower degrees of sinuosity (Type III) are found in mantles, and Type Ia and II are found in rims. This could represent transitional metasomatism, where the cores with the highest degree of sinuosity preserve more ancient fluid metasomatism, and humped and normal patterns record a more recent transition to melt metasomatism. Type III (humped) patterns may simply be transitional between Type IV (sinusoidal), reflecting an increase in the degree of melt metasomatism, and Type I (normal) patterns represent the highest degree of melt-metasomatism.

A closer examination of the fluids or melts responsible for metasomatizing the garnets is possible through a combination of Y and Zr concentrations in garnets. Griffin and Ryan (1995) delineated fields that represent mantle processes recorded in garnet from their Zr-Y systematics, which were derived mainly from the Kaapvaal craton (Figure 4.3.1). The Zr-Y systematics of garnets in this study that are coupled with REE_N patterns having the highest degree of sinuosity (0411K and 0413B), have very low Y (< 3 ppm) relative to the other garnets in the suite. Xenolith 0413B plots in the "depleted" field of Griffin and Ryan (1995), and 0411K plots near the origin of the "fluid metasomatism" field, having slightly elevated Ti (45 ppm). These two xenoliths are the only two containing garnets with cores of G10-like characteristics that were analyzed for trace elements (Figure 3.3.4). Garnets in melt-free Chidliak peridotites studied by Kopylova et al. (2021) with the highest degree of sinuosity in their REE_N patterns also have "depleted" Zr-Y systematics. This field is consistent with garnets with sinuous REE patterns that reflect ancient metasomatism superimposed on a depleted protolith (Griffin et al., 1999). Most of the other REE_N pattern types in garnets in this study plot in the high-temperature melt metasomatism field. All five xenoliths with a Type IV pattern, have lower Y than their respective humped or normal patterns from within the same xenolith, and four have lower Zr. This implies the melt metasomatic agent(s) that produced the flat and humped REE_N patterns had high Zr and Y, and perhaps did not completely overprint the moderately sinusoidal patterns. This is also consistent with the garnet compositions reported by Kopylova et al. (2021). Xenoliths 0405C and 0411I are noteworthy because they have significantly higher Zr and Y relative to the rest of the suite. This could imply they experienced a much higher degree of melt metasomatism, or perhaps were metasomatized by a melt containing higher Zr and Y than the others.

Shu and Brey (2015) used the Ti/Eu versus Zr/Hf systematics of garnets from the Kaapvaal craton to differentiate garnets that had been metasomatized by carbonatite and kimberlite (Figure 4.3.2). All of the garnets in this study have superchondritic Zr/Hf ratios (i.e. > 37) and a large portion have superchondritic Ti/Eu ratios (i.e. > 7815). All of the CH-1, -7, and -44 garnets reported by Kopylova et al. (2021) have superchondritic Zr/Hf ratios, and most have superchondritic Ti/Eu ratios. However, most of their reported CH-7 garnets have sinuous REE_N patterns with subchondritic Ti/Eu ratios. Garnets in CH-6 peridotites reported by Kopylova et al. (2021), exclusively have subchondritic Ti/Eu, and variably sub- to superchondritic Zr/Hf ratios. The Kaapvaal craton garnets analyzed by Shu and Brey (2015) with superchondritic Ti/Eu ratios were attributed to Fe-Ti metasomatism of residual high Cr, low Ca mantle. This agrees well with the interpreted silicate-carbonate metasomatism model of the Chidliak mantle that Kopylova et al. (2019) propose, in which this style of metasomatic agent was enriched in Fe, Ti and Al. This is also consistent with the existence of the superchondritic Ti/Eu ratios in garnets from CH-1, -7, and -44 peridotites, and fits with the observation that the Ti-metasomatism was spatially restricted and did not affect the mantle sampled by CH-6 (Kopylova et al., 2019).

The garnets with the highest degree of sinuosity in their REE_N patterns (0413B and 0411K), and 0411F1 with a Type II REE_N pattern, plot in the kimberlite metasomatism fields, suggesting they were metasomatized by a kimberlite melt. Peridotites 0405C and 0411I, which have the highest Zr and Y in the suite, plot in the carbonatitic metasomatism field. This suggests they were metasomatized by a melt with fractionated Ti/Eu and relatively enriched Zr/Hf, which is consistent with carbonatitic melt. All sinusoidal patterns in garnets in this study, as well as garnets studied by Kopylova et al. (2021), have correspondingly lower Ti/Eu than humped and/or normal patterns within the same xenolith. This suggests the Fe-Ti metasomatism occurred shortly prior to entrainment, which did not allow trace elements to diffuse homogenously in the garnets.

An alternative model was proposed by Kopylova et al. (2021) to explain the elemental heterogeneity observed in the Chidliak garnets. These authors suggest that the composition for a metasomatic agent that was in equilibrium with the garnets cannot be estimated, in part due to chromatographic effects caused by porous reactive flow of the metasomatic agent(s). This process was first modelled by Navon and Stolper (1987). Chromatographic columns in the mantle describe metasomatic agents that percolate through the wall rocks, which are not in equilibrium with each other. Therefore, the metasomatic agent reacts with the wall rocks and can result in extreme fractionation of different elements as it migrates and crystallizes minerals. This process may well be the reason for the observed scatter in the compositions of cores and rims of some garnets. Examples of this compositional scatter in garnets are observed in their CaO-Cr_2O_3 systematics (Figure 3.3.4), Zr versus Y (ppm) (Figure 4.3.1), and Ti/Eu versus Zr/Hf (Figure 4.3.2). Additionally, le Roex and Class (2016) suggested that different REE_N patterns in garnet and clinopyroxene can be generated by porous reactive flow of alkaline silicate melts, rather than requiring compositionally extreme melts. However, by separating each garnet analysis into one of the five REE_N pattern types and averaging those patterns for each xenolith, the results from this study and Kopylova et al. (2021) clearly show that garnets in CH-1, -7, and -44 peridotites record metasomatism by a Ti-rich melt (Figure 4.3.2), in contrast to garnets from CH-6, which have subchondritic Ti/Eu and plot in the kimberlitic metasomatism field of Shu and Brey (2015) (Figure 4.3.2). Therefore, peridotitic garnets in CH-1, -7, and -44 record relatively recent metasomatism by a Ti-rich melt, and garnets with ancient sinuous REE_N patterns in those xenoliths, as well as CH-6, record metasomatism consistent with kimberlite melt. In contrast, there is minimal evidence for superchondritic Zr/Hf and low Ti/Eu in the Chidliak garnets, and hence limited evidence for metasomatism of the Chidliak mantle by carbonatitic melts (Shu and Brey, 2015).

Metamorphic garnets produced from highly-depleted spinel-facies peridotites should form garnets with low TiO_2, as Ti is incompatible during melting (e.g. Prytulak and Elliott, 2007). Thus, garnet in peridotites with TiO_2 > 0.04 wt% suggest they have been metasomatically enriched (Stachel and Harris, 2008). On a plot of pressure versus TiO_2 (wt%) (Figure 4.3.3), the garnets in CH-7 xenoliths from this study that equilibrated at pressures > 50 kbar, usually have TiO_2 > 0.04 wt%. Kopylova et al. (2019) found the entire interval from 55 to 65 kbar in CH-1, -7, and -44 to have garnets and clinopyroxene with elevated TiO_2. This high-Ti feature in the garnets matches with the large xenolith equilibration temperature variation over the depth interval found by Pell et al. (2013) and Kopylova et al. (2019). Additionally, garnets in this study with TiO_2 > 0.9 wt% correspond exclusively to peridotites with sheared textures.

This matches the findings of Kopylova et al. (2019) and their suggestion that this metasomatic event occurred shortly prior to kimberlite emplacement and caused shearing of the mantle.

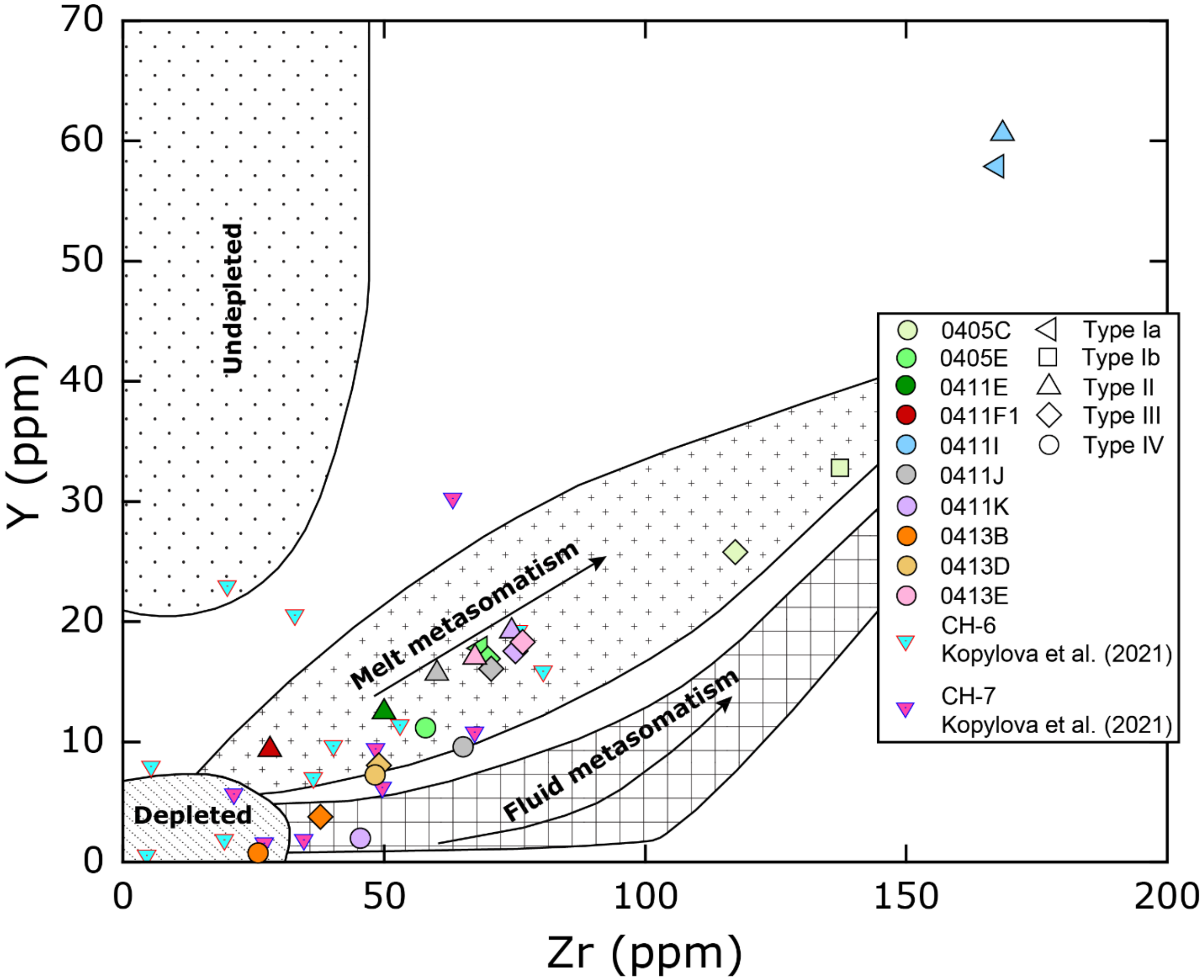

Figure 4.3.1 – Zr versus Y (ppm) plot of garnets from each REE$_N$ pattern type in xenoliths in this study compared with CH-6 and -7 garnet compositions from Kopylova et al. (2021) and fields of metasomatic trends after Griffin and Ryan (1995). Symbols correspond to the five chondrite-normalized REE patterns; data from Kopylova et al. (2021) are averaged REE$_N$ patterns from CH-6 and -7 xenoliths, but their symbology does not correspond to a REE$_N$ pattern type.

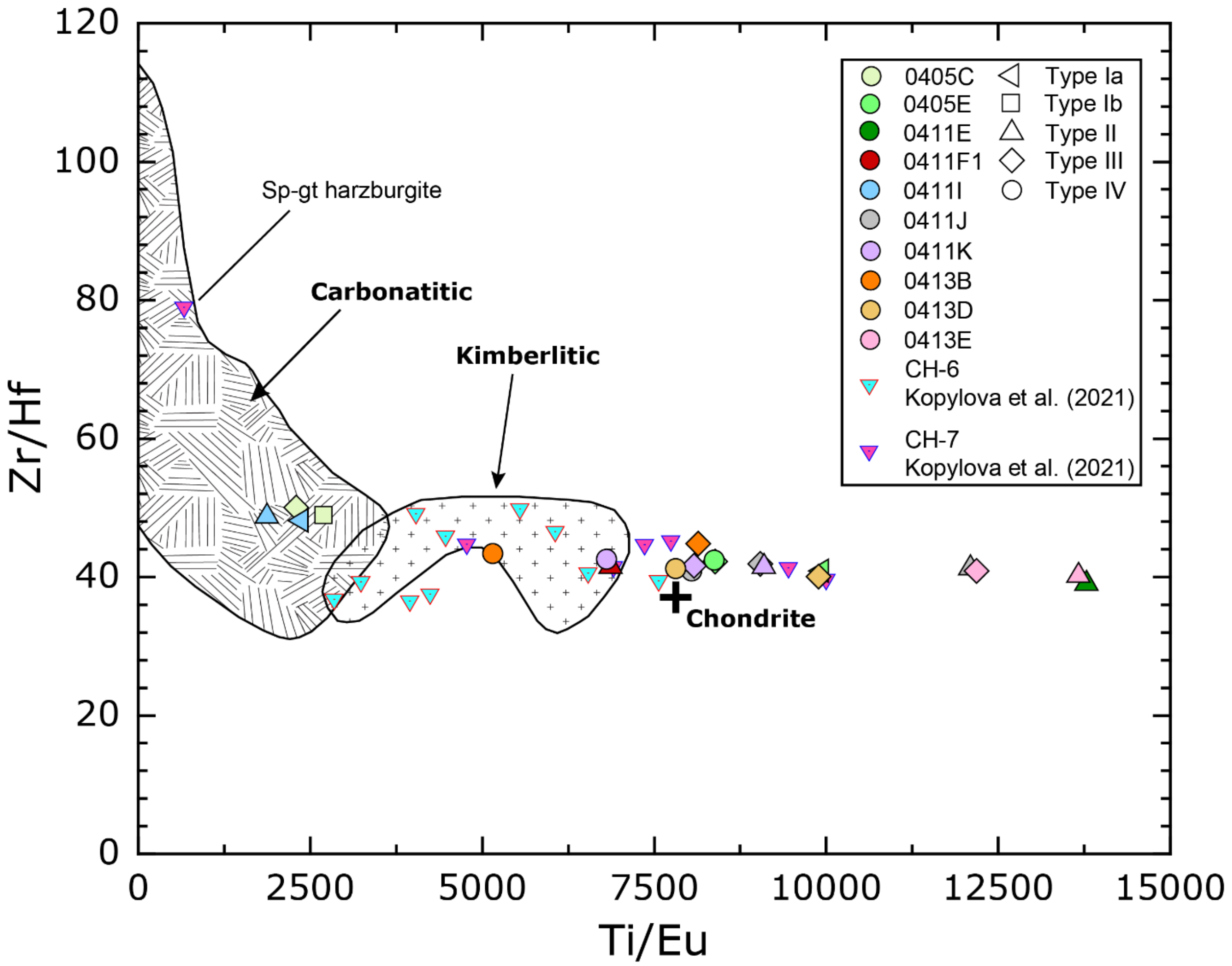

Figure 4.3.2 – Ti/Eu vs Zr/Hf plot of peridotitic garnets from this study compared with garnet data from Kopylova et al. (2021) and the fields of carbonatitic and kimberlitic metasomatism after Shu and Brey (2015). Symbols correspond to the five chondrite-normalized REE patterns. Data from Kopylova et al. (2021) are averaged REE_N patterns from each xenolith in CH-6 and -7 but their symbology does not correspond to a REE_N pattern type.

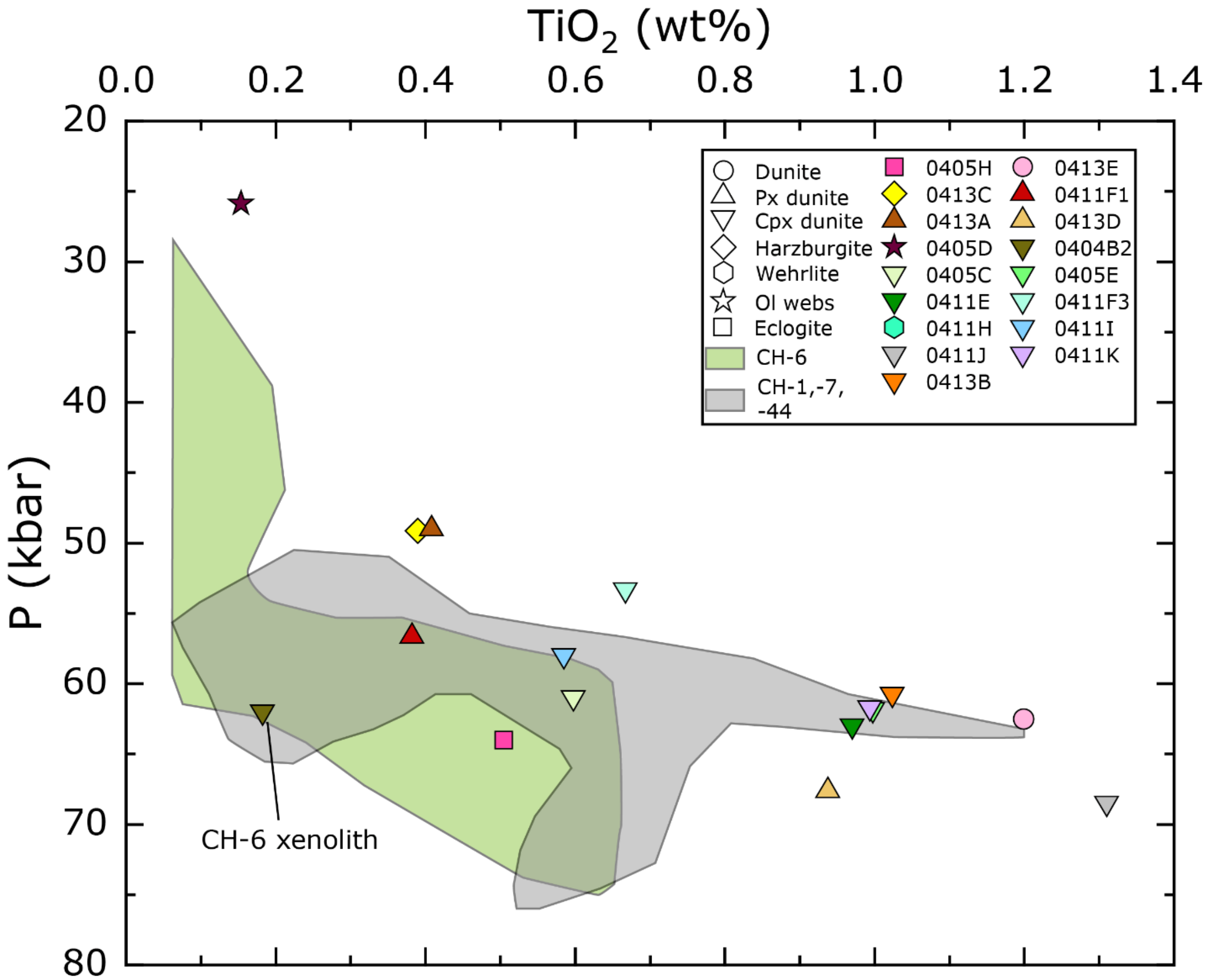

Figure 4.3.3 – TiO$_2$ (wt%) versus P (kbar) of garnets in this study compared to peridotitic garnets in xenoliths from CH-6 (green field), and CH-1, -7, -44 (grey field) (Kopylova et al., 2019).

4.3.2 Compositions of melts in equilibrium with garnet

Equilibrium melt compositions are calculated in this study using the trace element compositions in the CH-7 garnets, to constrain possible compositions of the metasomatic agent(s) with which the garnets equilibrated (Figure 4.3.4). Type Ia and II patterns, and Type Ib and III patterns are averaged together due to their similarities and to reduce complexity. The equilibrium melt compositions are calculated using the experimentally-determined partition coefficients (D) between carbonate-silicate melts and Cr-pyropes for lherzolites at 6 GPa and 1500 °C (Brey et al., 2008). The equilibrium melts are compared to the average trace element composition of CH-7 kimberlite whole-rocks and melt intrusions.

The REE$_N$ patterns for calculated melts in equilibrium with garnet are broadly similar to the composition of the CH-7 host kimberlite and CH-7 melt intrusions from Gd to Lu, but the calculated melts lack the near flat slope from Sm to Eu. The "kink" pattern observed in Y, Zr, and Hf is common to the calculated melts, kimberlite, and melt intrusions (Figure 4.3.4). In contrast, the Ba, Nb, La, and Ce are significantly higher in the CH-7 kimberlite and melt intrusions. Bussweiler et al. (2018) used the same set of partition coefficients to calculate melts in equilibrium with garnet megacrysts from Lac de Gras and found very similar discrepancies. This could be due to inaccuracies in the magnitude of the partition coefficients, as well as uncertainties associated with the composition of natural samples. Other experimentally-determined garnet-melt partition coefficients for carbonatites (Dasgupta et al., 2009) and basalt (Green et al., 2000) yield calculated equilibrium melts with much higher $LREE_N$, with negative slopes from La to Pr. This suggests that the discrepancy between the LREE and Ba of the calculated melts, kimberlite, and melt intrusions, could be due to uncertainties associated with the chosen partition coefficients, in addition to the type of melt for which the partition coefficients are used. Bussweiler et al. (2018) suggest instead that their calculated equilibrium melts using the partition coefficients from Brey et al. (2008), are a true reflection of a melt with distinctly lower contents of strongly-incompatible elements than the kimberlite. In this context, the trace element signature of the agent that metasomatized the CH-7 garnets could be viewed as similar to CH-7 kimberlite, but with distinctly lower LREE and Ba, and higher MREE and HREE. The calculated equilibrium melt for garnets with sinusoidal patterns is quite similar in shape, and concentration to many of the trace elements of the averaged CH-7 melt intrusions (Figure 4.3.4). Additionally, CH-7 garnets with sinusoidal REE_N patterns plot in the kimberlitic metasomatism field of Shu and Brey (2015) (Figure 4.3.2), and therefore calculated melt in equilibrium with such patterns would likely be compositionally similar to kimberlite.

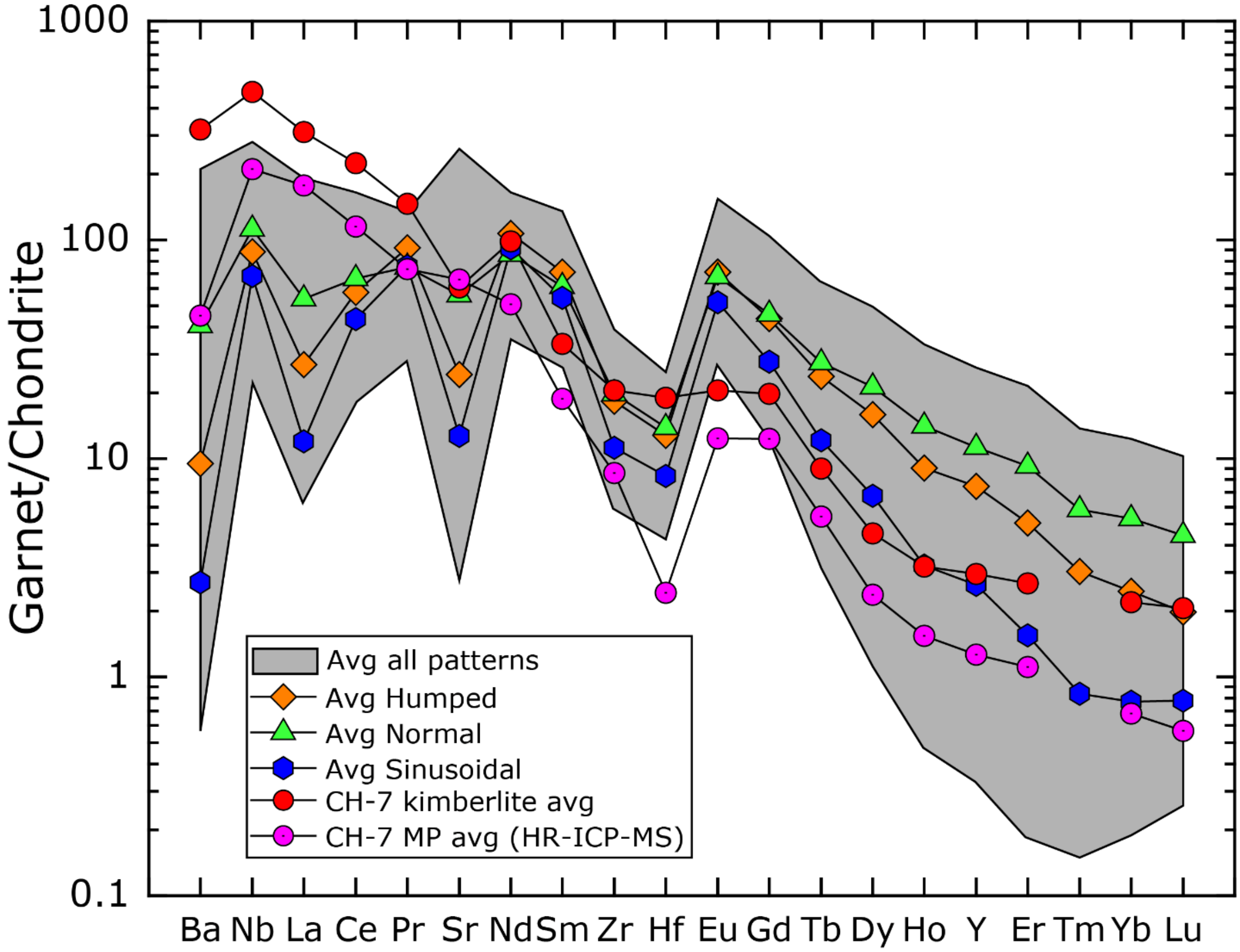

Figure 4.3.4 – Calculated equilibrium melts for garnets from each REE_N pattern type from this study. Type Ia and II compositions are averaged together for the “Avg Normal” composition, and Type Ib and III compositions are averaged together for the “Avg Humped” composition. The grey field represents the entire range of calculated equilibrium melts for each REE_N pattern shown in Figure 3.6.2 from each xenolith. Melt patterns are calculated using partition coefficients between carbonate-silicate melts and Cr-pyropes in lherzolites after Brey et al. (2008), and compared to the host kimberlite (CH-7) and melt pockets in CH-7 xenoliths.

4.3.3 Trace element equilibrium/disequilibrium between garnet and clinopyroxene

To assess the degree of chemical equilibrium between garnet and clinopyroxene in samples in this study, the trace element partitioning between both phases were calculated and compared to the experimental partition coefficients (*D*) between clinopyroxene and garnet in garnet pyroxenites of Zack et al. (1997) (Figure 4.3.5). The garnet compositions with different REE_N patterns in this study are averaged together because they have minimal variation in $D^{gt/cpx}$, except for Type IV patterns with the highest degree of sinuosity (0411J, 0411K, and 0413B), because they have significantly different $D^{gt/cpx}$. Figure 4.3.5 shows that garnet and clinopyroxene trace elements were not in equilibrium in 0405C and 0411I. Additionally, the garnets with the highest degrees of sinuosity in their REE_N were not in equilibrium with clinopyroxene, which is especially evident in 0411K and 0413B, which have significantly lower MREE and HREE relative to $D^{gt/cpx}$ values of Zack et al. (1997) . The remaining garnet-clinopyroxene pairs have $D^{gt/cpx}$ close to the values of Zack et al. (1997), except for Nb, LREE, Zr, and Hf, which are usually higher in this study. This could be due to the unsuitability of some of the experimentally determined $D^{gt/cpx}$ values for comparison to rocks in this study, since the experiments used garnet pyroxenites that equilibrated at different P-T conditions. However, the relatively similar calculated $D^{gt/cpx}$ of the MREE and HREE to the values of Zack et al. (1997) suggests these garnet-clinopyroxene pairs were in equilibrium.

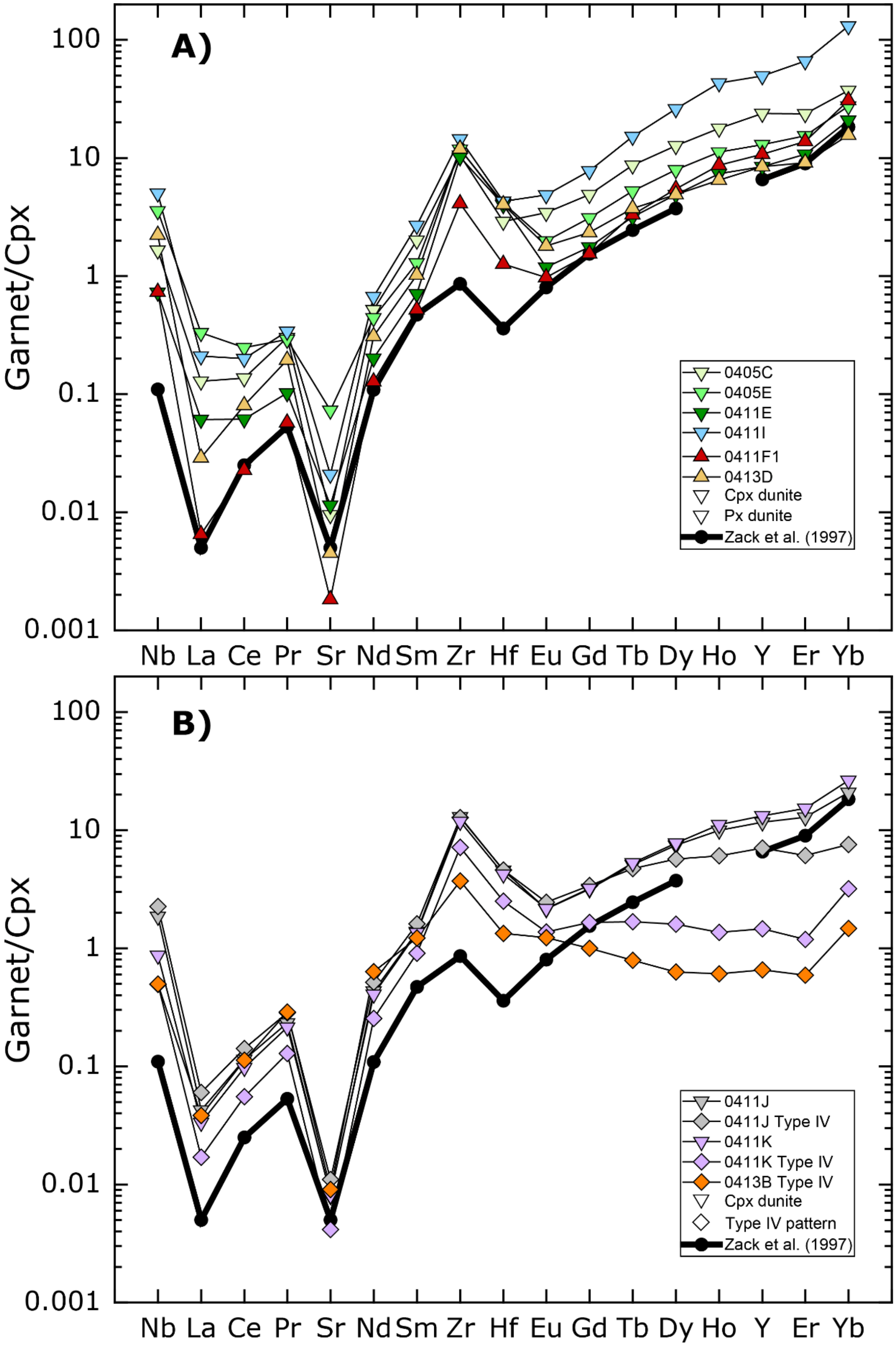

Figure 4.3.5 – Partitioning of trace elements between garnet and clinopyroxene for samples in this study, compared to equilibrium values of Zack et al. (1997).

4.3.4 Clinopyroxene equilibrium melts

To constrain the composition of a melt that the clinopyroxenes last equilibrated with (assuming equilibrium was achieved), equilibrium melts were calculated from the average clinopyroxene compositions in CH-7 clinopyroxene dunites and pyroxene dunites (Figure 4.3.6). Experimentally determined partition coefficients between carbonate-silicate melts and Cr-diopsides (Keshav et al., 2005) were used. The calculated equilibrium melts have similar MREE and HREE to CH-7 kimberlite and melt intrusions, although there are less calculated trace-elements for the equilibrium melt compositions due to a lack of partition coefficients. In contrast, the calculated equilibrium melts have significantly higher LREE (La to Eu), Sr, Ba, Zr, and Hf than CH-7 kimberlite and melt intrusions. Bussweiler et al. (2018) used the same set of partition coefficients to calculate melts that crystallized Cr-diopside megacrysts in Lac de Gras (Canada) kimberlites. They found very similar relative enrichments in Sr, LREE, Zr, and Hf in their calculated equilibrium melts, and suggested that the partition coefficients may have been inappropriate for the megacryst P-T-X conditions given the unrealistically high calculated LREE enrichment (e.g. Ce > 2000x chondrite). Since the calculated melts in equilibrium with clinopyroxenes in this study also have unrealistically high LREE-enrichment, the partition coefficients from Keshav et al. (2005) may be inappropriate for this study as well, or equilibrium, for these elements, was not closely approached.

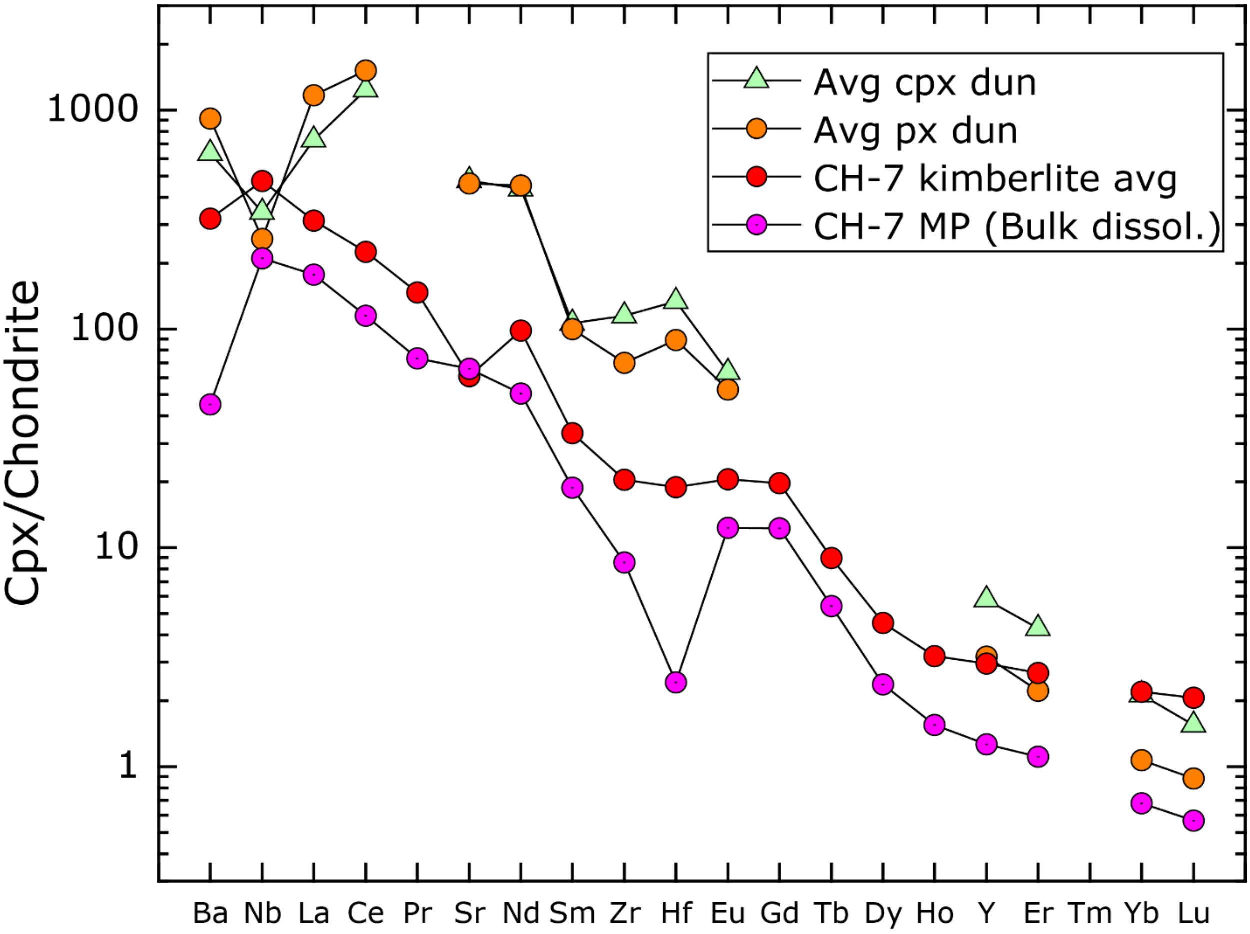

Figure 4.3.6 - Calculated equilibrium melts for averaged clinopyroxene compositions in clinopyroxene dunites and pyroxene dunites, compared with the composition of CH-7 kimberlite and melt pockets determined by bulk dissolution HR-ICP-MS. Melt patterns were calculated using partition coefficients between carbonate-silicate melts and Cr-diopsides after Keshav et al. (2005).

4.4 Late-stage metasomatism

4.4.1 Timing of late stage metasomatism in garnets

Three xenoliths have garnets that retained G10 chemistry in portions of some of their grain cores (0411K, 0413A, and 0413B). These garnets have considerable CaO and Cr_2O_3 variation, as well as in other oxides from core to rim. This suggests that a metasomatic event occurred on a timescale short enough that did not allow the grains to re-equilibrate with their parageneses before they were transported from the mantle to the crust. The time required for inwards diffusion of Ca in garnet can be calculated with $t = a^2/D$, where t is equal to time, D is the diffusion coefficient, and a is the radius. Considering a zoned garnet in 0413B with a concentric rim ~ 300 μm thick that has higher CaO than its core (Figure 4.4.1, garnet A), and using the diffusion coefficient of Ca in garnet of 0.15 x 10^{-13} cm^2/s that was determined using a pyrope-almandine couple at 40.0 Kbar and 1440 °C (Loomis et al., 1985), the diffusion time required to increase CaO in the 300 μm thick rim would be ~ 2000 years. This suggests a metasomatic event occurred in xenoliths with heterogenous garnets very shortly before, or perhaps during their entrainment and ascent in the kimberlite.

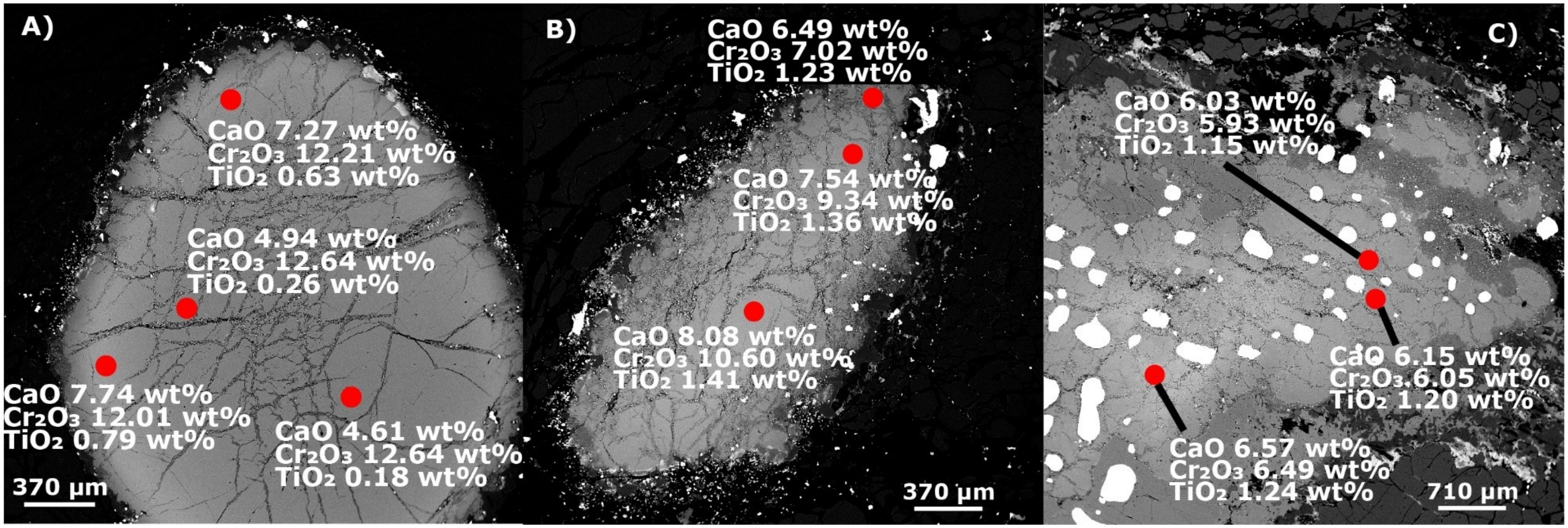

Figure 4.4.1 – BSE images of garnets in xenolith 0413B showing the CaO, Cr_2O_3, and TiO_2 content from individual EPMA analyses.

4.4.2 Xenoliths and mineral phases with evidence of late stage metasomatism

Similar "spongy", inclusion-rich rims on clinopyroxene grains that Kopylova et al. (2019) suggests are a product of decompression partial melting during ascent in the kimberlite, were observed on some of the grains. This study found spongy clinopyroxene rims to have higher Ca and lower Na and Al, which matches the results of Kopylova et al. (2019), except Cr, which was similar or slightly elevated in grains in this study. However, only three grains in two different xenoliths were analyzed to evaluate this. The thin overgrowths of clinopyroxene and potassic-richterite on orthopyroxene grains, rims of monticellite on clinopyroxene, and exsolution of phlogopite on clinopyroxene rims, are consistent with late-stage, low-pressure metasomatism during ascent in the kimberlite (e.g., Boyd, 1998; Boyd et al., 1997; Kopylova and Caro, 2004). Kopylova et al. (2019) suggests that the presence of monticellite rims on clinopyroxene constrain this metasomatic event to < 10 kbar. Kopylova et al. (2021) suggests the metasomatic agent that reacted with clinopyroxene to form monticellite rims, was CO_2-enriched fluids from the ascending kimberlite. Potassic richterite rims on orthopyroxene further constrain the metasomatic agent to containing appreciable K, Na and OH^-. These phases are consistent with the metasomatic agent being the host kimberlite and/or fluids related to the kimberlite that reacted with the orthopyroxene. Kopylova et al. (2021) further suggests that the monticellite rims on clinopyroxene formed by reaction with CO_2-rich fluids originating from the ascending kimberlite. They also add that the clinopyroxene overgrowths on orthopyroxene may have formed in the mantle, shortly prior to their entrainment in the kimberlite. These authors suggest the clinopyroxene rims could have formed on the orthopyroxene grains by the decarbonation reaction: $\text{Opx} + CaCO_3$ (liquid) $\rightarrow \text{Cpx} + CO_2$.

Garnet clinopyroxene dunite 0404B2 - the most heavily serpentinized xenolith in the suite - has a fabric defined by the parallel orientation of phlogopite and thin serpentine "stringers" containing fine-grained unidentified minerals. The olivine macrocrysts set in the kimberlite matrix in the same thin section are similarly serpentinized, suggesting serpentinization of the xenolith occurred during, or post-emplacement of the kimberlite. Discrete grains of potassic-richterite and phlogopite are both present in the xenolith, but do not appear to be in textural equilibrium with other minerals in the host xenolith, suggesting they may be late-stage metasomatic features or alteration products. The origin of the phlogopite may be kimberlite, or late-stage kimberlitic fluids, given its similar composition to kimberlite groundmass phlogopites (Figure 4.2.5).

Phlogopite and pargasite rims on pyroxenes and garnets are commonly observed in xenoliths entrained by kimberlite (e.g., Carswell, 1975). The textures of these phases suggest they are secondary. The phlogopite may have been produced by metasomatic reaction of the pyroxene grains, and kelyphite rims on garnet, with infiltrating kimberlite during their entrainment and ascent in the kimberlite. Similar rims of phlogopite in garnet kelphyite rims in contact with polymminerallic inclusions were reported by Bussweiler et al. (2016).

The tetraferriphlogopite grains in this study are both rims on phlogopite in contact with pyroxenes and melt, suggesting they are late-stage reaction products of the melt with pyroxene, which evolved to more oxidized (Fe^{3+}) composition during crystallization.

Chapter 5 : Conclusions

5.1 Key findings

A unique set of 21 mantle xenoliths containing crystallized melt pockets and veins were sampled from the CH-6 and -7 kimberlites, in the Chidliak kimberlite field, Baffin Island, Canada. Petrographic evidence in some of these xenoliths indicates that multiple melt intrusion events could have occurred. This is concluded from the occurrence of two different styles of melt pockets within the same xenolith. One has rounded edges in olivine porphyroclasts that appear brown in PPL. The other has non-rounded, irregular shaped edges that occur in-between grain boundaries in the xenoliths. In PPL they appear as fine grained "spotted" mixtures of white and black grains, or with relatively large sections that are texturally featureless and appear completely white to light green, or black to brown.

The mineralogy and compositions of phases in the crystallized melt pockets and veins in the Chidliak peridotites are consistent with kimberlite intrusion and crystallization. The compositions of some melt intrusion phases such as spinel group minerals, ilmenite, and perovskite, overlap with the host CH-6 and -7 kimberlite. Visible intrusion of the host kimberlite into xenoliths in the plane of a few thin sections provides additional support that the melt intrusion source was the host kimberlites. The major- and trace-element differences between the "bulk" melt pockets and the CH-6 and -7 kimberlite whole-rocks, is likely a result of deuteric alteration in the shallow subsurface following eruption, which resulted in serpentinization of the melt pockets, possible replacement of volcanic glass, and alteration of their bulk compositions.

Cr-rich spinels are rare in the melt intrusions; however, it suggests that the melt intrusions in these xenoliths are from an early phase of kimberlite that had the ability to crystallize the earliest-forming spinels observed in kimberlites. The lack of Cr-rich spinels in the other melt intrusions could be due to crystallization from a more evolved kimberlite. Alternatively, the intruding melts may have experienced fractional crystallization and chromatographic effects as they percolated through the host rocks. Thus, melt intrusions with the most primitive mineral compositions might yield the best information about the primitive kimberlite at depth. However, the rarity of fine-grained ilmenite in all the melt intrusions suggests that the intrusion event(s) did not occur until almost all the groundmass ilmenite and/or ilmenite megacrysts had crystallized in the kimberlite.

The host peridotites of the melt intrusions allow further insight into the nature of the Chidliak subcontinental lithospheric mantle. Modal metasomatism that occurred in the Chidliak mantle is dominated by anhydrous phases (clinopyroxene, ilmenite, rutile, jeppeite, freudenbergite, olivine), with the only evidence of hydrous-bearing modal mantle metasomatism represented by phlogopite and potassic-richterite in a single spinel-facies xenolith.

The high Cr_2O_3 compositions of most of the garnets in the peridotite xenoliths suggests they were produced via metamorphism from precursor peridotites that experienced partial melting in the spinel stability field. The shift from what were likely originally subcalcic G10 compositions to more calcic compositions (such as G9 and G12), may have occurred in conjunction with the metasomatic event(s) that re-introduced clinopyroxene into the xenoliths. The only garnets that were not completely overprinted by this metasomatic agent are those with cores with G10 compositions. These cores have highly sinuous REE_N patterns and are not in equilibrium with clinopyroxene based on their trace-element partition coefficients. Conversely, the rims show some equilibrium with clinopyroxene in these xenoliths. Trace element discrimination plots suggest these garnets with G10 composition were metasomatized by a kimberlitic agent. Most of the other garnets have a high Ti/Eu ratio, indicative of Fe-Ti melt metasomatism. Trace element discrimination plots of the two xenoliths with garnets that have core compositions exceeding 13 wt% CaO, have elevated Zr/Hf and lower Ti/Eu, suggesting they experienced carbonatitic melt metasomatism.

The Sr isotopic composition of the CH-6 and -7 kimberlite whole-rocks are more radiogenic relative to Sr isotopes from perovskite in those same kimberlites (Heaman et al., 2015). This indicates that their initial $^{87}Sr/^{86}Sr$ ratios may have been altered by a combination of crustal xenolith incorporation and hydrothermal alteration. The initial $^{143}Nd/^{144}Nd$ ratios appear to be more robust, given their relatively similar εNd values to CH-6 and -7 perovskite (Heaman et al., 2015).

This work has characterized the compositions and metasomatic history of Chidliak xenoliths containing melt pockets and veins. Melt pockets in these xenoliths record kimberlite infiltration that occurred shortly prior-to, or during mantle transit of CH-6 and -7 kimberlite magmas. The melt reacted with some pre-existing xenolith phases such as ilmenite, olivine, and orthopyroxene, however it did not introduce new minerals beyond the margins of the intrusions except potentially monticellite in a few cases. Furthermore, the garnets in the xenoliths appear to record metasomatism that occurred prior to the melt intrusion event, as the edge of most of their grains have high Ti/Eu, which is not consistent with the composition of the melt. These observations reveal how kimberlite melts intrude mantle wall-rocks and react with xenolith minerals over the short timespan of entrainment to eruption at surface.

5.2 Further work

Results presented as part of the current study provide new constraints on the nature of kimberlite melts that interact with mantle wall rocks prior-to, or during their entrainment and ascent to Earth's surface. However, there are several open research questions that require further study. At the time of writing, micromilled powders from melt pockets in CH-6 and -7 xenoliths are being analyzed for their Sr isotopic composition to compare to the CH-6 and -7 whole-rocks and perovskite data from those kimberlites (Heaman et al., 2015). If the initial isotopic compositions have been modified by deuteric alteration, the presence of perovskite in some of the melt intrusions could allow further micromilling and separation of perovskite fractions. This may facilitate U-Pb geochronology to constrain the precise age of the melt intrusion event(s), and allow Sr-Nd isotopic determination to compare with the CH-6 and -7 kimberlitic perovskite compositions from Heaman et al. (2015). This would help build a robust story of the mantle processes that occurred in the Chidliak mantle at, or near the time of kimberlite emplacement.

Bibliography

Abersteiner, A., Kamenetsky, V.S., Goemann, K., Golovin, A.V., Sharygin, I.S., Giuliani, A., Rodemann, T., Spetsius, Z.V. and Kamenetsky, M. (2019) Djerfisherite in kimberlites and their xenoliths: implications for kimberlite melt evolution. Contributions to Mineralogy and Petrology 174.

Abersteiner, A., Kamenetsky, V.S., Graham Pearson, D., Kamenetsky, M., Goemann, K., Ehrig, K. and Rodemann, T. (2018) Monticellite in group-I kimberlites: Implications for evolution of parental melts and post-emplacement CO2 degassing. Chemical Geology 478, 76-88.

Afanasyev, A.A., Melnik, O., Porritt, L., Schumacher, J.C. and Sparks, R.S.J. (2014) Hydrothermal alteration of kimberlite by convective flows of external water. Contributions to Mineralogy and Petrology 168.

Anzolini, C., Wang, F., Harris, G.A., Locock, A.J., Zhang, D., Nestola, F., Peruzzo, L., Jacobsen, S.D. and Pearson, D.G. (2019) Nixonite, Na2Ti6O13, a new mineral from a metasomatized mantle garnet pyroxenite from the western Rae Craton, Darby kimberlite field, Canada. American Mineralogist 104, 1336-1344.

Araújo, D.P., Griffin, W.L. and O'Reilly, S.Y. (2009) Mantle melts, metasomatism and diamond formation: Insights from melt inclusions in xenoliths from Diavik, Slave Craton. Lithos 112, 675-682.

Armstrong, J.P., Wilson, M., Barnett, R.L., Nowicki, T. and Kjarsgaard, B.A. (2004) Mineralogy of primary carbonate-bearing hypabyssal kimberlite, Lac de Gras, Slave Province, Northwest Territories, Canada. Lithos 76, 415-433.

Aulbach, S. (2020) Temperature-dependent Rutile Solubility in Garnet and Clinopyroxene from Mantle Eclogite: Implications for Continental Crust Formation and V-based Oxybarometry. Journal of Petrology 61.

Berg, G.W. and Allsopp, H.L. (1972) Low 87/Sr86Sr ratios in fresh South African kimberlites. Earth and Planetary Science Letters 16, 27-30.

Bernstein, S., Hanghøj, K., Kelemen, P.B. and Brooks, C.K. (2006) Ultra-depleted, shallow cratonic mantle beneath West Greenland: dunitic xenoliths from Ubekendt Ejland. Contributions to Mineralogy and Petrology 152, 335-347.

Birkett, T.C., McCandless, T.E. and Hood, C.T. (2004) Petrology of the Renard igneous bodies: host rocks for diamond in the northern Otish Mountains region, Quebec. Lithos 76, 475-490.

Bosi, F., Biagioni, C. and Pasero, M. (2019) Nomenclature and classification of the spinel supergroup. European Journal of Mineralogy 31, 183-192.

Boyd, F.R. (1998) The Origin of Cratonic Peridotites: A Major-Element Approach. International Geology Review 40, 755-764.

Boyd, F.R., Pokhilenko, N.P., Pearson, D.G., Mertzman, S.A., Sobolev, N.V. and Finger, L.W. (1997) Composition of the Siberian cratonic mantle: evidence from Udachnaya peridotite xenoliths. Contributions to Mineralogy and Petrology 128, 228-246.

Brey, G.P., Bulatov, V.K., Girnis, A.V. and Lahaye, Y. (2008) Experimental Melting of Carbonated Peridotite at 6-10 GPa. Journal of Petrology 49, 797-821.

Brey, G.P. and Köhler, T. (1990) Geothermobarometry in Four-phase Lherzolites II. New Thermobarometers, and Practical Assessment of Existing Thermobarometers. Journal of Petrology 31, 1353-1378.

Brey, G.P. and Shu, Q. (2018) The birth, growth and ageing of the Kaapvaal subcratonic mantle. Mineralogy and Petrology 112, 23-41.

Bussweiler, Y. (2017) Probing the Mantle Cargo of Kimberlites - A Geochemical Investigation of Different Mineral Components and Evaluation of their Potential as Petrogenetic and Exploration Tools. University of Alberta.

Bussweiler, Y., Brey, G.P., Pearson, D.G., Stachel, T., Stern, R.A., Hardman, M.F., Kjarsgaard, B.A. and Jackson, S.E. (2017) The aluminum-in-olivine thermometer for mantle peridotites — Experimental versus empirical calibration and potential applications. Lithos 272-273, 301-314.

Bussweiler, Y., Pearson, D.G., Stachel, T. and Kjarsgaard, B.A. (2018) Cr-rich megacrysts of clinopyroxene and garnet from Lac de Gras kimberlites, Slave Craton, Canada – implications for the origin of clinopyroxene and garnet in cratonic lherzolites. Mineralogy and Petrology 112, 583-596.

Bussweiler, Y., Stone, R.S., Pearson, D.G., Luth, R.W., Stachel, T., Kjarsgaard, B.A. and Menzies, A. (2016) The evolution of calcite-bearing kimberlites by melt-rock reaction: evidence from polymineralic inclusions within clinopyroxene and garnet megacrysts from Lac de Gras kimberlites, Canada. Contributions to Mineralogy and Petrology 171.

Canil, D. (1991) Experimental evidence for the exsolution of cratonic peridotite from high-temperature harzburgite. Earth and Planetary Science Letters 106, 64-72.

Carswell, D.A. (1975) Primary and secondary phlogopites and clinopyroxenes in garnet lherzolite xenoliths. Physics and Chemistry of the Earth 9, 417-429.

Carswell, D.A. and Gibb, F.G.F. (1987) Evaluation of mineral thermometers and barometers applicable to garnet lherzolite assemblages. Contributions to Mineralogy and Petrology 95, 499-511.

Chakhmouradian, A.R. and Mitchell, R.H. (2000) Occurence, alteration patterns and compositional variation of perovskite in kimberlites. The Canadian Mineralogist 38, 975-994.

Charlier, B.L.A., Ginibre, C., Morgan, D., Nowell, G.M., Pearson, D.G., Davidson, J.P. and Ottley, C.J. (2006) Methods for the microsampling and high-precision analysis of strontium and rubidium isotopes at single crystal scale for petrological and geochronological applications. Chemical Geology 232, 114-133.

Clement, C.R. (1982) A comparative geological study of some major kimberlite pipes in the Northern Cape and Orange Free State. University of Cape Town.

Cox, K., Smith, M. and Beswetherick, S. (1987) Textural studies of garnet lherzolites: evidence of exsolution origin from high-temperature harzburgites. Mantle xenoliths, 537-550.

Creighton, S. and Stachel, T. (2008) An empirical chromite classification for positive identification of kimberlite in diamond exploration, International Kimberlite Conference: Extended Abstracts.

Dasgupta, R., Hirschmann, M.M., McDonough, W.F., Spiegelman, M. and Withers, A.C. (2009) Trace element partitioning between garnet lherzolite and carbonatite at 6.6 and 8.6 GPa with applications to the geochemistry of the mantle and of mantle-derived melts. Chemical Geology 262, 57-77.

Dawson, J., Hill, P. and Kinny, P. (2001) Mineral chemistry of a zircon-bearing, composite, veined and metasomatised upper-mantle peridotite xenolith from kimberlite. Contributions to Mineralogy and Petrology 140, 720-733.

Dawson, J.B. (1984) Contrasting Types of Upper-Mantle Metasomatism?, in: Kornprobst, J. (Ed.), Developments in Petrology. Elsevier, pp. 289-294.

Dawson, J.B. and Smith, J.V. (1982) Upper-mantle amphiboles: a review. Mineralogical Magazine 45, 35-46.

Dawson, J.B. and Stephens, W.E. (1975) Statistical Classification of Garnets from Kimberlite and Associated Xenoliths. The Journal of Geology 83, 589-607.

Day, H.W. (2012) A revised diamond-graphite transition curve. 97, 52-62.

Desmons, J. and Smulikowski, W. (2007) High P/T metamorphic rocks. Metamorphic rocks. A classification and glossary of terms: recommendations by the IUGS Subcommission on the systematic on the metamorphic rocks, 1st edn. Cambridge University Press, Cambridge, 32-35.

Droop, G.T.R. (1987) A general equation for estimating Fe3+ concentrations in ferromagnesian silicates and oxides from microprobe analyses, using stoichiometric criteria. Mineralogical Magazine 51, 431-435.

Erlank, A. and Rickard, R. (1977) Potassic richterite bearing peridotites from kimberlite and the evidence they provide for upper mantle metasomatism, International Kimberlite Conference: Extended Abstracts, pp. 93-95.

Erlank, A.J. (1987) Evidence for mantle metasomatism in peridotite nodules from the Kimberley pipes, South Africa. In: Hawkesworth CJ and Menzies MA (eds.). Mantle Metasomatism, 221-311.

Foley, S.F., Barth, M.G. and Jenner, G.A. (2000) Rutile/melt partition coefficients for trace elements and an assessment of the influence of rutile on the trace element characteristics of subduction zone magmas. Geochimica et Cosmochimica Acta 64, 933-938.

Frey, F.A. and Green, D.H. (1974) The mineralogy, geochemistry and origin of Iherzolite inclusions in Victorian basanites. Geochimica et Cosmochimica Acta 38, 1023-1059.

Green, T.H., Blundy, J.D., Adam, J. and Yaxley, G.M. (2000) SIMS determination of trace element partition coefficients between garnet, clinopyroxene and hydrous basaltic liquids at 2–7.5 GPa and 1080–1200°C. Lithos 53, 165-187.

Griffin, W.L. and Ryan, C.G. (1995) Trace elements in indicator minerals: area selection and target evaluation in diamond exploration. Journal of Geochemical Exploration 53, 311-337.

Griffin, W.L., Shee, S.R., Ryan, C.G., Win, T.T. and Wyatt, B.A. (1999) Harzburgite to lherzolite and back again: metasomatic processes in ultramafic xenoliths from the Wesselton kimberlite, Kimberley, South Africa. Contributions to Mineralogy and Petrology 134, 232-250.

Grütter, H., Apter, D. and Kong, J. (1999) Crust–mantle coupling: evidence from mantle-derived xenocrystic garnets, Proceedings of the 7th International Kimberlite Conference. Red Roof Design Cape Town, pp. 307-313.

Grütter, H.S. (2009) Pyroxene xenocryst geotherms: Techniques and application. Lithos 112, 1167-1178.

Grütter, H.S., Gurney, J.J., Menzies, A.H. and Winter, F. (2004) An updated classification scheme for mantle-derived garnet, for use by diamond explorers☆. Lithos 77, 841-857.

Haggerty, S. and Boyd, F. (1975) Kimberlite inclusions in an olivine megacryst from Monastery, Kimberlite symposium. Cambridge.

Harley, S.L. (1984) An experimental study of the partitioning of Fe and Mg between garnet and orthopyroxene. Contributions to Mineralogy and Petrology 86, 359-373.

Harris, G.A., Pearson, D.G., Liu, J., Hardman, M.F., Snyder, D.B. and Kelsch, D. (2018) Mantle composition, age and geotherm beneath the Darby kimberlite field, west central Rae Craton. Mineralogy and Petrology 112, 57-70.

Harte, B. (1977) Rock Nomenclature with Particular Relation to Deformation and Recrystallisation Textures in Olivine-Bearing Xenoliths. The Journal of Geology 85, 279-288.

Harte, B. (1983) Mantle peridotites and processes—the kimberlite sample, UK volcanic studies group meeting, pp. 46-91.

Harte, B., Cox, K.G. and Gurney, J.J. (1975) Petrography and geological history of upper mantle xenoliths from the Matsoku kimberlite pipe, in: Ahrens, L.H., Dawson, J.B., Duncan, A.R., Erlank, A.J. (Eds.), Physics and Chemistry of the Earth. Pergamon, pp. 477-506.

Hasterok, D. and Chapman, D.S. (2011) Heat production and geotherms for the continental lithosphere. Earth and Planetary Science Letters 307, 59-70.

Heaman, L.M. (1989) The nature of the subcontinental mantle from SrNdPb isotopic studies on kimberlitic perovskite. Earth and Planetary Science Letters 92, 323-334.

Heaman, L.M. and Pearson, D.G. (2010) Nature and evolution of the Slave Province subcontinental lithospheric mantle. Canadian Journal of Earth Sciences 47, 369-388.

Heaman, L.M., Pell, J., Grütter, H.S. and Creaser, R.A. (2015) U–Pb geochronology and Sr/Nd isotope compositions of groundmass perovskite from the newly discovered Jurassic Chidliak kimberlite field, Baffin Island, Canada. Earth and Planetary Science Letters 415, 183-199.

Hoal, K.E.O., Hoal, B.G., Erlank, A.J. and Shimizu, N. (1994) Metasomatism of the mantle lithosphere recorded by rare earth elements in garnets. Earth and Planetary Science Letters 126, 303-313.

Hogberg, K., Stachel, T. and Stern, R.A. (2016) Carbon and nitrogen isotope systematics in diamond: Different sensitivities to isotopic fractionation or a decoupled origin? Lithos 265, 16-30.

Howarth, G.H. and Büttner, S.H. (2019) New constraints on archetypal South African kimberlite petrogenesis from quenched glass-rich melt inclusions in olivine megacrysts. Gondwana Research 68, 116-126.

Ionov, D.A., Griffin, W.L. and O'Reilly, S.Y. (1997) Volatile-bearing minerals and lithophile trace elements in the upper mantle. Chemical Geology 141, 153-184.

Jarosewich, E. and Boatner, L.A. (1991) Rare-Earth Element Reference Samples for Electron Microprobe Analysis. Geostandards Newsletter 15, 397-399.

Jarosewich, E. and MacIntyre, I.G. (1983) Carbonate reference samples for electron microprobe and scanning electron microscope analyses. Journal of Sedimentary Research 53, 677-678.

Jarosewich, E., Nelen, J.A. and Norberg, J.A. (1980) Reference Samples for Electron Microprobe Analysis*. Geostandards Newsletter 4, 43-47.

Jochum, K.P., Nohl, U., Herwig, K., Lammel, E., Stoll, B. and Hofmann, A.W. (2005) GeoReM: A New Geochemical Database for Reference Materials and Isotopic Standards. Geostandards and Geoanalytical Research 29, 333-338.

Jones, A.P., Smith, J.V. and Dawson, J.B. (1982) Mantle Metasomatism in 14 Veined Peridotites from Bultfontein Mine, South Africa. The Journal of Geology 90, 435-453.

Jordan, T.H. (1978) Composition and development of the continental tectosphere. Nature 274, 544-548.

Kamenetsky, V.S., Belousova, E.A., Giuliani, A., Kamenetsky, M.B., Goemann, K. and Griffin, W.L. (2014) Chemical abrasion of zircon and ilmenite megacrysts in the Monastery kimberlite: Implications for the composition of kimberlite melts. Chemical Geology 383, 76-85.

Kamenetsky, V.S., Kamenetsky, M.B., Golovin, A.V., Sharygin, V.V. and Maas, R. (2012) Ultrafresh salty kimberlite of the Udachnaya–East pipe (Yakutia, Russia): A petrological oddity or fortuitous discovery? Lithos 152, 173-186.

Keshav, S., Corgne, A., Gudfinnsson, G.H., Bizimis, M., McDonough, W.F. and Fei, Y. (2005) Kimberlite petrogenesis: Insights from clinopyroxene-melt partitioning experiments at 6 GPa in the CaO-MgO-Al2O3-SiO2-CO2 system. Geochimica et Cosmochimica Acta 69, 2829-2845.

Kinny, P.D. and Dawson, J.B. (1992) A mantle metasomatic injection event linked to late Cretaceous kimberlite magmatism. Nature 360, 726-728.

Kjarsgaard, B.A., Pearson, D.G., Tappe, S., Nowell, G.M. and Dowall, D.P. (2009) Geochemistry of hypabyssal kimberlites from Lac de Gras, Canada: Comparisons to a global database and applications to the parent magma problem. Lithos 112, 236-248.

Kopylova, M.G. and Caro, G. (2004) Mantle Xenoliths from the Southeastern Slave Craton: Evidence for Chemical Zonation in a Thick, Cold Lithosphere. Journal of Petrology 45, 1045-1067.

Kopylova, M.G., Ma, F. and Tso, E. (2021) Constraining carbonation freezing and petrography of the carbonated cratonic mantle with natural samples. Lithos, 106045.

Kopylova, M.G., Matveev, S. and Raudsepp, M. (2007) Searching for parental kimberlite melt. Geochimica et Cosmochimica Acta 71, 3616-3629.

Kopylova, M.G., Russell, J.K. and Cookenboo, H. (1999) Petrology of Peridotite and Pyroxenite Xenoliths from the Jericho Kimberlite: Implications for the Thermal State of the Mantle beneath the Slave Craton, Northern Canada. Journal of Petrology 40, 79-104.

Kopylova, M.G., Tso, E., Ma, F., Liu, J. and Pearson, D.G. (2019) The Metasomatized Mantle beneath the North Atlantic Craton: Insights from Peridotite Xenoliths of the Chidliak Kimberlite Province (NE Canada). Journal of Petrology 60, 1991-2024.

Krogh, E.J. (1988) The garnet-clinopyroxene Fe-Mg geothermometer — a reinterpretation of existing experimental data. Contributions to Mineralogy and Petrology 99, 44-48.

Kushiro, I. (1996) Partial melting of fertile mantle peridotite at high pressures: an experimental study using aggregates of diamond. Geophysical Monograph-American Geophysical Union 95, 109-122.

Lai, M.Y., Stachel, T., Breeding, C.M. and Stern, R.A. (2020) Yellow diamonds with colourless cores – evidence for episodic diamond growth beneath Chidliak and the Ekati Mine, Canada. Mineralogy and Petrology 114, 91-103.

Le Maitre, R.W., Streckeisen, A., Zanettin, B., Le Bas, M.J., Bonin, B. and Bateman, P. (2002) Igneous Rocks: A Classification and Glossary of Terms: Recommendations of the International Union of Geological Sciences Subcommission on the Systematics of Igneous Rocks, 2 ed. Cambridge University Press, Cambridge.

le Roex, A. and Class, C. (2016) Metasomatic enrichment of Proterozoic mantle south of the Kaapvaal Craton, South Africa: origin of sinusoidal REE patterns in clinopyroxene and garnet. Contributions to Mineralogy and Petrology 171.

Le Roex, A.P. (2003) Petrogenesis of Group I Kimberlites from Kimberley, South Africa: Evidence from Bulk-rock Geochemistry. Journal of Petrology 44, 2261-2286.

Liu, J., Pearson, G.D., Harris, G.A., Kopylova, M.G. and Tso, E. (2017) Age and evolution of the lithospheric mantle beneath southern Baffin Island, Nunavut, Canada. 11th International Kimberlite Conference Extended Abstract No. 11IKC-4584.

Locock, A.J. (2008) An Excel spreadsheet to recast analyses of garnet into end-member components, and a synopsis of the crystal chemistry of natural silicate garnets. Computers & Geosciences 34, 1769-1780.

Locock, A.J. and Mitchell, R.H. (2018) Perovskite classification: An Excel spreadsheet to determine and depict end-member proportions for the perovskite- and vapnikite-subgroups of the perovskite supergroup. Computers & Geosciences 113, 106-114.

Loomis, T.P., Ganguly, J. and Elphick, S.C. (1985) Experimental determination of cation diffusivities in aluminosilicate garnets. Contributions to Mineralogy and Petrology 90, 45-51.

Lugmair, G.W. and Marti, K. (1978) Lunar initial 143Nd/144Nd: Differential evolution of the lunar crust and mantle. Earth and Planetary Science Letters 39, 349-357.

Luth, R.W. (2009) The activity of silica in kimberlites, revisited. Contributions to Mineralogy and Petrology 158, 283-294.

Malarkey, J., Pearson, D.G., Kjarsgaard, B.A., Davidson, J.P., Nowell, G.M., Ottley, C.J. and Stammer, J. (2010) From source to crust: Tracing magmatic evolution in a kimberlite and a melilitite using microsample geochemistry. Earth and Planetary Science Letters 299, 80-90.

McDonough, W.F. and Sun, S.s. (1995) The composition of the Earth. Chemical Geology 120, 223-253.

McGuire, A.V., Francis, C.A. and Dyar, M.D. (1992) Mineral standards for electron microprobe analysis of oxygen. American Mineralogist 77, 1087-1091.

McKenzie, D. (1989) Some remarks on the movement of small melt fractions in the mantle. 95, 53-72.

Menzies, M.A. (1983) Mantle ultramafic xenoliths in alkaline magmas: evidence for mantle heterogeneity modified by magmatic activity. In: Hawkesworth CJ and Norry MJ (eds.). Shiva Publishing, Nantwich, UK.

Mitchell, R.H. (1986) Kimberlites: Mineralogy, Geochemistry, and Petrology. Plenum Press, New York, p. 442.

Mitchell, R.H. (1995) Kimberlites and orangeites, Kimberlites, Orangeites, and Related Rocks. Springer, pp. 1-90.

Mitchell, R.H. (2008) Petrology of hypabyssal kimberlites: Relevance to primary magma compositions. Journal of Volcanology and Geothermal Research 174, 1-8.

Mitchell, R.H., Bergman, S.C. and Bergman, S.C. (1991) Petrology of lamproites. Springer Science & Business Media.

Mitchell, R.H. and Chakhmouradian, A.R. (1998) Instability of perovskite in a CO2-rich environment; examples from carbonatite and kimberlite. The Canadian Mineralogist 36, 939-951.

Moore, R.O., Griffin, W.L., Gurney, J.J., Ryan, C.G., Cousens, D.R., Sie, S.H. and Suter, G.F. (1992) Trace element geochemistry of ilmenite megacrysts from the Monastery kimberlite, South Africa. Lithos 29, 1-18.

Morimoto, N. (1988) Nomenclature of Pyroxenes. Mineralogy and Petrology 39, 55-76.

Navon, O. and Stolper, E. (1987) Geochemical Consequences of Melt Percolation: The Upper Mantle as a Chromatographic Column. The Journal of Geology 95, 285-307.

Nichols, K. (2014) Diamond sources beneath the Hall Peninsula, Baffin Island, Nunavut: A preliminary assessment based on Chidliak diamonds University of Alberta.

Nickel, K.G. and Green, D.H. (1985) Empirical geothermobarometry for garnet peridotites and implications for the nature of the lithosphere, kimberlites and diamonds. Earth and Planetary Science Letters 73, 158-170.

Nielsen, T.F. and Sand, K.K. (2008) The Majuagaa kimberlite dike, Maniitsoq region, West Greenland: constraints on an Mg-rich silicocarbonatitic melt composition from groundmass mineralogy and bulk compositions. The Canadian Mineralogist 46, 1043-1061.

Nimis, P. and Grütter, H. (2010) Internally consistent geothermometers for garnet peridotites and pyroxenites. Contributions to Mineralogy and Petrology 159, 411-427.

Nimis, P. and Taylor, W.R. (2000) Single clinopyroxene thermobarometry for garnet peridotites. Part I. Calibration and testing of a Cr-in-Cpx barometer and an enstatite-in-Cpx thermometer. Contributions to Mineralogy and Petrology 139, 541-554.

Ottley, C.J., Pearson, D.G. and Irvine, G.J. (2003) A routine method for the dissolution of geological samples for the analysis of REE and trace elements via ICP-MS, Plasma Source Mass Spectrometry, pp. 221-230.

Paton, C., Hergt, J.M., Phillips, D., Woodhead, J.D. and Shee, S.R. (2007) New insights into the genesis of Indian kimberlites from the Dharwar Craton via in situ Sr isotope analysis of groundmass perovskite. Geology 35.

Pearson, D.G., Canil, D. and Shirey, S.B. (2003) 2.05 - Mantle Samples Included in Volcanic Rocks: Xenoliths and Diamonds, in: Holland, H.D., Turekian, K.K. (Eds.), Treatise on Geochemistry. Pergamon, Oxford, pp. 171-275.

Pearson, D.G., Canil, D. and Shirey, S.B. (2014) Mantle Samples Included in Volcanic Rocks, Treatise on Geochemistry, pp. 169-253.

Pearson, D.G. and Wittig, N. (2014) The Formation and Evolution of Cratonic Mantle Lithosphere – Evidence from Mantle Xenoliths, Treatise on Geochemistry, pp. 255-292.

Pearson, D.G., Woodhead, J. and Janney, P.E. (2019) Kimberlites as Geochemical Probes of Earth's Mantle. Elements 15, 387-392.

Pell, J., Grütter, H., Neilson, S., Lockhart, G., Dempsey, S. and Grenon, H. (2013) Exploration and Discovery of the Chidliak Kimberlite Province, Baffin Island, Nunavut: Canada's Newest Diamond District, Proceedings of 10th International Kimberlite Conference, pp. 209-227.

Pin, C., Briot, D., Bassin, C. and Poitrasson, F. (1994) Concomitant separation of strontium and samarium-neodymium for isotopic analysis in silicate samples, based on specific extraction chromatography. Analytica Chimica Acta 298, 209-217.

Pobric, V., Korolev, N. and Kopylova, M. (2020) Eclogites of the North Atlantic Craton: insights from the Chidliak eclogite xenoliths (S. Baffin Island, Canada). Contributions to Mineralogy and Petrology 175.

Pollack, H.N. and Chapman, D.S. (1977) On the regional variation of heat flow, geotherms, and lithospheric thickness. Tectonophysics 38, 279-296.

Prytulak, J. and Elliott, T. (2007) TiO2 enrichment in ocean island basalts. Earth and Planetary Science Letters 263, 388-403.

Ramsay, R.R. (1995) Geochemistry of diamond indicator minerals. University of Western Australia.

Roedder, E. (1984) Volume 12: Fluid Inclusions. Mineralogical Society of America.

Roeder, P.L. and Schulze, D.J. (2008) Crystallization of Groundmass Spinel in Kimberlite. Journal of Petrology 49, 1473-1495.

Ryan, C.G., Griffin, W.L. and Pearson, N.J. (1996) Garnet geotherms: Pressure-temperature data from Cr-pyrope garnet xenocrysts in volcanic rocks. Journal of Geophysical Research: Solid Earth 101, 5611-5625.

Schroeder-Frerkes, F., Woodland, A.B., Uenver-Thiele, L., Klimm, K. and Knapp, N. (2016) Ca-Eskola incorporation in clinopyroxene: limitations and petrological implications for eclogites and related rocks. Contributions to Mineralogy and Petrology 171.

Schulze, D.J. (1985) Evidence for Primary Kimberlitic Liquids in Megacrysts from Kimberlites in Kentucky, U.S.A. The Journal of Geology 93, 75-79.

Schulze, D.J. (1989) Constraints on the abundance of eclogite in the upper mantle. Journal of Geophysical Research: Solid Earth 94, 4205-4212.

Schulze, D.J. (1995) Low-Ca garnet harzburgites from Kimberley, South Africa: Abundance and bearing on the structure and evolution of the lithosphere. Journal of Geophysical Research: Solid Earth 100, 12513-12526.

Schulze, D.J. (1997) The significance of eclogite and Cr-poor megacryst garnets in diamond exploration. Exploration and Mining Geology 4, 349-366.

Scott, D.J. (1999) U-Pb geochronology of the eastern Hall Peninsula, southern Baffin Island, Canada: a northern link between the Archean of West Greenland and the Paleoproterozoic Torngat Orogen of northern Labrador. Precambrian Research 93, 5-26.

Scott Smith, B.H., Nowicki, T.E., Russell, J.K., Webb, K.J., Mitchell, R.H., Hetman, C.M., Harder, M., Skinner, E.M.W. and Robey, J.A. (2013) Kimberlite Terminology and Classification, Proceedings of 10th International Kimberlite Conference, pp. 1-17.

Scrivner, A., Vance, D. and Rohling, E. (2004) New neodymium isotope data quantify Nile involvement in Mediterranean anoxic episodes. Geology 32.

Shimizu, N. (1999) Young geochemical features in cratonic peridotites from southern Africa and Siberia. Mantle petrology: field observations and high pressure experimentation. 6, 47-55.

Shu, Q. and Brey, G.P. (2015) Ancient mantle metasomatism recorded in subcalcic garnet xenocrysts: Temporal links between mantle metasomatism, diamond growth and crustal tectonomagmatism. Earth and Planetary Science Letters 418, 27-39.

Simon, N. (2003) The origin of garnet and clinopyroxene in “depleted” Kaapvaal peridotites. Lithos 71, 289-322.

Skinner, E.M.W. (1986) Contrasting Group 1 and Group 2 kimberlite petrology: Towards a genetic model for kimberlites. Fourth International Kimberlite Conference: Extended Abstracts 4, 202-204.

Skinner, E.M.W. and Marsh, J.S. (2004) Distinct kimberlite pipe classes with contrasting eruption processes. Lithos 76, 183-200.

Smith, C.B. (1983) Pb, Sr and Nd isotopic evidence for sources of southern African Cretaceous kimberlites. Nature 304, 51-54.

Sobolev, N.V., Lavrent'ev, Y.G., Pokhilenko, N.P. and Usova, L.V. (1973) Chrome-rich garnets from the kimberlites of yakutia and their parageneses. Contributions to Mineralogy and Petrology 40, 39-52.

Soltys, A., Giuliani, A. and Phillips, D. (2020) Apatite compositions and groundmass mineralogy record divergent melt/fluid evolution trajectories in coherent kimberlites caused by differing emplacement mechanisms. Contributions to Mineralogy and Petrology 175.

Soto, J. and Soto, V. (1995) PTMafic (v. 2.0): Software package for thermometry, barometry, and activity calculations in mafic rocks using an IBM-compatible computer. Computers & Geosciences 21, 619-652.

Stachel, T., Aulbach, S., Brey, G.P., Harris, J.W., Leost, I., Tappert, R. and Viljoen, K.S. (2004) The trace element composition of silicate inclusions in diamonds: a review. Lithos 77, 1-19.

Stachel, T. and Harris, J.W. (2008) The origin of cratonic diamonds — Constraints from mineral inclusions. Ore Geology Reviews 34, 5-32.

Stachel, T., Viljoen, K.S., Brey, G. and Harris, J.W. (1998) Metasomatic processes in lherzolitic and harzburgitic domains of diamondiferous lithospheric mantle: REE in garnets from xenoliths and inclusions in diamonds. Earth and Planetary Science Letters 159, 1-12.

Takahashi, E., Shimazaki, T., Tsuzaki, Y. and Yoshida, H. (1993) Melting study of a peridotite KLB-1 to 6.5 GPa, and the origin of basaltic magmas. Philosophical Transactions of the Royal Society of London. Series A: Physical and Engineering Sciences 342, 105-120.

Taylor, W.R. (1998) An experimental test of some geothermometer and geobarometer formulations for upper mantle peridotites with application to the thermobarometry of fertile Iherzolite and garnet websterite. Neues Jahrb. Mineral.-Abh. 172, 381-408.

van Achterbergh, E., Griffin, W.L., Ryan, C.G., O'Reilly, S.Y., Pearson, N.J., Kivi, K. and Doyle, B.J. (2002) Subduction signature for quenched carbonatites from the deep lithosphere. Geology 30, 743-746.

van Achterbergh, E., Griffin, W.L., Ryan, C.G., O'Reilly, S.Y., Pearson, N.J., Kivi, K. and Doyle, B.J. (2004) Melt inclusions from the deep Slave lithosphere: implications for the origin and evolution of mantle-derived carbonatite and kimberlite. Lithos 76, 461-474.

Vance, D. and Thirlwall, M. (2002) An assessment of mass discrimination in MC-ICPMS using Nd isotopes. Chemical Geology 185, 227-240.

Waterton, P., Pearson, D.G., Mertzman, S.A., Mertzman, K.R. and Kjarsgaard, B.A. (2020) A Fractional Crystallization Link between Komatiites, Basalts, and Dunites of the Palaeoproterozoic Winnipegosis Komatiite Belt, Manitoba, Canada. Journal of Petrology 61.

Weis, D., Kieffer, B., Maerschalk, C., Barling, J., de Jong, J., Williams, G.A., Hanano, D., Pretorius, W., Mattielli, N., Scoates, J.S., Goolaerts, A., Friedman, R.M. and Mahoney, J.B. (2006) High-precision isotopic characterization of USGS reference materials by TIMS and MC-ICP-MS. Geochemistry, Geophysics, Geosystems 7, n/a-n/a.

Whalen, J.B., Wodicka, N., Taylor, B.E. and Jackson, G.D. (2010) Cumberland batholith, Trans-Hudson Orogen, Canada: Petrogenesis and implications for Paleoproterozoic crustal and orogenic processes. Lithos 117, 99-118.

Willcox, A., Buisman, I., Sparks, R.S.J., Brown, R.J., Manya, S., Schumacher, J.C. and Tuffen, H. (2015) Petrology, geochemistry and low-temperature alteration of lavas and pyroclastic rocks of the kimberlitic Igwisi Hills volcanoes, Tanzania. Chemical Geology 405, 82-101.

Wilshire, H. and Trask, N. (1971) Structural and textural relationships of amphibole and phlogopite in peridotite inclusions, Dish Hill, California. American Mineralogist: Journal of Earth and Planetary Materials 56, 240-255.

Wyatt, B.A., Baumgartner, M., Anckar, E. and Grutter, H. (2004) Compositional classification of "kimberlitic" and "non-kimberlitic" ilmenite. Lithos 77, 819-840.

Wyatt, B.A. and Lawless, P.J. (1984) Ilmenite in polymict xenoliths from Bultfontein and De Beers Mines, South Africa. Developments in Petrology 11, 43-56.

Xia, X. (2018) Mineral inclusions in diamonds from Chidliak (Nunavut, Canada): constraining diamond substrates. University of Alberta

Xu, Y., Pearson, D.G., Harris, G.A., Kopylova, M.G., Tso, E. and Liu, J. (2021) Age and provenance of the lithospheric mantle beneath the Chidliak kimberlite province, southern Baffin Island: Implications for the evolution of the North Atlantic Craton. Lithos 390-391.

Yavuz, F. (2013) WinPyrox: A Windows program for pyroxene calculation classification and thermobarometry. American Mineralogist 98, 1338-1359.

Zack, T., Foley, S.F. and Jenner, G.A. (1997) A consistent partition coefficient set for clinopyroxene, amphibole and garnet from laser ablation microprobe analysis of garnet pyroxenites from Kakanui, New Zealand. Neues Jahrbuch fur Mineralogie, Abhandlungen 172, 23-41.

Ziberna, L., Nimis, P., Kuzmin, D. and Malkovets, V.G. (2016) Error sources in single-clinopyroxene thermobarometry and a mantle geotherm for the Novinka kimberlite, Yakutia. American Mineralogist 101, 2222-223

Appendix A

A.1 Analytical conditions and standards

Table A.1 – EPMA analytical conditions and standards.

Standard material	Oxide	LLD (oxide wt%)	Crystal	Peak (s)	Minerals
1. Frank Smith pyrope garnet	SiO_2	0.02	TAP	20-40	Gt, Phl, Ap, MP
	Al_2O_3	0.01	TAP	20-40	Gt, Ol, Cpx, Opx, Oxides, Pvs
	MgO	0.02	TAP	20-40	Gt, Oxides, Phl, Amph, Ap, MP, Pvs
2. Fo90.5	SiO_2	0.02	TAP	20-40	Ol, Mtc, Cpx, Opx, Oxides
	MgO	0.02	TAP	20-40	Ol, Mtc, Cpx, Oxides
3. $CaMgSi_2O_6$ diopside Wakefield	SiO_2	0.02	TAP	20-40	Mtc, Cpx, Opx, Volatiles
	MgO	0.02	TAP	20-40	Mtc, Cpx, Opx
	CaO	0.01	PET	20-40	Ol, Mtc, Cpx, Opx, Oxides, Volatiles, MP
4. Enstatite $Mg_2Si_2O_6$	SiO_2	0.01	TAP	20-40	Opx
	MgO	0.01	TAP	20-40	Opx
5. TiO_2 Rutile MTI	TiO_2	0.02	PET	20-40	Gt, Ol, Mtc, Cpx, Opx, Oxides, Volatiles, MP, Pvs
6. $FeTiO_3$ Ilmenite 96189	TiO_2	0.02	PET	20-30	Gt, Sp, Il, Rt
7. $ZnAl_2O_4$ gahnite H111989	ZnO	0.02	LIF	20-30	Gt, Ol, Cpx, Opx, Oxides, Amph, Phl
	Al_2O_3	0.02	TAP	20-40	Oxides
8. Willemite Zn_2SiO_4	ZnO	0.02	LIF	20	Gt, Ol, Cpx, Opx, Oxides
9. Plagioclase (labradorite) 115900	Al_2O_3	0.03	TAP	20-30	Ol, Mtc, Cpx, Opx, Oxides, MP, Amph, Phl
	CaO	0.01	PET	20-40	Gt, Ol, Oxides, Amph, Phl
10. V vanadium Alfa	V_2O_3	0.02	PET	20-30	Ol, Mtc, Cpx, Opx, Oxides, Amph, Phl
11. Cr_2O_3 chromium oxide Alfa	Cr_2O_3	0.04	PET	20-40	Gt, Ol, Mtc, Cpx, Opx, Oxides, Volatiles, MP
12. Gore garnet	FeO	0.02	LIF	20	Gt, Amph, Phl
13.Fe_2SiO_4 fayalite Rockport	FeO	0.01	LIF	20-30	Gt, Ol, Mtc, Cpx, Opx, Oxides, Volatiles, MP, Pvs

14. Hematite Fe_2O_3 Elba	FeO	0.03	LIF	20	Oxides, Ap
15. Siderite	FeO	0.02	LIF	30	Volatiles
16. $Mg_{0.97}Al_{2.02}O_4$ spinel MTI	Al_2O_3	0.02	TAP	40	Sp
	MgO	0.03	TAP	30	Sp
17. Ni nickel Alfa	NiO	0.02	LIF	20-30	Gt, Ol, Cpx, Opx, Oxides, Volatiles, MP
18. Strontianite	SrO	0.03	TAP	30	Carb, Hydrous phases, Ap
19. $SrTiO_3$	SrO	0.06	TAP	20-30	Oxides, Ap, Volatiles, Pvs
20. Barite Ba_SO_4	BaO	0.10	PET	20	Oxides
21. $BaSi_2O_5$ Sanbornite, Fresno	BaO	0.07	PET	20-30	Oxides, Ap, Pvs
22. K-253 NIST RM glass Ba Mn Zn Si Co Cu	BaO	0.15	PET	30	Volatiles
23. Niobium, Nb - ESPI	Nb_2O_5	0.04	PET	20	Gt, Ol, Cpx, Opx, Oxides
		0.07	PET	30	Pvs
24. $NaAlSi_3O_8$ albite VA 131705	Na_2O	0.02	TAP	20-50	Gt, Ol, Mtc, Cpx, Opx, Oxides, Volatiles, MP, Pvs
25. $KAlSi_3O_8$ sanidine Itrongay	K_2O	0.01	PET	20-40	Gt, Ol, Mtc, Cpx, Opx, Oxides, Volatiles, MP, Pvs
26. $(Mn,Fe)_3Al_2Si_3O_{12}$ spessartine, Navegadora Mine	MnO	0.01	LIF	20	Gt, Ol, Mtc, Cpx, Opx, Oxides, Volatiles
27. Spessartine Little 3	MnO	0.02	LIF	20-30	Gt, Ol, Mtc, Cpx, Opx, Oxides, Volatiles
28. Calcite	CaO	0.01	PET	30	Carbonates
29. Dolomite	MgO	0.02	TAP	30	Carbonates
30. MgO Periclase	MgO	0.02	TAP	30	Hydrous phases
31. CaSiO3 wollastonite NY	CaO	0.02	PET	30	Pvs
32. Thorianite	ThO_2	0.07	PET	30	Pvs
33. $LaPO_4$	La_2O_3	0.05	LIF	30	Pvs
34. $PrPO_4$	Pr_2O_3	0.07	LIF	30	Pvs
35. $NdPO_4$	Nd_2O_3	0.07	LIF	30	Pvs
36. $CePO_4$	Ce_2O_3	0.05	LIF	30	Ap, Pvs
37. Tephroite Mn_2SiO_4	MnO	0.03	LIF	30	Ap
38. Tugtupite	Na_2O	0.02	TAP	30	Ap

	Cl	0.01	PET	30	Ap
39.Fluorapatite $Ca_5(PO_4)_3F$	P_2O_5	0.03	PET	30	Ap
	CaO	0.02	PET	30	Ap
40. Anhydrite ON $CaSO_4$	SO_3	0.02	PET	30	Ap
41. Apatite, Durango	F	0.03	PC0	120	Ap
	P_2O_5	0.03	PETH	20	Gt, Ol, Cpx, Opx, Oxides

Combined off-peak count times are equal to on-peak count times for each element. Melt pocket grid (MP grid) on-peak count times for each element was 10 s.

Amph = amphibole, Ap = apatite, Cpx = clinopyroxene, Gt = garnet, Il = ilmenite, Mtc = monticellite, MP = melt pocket grid, Ol = olivine, Opx = orthopyroxene, Pvs = perovskite, Rt = rutile, Sp = spinel, Volatiles = carbonates and hydrous phases

1. Frank Smith pyrope garnet: Frank Smith kimberlite, South Africa. Royal Ontario Museum collection.
2. Olivine: Harvard collection, Fo90.5.
3. Diopside: Wakefield, Quebec, Canada. Astimex (http://astimex.com/com/catalog/min.html).
4. Enstatite: Enstatite H131709 from Harvard collection (Sri Lanka). (McGuire et al., 1992).
5. Rutile: synthetic rutile standard from MTI corporation (http://www.mtixtl.com/tio2substrates.aspx)
6. Ilmenite: FeTiO3 ilmenite from Ilmen Mountains, Miask, Russia. USNM 96189.
7. Gahnite: Natural gahnite, #111989 Harvard collection.
8. Willemite Zn2SiO4: Willemite from Franklin, NJ, USA.
9. Plagioclase: Labradorite from Lake County, Oregon, USA. Sample ID USNM 115900. Similar to Jarosewich et al. (1980).
10. Vanadium: Synthetic vanadium metal wire, 99.8% purity, 0.5mm diameter. Alfa Aesar order 4009967.
11. Chromium oxide: Synthetic Cr_2O_3, 99.6% purity (metals basis). Alfa Aesar 36258 Lot I11T052.
12. Gore garnet: Barton Mine, NY, USA.
13. Fayalite: Fe_2SiO_4 fayalite from Rockport MA, USA. USNM 85276 (Jarosewich et al., 1980).
14. Hematite Fe_2O_3 Elba: Hematite from Elba, Rio Marina Mine, Italy Fe_2O_3.
15. Siderite: EPS3 Siderite, USNM R2460 (Jarosewich and MacIntyre, 1983).
16. $Mg_{0.97}Al_{2.02}O_4$ spinel: Synthetic spinel from MTI (https://www.mtixtl.com/mgal2o4spinel.aspx).
17. Nickel: Synthetic nickel wire, 99.98% purity. Alfa Aesar stock #43132, lot #F15S013.
18. Strontianite: EPS3 Strontianite, USNM R10065.
19. $SrTiO_3$: Strontium titanate (synthetic tausonite), MTI Corp.
20. Barite: U of A collection.
21. $BaSi_2O_5$: Sanbornite from Rush Creek, Fresno, CA, USA; from Excalibur Minerals Co.
22. K-253 NIST RM glass Ba Mn Zn Si Co Cu: NIST reference glass K-253.
23. Niobium, Nb – ESPI: Niobium foil, 25 microns thick. From ESPI, 99.9% purity, stock K3654J, Lot E1986.
24. $NaAlSi_3O_8$ albite VA 131705: Albite 131705, from the Harvard Mineralogical Museum (McGuire et al., 1992).
25. $KAlSi_3O_8$ sanidine Itrongay: Fe-bearing K-feldspar, similar to Ackermann et al., (2005).
26. $(Mn,Fe)_3Al_2Si_3O_{12}$ spessartine: Spessartine from the Navegadora Mine, Brazil.
27. Spessartine Little 3: Spessartine from the Little 3 pegmatite, California.
28. Calcite: USNM 136321 (Jarosewich and MacIntyre, 1983)

29. Dolomite: USNM 10057
30. MgO Periclase: Synthetic MgO, > 99.95% purity from MTI (https://www.mtixtl.com/MG-a-050505S1.aspx)
31. CaSiO3 wollastonite NY: Wollastonite from New York state (Dr. Tom Chacko)
32. Thorianite: synthetic thorium oxide ceramic from the standards library of the SPI Supplies and the C. M. Taylor Company.
33. LaPO4:Synthesized by L. Boatner (Jarosewich and Boatner, 1991)
34. PrPO4: Synthesized by John Hanchar, Memorial University of Newfoundland.
35. NdPO4: Synthesized by John Hanchar, Memorial University of Newfoundland.
36. CePO4: Synthesized by John Hanchar, Memorial University of Newfoundland.
37. Tephroite Mn_2SiO_4: Synthesized by John Hanchar, Memorial University of Newfoundland.
38. Tugtupite: Tugtupite from Ilimaussaq (Narsaq), Greenland. Obtained from Attard's Minerals. Ideal composition for $Na_4AlBeSi_4O_{12}Cl$.
39. Fluorapatite $Ca_5(PO_4)3F$: Synthesized by John Hanchar, Memorial University of 37. Newfoundland.
40. Anhydrite ON CaSO4: Anhydrite from McLaren's phosphate mine, Lot 4, Concession 8, North Burgess township, Lanark County, Ontario (near Perth).
41. Apatite, Durango: Apatite from Cerro de Mercado, Durango, Mexico (Jarosewich et al., 1980).

Table A.2 – LA-ICP-MS setup and primary and secondary standards used for each analyte.

Analyte	**Gt**	**Cpx**	**Opx**	**Ol**	**Melt pockets**	**Kimberlite groundmass**
Spot size (µm)	193	193	285	285	285, 193	90
On-Sample Fluence (J.cm^{-2})	3.63	3.63	3.41	3.38	3.55	3.77
Repetition rate (Hz)	5	5	5	6	5	5
Background time (s)	60	60	60	100	90	90
Ablation time (s)	40	40	40	40	40	40
Post-ablation washout time (s)	52	52	52	45	40	40
Primary standard	NIST612	NIST612	NIST612	NIST612	NIST612, NIST614	NIST612, NIST614
Secondary standard(s)	Garnet PHN3511, BIR-1G	Garnet PHN3511, BIR-1G	Garnet PHN3511, BIR-1G	SC-GB	Garnet PHN3511, BIR-1G	Garnet PHN3511, BIR-1G

Table A.3 - LA-ICP-MS secondary standards.

	K	**Ca**	**Sc**	**Ti**	**Mn**	**Co**	**Ni**	**Rb**	**Sr**	**Y**	**Zr**
B1R-IG avg	195	94306	44	6215	1327	56	187	0.214	107	13.8	13
B1R-IG 2SD	48	30946	15	2089	373	15	48	0.087	33	5.3	5
Average LOD	0.285	18	0.031	0.580	0.081	0.038	0.318	0.011	0.010	0.002	0.015
GeoReM value	183	95054	43	5400	1471	52	178	0.197	109	14.3	14
Accuracy %	**6**	**-1**	**2**	**15**	**-10**	**8**	**5**	**9**	**-1**	**-4**	**-7**
	Nb	**Ba**	**La**	**Ce**	**Pr**	**Nd**	**Sm**	**Eu**	**Gd**	**Tb**	
B1R-IG avg	0.47	6.3	0.562	1.75	0.33	2.19	1.02	0.471	1.70	0.31	
B1R-IG 2SD	0.14	1.8	0.193	0.54	0.11	0.63	0.33	0.157	0.62	0.12	
Average LOD	0.001	0.014	0.001	0.001	0.001	0.004	0.005	0.002	0.008	0.001	
GeoReM value	0.52	6.5	0.609	1.89	0.37	2.37	1.09	0.517	1.85	0.35	
Accuracy %	**-9**	**-3**	**-8**	**-8**	**-10**	**-8**	**-6**	**-9**	**-8**	**-11**	
	Dy	**Ho**	**Er**	**Tm**	**Yb**	**Lu**	**Hf**	**Pb**	**Th**	**U**	
B1R-IG avg	2.30	0.51	1.542	0.22	1.52	0.220	0.52	3.4	0.03	0.026	
B1R-IG 2SD	0.81	0.20	0.574	0.09	0.55	0.083	0.22	0.8	0.03	0.044	
Average LOD	0.003	0.001	0.002	0.001	0.010	0.003	0.008	0.002	0.001	0.001	
GeoReM value	2.55	0.56	1.7	0.24	1.64	0.248	0.57	3.7	0.03	0.023	
Accuracy %	**-10**	**-9**	**-9**	**-9**	**-7**	**-11**	**-9**	**-7**	**-1**	**13**	

LA-ICP-MS standards continued

	K	**Ca**	**Sc**	**Ti**	**Mn**	**Co**	**Ni**	**Rb**	**Sr**	**Y**	**Zr**
PHN3511 avg	0.61	29927	58.7	3363	2121	58.1	69.4	0.058	0.309	32.9	38.6
PHN3511 2SD	0.94	3145	7.5	341	108	3.3	4.4	0.277	0.182	5.2	8.4
Average LOD	0.19	13	0.02	0.4	0.06	0.02	0.3	0.008	0.007	0.001	0.02
M. Hardman	-	34091	-	3744	2246	-	72.6	-	0.312	38.5	43.6
Accuracy %	**-**	**-12**	**-**	**-10**	**-6**	**-**	**-4**	**-**	**-1**	**-14**	**-11**
	Nb	**Ba**	**La**	**Ce**	**Pr**	**Nd**	**Sm**	**Eu**	**Gd**	**Tb**	
PHN3511 avg	0.047	0.088	0.014	0.145	0.074	0.733	0.917	0.527	2.61	0.606	
PHN3511 2SD	0.115	0.330	0.024	0.112	0.115	0.103	0.149	0.095	0.39	0.108	
Average LOD	0.002	0.010	0.001	0.001	0.001	0.003	0.003	0.001	0.01	0.001	
M. Hardman	0.039	0.001	0.011	0.140	0.063	0.795	1.007	0.589	2.905	0.712	
Accuracy %	**21**	**7005**	**20**	**4**	**18**	**-8**	**-9**	**-11**	**-10**	**-15**	
	Dy	**Ho**	**Er**	**Tm**	**Yb**	**Lu**	**Hf**	**Pb**	**Th**	**U**	
PHN3511 avg	5.11	1.23	3.94	0.554	3.852	0.541	0.879	0.030	0.008	0.019	
PHN3511 2SD	0.82	0.20	0.58	0.088	0.596	0.096	0.176	0.132	0.050	0.119	
Average LOD	0.002	0.001	0.004	0.001	0.006	0.002	0.006	0.001	0.001	0.000	
M. Hardman	6.04	1.47	4.64	0.659	4.533	0.644	0.967	-	-	-	
Accuracy %	**-15**	**-16**	**-15**	**-16**	**-15**	**-16**	**-9**	**-**	**-**	**-**	

LA-ICP-MS standards continued

	K	**Ca**	**Sc**	**Ti**	**Mn**	**Co**	**Ni**	**Rb**	**Sr**	**Y**	**Zr**
NIST614 avg	28	82384	0.81	3.12	1.31	0.69	0.88	0.811	43.3	0.73	0.778
NIST614 2SD	2	2651	0.05	0.39	0.08	0.04	0.19	0.050	1.8	0.05	0.087
Average LOD	0.3	19	0.035	0.673	0.076	0.040	0.284	0.011	0.012	0.001	0.012
GeoReM value	30	-	0.74	3.61	1.42	0.79	1.1	0.855	45.8	0.79	0.848
Accuracy %	**-7**	**-**	**10**	**-13**	**-7**	**-13**	**-20**	**-5**	**-5**	**-8**	**-8**
	Nb	**Ba**	**La**	**Ce**	**Pr**	**Nd**	**Sm**	**Eu**	**Gd**	**Tb**	
NIST614 avg	0.771	3.06	0.66	0.715	0.699	0.698	0.726	0.70	0.718	0.671	
NIST614 2SD	0.045	0.15	0.03	0.042	0.044	0.051	0.052	0.08	0.054	0.064	
Average LOD	0.003	0.02	0.001	0.001	0.001	0.004	0.005	0.002	0.008	0.001	
GeoReM value	0.824	3.20	0.72	0.813	0.768	0.752	0.754	0.77	0.763	0.739	
Accuracy %	**-6**	**-4**	**-9**	**-12**	**-9**	**-7**	**-4**	**-9**	**-6**	**-9**	
	Dy	**Ho**	**Er**	**Tm**	**Yb**	**Lu**	**Hf**	**Pb**	**Th**	**U**	
NIST614 avg	0.685	0.688	0.70	0.661	0.712	0.674	0.655	2.21	0.694	0.720	
NIST614 2SD	0.070	0.035	0.02	0.021	0.057	0.031	0.119	0.07	0.044	0.144	
Average LOD	0.003	0.001	0.010	0.001	0.010	0.003	0.009	0.002	0.001	0.001	
GeoReM value	0.746	0.749	0.74	0.732	0.777	0.732	0.711	2.32	0.748	0.823	
Accuracy %	**-8**	**-8**	**-6**	**-10**	**-8**	**-8**	**-8**	**-5**	**-7**	**-13**	

Table A.4 – LA-ICP-MS secondary standard for olivine analysis.

	Al	**Ca**	**Sc**	**Ti**	**V**	**Cr**	**Mn**	**Co**	**Ni**	**Cu**	**Zn**	**Rb**
SC-GB avg	100	524	3.3	4.1	3.5	158	1074	149	3076	1.0	67	0.001
SC-GB 2SD	4	18	0.1	0.6	0.1	19	17	4	65	0.1	3	0.001
Average LOD	0.022	1.358	0.005	0.050	0.001	0.039	0.013	0.002	0.017	0.005	0.013	0.001
Average LOQ	0.066	4.075	0.014	0.149	0.003	0.118	0.040	0.006	0.052	0.016	0.040	0.003
Bussweiler (2017)	85	452	3.2	3.9	3.4	166	1160	146	3329	0.99	65	-
Accuracy %	**18**	**16**	**2**	**5**	**3**	**-5**	**-7**	**2**	**-8**	**-1**	**4**	**-**
	Sr	**Y**	**Zr**	**Nb**	**Ba**	**La**	**Ce**	**Pr**	**Nd**	**Sm**	**Eu**	**Gd**
SC-GB avg	0.004	0.039	0.026	0.0030	0.0012	0.0004	0.0010	0.0001	0.0008	0.0005	0.0002	0.0010
SC-GB 2SD	0.002	0.004	0.006	0.0025	0.0002	0.0005	0.0015	0.0001	0.0007	0.0002	0.0002	0.0005
Average LOD	0.001	0.0001	0.001	0.0001	0.0010	0.0001	0.0001	0.0001	0.0004	0.0004	0.0001	0.0006
Average LOQ	0.002	0.0004	0.002	0.0004	0.0029	0.0004	0.0002	0.0002	0.0012	0.0012	0.0004	0.0017
Bussweiler (2017)	0.003	0.04	0.026	0.002	-	-	0.0003	-	-	-	-	-
Accuracy %	**45**	**-3**	**-1**	**48**	**-**	**-**	**221**	**-**	**-**	**-**	**-**	**-**
	Tb	**Dy**	**Ho**	**Er**	**Tm**	**Yb**	**Lu**	**Hf**	**Pb**	**Th**	**U**	
SC-GB avg	0.0003	0.0036	0.0013	0.0070	0.0017	0.0181	0.0044	b.d.l.	0.0025	0.0003	0.0001	
SC-GB 2SD	0.0002	0.0011	0.0004	0.0009	0.0004	0.0035	0.0008	b.d.l.	0.0053	0.0003	0.0001	
Average LOD	0.0001	0.0003	0.0001	0.0002	0.0001	0.0014	0.0004	0.0010	0.0003	0.0001	0.0001	
Average LOQ	0.0002	0.0008	0.0002	0.0006	0.0004	0.0043	0.0011	0.0031	0.0008	0.0002	0.0002	
Bussweiler (2017)	-	-	-	-	-	-	-	-	-	-	-	
Accuracy %	**-**	**-**	**-**	**-**	**-**	**-**	**-**	**-**	**-**	**-**	**-**	

b.d.l. = below detection limit.

Table A.5 – HR-ICP-MS secondary standards for melt pocket analysis.

Isotope	**Rb85**	**Sr88**	**Y89**	**Nb93**	**Mo98**	**Cs133**	**Ba138**	**La139**	**Ce140**
OKUM avg	0.816	14.395	8.047	0.303	0.316	0.169	5.537	0.368	1.193
GeoReM value	0.894	15.692	9.432	0.367	0.200	0.173	5.839	0.393	1.250
Accuracy (%)	**9**	**8**	**15**	**18**	**-58**	**3**	**5**	**6**	**5**
Isotope	**Pr141**	**Nd143**	**Sm147**	**Eu151**	**Gd157**	**Tb159**	**Dy163**	**Ho165**	**Er167**
OKUM avg	0.220	1.424	0.688	0.285	1.057	0.215	1.531	0.343	1.042
GeoReM value	0.232	1.464	0.697	0.304	1.168	0.224	1.557	0.338	1.009
Accuracy (%)	**5**	**3**	**1**	**6**	**9**	**4**	**2**	**-1**	**-3**
Isotope	**Yb173**	**Lu175**	**Hf178**	**Ta181**	**Pb208**	**Th232**	**U238**	**Mg24**	**Ca43**
OKUM avg	0.988	0.151	0.544	0.022	0.200	0.028	0.010	#######	47219.696
GeoReM value	0.992	0.148	0.537	0.018	0.218	0.027	0.010	128808	55103
Accuracy (%)	**0**	**-2**	**-1**	**-24**	**8**	**-3**	**-2**	**-16**	**14**
Isotope	**Sc45**	**Ti47**	**Ti49**	**V51**	**Cr52**	**Mn55**	**Co59**	**Cu63**	**Ga69**
OKUM	29.414	1975.175	2007.938	156.604	######	1215.191	83.096	41.143	8.270
GeoReM value	27.9	2098	2098	167.8	2385	1394.026	88	42.1	8.05
Accuracy (%)	**-5**	**6**	**4**	**7**	**7**	**13**	**6**	**2**	**-3**
Isotope	**Zr90**								
OKUM	13.721								
GeoReM value	14.9								
Accuracy (%)	**8**								

HR-ICP-MS secondary standards for melt pockets continued.

Isotope	**Rb85**	**Sr88**	**Y89**	**Nb93**	**Mo98**	**Cs133**	**Ba138**	**La139**	**Ce140**
MUH	0.213	7.569	0.820	0.033	0.573	0.090	4.479	0.135	0.220
GeoReM value	0.270	8.500	0.970	0.062	0.171	0.099	4.980	0.134	0.200
Accuracy (%)	**21**	**11**	**15**	**47**	**-235**	**9**	**10**	**0**	**-10**
Isotope	**Pr141**	**Nd143**	**Sm147**	**Eu151**	**Gd157**	**Tb159**	**Dy163**	**Ho165**	**Er167**
MUH	0.035	0.174	0.068	0.025	0.104	0.021	0.152	0.034	0.107
GeoReM value	0.035	0.177	0.068	0.026	0.110	0.021	0.153	0.036	0.108
Accuracy (%)	**0**	**2**	**0**	**3**	**5**	**3**	**1**	**4**	**1**
Isotope	**Yb173**	**Lu175**	**Hf178**	**Ta181**	**Pb208**	**Th232**	**U238**	**Mg24**	**Ca43**
MUH	0.118	0.019	0.030	0.002	0.412	0.018	0.014	265400.660	7232.974
GeoReM value	0.118	0.019	0.029	0.002	0.420	0.018	0.014	229500	8672.95
Accuracy (%)	**0**	**0**	**-6**	**-11**	**2**	**1**	**2**	**-16**	**17**
Isotope	**Sc45**	**Ti47**	**Ti49**	**V51**	**Cr52**	**Mn55**	**Co59**	**Cu63**	**Ga69**
MUH	9.381	171.897	173.419	34.739	2030.679	767.148	97.146	16.346	1.164
GeoReM value	9.7	206.4	206.4	41	2710	742.77	106	22.4	1.38
Accuracy (%)		**17**	**16**	**15**	**25**	**-3**	**8**	**27**	**16**
Isotope	**Zr90**								
MUH	0.481								
GeoReM value	0.69								
Accuracy (%)	**30**								

Table A.6 – Kimberlite whole rock HR-ICP-MS secondary standards.

	Rb85	**Sr88**	**Y89**	**Nb93**	**Mo98**	**Cs133**	**Ba138**	**La139**	**Ce140**	**Pr141**
TE340 BHVO-2	9.15	420.03	24.31	17.63	3.31	0.10	135.20	14.88	36.56	5.28
GeoReM value	9.11	396.00	26.00	18.10	4.00	0.10	131.00	15.20	37.50	5.35
Accuracy (%)	**0.4**	**6.1**	**-6.5**	**-2.6**	**-17.1**	**-3.9**	**3.2**	**-2.1**	**-2.5**	**-1.3**
	Nd143	**Sm147**	**Eu151**	**Gd157**	**Tb159**	**Dy163**	**Ho165**	**Er167**	**Yb173**	**Lu175**
TE340 BHVO-2	24.24	5.92	2.01	6.13	0.93	5.20	0.97	2.50	1.96	0.27
GeoReM value	24.50	6.07	2.07	6.24	0.92	5.31	0.98	2.54	2.00	0.27
Accuracy (%)	**-1.1**	**-2.4**	**-2.8**	**-1.8**	**0.8**	**-2.0**	**-0.8**	**-1.5**	**-1.8**	**-0.9**
	Hf178	**Ta181**	**Pb208**	**Th232**	**U238**	**Mg24**	**Ca43**	**Sc45**	**Ti47**	**Ti49**
TE340 BHVO-2	4.39	1.07	1.47	1.13	0.40	47463.77	79083.41	35.64	17228.87	17020.66
GeoReM value	4.36	1.14	1.60	1.22	0.40			32.00	16300.00	16300.00
Accuracy (%)	**0.7**	**-6.3**	**-8.1**	**-7.3**	**-1.0**			**11.4**	**5.7**	**4.4**
	V51	**Cr52**	**Mn55**	**Co59**	**Ni60**	**Cu63**	**Zn64**	**Ga69**	**Zr90**	
TE340 BHVO-2	352.00	312.54	1323.81	48.21	127.87	135.57	113.11	22.59	177.20	
GeoReM value	317.00	280.00		45	119.00	127.00	103.00	22.00	172.00	
Accuracy (%)	**11.0**	**11.6**		**7.1**	**7.5**	**6.7**	**9.8**	**2.7**	**3.0**	

Kimberlite whole rock HR-ICP-MS secondary standards continued.

	Rb85	**Sr88**	**Y89**	**Nb93**	**Mo98**	**Cs133**	**Ba138**	**La139**	**Ce140**	**Pr141**
TE 341 BCR-2	46.24	359.86	33.66	12.10	247.40	1.16	706.41	25.07	53.87	6.80
GeoReM value	46.02	337.40	36.07	12.44	250.60	1.16	683.90	25.08	53.12	6.83
Accuracy (%)	**0.5**	**6.7**	**-6.7**	**-2.7**	**-1.3**	**-0.1**	**3.3**	**0.0**	**1.4**	**-0.4**
	Nd143	**Sm147**	**Eu151**	**Gd157**	**Tb159**	**Dy163**	**Ho165**	**Er167**	**Yb173**	**Lu175**
TE 341 BCR-2	28.99	6.67	1.99	6.87	1.07	6.42	1.30	3.73	3.41	0.50
GeoReM value	28.26	6.55	1.99	6.81	1.08	6.42	1.31	3.67	3.39	0.50
Accuracy (%)	**2.6**	**1.9**	**0.0**	**0.8**	**-0.7**	**0.0**	**-0.8**	**1.7**	**0.5**	**0.0**
	Hf178	**Ta181**	**Pb208**	**Th232**	**U238**	**Mg24**	**Ca43**	**Sc45**	**Ti47**	**Ti49**
TE 341 BCR-2	5.05	0.74	9.46	5.71	1.66	23329.18	48868.94	36.73	14117.48	13703.67
GeoReM value	4.97	0.79	10.59	5.83	1.68	21594.00	50865.10	33.53	13590.00	13590.00
Accuracy (%)	**1.5**	**-6.0**	**-10.6**	**-2.1**	**-1.3**	**8.0**	**-3.9**	**9.5**	**3.9**	**0.8**
	V51	**Cr52**	**Mn55**	**Co59**	**Ni60**	**Cu63**	**Zn64**	**Ga69**	**Zr90**	
TE 341 BCR-2	454.06	15.88	1537.85	40.04	12.26	17.94	136.85	22.80	191.01	
GeoReM value	417.60	15.85	1513.82	37.33	12.57	19.66	129.50	22.27	186.50	
Accuracy (%)	**8.7**	**0.2**	**1.6**	**7.3**	**-2.5**	**-8.7**	**5.7**	**2.4**	**2.4**	

Kimberlite whole rock HR-ICP-MS secondary standards continued.

	Rb85	**Sr88**	**Y89**	**Nb93**	**Mo98**	**Cs133**	**Ba138**	**La139**	**Ce140**	**Pr141**
TE 342 AGV-2	69.74	686.33	18.70	13.52	1.97	1.15	1158.19	36.76	71.23	8.11
GeoReM value	66.30	661.00	19.00	14.50		1.20	1130.00	37.90	68.60	7.84
Accuracy (%)	**5.2**	**3.8**	**-1.6**	**-6.8**		**-3.9**	**2.5**	**-3.0**	**3.8**	**3.4**
	Nd143	**Sm147**	**Eu151**	**Gd157**	**Tb159**	**Dy163**	**Ho165**	**Er167**	**Yb173**	**Lu175**
TE 342 AGV-2	30.49	5.44	1.58	5.07	0.65	3.51	0.66	1.84	1.65	0.25
GeoReM value	30.50	5.49	1.53	4.52	0.64	3.47	0.65	1.81	1.62	0.25
Accuracy (%)	**0.0**	**-0.9**	**3.2**	**12.1**	**2.2**	**1.3**	**1.4**	**1.7**	**1.8**	**1.6**
	Hf178	**Ta181**	**Pb208**	**Th232**	**U238**	**Mg24**	**Ca43**	**Sc45**	**Ti47**	**Ti49**
TE 342 AGV-2	5.30	0.80	12.64	5.84	1.82	11437.85	35681.34	13.89	6233.27	6265.81
GeoReM value	5.00	0.87	13.20	6.10	1.86			13.00		
Accuracy (%)	**5.9**	**-8.4**	**-4.3**	**-4.2**	**-2.3**			**6.9**		
	V51	**Cr52**	**Mn55**	**Co59**	**Ni60**	**Cu63**	**Zn64**	**Ga69**	**Zr90**	
TE 342 AGV-2	127.91	16.16	750.30	16.62	18.84	52.85	91.57	21.35	238.73	
GeoReM value	122.00	16.00		16.00	20.00	53.00	86.00	20.00	230.00	
Accuracy (%)	**4.8**	**1.0**		**3.9**	**-5.8**	**-0.3**	**6.5**	**6.7**	**3.8**	

Table A.7 – JNdi primary TIMS standards.

Sample Name	**$^{143}Nd/^{144}Nd$ (meas)**	**2σ**	**$^{145}Nd/^{144}Nd$**	**2σ**	**$^{148}Nd/^{144}Nd$**	**2σ**
Jndi-50ppb 1	0.512037	0.000016	0.348427	0.000009	0.241501	0.000014
Jndi-50ppb 2	0.512030	0.000016	0.348418	0.000008	0.241498	0.000013
Jndi-50ppb 3	0.512032	0.000016	0.348423	0.000011	0.241480	0.000014
Jndi-50ppb 4	0.512062	0.000018	0.348429	0.000013	0.241487	0.000015
Jndi-50ppb 5	0.512054	0.000021	0.348420	0.000010	0.241512	0.000014
Jndi-50ppb 6	0.512048	0.000017	0.348419	0.000010	0.241489	0.000012
Jndi-50ppb 7	0.512041	0.000022	0.348422	0.000011	0.241498	0.000013
Jndi-50ppb 8	0.512033	0.000018	0.348428	0.000012	0.241503	0.000013
Jndi-50ppb 9	0.512059	0.000017	0.348434	0.000012	0.241503	0.000013
Jndi-50ppb 10	0.512036	0.000016	0.348426	0.000012	0.241482	0.000017
Average	**0.512043**		**0.348425**		**0.241495**	
2SD	**0.000024**		**0.000010**		**0.000020**	
Jndi GeoReM	**0.512103**		**0.348399**		**0.241581**	
Offset from accepted (ppm)	**-116.45**		**72.61**		**-353.69**	

Table A.8 – BHVO-2 secondary TIMS standards.

Sample Name	**^{143}Nd/^{144}Nd**	**2SE**	**^{145}Nd/^{144}Nd**	**2SE**	**^{148}Nd/^{144}Nd**	**2SE**
BHVO-2-1	0.513004	0.000011	0.348427	0.000006	0.241528	0.000009
BHVO-2-2	0.512980	0.000008	0.348418	0.000005	0.241545	0.000007
Average	**0.512992**		**0.348423**			
2SD	**0.000035**		**0.000012**			
BHVO-2 (Weis et al., 2006)	**0.512984**		**0.348407**			
Offset from accepted (ppm)	**15.92**		**43.71**			

Table A.9 – NBS987 primary TIMS standards.

Sample Name	**$^{87}Sr/^{86}Sr$**	**2σ**	**2σ propagated**
NBS987-2	0.710260	0.000010	0.000016
NBS987-3	0.710270	0.000011	0.000017
NBS987-4	0.710243	0.000011	0.000017
NBS987-5	0.710252	0.000008	0.000015
NBS987-6	0.710256	0.000008	0.000015
NBS987-7	0.710257	0.000013	0.000018
NBS987-8	0.710251	0.000008	0.000015
NBS987-9	0.710259	0.000006	0.000014
NBS987-10	0.710244	0.000006	0.000014
Average	**0.710255**		
2SD	**0.000017**		
NBS 987 accepted val	**0.71025**		
Offset from accepted (ppm)	**6.43**		

Table A.10 – BHVO-2 secondary TIMS standards.

Sample Name	**$^{87}Sr/^{86}Sr$**	**2σ**	**2σ propagated**
BHVO2_1b	0.703470	0.000009	0.000016
BHVO2_1c	0.703479	0.000007	0.000015
BHVO2-2a	0.703467	0.000008	0.000015
BHVO2-2b	0.703481	0.000017	0.000021
BHVO2-2c	0.703473	0.000009	0.000016
BHVO2-3a	0.703483	0.000009	0.000016
BHVO2-3b	0.703487	0.000007	0.000015
Average	**0.703477**		
2SD	**0.000014**		
BHVO-2 GeoRem	**0.703478**		
Offset from accepted (ppm)	**-1.16**		

Appendix B

B.1 Petrography

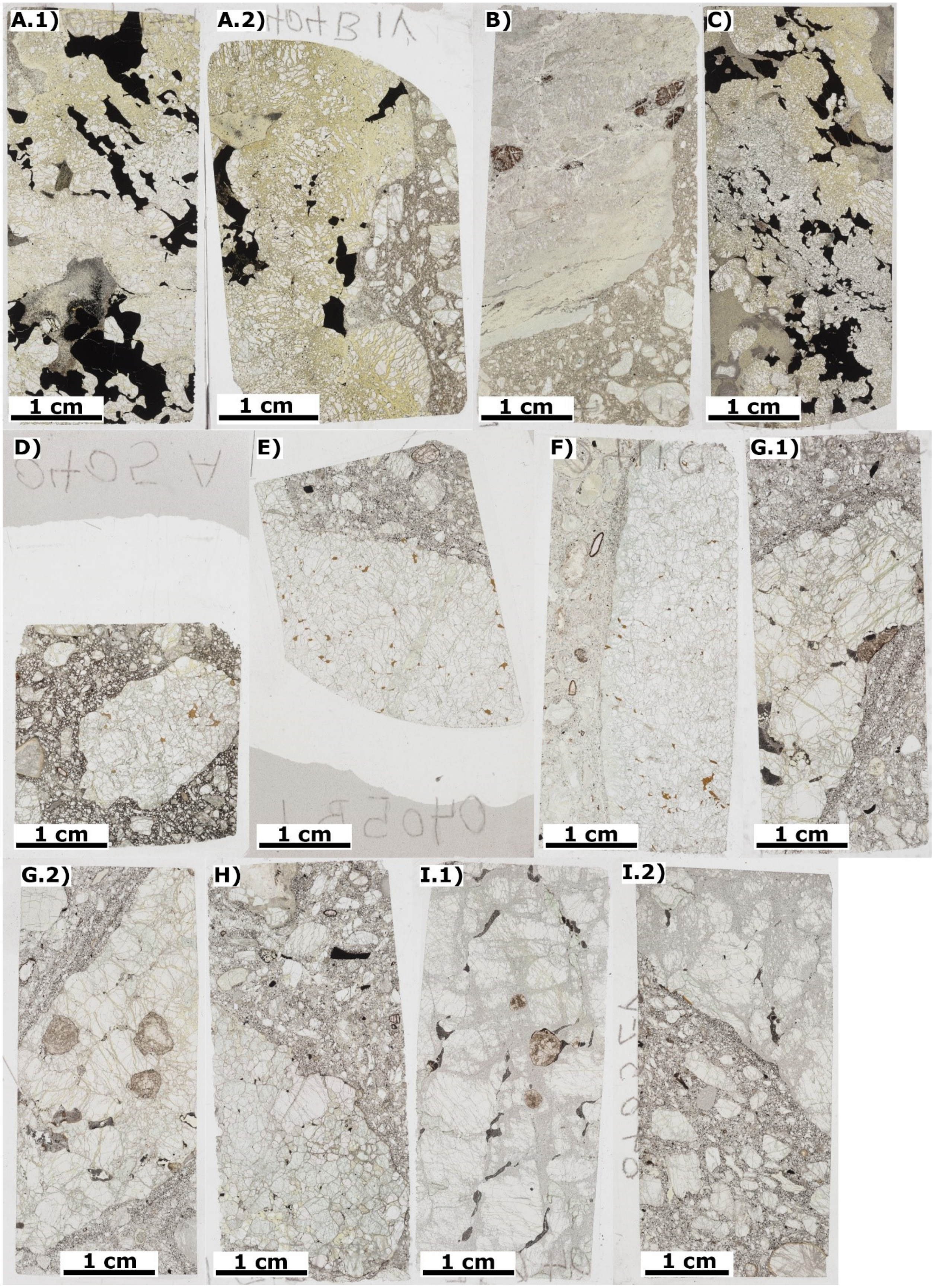
A.1)
1 cm
A.2)
1 cm
B)
1 cm
C)
1 cm
D)
1 cm
E)
1 cm
F)
1 cm
G.1)
1 cm
G.2)
1 cm
H)
1 cm
I.1)
1 cm
I.2)
1 cm

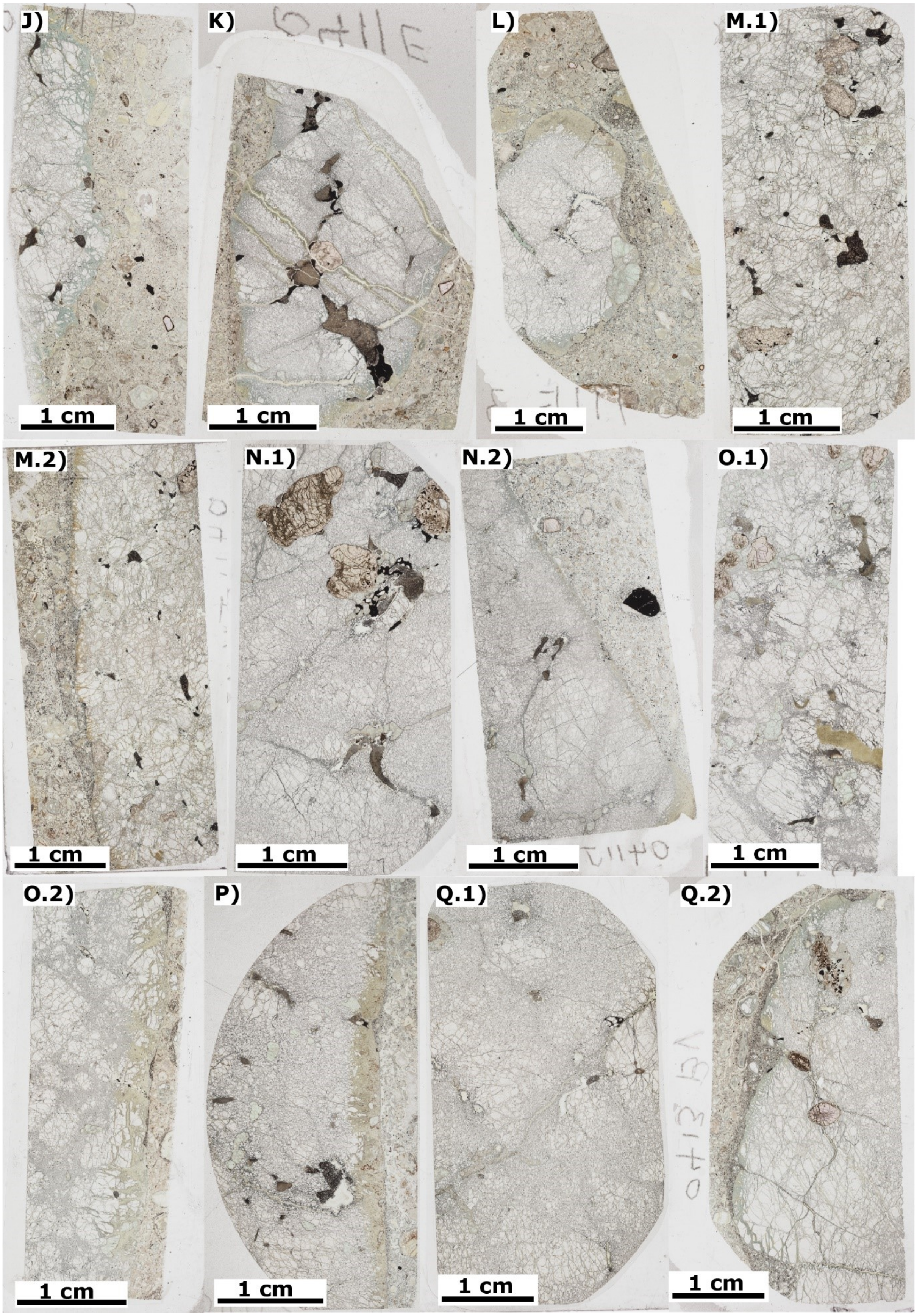
J)
1 cm
K)
1 cm
L)
1 cm
M.1)
1 cm
M.2)
1 cm
N.1)
1 cm
N.2)
1 cm
O.1)
1 cm
O.2)
1 cm
P)
1 cm
Q.1)
1 cm
Q.2)
1 cm

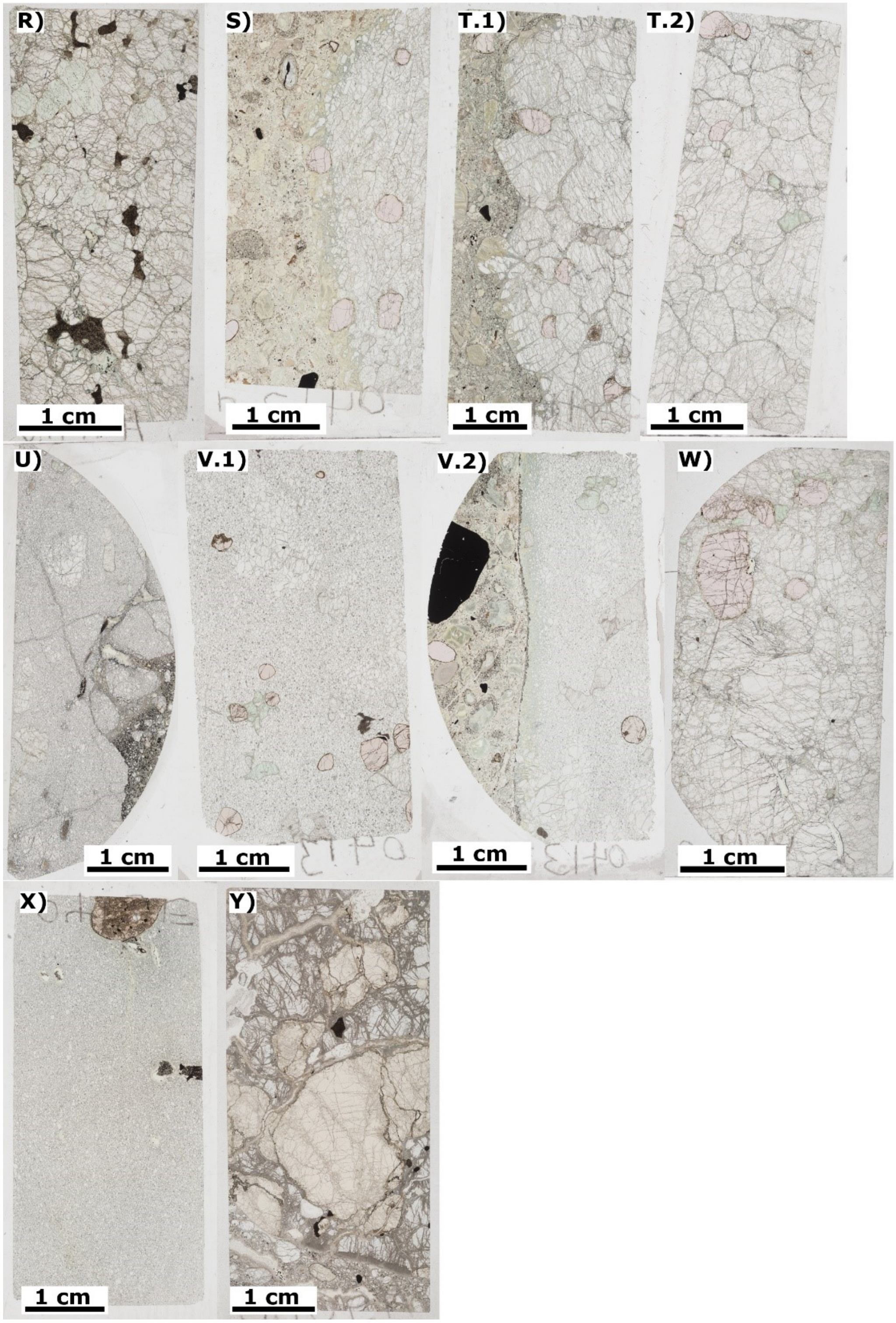

Figure B.1 - Visible light thin section scans of xenoliths: A.1) 0404B1, A.2) 0404B1V, B) 0404B2, C) 0404C, D) 0405A, E) 0405B, F) 0411C, G.1) 0405C, G.2) 0405CM, H) 0405D1, I.1) 0405E, I.2) 0405EV, J) 0411D, K) 0411E, L) 0411F3, M.1) 0411I, M.2) 0411IV, N.1) 0411J, N.2) 0411JV, O.1) 0411K, O.2) 0411KV, P) 0411G, Q.1) 0413B, Q.2) 0413BV, R) 0411H, S) 0413C, T.1) 0411F1, T.2) 0411F1M, U) 0411F2V, V.1) 0413D, V.2) 0413DV, W) 0413A, X) 0413E, Y) 0405H.

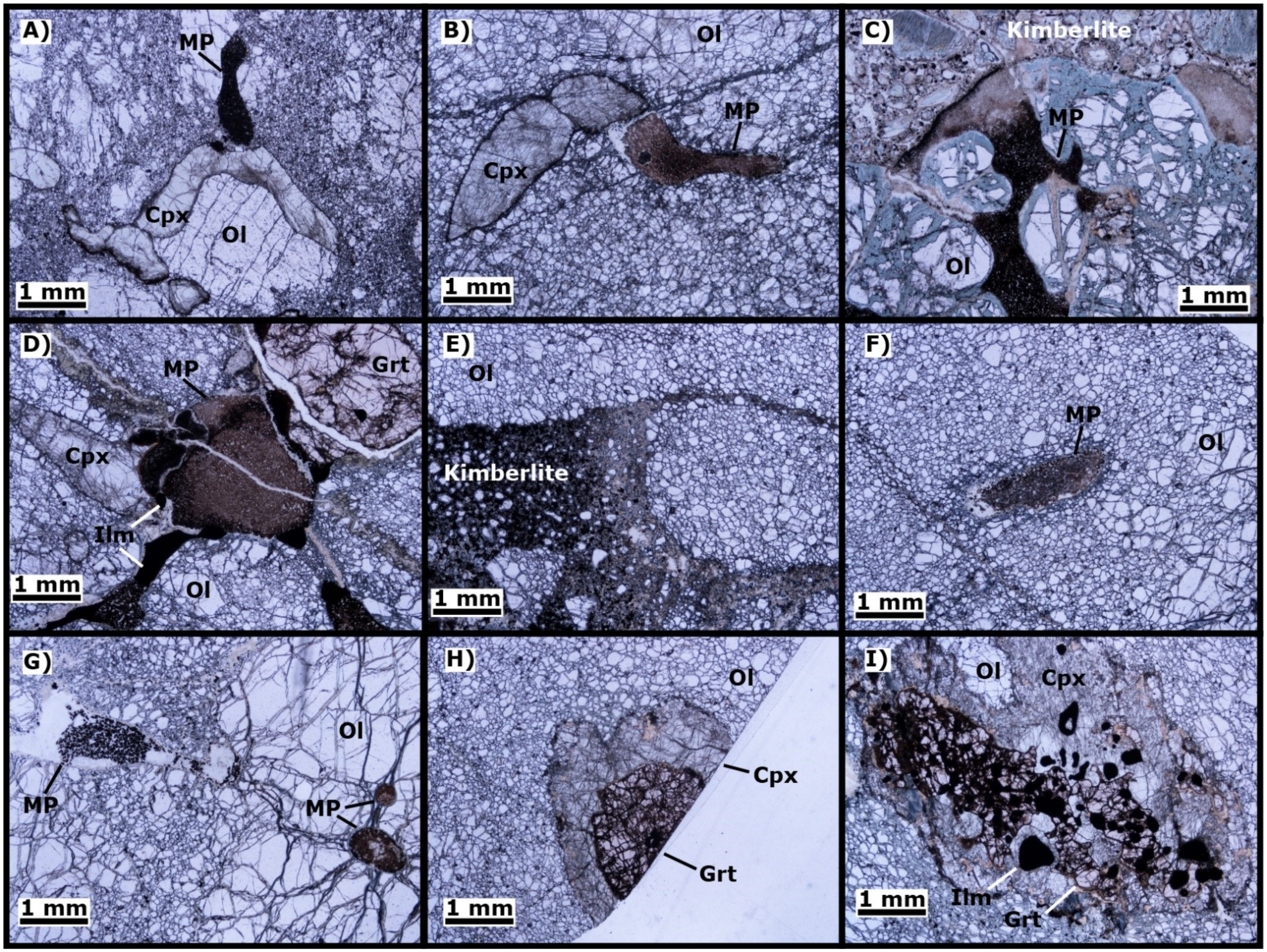

Figure B.2 - Thin section photomicrographs in PPL of features observed in xenoliths (MP = Melt pocket): A) 0405EV, B) 0411JV, C) 0411DV, D) 0411E, E) 0411F2V, F) 0411F2V, G) 0413B, H) 0413B, I) 0413BV.

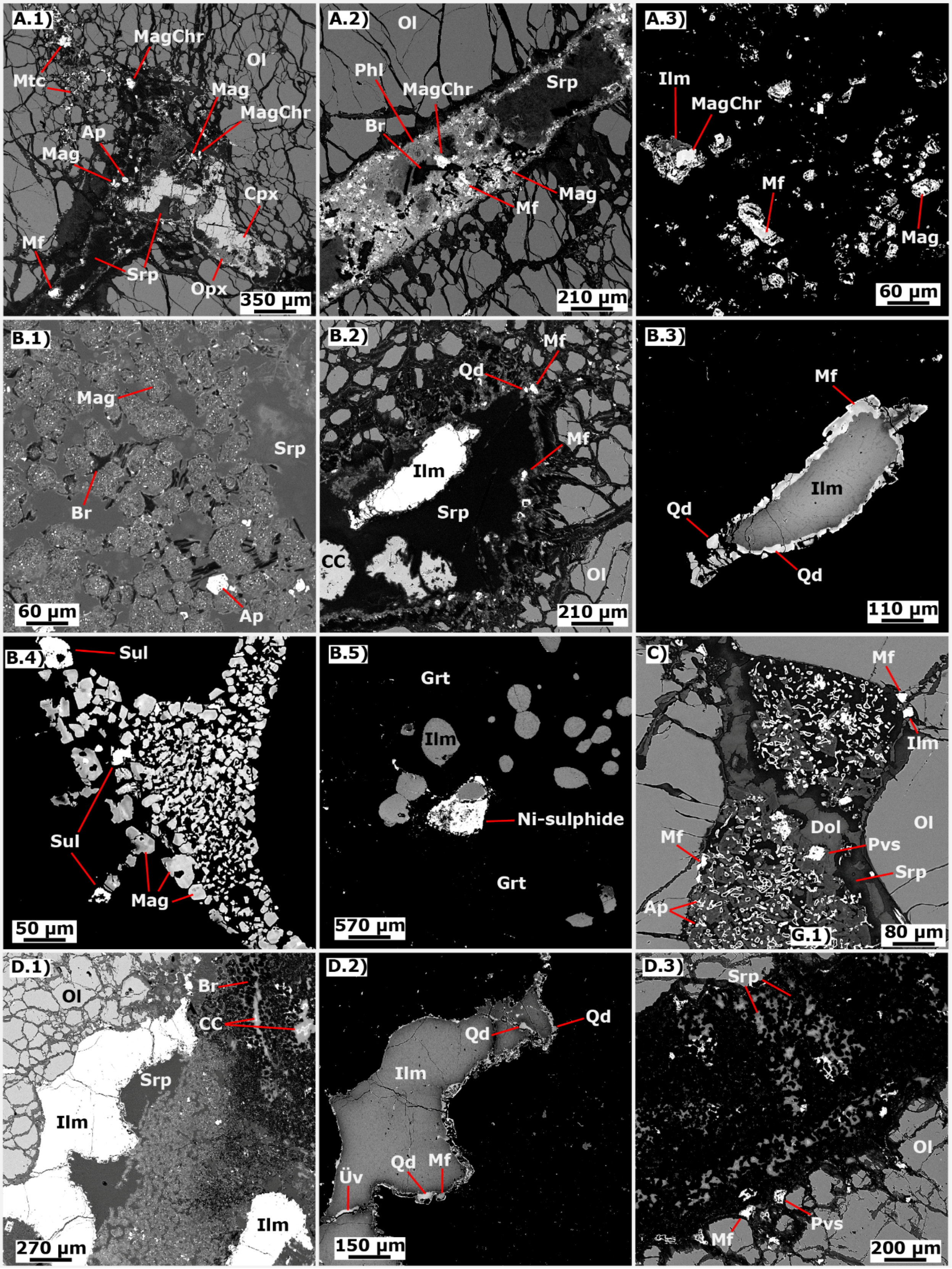
A.1)
MagChr
Ol
Mtc
Mag
MagChr
Ap
Mag
Cpx
Mf
Srp
Opx
350 µm
A.2)
Ol
Phl
MagChr
Srp
Br
Mag
Mf
210 µm
A.3)
Ilm
MagChr
Mf
Mag
60 µm
B.1)
Mag
Srp
Br
Ap
60 µm
B.2)
Mf
Qd
Mf
Ilm
Srp
CC
Ol
210 µm
B.3)
Mf
Ilm
Qd
Qd
110 µm
B.4)
Sul
Sul
Mag
50 µm
B.5)
Grt
Ilm
Ni-sulphide
Grt
570 µm
C)
Mf
Ilm
Ol
Dol
Mf
Pvs
Srp
Ap
G.1)
80 µm
D.1)
Ol
Br
CC
Srp
Ilm
Ilm
270 µm
D.2)
Qd
Qd
Ilm
Qd
Mf
Üv
150 µm
D.3)
Srp
Ol
Pvs
Mf
200 µm

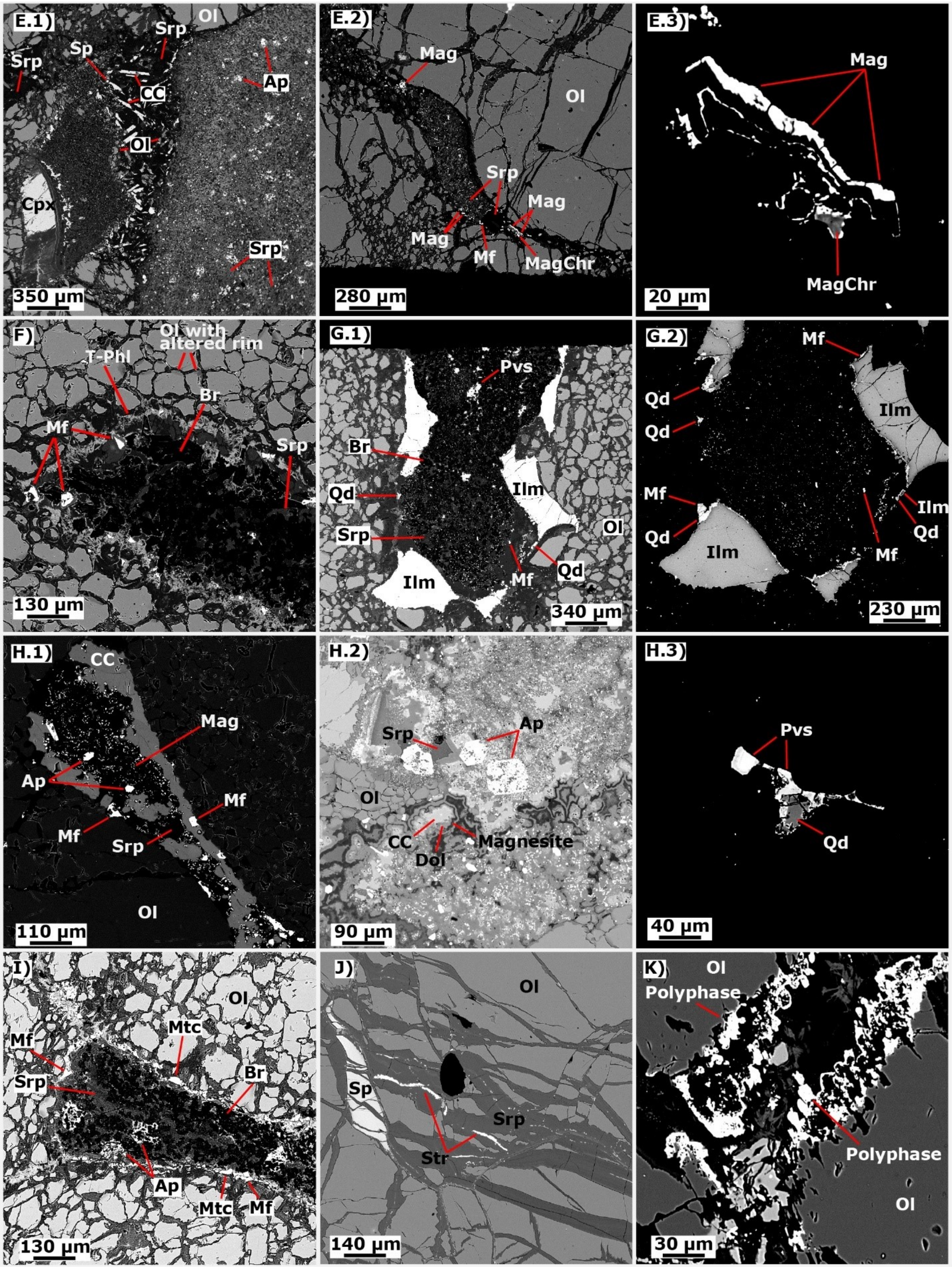
E.1)
Ol
Srp
Sp
Srp
Ap
CC
Ol
Cpx
Srp
350 µm
E.2)
Mag
Ol
Srp
Mag
Mag
Mf
MagChr
280 µm
E.3)
Mag
MagChr
20 µm
F)
Ol with altered rim
T-Phl
Br
Mf
Srp
130 µm
G.1)
Pvs
Br
Qd
Ilm
Srp
Ol
Ilm
Mf
Qd
340 µm
G.2)
Mf
Qd
Qd
Ilm
Mf
Ilm
Qd
Qd
Ilm
Mf
230 µm
H.1)
CC
Mag
Ap
Mf
Mf
Srp
Ol
110 µm
H.2)
Srp
Ap
Ol
CC
Dol
Magnesite
90 µm
H.3)
Pvs
Qd
40 µm
I)
Ol
Mf
Mtc
Srp
Br
Ap
Mtc
Mf
130 µm
J)
Ol
Sp
Srp
Str
140 µm
K)
Ol
Polyphase
Polyphase
Ol
30 µm

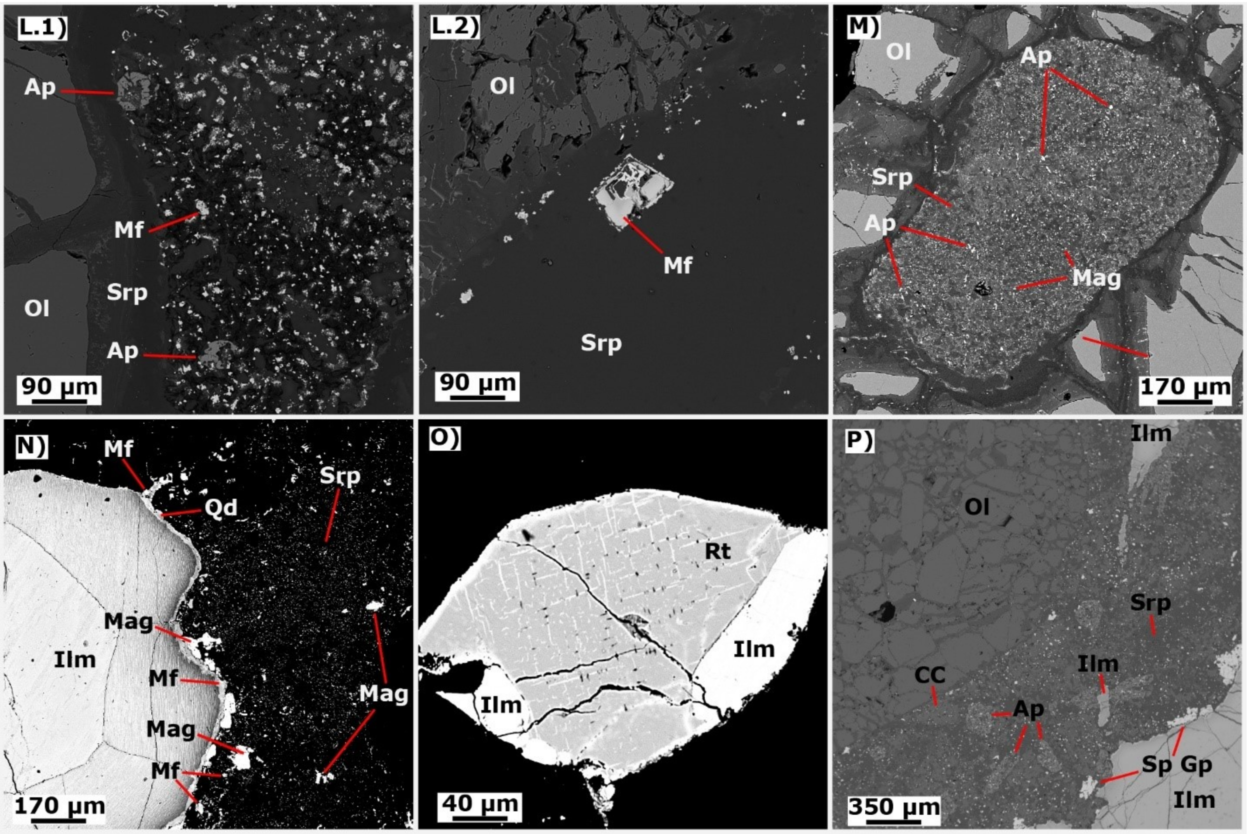

Figure B.3 - BSE images of melt intrusions within xenoliths, except image B.5) and O), which is ilmenite and sulphide inclusions in a garnet in 0413BV, and a rutile grain within melt-free xenolith 0405D1, respectively. Annotations: CC = calcite, Dol = dolomite, Str = strontianite, Ap = apatite, Srp = serpentine, T-Phl = tetraferriphlogopite, Mag = magnetite, Mf = magnesioferrite, Qd = qandilite, Ilm = ilmenite, Rt = rutile, MagChr = magnesiochromite, Mtc = monticellite, Br = brucite, Polyphase = mineral mixture, Pvs = perovskite, Sp Gr = spinel group, Sp = spinel, Sul = sulphide. Xenoliths in the images correspond to: A.1) – A.3) = 0411F3, B.1) – B.5) 0413BV, C) 0405CM, D.1) – D.3) 0411J, E.1) – E.3) 0411K, F) 0411F2V, G.1) – G.2) 0413E, H.1) – H.3) 0405E, I) 0411E, J) 0405B, K) 0411DV, L.1) – L.2) 0411IV, M) 0413DV, N) 0404B1V, O) 0405D, P) 0404C.